Improving the performance of nano-optomechanical systems for use as mass sensors

by

Jocelyn Bachman

A thesis submitted in partial fulfillment of the requirements for the degree of

Doctor of Philosophy

Department of Physics
University of Alberta

Abstract

Coupling optical cavities to freely moving mechanical devices results in optomechanical systems. Enabled by advancing fabrication techniques, optomechanical systems are now easily fabricated using silicon-on-insulator chips at the micro- and nanoscale. These nano-optomechanical systems (NOMS) combine nanomechanical devices with photonic integrated circuits for sensitive readout of mechanical displacement. NOMS have many potential applications, including mass detection. In this thesis, we work towards improving the dynamic range of cantilevers coupled to photonic circuits for mass sensing applications. We use an all-optical pump-and-probe approach. First, we derive and demonstrate a simple model for designing optomechanical systems for efficient actuation via the optical gradient force. We achieve large amplitudes of vibration and show the power required to achieve these amplitudes is nearly four times smaller than an unoptimized design. When driving the cantilever to large amplitudes, we observe multiple simultaneous nonlinearities. To understand the source of these nonlinearities, we derive and solve a numerical model that allows us to determine that there are three nonlinearities present in the system; a readout nonlinearity and two distinct optical force nonlinearities. The model is unique in that it incorporates the effect of the pump laser on the optomechanical system. Of all the nonlinearities, the readout nonlinearity is the most detrimental to mass sensing performance as it hinders our ability to determine the amplitude of the mechanical device. To mitigate the readout nonlinearity, we design a photonic integrated circuit to increase the linear range of NOMS readout. This photonic architecture successfully increases the linear range by a factor of four while maintaining the sensitivity of the previous design. These improvements increase the dynamic range, and therefore the limit of detection, by a factor of 2.8. The work presented here will help to improve the viability of NOMS mass sensors in a variety of applications, including portable health care diagnostic tools.

Preface

Some of the research conducted for this thesis was completed as part of collaborations. Section 3.1.3 was part of a Mitacs research project. This project was supervised by Dr. Vien Van from the University of Alberta and completed in collaboration with the Alberta Centre for Advanced MNT Products (ACAMP), a not-for-profit organization. I completed the device simulation, fabrication, and analysis with assistance from Dr. Van and Mr. William Cully at ACAMP. Chapter 5 was completed in collaboration with staff at the Nanotechnology Research Centre led by Dr. Wayne Hiebert. The code for the numerical model in this chapter was created and run by Dr. Alexander Kobryn at the Nanotechnology Research Centre. The analysis of the numerical model's results, the experimental data collection, and the experimental data analysis are my original work. Chapter 6 was completed in collaboration with Dr. Vien Van from the University of Alberta. The initial concept and mathematical description for the device fabricated in this chapter was provided by Dr. Van. The device design, experiment, and data analysis are my original work. Focused ion beam imaging was completed by Mr. Doug Vick from the Nanotechnology Research Centre. The data collection and analysis in Sections 3.2 and 3.3, the concept, data collection, and analysis in Sections 3.1.1, 3.1.2, and Chapter 4, and the literature review in Chapter 2 are my original work.

Section 3.2 of this thesis has been published as J. N. Westwood-Bachman, Z. Diao, V. T. K. Sauer, D. Bachman, and W. K. Hiebert, Even nanomechanical modes transduced by integrated photonics, Applied Physics Letters, vol. 108, page 061103. I was responsible for the device fabrication, data collection, data analysis, and manuscript composition. Z. Diao provided the concept and contributed to the manuscript edits. V. T. K. Sauer contributed to the data analysis and the manuscript edits. D. Bachman contributed to the data analysis. W. K. Hiebert was the supervisory author, and was involved with concept formation, data analysis, and manuscript edits.

Acknowledgements

First of all, I would like to thank my supervisor, Wayne Hiebert, for introducing me to optomechanics during my undergraduate capstone project many years ago. During my Ph.D., Wayne permitted me great freedom to study whatever topics I chose and encouraged me to attend many conferences and workshops, which was invaluable experience.

During my Ph.D., I completed an 8 month internship at the Alberta Centre for Advanced MNT Products (ACAMP) through the Mitacs Accelerate internship program. This industrial experience was invaluable for my career development. All of the work in Section 3.1.3 was completed in partnership with ACAMP and Dr. Vien Van from Electrical and Computer Engineering. I would like to thank Dr. Van, Mitacs, and ACAMP for this opportunity. I would also like to thank the people at ACAMP who helped with my project including Jia, Golam, and Mara. Most of all, I would like to thank Will for getting the project off the ground and creating this opportunity.

There were many people at the University of Alberta who contributed to this work by providing me with advice, training, and ideas. The NanoFab staff, especially Scott Munro and Aaron Hryciw, provided training and cleanroom expertise. Aaron also did the helium ion microscope imaging. I would like to thank Anandram Venkatasubramanian and Haifa Qadi for their assistance with fabricating samples in the NanoFab. My Ph.D. benefited significantly from the photonics expertise of Dr. Van and Dr. Bachman. The staff at the Nanotechnology Research Centre provided access and training for the SEM and AFM characterization tools. Doug Vick did the FIB imaging of the samples. Alexander Kobryn contributed significantly by creating numerical models of my devices. Input from postdoctoral fellows Zhu Diao and Vincent Sauer was instrumental for much of this work. Finally, I would like to thank my fellow Ph.D. students, especially Mariana Alvarado and Swapan Roy, for their support along the way.

Additionally, I received support from CMC Microsystems and the SiEPIC program. I attended SiEPIC workshops, which were valuable learning experiences. Fabrication of my photonic samples would not have been possible without CMC Microsystems and the foundry access they provide.

Pursuing a Ph.D. would not have been possible without my funding sources, including Vanier Canada Graduate Scholarships, Alberta Innovates Technology Futures, the Government of Alberta, the Natural Sciences and Engineering Research Council of Canada, and the University of Alberta.

Lastly I would like to thank my family for their ongoing support in this journey. Mom, Dad, Erica, and most of all Danny – I could not have done this without your support and encouragement.

Contents

List of Figures

List of Tables

Chapter 1

Introduction

Sensors are an integral part of our daily lives. Through advances in micro- and nanofabrication, sensors have become smaller and less costly. Sensor technology is now portable and even wearable, as demonstrated by commercial wearable fitness trackers that monitor heart rates and count steps. Portable sensor technology has many potential applications, including point-of-care health diagnostic tools, environmental monitoring, and gas analysis.

Improvements in nanofabrication techniques have also decreased the detection limit of nanoscale sensors. The detection limit describes the smallest mass or concentration of an analyte that the sensor can resolve. For example, carbon nanotubes have been used to detect masses as small as 1.66 yg (1 yoctogram $= 1 \times 10^{-24}$ g), which is the mass of a single proton [1]. However, the experimental conditions were ultra high vacuum and a low temperature of 6 K. Although the sensor itself has an exquisite detection limit, it is not suitable for use in a portable sensing application.

For applications where portable sensors are desirable, we must achieve a balance between obtaining an exceptional detection limit and operating at ambient conditions. A technology that may be able to meet these requirements is mass sensors based on nanomechanical devices. Nanomechanical devices have mechanical degrees of freedom and vibrate with a characteristic resonance frequency that is dependent on the device geometry. When an analyte molecule is adsorbed on the surface of the nanomechanical device, the increase in mass introduced by the analyte results in a decrease in the mechanical resonance frequency. Therefore, the mass of the analyte molecule is detected as a shift in the resonance frequency of the nanomechanical device. Nanomechanical devices have been used to demonstrate detection of biological molecules [2, 3, 4, 5] and various gases [6, 7, 8, 9]. Clearly this technology is suitable for sensing different types of analytes, and may find use in health care applications, or gas sensing and analysis.

In addition to the mass sensor itself (the nanomechanical device), we also require a transducer to actuate and read out the sensor. One transduction method is integrated photonics. Integrated photonics was originally developed for use in telecommunications. Waveguides, with dimensions on the order of hundreds of nanometres, carry light across the surface of a silicon-on-insulator (SOI) chip. With improvements in fabrication techniques leading to decreasing cost, silicon photonics has become more accessible for applications beyond telecommunications. Silicon photonic devices, originally designed as filters, have been re-purposed as sensors. For example, the resonant frequency of a microring optical cavity is sensitive to changes in the external environment. While this can be detrimental for filter performance, it means that optical cavities are excellent sensors. Microring resonators have been used to detect biological molecules with nanogram concentration [10]. The same sensing principles can be used to detect the motion of nanomechanical devices. This readout technique, called nanophotonic transduction, decreases the noise floor and increases the displacement sensitivity compared to other transduction techniques [11]. The bandwidth of the technique is also very high, since integrated photonic devices were originally designed for telecommunication applications that typically require modulation frequencies in the tens of gigahertz. The bandwidth is therefore only limited by electronics external to the nanophotonic transducer. The high bandwidth allows for high frequency nanomechanical devices, which in turn improves the detection limit of the nanomechanical mass sensor. Nanomechanical devices and optical cavities can be integrated onto the same platform, an SOI wafer, using standard CMOS processing techniques. This drives down the cost per device substantially, as millions of these devices can be fabricated in a small area [12].

The mass sensor and transducer together are called a nano-optomechanical system. The field of study that encompasses the combined system of a mechanical device and an optical cavity is called optomechanics. Much of the current work in optomechanics focuses on developing systems for use in quantum computing [13, 14, 15]. To date, the application of optomechanical systems to mass sensing has been fairly limited. Some work has been done to develop optomechanical systems for sensing in liquid [16, 17]. Gas sensing using optomechanical doubly clamped beams has been demonstrated with 1 ppb sensitivity [9]. Recently, sensitivity has even been shown to improve with higher damping [18].

With the proof-of-concept demonstrated for nano-optomechanical mass sensing systems, we must now work towards improving the technology with the end goal of a low-power, low-cost, portable sensing device in mind. In particular, we focus on improvements that will help propel this technology towards use in health diagnostic tools or in gas analysis. In this work, we will discuss several different approaches to solving these challenging problems, and work towards creating a practical mass sensing device. In the third chapter of the thesis, we focus on several practical considerations. Reducing the size and complexity of the entire sensing system including electronics and packaging is an important consideration. We will demonstrate a technique for reading out high frequency nanomechanical signals at low frequency to reduce the cost and complexity of the external electronics. An approach for incorporating spatial resolution [19] through the use of multiple mechanical modes of vibration in optomechanical systems to correctly determine the added mass of an analyte molecule is also discussed. Finally, sensors that are compatible with not only gaseous but fluidic samples are desirable as well. Analysis of fluidic samples will allow the devices to be used in health diagnostic tools since this application typically requires analysis of fluidic samples. A new device architecture designed specifically for operation in fluid is presented, along with a package for low-cost, temperature stabilized microfluidics measurements.

We wish to continue improving the detection limit, while decreasing the power consumption and improving the portability. In the main section of the thesis, comprised of Chapters 4 – 6, we will show that by designing the mass sensor and transducer together, we can improve the efficiency of actuation, which lowers the input power requirement. The detection limit may be improved by increasing the dynamic range, since as the dynamic range increases, the minimum detectable mass decreases [20]. One approach that may be used to improve the dynamic range is to increase the amplitude of vibration of the nanomechanical device. While increasing the amplitude, nonlinearities in the sensor and transducer must also be reduced or eliminated. We present an in-depth study of the sources of nonlinearity in a nano-optomechanical system, and suggest an alternative transducer design that can help eliminate the observed nonlinearities.

As a relatively new field, there is a significant area to explore to enhance and improve mass sensing performance using nano-optomechanical systems. We will demonstrate several promising options for device optimization that help to reduce cost, complexity, power use, and improve overall performance of the sensor and transducer.

1.1 Outline

In Chapter 2, we provide background information on the topics of nanomechanics, integrated photonics, and how these technologies can be combined into optomechanical systems. This section consolidates important details of optomechanical systems that may be of use to future students, such as equations describing the behaviour of optical cavities using both the power and energy coupling formalisms, the equations for modeling coherent backscattering in optical cavities, and equations describing optomechanics in integrated photonics systems including the transduction coefficient. We also provide details of our experimental setup.

Chapter 3 is a collection of several different experiments in which we work towards improving practical mass sensing systems by addressing the difficulties in packaging, portability, and operation in fluidic environments. In Section 3.1, the possibility of optomechanical sensing in fluid and the requirements of both photonic and mechanical design to make fluid sensing feasible are explored. In particular, designs for and fabrication of narrow mechanical fin resonators as thin as 20 nm are carried out. It also includes work towards developing an inexpensive package for microfluidic sensors, including a built-in plastic photonic temperature sensor. All of the work done in this section is intended to improve operation in fluidic environments. Section 3.2 discusses the design and fabrication of integrated photonics circuits for detecting even modes in doubly clamped beams. It is based on the work published in [21]. Section 3.3 shows the design of, and results from, a measurement scheme for detecting high frequency mechanical signals at DC with a single laser for both drive and detection. This work is a step towards simplifying the experimental setup for commercial applications.

In the main body of the thesis, comprised of Chapters 4 – 6, we focus specifically on improving the dynamic range of the nano-optomechanical system for gas sensing applications. In Chapter 4, we discuss how to design an optomechanical system to maximize the efficiency of the optical driving force applied to a nanomechanical beam in the pump-and-probe configuration. We derive a simple model that can be used to design efficient optomechanical systems. Experimental results verify the derived model. By applying a moderate driving force, we achieve large amplitudes of vibration and begin to see nonlinear effects in the experimental results.

Chapter 5 studies further the nonlinearities first observed in Chapter 4. We show detailed experimental results of the nonlinearities, including some unexpected results that cannot be explained using existing work. We adapt an existing analytic model for our pump-and-probe configuration, which accurately describes some, but not all, of our experimental results. We then derive a numerical model that accounts for the presence of two lasers in our optomechanical system to more accurately match the experimental conditions. This model allows us to determine that there are three different types of nonlinearity present; a readout nonlinearity, and two distinct optical force nonlinearities. This valuable insight cannot be obtained through experiment as the nonlinearities cannot be separated in the observed results. The numerical model delivers excellent qualitative agreement with the experimental results, and allows for a direct estimation of the mechanical amplitude. By comparing the numerical model to the experimental results, we gain an improved understanding of how nonlinearities arise in nano-optomechanical systems actuated using a pump-and-probe approach.

The readout nonlinearity observed in Chapter 5 is problematic as it prevents proper estimation of the nanomechanical amplitude. For this reason, we wish to address the readout nonlinearity and reduce its effect. That is the focus of Chapter 6. In this chapter, we design an alternative photonic circuit for transducing nanomechanical motion. The circuit is a racetrack-loaded Mach Zehnder interferometer that provides phase-sensitive detection of nanomechanical displacement. The circuit is designed to have a large linear range to reduce the readout nonlinearity observed in Chapter 5. We explore a wide parameter space in the design of these devices to find the most linear designs for future mass sensors. The devices are fabricated and measured experimentally. Both optical and mechanical measurements demonstrate that the performance of the photonic circuit is as expected from the design. The results verify that the racetrack-loaded MZI has a larger linear range without sacrificing sensitivity, and will be beneficial for creating more powerful mass sensors.

Chapter 2

Background

Optomechanics is an extremely multidisciplinary field where a strong understanding of both optics and mechanics is required. To provide sufficient context for the work done in this thesis, we will describe the necessary background information in both nanomechanics and integrated photonics. We will then discuss how these two technologies couple together to create optomechanical systems.

First, we will discuss nanomechanics. We will cover the essential types of nanomechanical systems and the governing equations. In particular, we will discuss the experimentally relevant procedure for converting the measured data in volts to metres, which is useful in data analysis.

We will then cover the relevant subjects in integrated photonics. This is a well-established field with many different applications and devices. We will discuss the fundamentals of ring resonators and directional couplers, the main devices used in this thesis. We will also discuss coherent backscattering, which is an effect that can occur in silicon photonics, and appears in many of our experimental results.

Lastly, we will discuss how the nanomechanics and optomechanics interact to form a single optomechanical system. This section will show how our measurements are done, and how we extract the mechanical properties of the system from optical measurements.

2.1 Nanomechanics

With improvements in fabrication processes in the past decade, microelectromechanical systems have been scaled down to create nanomechanical devices. These small resonators take a variety of forms. Most commonly nanomechanical devices are cantilevers, doubly clamped beams, or disks. They vibrate with very small amplitudes and have very small motional mass (effective mass, m_{eff}), on the order of picograms or less. Nanomechanical devices have a characteristic resonance frequency ($\Omega_{\text{n}} = 2\pi f_{\text{n}}$) that is dependent on the device dimensions. For thin beams, the resonance frequency and amplitude can be determined by solving the wave equation [22, 23];

$$EI\frac{\partial^2 u_{\mathrm{n}}(x,t)}{\partial x^4} = -\rho A\frac{\partial^2 u_{\mathrm{n}}(x,t)}{\partial x^2}, \tag{2.1}$$

where $u_{\mathrm{n}}(x,t)$ is the amplitude of the n^{th} mode shape, and is a function of time and x. x is the spatial coordinate along the length of the beam. E is the Young's modulus, I is the moment of inertia, ρ is the density of the material in units of $\mathrm{kg/m^3}$, and A is the cross-sectional area of the nanomechanical device. Solving Eq. (2.1) for the appropriate boundary conditions allows for the solutions for both doubly and singly clamped beams (cantilevers). One important use of the mode shape function $u_{\mathrm{n}}(x,t)$ is to calculate the effective mass of the nanomechanical device. The effective mass is the mass of the device modified by a factor that accounts for the normalized mode shape ($\hat{u_{\mathrm{n}}}$) of the n^{th} mode of vibration. The effective mass is calculated using Eq. (2.2) [24, 25];

$$m_{\mathrm{eff}} = \rho A\int_0^l \hat{u_{\mathrm{n}}}^2(x)\mathrm{d}x, \tag{2.2}$$

where the amplitude of the mode shape u_{n} has been normalized to one, which is represented by the hat notation.

In many cases, it is sufficient to consider the nanomechanical device as a simple harmonic oscillator instead of requiring the full solution to Eq. (2.1). The behaviour of a simple harmonic oscillator, a system of a spring connected to a point mass m, is defined by

$$m\frac{\mathrm{d}^2x}{\mathrm{d}t^2} = -kx, \tag{2.3}$$

where $k = m\Omega_{\mathrm{n}}^2$ is the spring constant of the simple harmonic oscillator. The solution to this equation is $x(t) = B\cos(\Omega t + \varphi)$ where B is the amplitude and φ is the phase. In many cases we apply a driving force to the simple harmonic oscillator. In the presence of a driving force we must also consider damping of the simple harmonic oscillator. Damping can be expressed by the quality factor Q of the system. The quality factor is defined as the stored energy divided by the energy lost per cycle [26]. The equation for a damped, driven simple harmonic oscillator is

$$m\frac{\mathrm{d}^2x}{\mathrm{d}t^2} + \frac{m\Omega}{Q}\frac{\mathrm{d}x}{\mathrm{d}t} + kx = F(t), \tag{2.4}$$

where the driving force is defined as $F(t)$. If $F(t)$ is sinusoidal such that $F(t) = F_0\cos(\Omega t + \varphi_d)$ where F_0 is the amplitude and φ_{d} is the phase of the driving force, then the steady state solution to Eq. (2.4) is the same as the simple harmonic oscillator. The amplitude of the driven, damped harmonic oscillator is a Lorentzian of the form:

$$B = \frac{F_0/m}{\sqrt{[\Omega_0^2 - \Omega^2]^2 + (\Omega\Omega_0/Q)^2}}. \tag{2.5}$$

This amplitude is referred to as the driven amplitude, as it is the amplitude of the device when it is driven by an external driving force. We can simplify this expression for the case where $\Omega_0 = \Omega$. In that case, the relationship between the force and amplitude is

$$F_0 = \frac{kB}{Q}. \tag{2.6}$$

The expressions for the simple harmonic oscillator and the driven damped simple harmonic oscillator are often used to approximate the behaviour of nanomechanical devices. In particular, Eq. (2.6) is a useful expression as the force applied to a device can often be calculated with relative ease, allowing an estimate of the nanomechanical amplitude to be obtained. Damping in nanomechanical systems can be introduced by a range of different mechanisms, such as viscous damping [27, 28], thermoelastic dissipation [29, 30], and clamping loss [31, 32] to name a few. Forces can be applied to nanomechanical devices in many different ways as well. This is referred to as actuation of the nanomechanical device and can be achieved using different techniques such as electrostatically [33, 34, 35, 36], physically shaking the devices with a piezoelectric disk [37, 38, 39, 40], on-chip piezoelectric actuation [41, 42, 43, 44], photothermal actuation [45, 46, 47, 48, 49], or through the optical gradient force [50, 51, 52, 53, 54]. Readout of the motion of nanomechanical devices can occur in a number of ways including capacitive detection [55, 56, 57], with piezoelectric or piezoresistive circuits [27, 58, 59, 60, 61, 62], using optical interferometry [63, 64, 65, 66], or more recently using integrated photonics and evanescent detection [67, 68, 69]. The combined procedure of detection and actuation of nanomechanical devices is called transduction.

Nanomechanical systems are a promising technology for use as mass sensors. When mass is added to a nanomechanical device, the resonance frequency shifts. By tracking the size of this frequency shift, the magnitude of the mass can be determined. To first order, the mass sensitivity (δm) of nanomechanical systems is described as

$$\delta m = 2m_{\text{eff}}\frac{\delta\Omega_0}{\Omega_0}, \tag{2.7}$$

where $\delta\Omega_0$ is the minimum resolvable frequency shift and is dependent on the sources of noise in the measurement system. If the instrument noise level is independent of the driven amplitude, $\delta\Omega_0/\Omega_0$ is inversely proportional to the driven amplitude of the sensor, since $< \delta\Omega_0/\Omega_0 > \approx a_{\text{noise}}/(2QB)$ [18]. B is the amplitude of the nanomechanical device when a driving force is applied, as previously defined in

Eq. (2.5). a_{noise} is the amplitude of the nanomechanical noise floor, which is often the thermomechanical noise as we will see in the following section. By operating the nanomechanical device at its maximum linear driven amplitude, we ensure that the optimal mass sensitivity for a given system is achieved [20]. The amplitude is linear if an increase in the driving force produces a linear increase in the amplitude, that is, the behaviour of the nanomechanical device is governed by Eq. (2.5).

Eq. (2.7) only takes into account the added mass, and not its location on the device. The location where the mass is added on the device can also affect the frequency shift [70]. This can be accounted for by using a technique called inertial imaging [19]. Even with the added complexity of adsorbate position, the trends shown by Eq. (2.7) hold true; the smaller the device, the lower the minimum detectable mass. As the devices scale down in size, the effective mass decreases and the resonance frequency increases.

2.1.1 Thermomechanical Noise and Obtaining the Responsivity

The thermomechanical (TM) noise of a mechanical resonator is detected when no actuation force is applied, and is the Brownian motion of the device. When measured, the TM noise has an amplitude signal, but no coherent phase signal. When considering the dynamic range of a nanomechanical mass sensor, the TM noise represents a lower limit for the bottom end of the dynamic range [20, 71]. This is because the thermomechanical noise is the smallest amount of mechanical noise present in the device. This definition for the bottom end of the dynamic range assumes that the thermomechanical noise can be measured (that the transduction scheme has a sufficiently low noise level) and that there are no other significant sources of noise, which is typically the case for sensitively transduced nanomechanical devices at room temperature [9, 18].

We measure the TM noise with the experimental setup described in Section 2.4 using a lock-in amplifier or a spectrum analyzer to obtain the power spectral density (S_{v}) of the thermomechanical noise in units of V^2/Hz. We do not apply any driving forces. S_{v} is a Lorentzian function described by

$$S_{\mathrm{v}} = S_{\mathrm{v},0} + \frac{\alpha k_{\mathrm{b}} T f_0}{2\pi^3 m_{\mathrm{eff}} Q[(f^2 - f_0^2)^2 + (f f_0/Q)^2]}, \tag{2.8}$$

where T is the temperature, Q is the mechanical quality factor, and k_{b} is the Boltzmann constant. α is a fitting parameter that describes the conversion of the mechanical amplitude to a measured voltage by the transduction technique. By fitting the measured data with Eq. (2.8), we extract α, Q, f_0, and the noise floor $S_{\mathrm{v},0}$. These values can be used to calculate S_{v} on resonance. The value of S_{v} on resonance is defined as $S_{\mathrm{v,peak}}$ and calculated using Eq. (2.8) for $f = f_0$.

The peak height of the amplitude noise in meters ($S_{\mathrm{z,peak}}$) is well-understood due to the equipartition theorem [27]. It can be described by

$$S_{\mathrm{z,peak}} = \frac{4k_{\mathrm{b}}TQ}{m_{\mathrm{eff}}\Omega_0^3}. \tag{2.9}$$

We calculate the effective mass using Eq. (2.2). Although the effective mass can be calculated using numerical techniques such as the finite element method, for simple cantilevers and doubly clamped beams the mode shape $\hat{u_{\mathrm{n}}}$ is known analytically from the solution to Eq. (2.1). Therefore, in this work, the effective mass is calculated using an analytic expression solved with trapezoidal numerical integration. Since $S_{\mathrm{z,peak}}$ is known theoretically for a given device, we can use it to obtain a responsivity in units of volts/metre. The responsivity can be used to estimate the mechanical amplitude in metres from the measured signal in volts when a driving force is applied to the nanomechanical device. The transduction responsivity in volts per metre can be calculated using the following expression [27]:

$$\Re = \sqrt{\frac{S_{\mathrm{v,peak}} - S_{\mathrm{v,0}}}{S_{\mathrm{z,peak}}}}. \tag{2.10}$$

When using the responsivity to obtain an estimate of the amplitude of the mechanical device when subject to a driving force, it is important to carefully maintain the experimental parameters between the measurement of the thermomechanical noise and the measurement of the driven response. The amplitude in metres is obtained by dividing the measured signal in volts by $\Re$. By converting the data to metres, we are able to eliminate the effects of the transduction efficiency on the data and provide meaningful comparison between data sets.

2.2 Integrated Photonics

For detection of nanomechanical devices on-chip, we can make use of integrated photonics. Integrated photonics is a planar technology where light is guided across the surface of a substrate. The light travels through structures called waveguides. Waveguides are the building blocks of many other integrated photonics circuit components, including microring resonators or racetrack resonators. To couple light into the waveguides, integrated photonics components called grating couplers [72, 73] or alternative techniques such as edge coupling [74, 75] can be used.

In this section, we will discuss the physics of waveguiding structures and how they can be used to direct the flow of light on a substrate. The coupling of light onto the chip will also be described in detail. We will use the principles of waveguide operation to explain the design of the racetrack resonator cavities, including directional couplers [76, 77] to couple light from the bus waveguide into the racetrack.

We will also discuss the different formalisms used to describe optical cavities; the power coupling formalism often used in integrated photonics design, and the energy coupling formalism used by those studying optomechanics. We will show how to convert between the different formalisms. Finally, we will end with a discussion of one of the common issues in silicon photonics, which is coherent backscattering, and how this can be modeled and understood using the power coupling formalism.

2.2.1 Light Propagation through Waveguides

Waveguides are the simplest integrated photonic structure. Waveguide are planar structures made up of two components, the core and the cladding. The core is the interior of the waveguide. The cladding of a waveguide surrounds the core. The substrate is the surface on which the waveguide is fabricated. Waveguides can be fabricated in several different geometries. Cross-sectional schematics of three types of planar waveguides are shown in Figure 2.1. In these schematics, light travels in the z-direction as marked in the top right hand corner of the figure. Slab waveguides, shown in (a), are the simplest type of waveguide. In this type of waveguide, light is confined only in the vertical direction. Strip waveguides are shown in (b). These waveguides confine the light in both the vertical and horizontal directions. Rib waveguides, shown in (c), are a more complex type of waveguide and show that waveguides can have many different geometries so long as the conditions for light propagation in the structure are met.

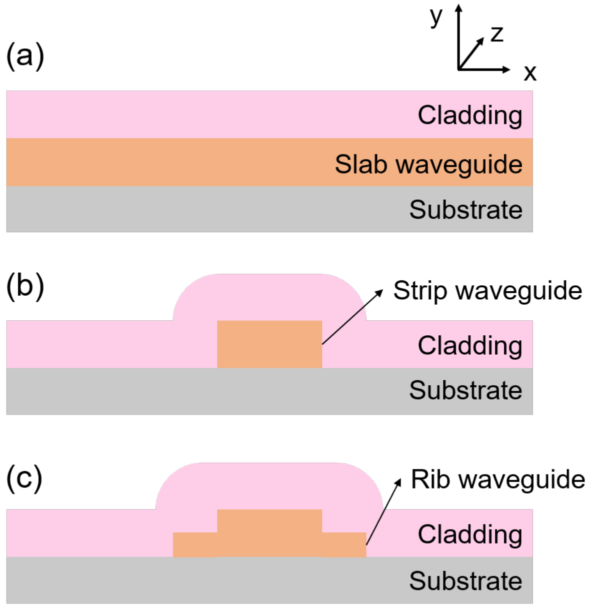

Figure 2.1: Cross-sectional schematics of (a) a slab waveguide, (b) a strip waveguide, and (c) a rib waveguide. Light propagates in the z-direction.

The first condition for light propagation in the waveguide is that the waveguide core must have a higher index of refraction than the surrounding cladding and substrate materials. Typically, this means that the waveguide core and cladding are made of different materials. The substrate can be made of the same material as the cladding or a different material, so long as the index of refraction of the substrate is also less than the core material. The condition that the core index of refraction must be higher than the cladding and substrate indices occurs because waveguides operate on the principle of total internal reflection. Rigorous derivation of this requirement is done by imposing the boundary conditions of Maxwell's equations to the waveguide core, and is detailed in many photonics textbooks [78, 79, 80]. For a simplistic derivation of this requirement, we can examine Snell's Law. Let us assume that light has been injected into the core material and arrives at the interface between the core and cladding at some incident angle θ_i. For the light to remain in the core of the waveguide, total internal reflection must occur. Therefore the sine of the angle of light transmitted at the interface must be greater than 1, that is $\sin\theta_\mathrm{t} > 1$. By Snell's Law we can state: $\sin\theta_\mathrm{i} > n_\mathrm{t}/n_\mathrm{i}$, where n_i and n_t are the indices of the incident (core) and transmitted (cladding) media, respectively. Since $\sin\theta_\mathrm{i} < 1$, the ratio $n_\mathrm{t}/n_\mathrm{i}$ must also be less than one. Therefore, the cladding index n_t cannot be larger than the core index n_i for light to propagate in the waveguide. If this condition is not met, light incident on the interface between the cladding and the core will be transmitted, and the light will exit the waveguide at this interface instead of propagating in the z-direction through the waveguide core.

The second condition for light propagation is due to the diffraction limit. The thickness of the waveguide slab must be greater than or equal to $\lambda/2$, where λ is the wavelength of light inside the slab. Below this thickness, propagation in the slab waveguide is cut-off [81, 82]. An example of this will be discussed later in the section when we describe common waveguide materials and fabrication techniques.

If these two conditions are met, we say the light is "confined" in the waveguide. In this case, total internal reflection is occurring and the waveguide thickness is above the diffraction limit, and the light is propagating within the waveguide. If the light is not confined, the light leaks out of the waveguide.

One of the outcomes of the fact that waveguides operate on the principle of total internal reflection is the formation of an evanescent wave at the interface between the waveguide core and cladding. This arises because of the boundary conditions at the dielectric interface. The evanescent wave is a wave that is bound to the core-cladding interface and propagates in the z-direction. The existence of the evanescent wave satisfies the boundary conditions under the condition of total internal reflection. The mathematical description of the evanescent wave can be derived using Snell's Law and assuming $\sin\theta_\mathrm{i} > n_\mathrm{t}/n_\mathrm{i}$ for the case of total internal reflection [83];

$$\mathbf{E}(t,z) = \mathbf{E}(t,0)\exp\left[-k_{\mathrm{t}}y\left(\frac{n_{\mathrm{i}}^2}{n_{\mathrm{t}}^2}\sin^2\theta_{\mathrm{i}} - 1\right)^{1/2}\right]\exp\left[i\left(k_{\mathrm{t}}z\frac{n_{\mathrm{i}}}{n_{\mathrm{t}}}\sin\theta_{\mathrm{i}} - \omega t\right)\right], \tag{2.11}$$

where $\mathbf{E}(t,z)$ is the transmitted wave, $\mathbf{E}(t,0)$ is the initial amplitude, k_{t} is the wave vector of the transmitted evanescent wave, ω is the frequency of the wave, and t is time. This wave propagates in the z direction but also extends into the cladding in the y direction, perpendicular to the interface between the waveguide and the cladding. This y component of the evanescent wave, which we can term the evanescent field, has an exponential decay. The decay length depends on the ratio of the waveguide (incident) and cladding (transmitted) indices. For large incident angles, $\sin\theta \approx 1$, therefore the decay length of the evanescent field can be approximated as $\lambda/(2\pi n_{\mathrm{t}}\sqrt{n_{\mathrm{i}}^2/n_{\mathrm{t}}^2 - 1})$ [84].

If the waveguide index is much larger than the cladding index ($n_{\mathrm{i}} >> n_{\mathrm{t}}$), this is called a high contrast waveguide. We can see in the first exponential term of Eq. (2.11) that the evanescent field decays over a shorter distance in this case. In low-contrast waveguides, the waveguide index is only slightly larger than the cladding index, and the decay length of the evanescent field increases. This is an important consideration when designing waveguides, as the decay length of the evanescent field may be important in determining whether to utilize high contrast or low contrast waveguides.

Although we can identify the condition for propagation using Snell's Law, a more detailed understanding of these waveguides is obtained by finding the electric field distribution. The wave equation for propagation of a wave in a linear, homogeneous material is shown by

$$\nabla^2\mathbf{E}(x,y,z) + n^2k^2\mathbf{E}(x,y,z) = 0, \tag{2.12}$$

where $\mathbf{E}(x,y,z)$ is the electric field vector, n is the index of refraction of the material, and k is the wave vector in free space. This equation is derived using Maxwell's laws and assuming that there are no current sources or free charges [85]. We can solve this equation for the one-dimensional slab waveguide shown in Figure 2.1(a). For the case of the simple slab waveguide, the waveguide core, cladding, and substrate indices are simply the bulk material indices. Let the direction of propagation be in the z-direction, such that $\mathbf{E}(x,y,z) = \mathbf{E}(x,y)\exp(i\beta z)$, where β is the propagation constant of the waveguide mode. Additionally, the slab waveguide is invariant in the x-direction, and therefore $\partial\mathbf{E}(x,y)/\partial x = 0$. The last step to simplifying Eq. (2.12) is to use the fact that the input plane wave is polarized in either the x or y direction, which means that predominantly only the x or y electric field component will be present in the waveguide. Waves with orthogonal polarizations will have different behaviour at the slab waveguide boundaries [86]. If only the x component of the electric field exists, this solution is called the transverse electric or TE polarization. Since this is a one-dimensional geometry, the TE polarized wave is invariant in the x direction and the wave equation for TE polarization then becomes [87]:

$$\frac{d^2 E_\mathrm{x}}{dy^2} + (n(y)^2 k^2 - \beta^2) E_\mathrm{x} = 0. \tag{2.13}$$

Eq. (2.13) has a characteristic equation with a finite number of solutions. The solutions to the characteristic equation are the propagation constants for different modes supported by the slab waveguide. Modes obtained by solving the characteristic equation of Eq. (2.13) are called TE modes. The characteristic equation is

$$2k_\mathrm{y} d - 2\arctan\left(\frac{\beta^2 - n_1^2 k^2}{k_\mathrm{y}}\right) - 2\arctan\left(\frac{\beta^2 - n_3^2 k^2}{k_\mathrm{y}}\right) = 2m\pi, \tag{2.14}$$

where m is an integer, k_y is the wave vector in the y direction, n_1 is the index of refraction of the substrate, n_3 is the index of the cladding, and d is the thickness of the waveguide layer. Once the propagation constant for each mode number m has been obtained, we can solve Eq. (2.13) for the electric field distribution for each mode. This allows us to see the electric field profile in the one-dimensional slab waveguide for each mode.

The same analysis can be followed for the magnetic field vector $\mathbf{B}(x, y, z)$ to obtain the results for the orthogonal polarization. This results in solutions for the transverse magnetic or TM polarization. The wave equation for the magnetic field B_x in the slab waveguide is

$$\frac{d^2 B_\mathrm{x}}{dy^2} + (n(y)^2 k^2 - \beta^2) B_\mathrm{x} = 0, \tag{2.15}$$

where the only component is the transverse magnetic field B_x. The characteristic equation for TM modes includes the index of refraction of the waveguide layer n_2:

$$2k_\mathrm{y} d - 2\arctan\left(\frac{n_2^2[\beta^2 - n_1^2 k^2]}{n_1^2 k_\mathrm{y}}\right) - 2\arctan\left(\frac{n_2^2[\beta^2 - n_3^2 k^2]}{n_3^2 k_\mathrm{y}}\right) = 2m\pi. \tag{2.16}$$

For the dielectric strip and rib waveguides pictured in Figure 2.1(b) and (c), no analytic solution for the electric and magnetic fields or propagation constants exists. These structures are complicated by the fact that the light propagating in the waveguide is confined in two dimensions, and not just one. For this reason, numerical techniques such as finite difference or finite element analysis are commonly used in waveguide design [88]. An alternative technique is the effective index method [89, 90, 91]. The effective index method uses the analytic solutions of the slab waveguide to approximate solutions for other geometries. Here we demonstrate the use of the effective index method (EIM) for a TE polarized mode in the strip waveguide geometry shown in Figure 2.1(b). The general approach of the EIM is depicted in Figure 2.2. In part (a), the waveguide cross-section is divided into three sections. If we examine region 2, we see that in this region the waveguide can be approximated as a slab waveguide that is confined in the y direction. To solve for the TE mode in the overall system, we begin by solving the wave equation for the TE polarization in the slab waveguide in region 2.

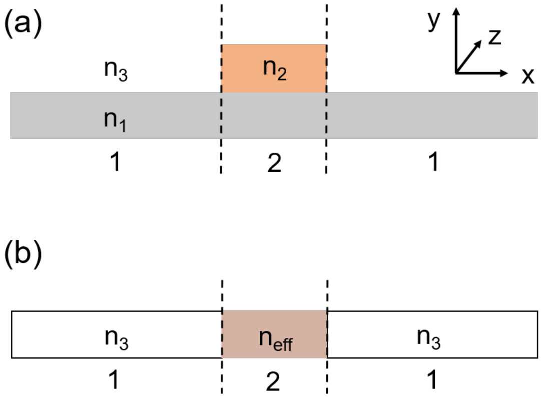

Figure 2.2: Effective index method applied to a strip waveguide. (a) The strip waveguide is divided into three regions. The propagation constant for the inner region, region 2, can be solved analytically using the equations for a slab waveguide that confines the light in the y direction. Once this propagation constant is found, it can be used to calculate the effective index of region 2. (b) The strip waveguide can be simplified into one slab waveguide structure that confines the light in the x direction. The propagation constant, and therefore the effective index, of the overall system is then solved using the analytic one-dimensional slab waveguide equations.

We solve Eq. (2.14) for the propagation constant for a given mode of integer m, β_{m}. The propagation constant can then be used to define the effective refractive index of that particular mode, $n_{\mathrm{eff,m}}$, of the dielectric stack in region 2 [92]:

$$n_{\mathrm{eff,m}} = \frac{\beta_{\mathrm{m}}}{k}. \tag{2.17}$$

Figure 2.2(b) shows the simplified strip waveguide system using the effective index for region 2. The system in (b) is again a slab waveguide system, this time with a slab confined in the x direction. Regions 1 on either side of the central effective index region are approximated to have the index of the cladding only, since the wave propagating in the central strip waveguide will only “see” the indices to either side of the waveguide in region 1. To obtain a solution for the mode profile of this structure, we solve for the propagation constant using Eq. (2.16), which is the characteristic equation for the TM polarization. The reason that we use the equation for the TM polarization is that the slab waveguide shown in Figure 2.2(b) is confined in the orthogonal direction to the initial solution from part (a) of the same figure. By solving for the TM modes of the slab in Figure 2.2(b), we obtain a solution for the TE modes of the original strip waveguide structure. Once the propagation constant has been obtained for the second slab structure, we can calculate the effective index of the overall strip waveguide structure using Eq. (2.17).

The effective index method is a versatile and simple technique that requires only the solution to two one-dimensional slab waveguides to obtain estimates for the effective index of waveguides with geometries that cannot be solved analytically. We can use the EIM to calculate the TM modes as well. Instead of calculating the propagation constant for the TE mode for Figure 2.2(a), the propagation constant for the TM mode is calculated. Then when simplifying the strip waveguide as in Figure 2.2(b), the propagation constant for the TE mode is calculated. The EIM can be used for different waveguide geometries as well, including the rib waveguide in Figure 2.1(c). The same process of splitting the device into three regions and finding the effective index in each region is used. From this discussion of the EIM, we can see that the effective refractive index of the waveguide depends on the waveguide geometry, the mode number m, and the polarization of the mode. For this reason, the effective index is sometimes called the modal index. The effective refractive index of a particular waveguide mode is the analogue of the refractive index for a bulk material. It can be used to describe the speed v of the wave propagating in the material through the relation $v = c/n_{\text{eff}}$. It also can be used to calculate the wavelength of light in the material λ with respect to the vacuum wavelength λ_0 as per $\lambda = \lambda_0/n_{\text{eff}}$. The effective index is a useful parameter for describing the propagation of light in the waveguide. It is also important in waveguide design, as we will see in the following paragraphs.

The EIM is powerful tool for approximating the effective index. It is, however, an approximation only. Errors in the method arise from assuming that the x and y directions in the waveguide are separable, when in fact they are not for a rectangular dielectric waveguide [93]. For dielectric waveguides with confinement in two dimensions, the polarizations are not perfectly TE or perfectly TM polarized. These waveguides have some hybridization of these polarizations and for this reason they are often called the quasi-TE or quasi-TM polarizations [94]. To eliminate errors from the EIM approximation and to quickly obtain the full solution for each waveguide mode of interest, we will use numerical methods in the remainder of this work to determine the field distributions and the effective indices of the waveguide modes. This will reduce any numerical errors, provide more accurate modeling of the waveguides, and increase the speed of the calculations.

Previously, we discussed the condition for propagation of light in a waveguide, and the cut-off condition for the slab waveguide mode. We derived using Snell's Law that the index of the waveguide core must be larger than the cladding and substrate indices. We also provided a rule of thumb for waveguide thickness based on the diffraction limit, that the waveguide slab should be at least as thick as half the wavelength in the slab. We can re-frame this discussion in terms of the effective index. As established earlier, for light to be confined in an integrated photonic waveguide, the index of the core must be greater than the cladding. The same principle holds for each mode in the waveguide. If the effective index (modal index) is larger than the substrate and cladding refractive indices, then the mode is confined in the waveguide and will propagate. If the effective index is equal to or lower than the surrounding refractive indices, then the mode does not meet the conditions for total internal reflection and the light will leak out of the waveguide. This condition is called the cut-off condition for integrated photonic waveguides [95, 96]. The cut-off index is the cladding index or the substrate index, whichever is larger. A waveguide mode with an effective index below cut-off will not be confined.

When designing waveguides, it is important to ensure that the effective index is above cut-off. A second consideration is the number of modes that will propagate in the waveguide. The larger the waveguide is, the more modes will propagate simultaneously in the waveguide because the effective index of the all modes increases with increasing waveguide size. Larger waveguides may have multiple TE and TM modes above cut-off. Multiple modes are detrimental for some applications where measurement of a specific mode is desired [97]. When designing waveguides it is important to first determine the cut-off level, and then to determine the number of modes above cut-off. If no modes are above cut-off, a larger waveguide is required. If many modes are above cut-off, then the waveguide dimensions may be reduced.

2.2.2 Waveguide Materials and Fabrication

The most common materials system for integrated photonics is silicon [98, 99, 100]. Silicon photonic devices are fabricated using silicon-on-insulator (SOI) wafers. SOI substrates have a thin silicon device layer atop a buried oxide layer, typically 2 μm thick. The bottom layer is a silicon handle layer. The silicon handle layer is a thick layer, usually 675 μm thick. The buried oxide layer acts as a buffer between the thin silicon device layer and the handle layer. The purpose of this low-index layer is to prevent light from leaking out of the silicon device layer and into the handle layer. A cladding layer, often silicon dioxide or sometimes simply air, completes the photonic device.

There are several reasons why silicon photonics is one of the most common photonics materials systems. First of all, fabrication of silicon devices has already been developed for CMOS devices, and so many of the techniques are well-established. The most common lithographic techniques for fabricating waveguides using SOI wafers are deep UV lithography and electron beam lithography, to obtain the small feature sizes required. Secondly, silicon is transparent in one of the wavelength ranges commonly used in telecommunications (C-band, 1530–1565 nm), which means that silicon waveguides have low loss at these wavelengths. Finally, silicon has an index of refraction of 3.45 at a wavelength of 1550 nm. This means that silicon waveguides are a high contrast waveguide relative to air or silicon dioxide cladding. This is beneficial for reducing the device footprint, as smaller waveguiding structures can be fabricated in high contrast materials systems [101]. Smaller features mean that the density of features increases and the cost per device decreases.

The silicon device layer is the layer in which the waveguides are fabricated. The standard thickness of this layer is 220 nm. If we refer back to the rule of thumb for slab thickness in the previous section and use the wavelength in the C-band, $(1550/3.45)/2 \approx 220$ nm. Therefore, 220 nm thickness is half of the wavelength in a silicon slab waveguide. This standardized thickness helps to prevent cut-off and achieve single mode operation in silicon photonic waveguides.

In addition to waveguides fabricated using SOI wafers, photonic waveguides can also be fabricated from other materials such as polymers [102, 103, 104, 105] or silicon nitride [106]. These types of waveguides are low-contrast materials systems compared to silicon. Low-contrast waveguides may be useful as sensors or for coupling light into high contrast silicon waveguides [74, 107].

2.2.3 Coupling of Light into Photonic Waveguides

In this section, we will consider approaches for coupling external laser sources into on-chip photonic devices. Several techniques are commonly used, including edge coupling, grating couplers, or tapered optical fibers [108, 109, 110]. We will discuss the two techniques used in this work, edge coupling and grating couplers. Edge coupling is the simpler of the two techniques, however, grating couplers are more versatile.

For edge coupling, the waveguide is placed such that its cross section is immediately at the chip edge, as shown in Figure 2.3 [74, 75, 111]. The exposed end of the waveguide, sometimes called the end facet, must be cleanly cut. An optical fiber carries the laser light from the laser output to the waveguide facet. The light output from the laser is then input to the waveguide by carefully controlling the position of the fiber. Although straightforward in principle, edge coupling is complicated by the fact that the fiber optical mode spot size can be significantly larger than the waveguide. Typical dimensions of high contrast waveguides are 220 nm tall by 500 nm wide. Standard single mode optical fibers, on the other hand, have output mode field diameters on the order of 10 μm. This mode size mismatch reduces the coupling efficiency of edge coupling. To reduce the mode size mismatch, lensed fibers can be used which have much smaller beam waists than traditional optical fibers. Alternatively, nano-tapered edge couplers or polymer mode converters can be used to improve the coupling efficiency [112, 113]. The main benefit of edge coupling, aside from its simplicity, is that it is a high-bandwidth coupling technique compared to grating couplers.

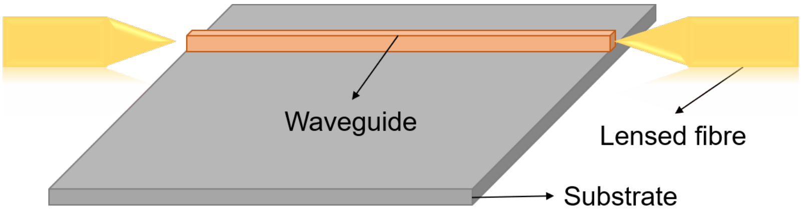

Figure 2.3: Cartoon demonstrating the edge coupling technique. In this case, coupling to a waveguide is accomplished using lensed fibers. The diagram is not to scale.

Grating couplers are another important coupling mechanism [72, 73, 114, 115, 116]. Grating couplers are fabricated on-chip simultaneously with the waveguides. They are comprised of two parts; the first part is a grating with a periodicity and duty cycle designed specifically for the desired wavelength and input angle. In silicon photonics, the grating has a top-down area of tens of microns. The grating may be partially etched or fully etched. Partially etched means that some areas of the grating are at the full waveguide height, and others have a reduced height as they have been etched partially. A partially etched grating coupler is shown by Figure 2.4(a). Fully etched grating couplers have areas where the grating is the full waveguide height, and areas where the waveguiding material has been etched away completely. Often, these types of grating couplers alternate feature sizes larger than one half wavelength of light in the material ($> (\lambda/n)/2$) with features much smaller than one-half the wavelength of light in the material ($<< (\lambda/n)/2$) to form sub-wavelength gratings [117]. An example of a fully-etched sub-wavelength grating is shown in Figure 2.4(b). The second part of the grating coupler is a triangular silicon taper that acts to focus the light from the large grating region into the small waveguide dimensions. In the case of silicon photonics, this slab at its widest is on the order of a few microns, and tapers adiabatically to hundreds of nanometers. Grating couplers provide coupling efficiency on the order of approximately 15% [118] and allow for a wider variety of applications than edge coupling. Grating couplers can accept light from fibers positioned directly at the chip surface. Since the gratings have a large top-down area, they can accept light from standard optical fibers without the need for lensed fibers. The fibers may be glued in place for applications that require a more robust or permanent coupling mechanism. Grating couplers can also accept light that is focused on them at a distance. This is beneficial for applications where the grating coupler may be submerged in fluid or within a vacuum, as we will see later in this thesis.

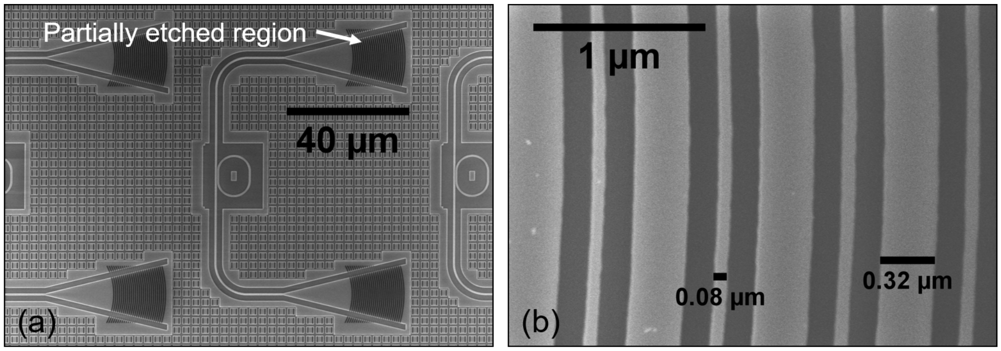

Figure 2.4: Scanning electron microscope images of (a) partially etched grating couplers and (b) the grating of a fully-etched sub-wavelength grating coupler in a silicon-on-insulator materials system. In (a), the large area of the grating coupler is emphasized by the scale bar indicating the full size of the coupler to be 40 μm wide. The partially etched region is indicated. In (b) one of the gratings is a sub-wavelength grating that is 80 nm wide and is much smaller than 220 nm, which is one half the wavelength of light in silicon.

Light incident on the grating is diffracted. Since the grating is periodic, the light is diffracted in a specific direction as described by the Bragg condition [77];

$$k_{\mathrm{z,b}} = \beta_{\mathrm{m}} - b\frac{2\pi}{\Lambda}, \tag{2.18}$$

where $k_{\mathrm{z,b}}$ is the wave vector of the diffracted light in the direction of propagation of order b, β_{m} is the propagation constant for a specific mode m, and Λ is the period of the grating. The wave vector $k_{\mathrm{z,b}}$ is related to the input angle θ of the light by $\sin\theta = k_{\mathrm{z,b}}/k_{\mathrm{cladding}}$, where k_{cladding} is the wave vector of the light traveling through the cladding material to reach the surface of the waveguide device layer. θ is defined as the angle between the incident light and the surface normal. It is often set by the experimental conditions. For example, an experimental setup may be designed to measure specifically at 10° from normal. From this, we can calculate $k_{\mathrm{z,b}}$. Since we know the modal propagation constant from our earlier analysis of slab waveguides, this relation can be used to determine the period of the grating.

For maximum coupling efficiency, $b = 1$, so that only the lowest order diffraction is present [119]. This means that as the wavelength increases (or decreases) and therefore $k_{\mathrm{z,1}}$ decreases (or increases), the grating couplers will become less efficient since Eq. (2.18) is no longer exactly equal to $k_{\mathrm{z,1}}$. For this reason, grating couplers have a smaller bandwidth of operation than edge couplers. In silicon photonic devices, grating couplers typically operate in the range of 1500–1580 nm, with peak efficiencies in the range of 1530–1560 nm [120]. The shape of the grating coupler transmission is often referred to as the "envelope" of the grating coupler [121].

2.2.4 Racetrack Resonators

Microring resonators, a type of optical cavity, are created when a waveguide is formed into circle. Racetrack resonators have the same principles of operation as microring resonators, only with a slightly different geometry. Straight sections within the circles result in formation of directional couplers for coupling light into and out of the racetrack resonator. In this work, racetrack resonators have been selected because the straight sections create a longer area for the optical cavity to interact with the mechanical device. Figure 2.5 shows a cartoon of a racetrack resonator. The cladding layer is omitted for clarity. The waveguide that carries light from the input to the output grating coupler is called the bus waveguide. The location of the directional coupler is also specified. Directional couplers are comprised of two adjacent waveguides separated by a gap; in this case, the bus waveguide and the straight section of the racetrack resonator are separated by the coupling gap. Directional couplers allow for light traveling in the bus waveguide to enter the optical cavity, and allow a high degree of control over the coupling of light into and out of the racetrack resonators. Several other important properties of the racetrack resonator that are highlighted in this figure include the radius of the racetrack resonator, the coupling length of the directional coupler, and the coupling gap of the directional coupler.

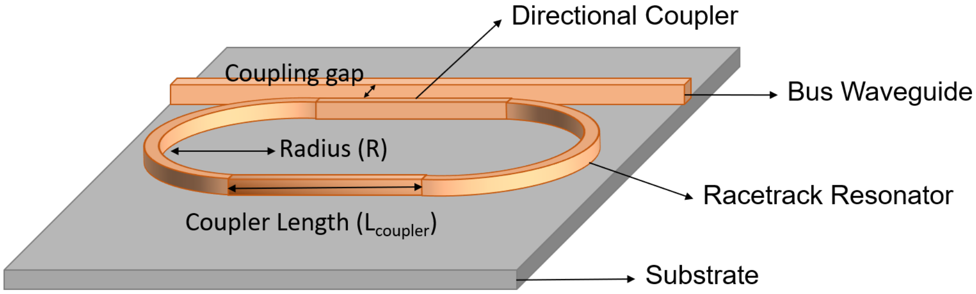

Figure 2.5: Cartoon showing the important components of a racetrack resonator, including the bus waveguide for input and output of light. The directional coupler is formed by the bus waveguide and the straight section of the racetrack resonator. The directional coupler is defined by the coupling length L_{coupler} and the coupling gap. The radius of the racetrack R is also an important property of the system.

As mentioned previously, racetrack resonators are a specific type of optical cavity. Light will be coupled into the optical cavity when the wavelength of light meets the resonant condition for the racetrack resonators. This resonance condition is that total length of the racetrack resonator cavity is equal to an integer M times the wavelength of light in the waveguide, $L_\mathrm{c} = M\lambda/n_\mathrm{eff}$ [122]. This is defined by the effective index of the waveguide, so the resonant condition is defined for a single mode.

When designing racetrack resonators, the cavity length $L_\mathrm{c} = 2\pi R + 2L_\mathrm{coupler}$ is an important parameter to consider because it can be used to define the free spectral range (FSR, $\mathcal{F}$). L_c is inversely proportional to the FSR. The FSR is a measurement of the wavelength spacing between optical resonances and is equal to $\lambda^2/(n_\mathrm{g}L_\mathrm{c})$, where λ is the optical wavelength and n_g is the group index. The group index describes the dispersion in the optical waveguide and can be obtained from FDTD simulations. It is also related to the effective index via [123]:

$$n_\mathrm{g} = n_\mathrm{eff} - \lambda\frac{\mathrm{d}n_\mathrm{eff}}{\mathrm{d}\lambda}. \tag{2.19}$$

The FSR, and therefore L_c, should be selected for the specific application for which the racetrack will be used. The following example will describe how to choose an appropriate cavity length for the case of optomechanical measurements. Racetrack resonators can be fabricated using the SOI platform. Let us assume that light is coupled in and out of the photonic circuit using grating couplers. The bandwidth of the overall photonic circuit is limited to the C-band by the grating couplers, as described in Section 2.2.3. For optomechanical measurements, one optical resonance is required for probing the mechanical device and one is required for pumping the device. The reason for this requirement will be discussed in more detail in Section 2.3. When combining the requirements of the optomechanical devices with the limited bandwidth introduced by the grating couplers, we see that the FSR must be small enough that at least two optical resonances are observed in the C-band. A racetrack resonator fabricated using SOI and using the fundamental TE mode will have an effective index of approximately 2.4 and the group index is approximately 4.3. A racetrack resonator with this group index and a cavity length of 35 μm will have an FSR of approximately 16 nm. This cavity will have at least two resonances in the C-band. The cavity length should be equal to or greater than 35 μm. The FSR should be large enough so that the optical resonances are well-separated so that the pump laser may be filtered out successfully. The cavity length should then be chosen to be close to 35 μm for a larger FSR. In the case of optomechanics, a coupling length of 3 μm is desirable, such that the length of the straight section is comparable to the length of the mechanical device. The curved section of the cavity then has a total length of 29 μm, which gives a radius of approximately 5 μm. For all optomechanical measurements, then, the racetrack resonators fabricated using SOI will have a radius of 5 μm and a straight section of 3 μm.

Once the size of the racetrack resonator is known, the directional coupler can be designed. The coupling length of the directional coupler is often selected as part of the optical cavity length design as demonstrated in the previous example, and so the only remaining free parameter is the coupling gap. Directional couplers are described using coupled mode theory, and one specific approach is the perturbation approach [76, 124]. When a waveguide (the racetrack resonator coupling length) is brought into close proximity with a second waveguide carrying an optical signal (the bus waveguide), the evanescent field of the second waveguide is perturbed. This perturbation results in a transfer of energy between the two waveguides. In this way, the original optical signal is coupled into the racetrack resonator. In the case of symmetric waveguides, complete energy transfer from one waveguide to next occurs over a length called the cross-over length, L_{cross}. The cross-over length can be calculated by finding the first two modes of the entire directional coupler, that is, the two-waveguide system. The modes of the overall system are not the same as the individual waveguide modes. Since these modes are of the two-waveguide system and not just one waveguide, they are often called "supermodes" [125, 126]. The first supermode is the symmetric, or even, supermode. The second supermode is the anti-symmetric, or odd, supermode. Cartoons of these mode profiles are shown in Figure 2.6.

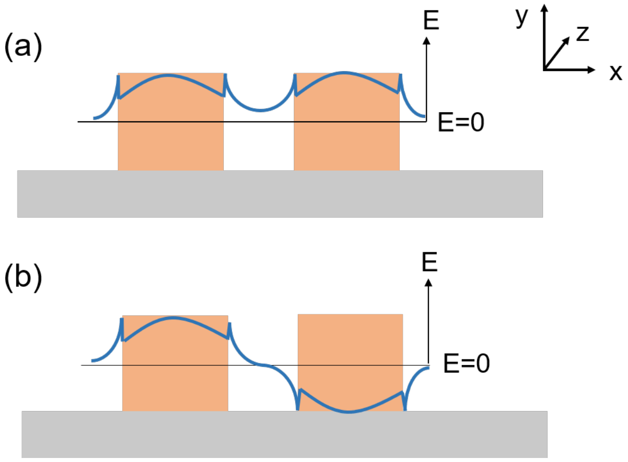

Figure 2.6: A cross-sectional diagram of a directional coupler. The coupler is comprised of two identical waveguides separated by a gap. The blue lines show the (a) even (symmetric) supermode and (b) the odd (anti-symmetric) supermode electric field profiles in the x direction (E_{x}). This example is for TE polarization.

Each supermode has a different propagation constant, and therefore also a different effective index (recall Eq. (2.17)). The cross-over length is defined as [77]

$$L_{\text{cross}} = \frac{\lambda}{2(n_{\text{eff,even}} - n_{\text{eff,odd}})}, \tag{2.20}$$

where $n_{\text{eff,even}}$ is the even effective index of refraction of the supermode, $n_{\text{eff,odd}}$ is the odd effective index of refraction of the supermode, and λ is the wavelength.

As the coupling gap increases, the difference between the effective indices of the odd and even supermodes decreases. Therefore, the cross-over length increases with increasing coupling gap. For a very large coupling gap, the racetrack waveguide will no longer perturb the bus waveguide field, and no energy will be transferred between the waveguides. At this point, the cross-over length is infinite. This indicates that the directional coupler no longer truly exists, rather there are simply two disparate waveguides.

To choose an appropriate coupling gap for the directional coupler, we need to relate the cross-over length to the coupler length L_{coupler}. These two parameters are connected via the field coupling coefficient κ. The field coupling coefficient, referred to from now on as the coupling coefficient for brevity, is a unitless number between zero and one. It is defined as

$$\kappa = \sin\left(\frac{\pi}{2}\frac{L_{\text{coupler}}}{L_{\text{cross}}}\right). \tag{2.21}$$

We can see from Eq. (2.21) that if $L_{\text{coupler}} = L_{\text{cross}}$, then $\kappa = 1$ and all of the energy from the bus waveguide is coupled into the racetrack. In the opposite case, where $\kappa = 0$, all of the energy remains in the bus waveguide. We can define the field transmission coefficient τ, which describes the field remaining in the bus waveguide [94]:

$$\tau = \cos\left(\frac{\pi}{2}\frac{L_{\text{coupler}}}{L_{\text{cross}}}\right). \tag{2.22}$$

For conservation of power, $\kappa^2 + \tau^2 = 1$. From Eqs. (2.21–2.22) we can see that by varying the ratio of the coupler length to the cross-over length, we can determine what fraction of power is coupled between the bus waveguide and the racetrack resonator. Returning to Eq. (2.20), the cross-over length is varied by adjusting the difference between the even and odd effective indices of the directional coupler supermodes. We can adjust this difference by increasing or decreasing the coupling gap, since we have assumed that the coupler length is fixed from our initial design of the cavity length. κ and τ are shown diagrammatically in Figure 2.7. In this figure, s_{i} is the complex input electric field amplitude and s_{t} is the complex electric field amplitude output through the bus waveguide. s_{i} is normalized such that $|s_{\text{i}}|^2 = |E_0|^2$, where E_0 is the amplitude of the input electric field. The complex amplitude of the light coupled into the racetrack resonator can then be represented by $i\kappa s_{\text{i}}$. R is the radius of the microring or racetrack resonator.

It is important to choose κ and τ, and therefore the coupling gap, appropriately to achieve the desired coupling condition for the racetrack resonator. There are three possible coupling conditions for a racetrack resonator; critically coupled, over-coupled, and under-coupled [94, 127, 128, 129, 130]. At critical coupling, all of the

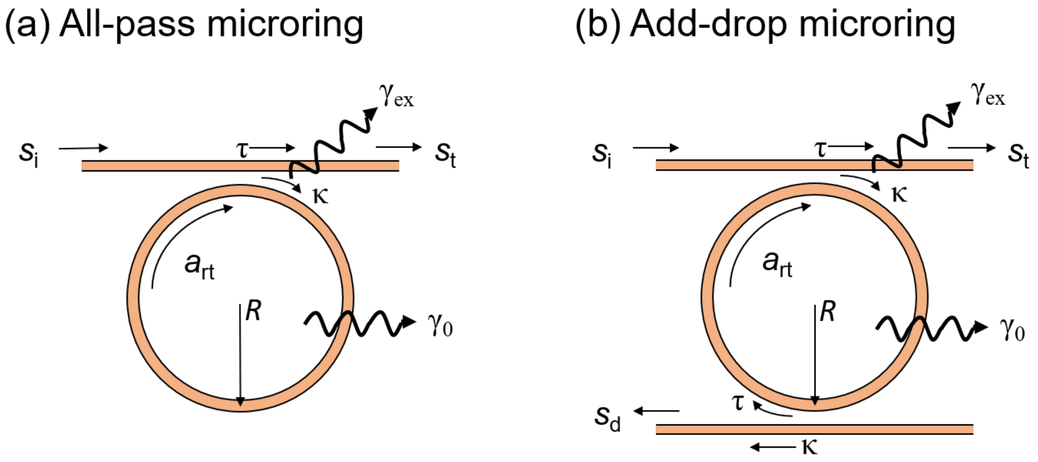

Figure 2.7: Schematic of (a) an all-pass microring resonator and (b) an add-drop microring microring resonator. In (a), there is only one bus waveguide and therefore only one output, the output complex amplitude labeled s_{t}. In (b), the add-drop microring has two bus waveguides called the through port with output signal s_{t} and the drop port with output signal s_{d}. In both schematics, the radius of the microring is labeled R. The input signal is s_{i}, the complex input electric field amplitude. The microring coupling parameters are described by τ and κ and are labeled at the locations of the couplers. The round-trip loss, the fraction of field amplitude that remains in the racetrack after one round trip, is denoted by a_{rt} and its placement at the output of the microring emphasizes that this parameter is defined after the light completes one full round trip through the optical cavity. All of these parameters are part of the power coupling formalism. γ_{ex} is the coupling loss rate in units of 1/s. γ_0 is the intrinsic loss rate in units of 1/s. These two parameters are part of the energy coupling formalism.

light exiting the racetrack resonator destructively interferes with the light in the bus waveguide. This results in zero transmission through the bus waveguide at the optical resonance wavelength. Over- and under-coupled racetracks do not meet this condition for perfect destructive interference and in both of these cases there will be non-zero transmission through the bus waveguide at the resonant wavelength. Another way to describe the coupling conditions of the racetrack resonator is in terms of the loss in the racetrack [131]. At critical coupling, the power coupled into the racetrack resonator is equal to power dissipated by the optical cavity. In the case of over-coupling, more power is coupled into the racetrack resonator than is dissipated. The over-coupled optical resonance has a lower optical quality factor (Q_{opt}) compared to the critical and under-coupled cases. In the case of under-coupling, less power is coupled into the racetrack resonator than is dissipated.

To set the coupling condition of the racetrack resonator, it is necessary to have an estimate of the power loss in the racetrack resonator. One parameter that can be used to characterize the loss in a racetrack resonator is the round trip loss, $a_{\mathrm{rt}} = e^{-\alpha_0 L_{\mathrm{c}}/2}$. In this definition, α_0 is the propagation loss of the waveguide in units of 1/metres, and L_{c} is the cavity length in units of metres. The round trip loss describes the fraction of field amplitude that remains in the racetrack after one round trip and is between zero (all amplitude lost) and one (no loss). Bending loss is one source of loss and includes radiative loss in the bend, which is especially prevalent in rib waveguides [132, 133]. Absorption of energy by the waveguide material or cladding is another source of loss [134]. The primary source of loss, especially in high contrast strip waveguides, is surface roughness [135, 136, 137, 138, 139, 140, 141, 142]. Surface roughness is often introduced by the waveguide etching process and can cause scattering loss and radiative loss of power. For this reason, the propagation loss is dependent on the fabrication process.

By comparing a_{rt} to the transmission coefficient τ, we can determine whether the racetrack resonator will be over, under, or critically coupled. If $\tau = a_{\mathrm{rt}}$, the racetrack will be critically coupled because the fraction of field amplitude remaining in the ring after one round trip, and therefore what is coupled out of the racetrack resonator, is exactly equal to the fraction of field transmitted through the bus waveguide. This is the condition that permits complete destructive interference on resonance. By the same logic, if $\tau > a_{\mathrm{rt}}$, the racetrack will be under-coupled because the fraction of field amplitude in the bus waveguide is greater than the required fraction for perfect cancellation. Similarly, if $\tau < a_{\mathrm{rt}}$, the racetrack is over-coupled because the fraction of field amplitude in the bus waveguide is less than required for perfect cancellation, and therefore more power than required has been coupled into the racetrack resonator.

By using these definitions, the coupling condition of the racetrack resonator can be designed for specific applications. For example, a transmission function with a low optical quality factor may be desirable for certain applications. To obtain a lower quality factor, we may wish to over-couple the racetrack resonator since the optical quality factor is proportional to $1/\kappa^2$. As the the coupling increases in a racetrack resonator, κ increases and therefore Q_{opt} decreases. To obtain over-coupling if the round trip loss is known to be 0.98, τ should be less than 0.98. Therefore, the coupling gap can be chosen by calculating the cross-over length from Eq. (2.22). The cross-over length can then be used to determine the coupling gap from Eq. (2.20) and the supermode even and odd effective indices.

2.2.5 The Power Coupling and Energy Coupling Formalisms for Optical Cavities

In the previous section, we introduced the parameters τ, κ, and a_{rt}, and demonstrated how to use these parameters to select the coupling condition for the racetrack resonator. In this section, we will use these parameters to describe the transfer function of the racetrack resonator. We will describe the transfer function of the racetrack resonator for both the power coupling formalism and the energy coupling formalism for the simple case of an all-pass microring resonator as shown in Figure 2.7(a). The all-pass microring resonator (APMR) has a single bus waveguide and therefore only one directional coupler. The output is measured at this single bus waveguide and is called the through port. The add-drop microring resonator (ADMR, Figure 2.7(b)) has one bus waveguide on each side of the racetrack resonator. The output of the second bus waveguide, on the opposite side of the input, is referred to as the drop port. The APMR is a simpler geometry to demonstrate the derivation of these transfer functions, but the same approach can be applied to an ADMR.

The power coupling formalism uses the parameters τ, κ, and a_{rt} to describe the spatial coupling of optical power into and out of a microring or racetrack resonator. To derive the equations for the transmission of an all-pass microring resonator, we start with the complex input electric field amplitude s_{i}. The field amplitude coupled into the racetrack resonator from the bus waveguide is described as $i\kappa s_{\text{i}}$. The field then completes one round trip of the optical cavity. We can represent the effect of one round trip by multiplying the field amplitude by $a_{\text{rt}}e^{i\phi}$. a_{rt} accounts for the loss as the field travels one round trip in the racetrack. The phase shift that the field experiences is represented by the exponential term. ϕ is the round-trip phase of the microring. This field is then coupled back out of the racetrack resonator.

This description shows how to track the electric field as it is coupled into the racetrack resonator through the directional coupler. To derive the full expression for the racetrack resonator's transfer function, we can follow the same process and account for fields already present in the racetrack, since photons will make many round trips before exiting the racetrack resonator. Therefore, the field amplitude immediately after the coupler is

$$A = i\kappa s_{\mathrm{i}} + \tau D, \tag{2.23}$$

where A is the field amplitude immediately after the coupler and D is the field amplitude immediately before the directional coupler. The first term in Eq. (2.23) shows the field amplitude coupled in through the directional coupler, and the second term represents the field amplitude remaining in the racetrack after the directional coupler, which is why this term is multiplied by the transmission coefficient τ. We define D as the field after one round trip such that $D = Aa_{\mathrm{rt}}e^{i\phi}$. The transfer function of the racetrack resonator is defined by $s_{\mathrm{t}}/s_{\mathrm{i}}$, where s_{t} is the output complex field amplitude. s_{t} is defined by

$$s_{\mathrm{t}} = \tau s_{\mathrm{i}} + i\kappa D. \tag{2.24}$$

To find the transfer function, we substitute $D = Aa_{\mathrm{rt}}e^{i\phi}$ into Eq. (2.24). We also substitute the expression for D into Eq. (2.23) and solve for A. Inserting this new expression for A into the modified Eq. (2.24) eliminates both A and D from the expression. This new equation is a function of only s_{i} and s_{t}, and so we can solve for the transfer function $s_{\mathrm{t}}/s_{\mathrm{i}}$. To obtain the transfer function in terms of the optical power, which is the transmission function of the racetrack resonator, we take the square of the absolute value of $s_{\mathrm{t}}/s_{\mathrm{i}}$. Simplifying this expression using the power conservation requirement $\kappa^2 + \tau^2 = 1$ gives the transmission of the APMR:

$$T_{\mathrm{ap}} = \left|\frac{s_{\mathrm{t}}}{s_{\mathrm{i}}}\right|^2 = \left|\frac{\tau - a_{\mathrm{rt}}e^{i\phi}}{1 - \tau a_{\mathrm{rt}}e^{i\phi}}\right|^2. \tag{2.25}$$

Since ϕ can be expressed in terms of experimentally relevant parameters as $\phi = 2\pi(\lambda - \lambda_0)/\mathcal{F}$, Eq. (2.25) can be used to fit experimental data to determine τ and a_{rt}. The power coupling formalism applies equally well to over, under, and critically coupled optical cavities, as no assumptions are made about the cavity coupling condition during this derivation.

The same approach can be used to calculate the power enhancement of the optical cavity. The power enhancement (PE) is the factor by which the power in the ring is amplified on resonance. The power enhancement is an important parameter as it provides an understanding of the actual power in the racetrack resonator. The power enhancement is defined as

$$PE = \left|\frac{A}{s_{\mathrm{i}}}\right|^2 = \frac{\kappa^2}{|1 - \tau a_{\mathrm{rt}}e^{i\phi}|^2}, \tag{2.26}$$

where A was previously defined in Eq. (2.23).

The energy coupling approach is an alternative method to the power coupling technique. It is the formalism commonly used in optomechanics. This formalism describes the coupling of energy in time, and is valid only for weakly coupled cavities. Instead of the parameters τ, κ, and a_{rt}, this approach uses the amplitude loss rate γ to define the overall loss of the cavity, and is one half of the cavity width at half maximum. γ can be related to the physical properties of the optical cavity by the optical quality factor, $Q_{\mathrm{opt}} = \omega_0/2\gamma = \pi c/\gamma\lambda_0$ where λ_0 is the cavity resonance wavelength and c is the speed of light. To separate losses caused by coupling and those due to the intrinsic cavity loss, we can write $\gamma = \gamma_{\mathrm{ex}} + \gamma_0$. γ_{ex} is the decay rate associated with coupling, and $\gamma_0 = \alpha_0 v_{\mathrm{g}}/2$ is the intrinsic loss rate of the optical cavity, and is defined in terms of the propagation loss and the group velocity v_{g}. As these parameters are expressed as rates in units of radians/second, it makes sense to use the optical frequency, instead of the optical wavelength. Specifically, we will express the frequency as a detuning from the resonance frequency of the optical cavity, $\Delta = \omega - \omega_0$, where ω_0 is the resonance frequency of the optical cavity corresponding to $\omega_0 = 2\pi c/\lambda_0$. With these definitions in mind, the equation for the all-pass microring resonator can be re-written as follows [143]:

$$T_{\mathrm{ap}} = \left| \frac{\gamma_0 - \gamma_{\mathrm{ex}} - i\Delta}{\gamma - i\Delta} \right|^2 . \tag{2.27}$$

It is important to understand both formalisms, as each formalism is valuable in different situations. For example, the energy coupling formalism greatly simplifies the design of microring filters where several microrings are coupled together [144]. It is also useful to convert between the two formalisms. The full derivation for this conversion is shown in detail in [94]. Here, we will summarize the most useful equations to easily translate between formalisms. Mainly, it is useful to convert the parameters a_{rt} and τ to the parameters γ_0 and γ_{ex}. From these two connections between formalisms, all other parameters can be obtained. To convert a_{rt} to γ, we can connect them through the propagation loss α_0, which is present in the definitions of γ_0 and a_{rt}. This results in the following expression linking a_{rt} and γ_0:

$$a_{\mathrm{rt}} = e^{-\gamma_0 L_{\mathrm{c}}/v_{\mathrm{g}}}. \tag{2.28}$$

To obtain a relationship between τ and γ_{ex}, we recall that for power conservation in a directional coupler, $\kappa^2 + \tau^2 = 1$. We can relate κ and γ_{ex} by comparing the through port response of the microring resonator in both formalisms [94]. This allows us to state

$$\kappa^2 = \frac{L_{\mathrm{c}}}{v_{\mathrm{g}}} 2\gamma_{\mathrm{ex}}. \tag{2.29}$$

Then, by using the relationship between the coupling and transmission coefficients, we can write

$$\tau^2 = 1 - \frac{L_\mathrm{c}}{v_\mathrm{g}} 2\gamma_\mathrm{ex}. \tag{2.30}$$

The relationships described in Eqs. (2.28) and (2.30) allow us to convert easily between the two formalisms, so that we can use the method best suited for each application.

2.2.6 Coherent Backscattering

In this section, we will discuss the effects of coherent backscattering on racetrack resonators fabricated using the SOI platform. As discussed previously, photonic devices fabricated on SOI are high index contrast, especially when air-clad. Although this makes silicon photonic integrated circuits easier to miniaturize because smaller bending radii can be achieved while maintaining low loss [122], it also makes them susceptible to a phenomenon called coherent backscattering. In high contrast waveguides, the propagating mode is very sensitive to the surface roughness of the waveguide, as previously described in the discussion on sources of loss in Section 2.2.4. If the surface is rough, many reflections in the microring occur and form a counter-propagating wave. When the counter-propagating wave interferes with the forward-propagating traveling wave, the result is a standing wave in the microring or racetrack resonator. In terms of the optical spectrum, it manifests as a peak splitting in the optical resonance [145]. Backscattering is more easily observed in rings with large quality factors, since there are few other significant sources of loss. Backscattering can limit the performance of ring or racetrack resonators with an optical quality factor greater than 10^4 [146].

Although backscattering does not affect the racetrack resonator's ability to read out a nanomechanical device, as we will demonstrate in Chapter 4, it does complicate the transmission transfer function of the optical cavity, as well as the power enhancement. The transmission and power enhancement are necessary to model the behaviour of the cavities in order to calculate optomechanically-relevant parameters such as the optical force. To model the effect that coherent backscattering has on the optical response of the cavity, we use the power coupling approach. We model the backscattering effect as a lumped element reflector [147]. The reflector has a reflection coefficient r, transmission coefficient t, and position θ measured in radians. A schematic of the model used to derive the equations describing coherent backscattering are shown in Figure 2.8.

First, we derive the amplitude in the microring for the add-drop configuration, assuming that the coupling is identical at the add and drop ports. To determine the overall equation that describes the transmission through a backscattered add-drop

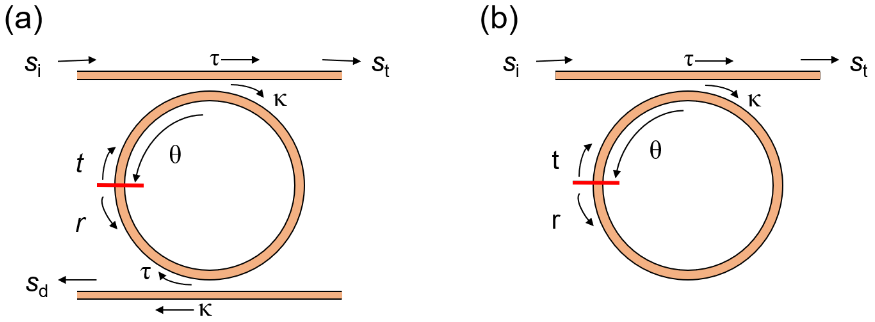

Figure 2.8: Schematics including backscattering effect for (a) an add-drop microring and (b) an all-pass microring. The lumped element reflector (red line) is included to account for coherent backscattering. The input amplitude to the microring is s_i. The amplitude at the through port is labelled s_t. For the add-drop microring in (a), the drop port amplitude is shown as s_d. The microring coupling parameters are described by τ and κ. The transmission through the reflector element is t and the reflection is r. The location of the lumped reflector within the microring is denoted by θ.

microring, we follow the same approach used in the previous section to derive the transfer function for the APMR with the power coupling formalism. This allows us to derive equations for the electric field amplitude at various locations in the racetrack resonator [147]. By rearranging these equations, we determine the amplitude of the forward propagating wave after the input coupling junction (A_1), and the amplitude of the backward propagating wave at the same point (B_1). These expressions are as follows:

$$A_1 = \frac{i\kappa}{1 - a_\mathrm{rt}\tau^2 C_\mathrm{ad} e^{i\phi}} s_\mathrm{i}, \tag{2.31}$$

$$B_1 = \frac{-r\kappa a_\mathrm{rt} e^{2i\theta}}{1 - 2a_\mathrm{rt} t\tau^2 e^{i\phi} + a_\mathrm{rt}^2 \tau^4 e^{2i\phi}} s_\mathrm{i}, \tag{2.32}$$

where ϕ is the round trip phase of the forward propagating wave. C_ad is defined as:

$$C_\mathrm{ad} = \frac{t - a_\mathrm{rt}\tau^2 e^{i\phi}}{1 - a_\mathrm{rt} t\tau^2 e^{i\phi}}. \tag{2.33}$$

These counter-propagating waves interfere, resulting in the formation of a standing wave in the racetrack. Therefore, the total amplitude in the microring is the summation of A_1 and B_1. In the case of the all-pass microring, the amplitudes are similar. A_1 and B_1 are obtained by setting $\tau^2 = \tau$ in Eqs. (2.31) and (2.32), since the transmission through the second coupler is equal to unity in the case of an all-pass configuration. For the all-pass configuration:

$$C_\mathrm{ap} = \frac{t - a_\mathrm{rt}\tau e^{i\phi}}{1 - a_\mathrm{rt} t\tau e^{i\phi}}. \tag{2.34}$$

To obtain the transmission at the through port of both the add-drop microring and the all-pass microring, we must find the solution for s_t/s_i. Combining Eqs. (2.31) and (2.32) with the remaining electric field amplitude equations in Ref. [147], we derive the following results for the add-drop microring (Eq. (2.35)) and the all-pass microring (Eq. (2.36)):

$$T_\text{ad} = \left|\frac{s_\text{t}}{s_\text{i}}\right|^2 = \left|\frac{\tau - C_\text{ad}\tau a_\text{rt} e^{i\phi}}{1 - C_\text{ad}\tau^2 a_\text{rt} e^{i\phi}}\right|^2, \tag{2.35}$$

$$T_\text{ap} = \left|\frac{s_\text{t}}{s_\text{i}}\right|^2 = \left|\frac{\tau - C_\text{ap} a_\text{rt} e^{i\phi}}{1 - C_\text{ap}\tau a_\text{rt} e^{i\phi}}\right|^2. \tag{2.36}$$

Finally, we have discussed the importance of the power enhancement in the previous section, as it describes how the power in the microring is amplified at resonance compared to the input power. However, backscattering greatly complicates the calculation of the power enhancement since the standing wave pattern caused by backscattering results in minimum and maximum power enhancement at various positions in the microring. To calculate the power enhancement, we need to calculate the mean value of the power of the standing wave at resonance. To set the wavelength to the resonance condition, we can set $\phi = 2\pi$ and use Eq. (2.37) to calculate the backscattered power enhancement, PE_b, for both the add-drop and all-pass microrings. The subscript b indicates that the cavity is backscattered,

$$PE_\text{b} = \left|\frac{A_1 + B_1}{s_\text{i}}\right|^2. \tag{2.37}$$

Eq. (2.37) gives a range of values depending on the location of the reflector element θ. Since the location of the reflector element is not known exactly, we can calculate the average PE_b by determining the power enhancement for $\theta = 0$ to 2π and taking the average value. This approach is verified experimentally in Section 3.2 and detailed graphically in Section 4.2.2.

Although the presence of coherent backscattering does complicate the model for the add-drop and all-pass microrings, we have shown here that using methods already established in the literature, we are able to account for these complications. We will use the equations derived in this section in our experimental results later in the thesis and demonstrate that they fit the data well.

2.3 Optomechanics

Until this point, we have described optical cavities only as isolated structures. However, optical cavities can be coupled to mechanical devices to form optomechanical systems [148]. There are a wide range of optomechanical systems, as large as the LIGO interferometer for detection of gravitational waves [149] or as small as the breathing modes of nanoscale photonic crystals [150]. There are several different mechanisms by which optomechanical coupling can arise. The most conceptually simple optomechanical system is a Fabry-Perot cavity with one end mirror that is free to move. The photons in the Fabry-Perot cavity impinge on this mirror, resulting in a direct transfer of the photon momentum to the end mirror with a mechanical degree of freedom [151, 152, 153, 154]. The force associated with this momentum transfer is called the radiation pressure force. Other optomechanical systems that make use of the radiation pressure force include membrane in the middle systems where a mechanical membrane is placed in the centre of a Fabry-Perot cavity [40] and microtoroid resonators [110, 155].

Coupling between optical cavities and mechanical devices can also be achieved through the optical gradient force [50, 51, 52, 53, 67]. The optical gradient force occurs when a dielectric particle (or dielectric structure) is placed in a spatially varying electromagnetic field. Mathematically, the optical gradient force can be described by $F = -\nabla U$ where U is the energy in the electromagnetic field. Spatial variation in the electromagnetic field can occur, for example, in a tightly focused laser, which is the principle behind optical tweezers [156]. In the case of a dielectric particle, a dipole is formed. The charged particle experiences a force due to the electromagnetic field and is accelerated to the region of highest intensity. For a tightly focused laser, the intensity is highest at the focal point, and decreases away from the focal point. A dielectric structure in a spatially varying electromagnetic field experiences the same phenomenon and can be considered to be a collection of dipoles [54]. Spatial variation in the electromagnetic field can also occur in photonic waveguides. A well-confined optical mode in a waveguide will decay exponentially outside the waveguide due to the evanescent field decay, as described in Section 2.2.1. Therefore, a dielectric object such as a cantilever or doubly clamped beam placed within the evanescent field of a waveguide will experience an attractive force [157]. In this example, the cantilever or doubly clamped beam will be pulled towards the waveguide.

Both optical gradient forces and radiation pressure forces result in displacement-dependent shifts in the optical cavity resonance. As the mechanical device moves, it alters the effective index of the optical cavity. The change in the effective index, and therefore the propagation constant according to Eq. (2.17), results in a change in the optical cavity resonance wavelength. This is called dispersive coupling [158]. One way to measure the cavity shift is to position a probe laser on one side of the optical cavity resonance, and measure the transmitted optical power. As the cavity's resonance condition changes due to the mechanical displacement, a power change is observed at the output, because the probe wavelength position is stationary. This measurement can be completed by positioning the probe laser on either the blue (low wavelength, high frequency) or red (high wavelength, low frequency) side of the optical cavity.

For both the radiation pressure force and the optical gradient force, the strength of the interaction between the optical cavity and the mechanical device can be described by the optomechanical coupling coefficient, $G = \partial\omega/\partial x$ where ω is the optical cavity frequency and x is the displacement of the mechanical device. This parameter describes how much the optical cavity shifts in frequency for a given mechanical displacement. The optomechanical coupling can be measured directly. There are several techniques available to do this, including the injection of a calibration tone [159]. One of the simplest approaches is to measure the frequency shift caused by the optical spring effect, provided that the optomechanical coupling is strong enough to cause a detectable frequency shift.

The optical spring effect is a phenomenon that occurs when the spring constant of the mechanical device increases (stiffening) or decreases (softening) by the placement of the probe laser on the blue or red side of the cavity, respectively [160]. It is one result of back action effects that the optomechanical interaction has on the mechanical motion. As the mechanical motion shifts the cavity resonance, it also alters the driving force. When this changing force is in phase with the motion, it becomes an optical spring constant. When there is a delay to the interaction, introduced by a finite cavity lifetime, the changing force can become out of phase with the motion and alter the mechanical damping. This is called dynamical backaction. When the mechanical motion is oscillating, we can understand the interaction between the optical cavity, the mechanical resonator, and the probe laser by describing the system using the input-output formalism for optomechanics, and discussing the interaction in terms of quantized scattering [143, 161]. The oscillatory cavity shift induced by the mechanical motion produces a set of intracavity field sidebands with frequencies equal to $\omega_\mathrm{L} \pm n\Omega_0$ where ω_L is the laser frequency, Ω_0 is the mechanical frequency, and n is an integer. In particular, the $\omega_\mathrm{L} + \Omega_0$ sideband is called the Stokes sideband, and the $\omega_\mathrm{L} - \Omega_0$ sideband is called the anti-Stokes sideband. For the case where the cavity linewidth $2\gamma >> \Omega_0$, many sidebands will be present within the optical cavity resonance, as shown by the green arrows in Figure 2.9. This is called the unresolved-sideband regime, or the Doppler regime. In the opposite case, only either the Stokes or anti-Stokes sideband will lie within the optical cavity resonance. This is called the sideband resolved regime. Here, we will focus on the specific example of the Doppler regime, as this is the regime that is used for all following experiments. The same principles hold true for the resolved sideband regime but involves only the Stokes and anti-Stokes sidebands instead of the full set of sidebands.

When the probe laser is positioned off of the cavity resonance, the scattering

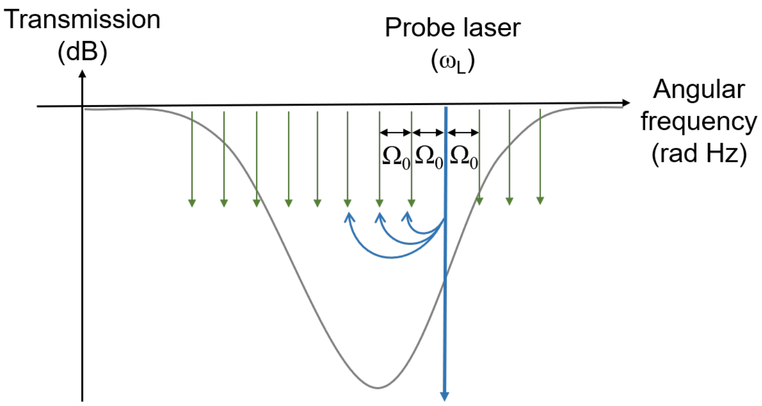

Figure 2.9: A schematic showing the mechanism of energy transfer in the Doppler regime of optomechanics, adapted from [161]. The gray curve is the optical cavity transmission in dB. The transmission is plotted versus the angular frequency. The position of a blue-detuned probe laser is shown by the blue arrow and labeled ω_L. The sidebands are generated at a frequency spacing of Ω_0 by the mechanical displacement, which is represented by the green arrows. In the case of a blue-detuned laser, a scattered photon can become a lower energy photon. The remaining energy creates a quantized number of phonons. In this way, energy can be distributed to multiple sidebands, as shown by the curved blue arrows.

probability into the sidebands becomes asymmetric due to the cavity density of states. When the probe laser is positioned on the blue side of the cavity resonance, the scattering rate for the set of $\omega_\mathrm{L} - n\Omega_0$ sidebands is enhanced, while the scattering rate for the set of $\omega_\mathrm{L} + n\Omega_0$ sidebands is suppressed. Similarly, when the probe laser is positioned on the red side of the cavity resonance, the set of $\omega_\mathrm{L} - n\Omega_0$ is enhanced while the set of $\omega_\mathrm{L} + n\Omega_0$ is suppressed. Energy must also be conserved in the system. For the blue-detuned probe, energy conservation is achieved by the transfer of vibrational energy from the optical field to the mechanical resonator in phonons of quantized energy $\hbar\Omega_0$. This results in amplification of the mechanical motion and a reduction in the damping. The opposite is true for the red-detuned probe, where vibrational energy is transferred to the optical field from the mechanical resonator. In this case, damping is increased and the mechanical amplitude decreases. These two cases can also be thought of as heating (adding phonons) and cooling (removing phonons) of the mechanical resonator. In the case of the Doppler regime, many sidebands are present within the optical cavity and so in the case of a blue-detuned laser, many phonons can be generated by a single photon [161]. This makes the Doppler regime preferable for amplification compared to the resolved sideband regime, where the photon scattering has only one sideband and that sideband generates only one phonon.

In addition to the amplification (damping) experienced by a mechanical device due to a blue (red) detuned probe laser, the mechanical device also experiences an increase (decrease) in its spring constant [162]. The change in the spring constant is introduced by the optical force according to $\partial F_{\mathrm{opt}}/\partial x = k_{\mathrm{opt}}$, where x is the displacement of the simple harmonic oscillator and k_{opt} is the optical spring constant. The optical force can be produced by the radiation pressure force or by the optical gradient force. Both of these optical forces are proportional to the lineshape of the optical cavity resonance. Therefore, $\partial F_{\mathrm{opt}}/\partial x$ can have a negative or positive value depending on whether the probe laser is detuned to the red or the blue side of the optical cavity resonance. On the red side, $k_{\mathrm{opt}} < 0$, resulting in a decrease in the overall spring constant. The resonance frequency will also decrease, since $\Omega_0 = (k/m_{\mathrm{eff}})^{1/2}$. This is referred to as a spring softening effect. On the blue side, $k_{\mathrm{opt}} > 0$ and therefore both the effective spring constant and the resonance frequency will increase. This is a spring stiffening effect. In the Doppler regime, the frequency shift caused by the optical spring effect can be described by [143]

$$\delta\Omega = g_0^2 n_{\mathrm{cav}} \frac{2\Delta}{\gamma^2 + \Delta^2}, \tag{2.38}$$

where g_0 is single-photon optomechanical coupling rate and quantifies the interaction between a single optical photon and a single phonon. n_{cav} is the number of photons in the cavity. The number of photons in the cavity can be expressed as

$$n_{\mathrm{cav}} = \frac{2\gamma_{\mathrm{ex}}}{\gamma^2 + \Delta^2} \frac{P_{\mathrm{bus}}}{\hbar\omega}, \tag{2.39}$$

where P_{bus} is the optical power in the bus waveguide and ω is the laser frequency. Finally, the single-photon optomechanical coupling rate can be related to the optomechanical coupling via $G = g_0/x_{\mathrm{ZPF}}$. $x_{\mathrm{ZPF}} = (\hbar/2m_{\mathrm{eff}}\Omega_0)^{1/2}$ is the zero-point fluctuation of the mechanical device [143]. Combining these definitions and Eqs. (2.38) and (2.39) gives the final result for relating the shift in resonance frequency caused by the optical spring effect to the optomechanical coupling G:

$$\delta\Omega = G^2 x_{\mathrm{ZPF}}^2 \frac{4\gamma_{\mathrm{ex}}\Delta}{(\gamma^2 + \Delta^2)^2} \frac{P_{\mathrm{bus}}}{\hbar\omega}. \tag{2.40}$$

Since all of the optical cavity parameters in this equation are known, all that is required to calculate the optomechanical coupling is the frequency shift and corresponding detuning. This provides a straightforward method to experimentally measure the optomechanical coupling for a given device.

2.3.1 Optical Actuation

As discussed in Section 2.1, there are many potential methods for actuation of nanomechanical devices. Actuation, often referred to as driving, of the nanomechanical devices is essential for mass sensing applications. Although the thermomechanical noise can used for mass sensing [17], the nanomechanical mass sensor should ideally be driven at its onset of nonlinearity to provide the highest dynamic range for mass sensing experiments [18, 20]. Optomechanical transduction allows for the actuation of nanomechanical devices using optical forces such as the radiation pressure force or the optical gradient force. This is ideal, as the optomechanical system is already designed for optical interactions and therefore the physical mechanism for the actuation force is already built into the optomechanical system. Optical actuation can be applied at high powers to achieve large amplitudes. It is also a high-bandwidth approach, which makes it preferable to actuation using piezoelectric disks. Actuation with piezoelectric disks is simple and often used in mass sensing with nanomechanical systems [9], however, these disks are limited to frequencies in the range of tens of megahertz. Optical actuation clearly has many benefits compared to other types of actuation. For these reasons, we will use optical actuation in the remainder of this work. We will focus on actuation via the optical gradient force, as this is the force used in the remainder of this work. The radiation pressure force can also be used for optical actuation [50, 163, 164]. The discussion here is not specific to nanoscale mechanical devices; these principles can be extended to any cavity optomechanical system.

The optical gradient force is a dispersive force generated by the gradient of the optical cavity field, as discussed in the previous section. The optical gradient force acting on a mechanical device external to the optical cavity can be described mathematically by [157]

$$F(x) = -\frac{2P_{\mathrm{bus}}\gamma_{\mathrm{ex}}G}{\omega(\Delta^2+\gamma^2)}, \tag{2.41}$$

and is a function of the laser detuning from the cavity resonance Δ. P_{bus} describes the optical power in the bus (input) waveguide coupled to the optical cavity. Eq. (2.41) can be used to calculate a DC or an AC optical force, depending on whether P_{bus} is the AC or DC optical power in the bus waveguide. The generation of an AC optical force will be described in more detail in Section 2.4. Eq. (2.41) is defined such that a negative force is an attractive force that pulls the nanomechanical device towards the optical cavity.

There are two types of optical actuation that can be achieved with the optical gradient force. The first is self-oscillation, a common approach in optomechanics [16, 165]. Self-oscillation uses a single laser to act as both the pump and the probe. The laser is detuned to the blue side of the optical cavity, and the power is increased. As discussed in Section 2.3, a blue-detuned laser will introduce energy into the system, resulting in amplification of the mechanical motion. The amplification provided by the optical cavity can be expressed in terms of the optical damping rate Γ_{opt}. For a blue-detuned laser providing amplification (anti-damping), the optical damping rate is negative. The optical damping rate depends on the optical power of the laser. The damping of the mechanical system is expressed as $\Gamma_{\mathrm{m}} = \Omega_0/Q$, where Q is the quality factor of the mechanical resonance. When $\Gamma_{\mathrm{opt}} + \Gamma_{\mathrm{m}} < 0$, the optical amplification becomes larger than the intrinsic mechanical damping, and the damping of the overall system becomes negative. This is the threshold for self-oscillation. Above this threshold, the mechanical vibrations are self-sustained and the mechanical quality factor increases. Although self-oscillation has been used for mass sensing [166], it is less sensitive for mass sensing in comparison to a tight feedback loop with clean reference oscillator, as there is significant phase-walking of the self-oscillator in nanoscale systems [18].

The second type of optical actuation that can be used is a pump-and-probe approach [69]. This technique does require additional resources, as two tunable lasers are required. However, this technique has a high-bandwidth and tunable power to reach the upper limits of the mass sensor's dynamic range. The pump-and-probe approach also is compatible with phase lock loop operation, and so the phase noise of the mass sensing system is reduced compared to self-oscillation. The pump-probe technique uses a weak probe laser and a strong pump laser. The pump laser is amplitude-modulated at the mechanical resonance frequency, which results in an oscillatory optical force at the nanomechanical device. Therefore, the nanomechanical resonator behaves as a driven damped harmonic oscillator with a coherent phase signal, and can be tracked in a phase lock loop. An amplitude modulator consisting of an electro-optic modulator (EOM) embedded within a Mach Zehnder interferometer is used for amplitude modulation. The EOM is designed for telecommunications and has a maximum frequency of 10 GHz, allowing for very large actuation frequencies. The wavelength of the pump is set to the minimum of one optical resonance, at zero detuning. This position of the pump laser is important, as setting the laser at zero detuning avoids accidentally actuating the device through the self-oscillation mechanism. To obtain the maximum output signal from the nanomechanical device, the probe laser wavelength is set to the point of maximum slope on the side of a different optical resonance. The probe laser must be set to a power less than the threshold for self-oscillation, or the probe laser may inadvertently introduce amplification when the probe laser is blue detuned. Similarly, the probe could introduce damping on the red side if the power is too high, reducing the signal-to-noise ratio and decreasing the mechanical quality factor. Selection of a suitable probe power is therefore an important consideration.

2.3.2 Optomechanics and Silicon Photonic Integrated Circuits

Optomechanical devices can be fabricated in a straightforward way using silicon-on-insulator substrates. Since integrated photonics allows for the fabrication of optical cavities on a chip, optical cavities can easily be placed adjacent to mechanical components on the same chip. Both optical and mechanical devices are fabricated from CMOS processes and are conveniently both suited for fabrication using SOI substrates. The photonic and mechanical devices are made from the thin silicon device layer (220 nm thick) and the oxide layer underneath (2 μm thick) acts as a buffer layer for the silicon photonics, to prevent leakage into the silicon handle wafer. The oxide layer also acts as a sacrificial release layer for the mechanical components. The mechanical components are placed adjacent to the photonic components, such that the mechanical device is within the evanescent field of the photonic waveguide. The photonic cavities used in this work are racetrack resonators, as previously mentioned. The high finesse of the racetrack resonators allows photons to interact with the mechanical component several times, increasing the signal-to-noise ratio (SNR) compared to interaction with a straight waveguide.

To create the mechanical component, the buried oxide layer is etched to release the mechanical device. This can be done using a masked process, so that only the mechanical components are released, or a maskless process in which case all of the photonic components are undercut slightly by the isotropic etch process. Previous work has demonstrated that etching the silicon buffer layer beneath the photonic devices does not substantially impact the device performance for 430 nm wide waveguides [68]. This makes intuitive sense based on the effective index method described in Section 2.2.1, since the removal of a small amount of oxide at the edges of the waveguide base does not substantially change the waveguide effective index, and the waveguides are well above cut-off. Once released from the sacrificial oxide layer, the mechanical device will vibrate at its characteristic resonance frequency. The motion of the mechanical device modulates the effective index of the waveguide, which in turn modulates the resonance condition of the racetrack resonator. As a result, an AC power modulation at the mechanical resonance frequency is observed at the optical cavity output, and is recorded by a photodiode. The strength of the signal received at the photodiode can be discussed in terms of the transduction coefficient. The transduction coefficient $\mathrm{d}T/\mathrm{d}x$ is defined as the change in the transmission of the racetrack resonator for a given change in the amplitude of the mechanical signal. The transduction coefficient is expressed in watts per metre. The measured voltages are converted to optical powers using the conversion factor of the photodiode used in the measurement. The higher the transduction coefficient, the higher the signal received at the photodiode for a given amplitude of vibration. The mathematical expression for the transduction coefficient of a racetrack resonator is [69]

$$\frac{\mathrm{d}T}{\mathrm{d}x} = \left(\frac{\mathrm{d}T}{\mathrm{d}\lambda}\frac{\mathcal{F}}{2\pi}\right)\left(\frac{2\pi}{\lambda}\frac{\partial n_{\mathrm{eff}}}{\partial x}\beta l_{\mathrm{m}}\right), \tag{2.42}$$

where l_{m} is the length of the mechanical resonator, and β is a factor that describes how much of this overall length is interacting with the optical resonator. For example, a short cantilever of length less than 3 μm has $\beta = 0.394$, because that is the normalized average amplitude of the cantilever. The calculation of β becomes more complicated if the device is a long doubly clamped beam that is interacting with a short optical cavity length. $\mathrm{d}T/\mathrm{d}\lambda$ is the slope of the optical cavity where the probe laser is positioned. This can be recorded directly, making all of the parameters in Eq. (2.42) straightforward to obtain experimentally with the exception of $\partial n_{\mathrm{eff}}/\partial x$. This parameter is the change in the effective index over the change in the gap between the mechanical device and the cavity. It is an exponential function because, as discussed in Section 2.2.1, the evanescent field decay outside the waveguide is exponential. For an SOI waveguide without a cladding layer, we can use the rule of thumb established from Eq. (2.11). A waveguide operating at 1550 nm in the TE mode with air cladding has an effective index of 2.4, and therefore the decay length of the evanescent field is approximately 110 nm. The evanescent field at a distance x in nanometers is of the form $\exp(-x/110)$. Therefore, placing the nanomechanical beam at different gap spacings within that evanescent field will have an exponentially decreasing effect as the gap spacing is increased. The effective index at different gap spacings could be calculated by applying multiple iterations of the effective index method. However, this type of calculation is more suited to numerical solvers, to increase the efficiency of the calculation. The effective index of the entire system of the waveguide and mechanical device together can be calculated for varying gap spacing, and the derivative calculated to produce $\partial n_{\mathrm{eff}}/\partial x$.

The optomechanical coupling can also be calculated using the parameter $\partial n_{\mathrm{eff}}/\partial x$, providing a way to theoretically calculate this value through a simple formula derived in [69]:

$$G = \frac{\partial \omega}{\partial x} = \frac{\omega_0 \beta l_{\mathrm{m}}}{n_{\mathrm{g}} L_{\mathrm{c}}} \frac{\partial n_{\mathrm{eff}}}{\partial x}. \tag{2.43}$$

This expression uses only two simulated parameters. The first simulated parameter is $\partial n_{\mathrm{eff}}/\partial x$. The other parameter obtained from simulation is the group index (n_{g}), which can also be obtained from mode solver simulations by recording the index at various wavelengths. The other parameters in this equation are known from the geometry of the optomechanical system, and so the optomechanical coupling can be easily calculated.

2.4 Experimental Setup

As previously mentioned, there are many options when considering how to couple light into and out of photonic chips. These methods include: edge or butt coupling [167] where the output of a fiber is placed adjacent to the input of an on-chip waveguide; tapered fibers [108] where an unclad, stretched fiber is positioned over top of a bus waveguide; or grating couplers [72]. For grating couplers, the input light must arrive at the correct angle, as discussed in Section 2.2.3. To couple light into grating couplers, a fiber will be held or glued at the desired angle immediately above the grating coupler on the chip [77].

For mechanical devices, it is often desirable to measure them in vacuum to reduce air damping and improve the signal-to-noise ratio, especially for testing new devices. In this case, the devices must be placed in a vacuum chamber and directly positioning optical fibers on top of grating couplers becomes a significant challenge. To overcome this challenge, we use a free-space confocal microscope setup to focus the light onto the grating couplers from a distance. This eliminates the need for exact positioning of the input/output fibers inside a vacuum. By using free space optics to align the laser spot, we can also improve the tunability of our setup, as the input angle of our light can be varied easily. This allows for the grating couplers to be fully optimized, even when submerged in water (Section 3.1.1).

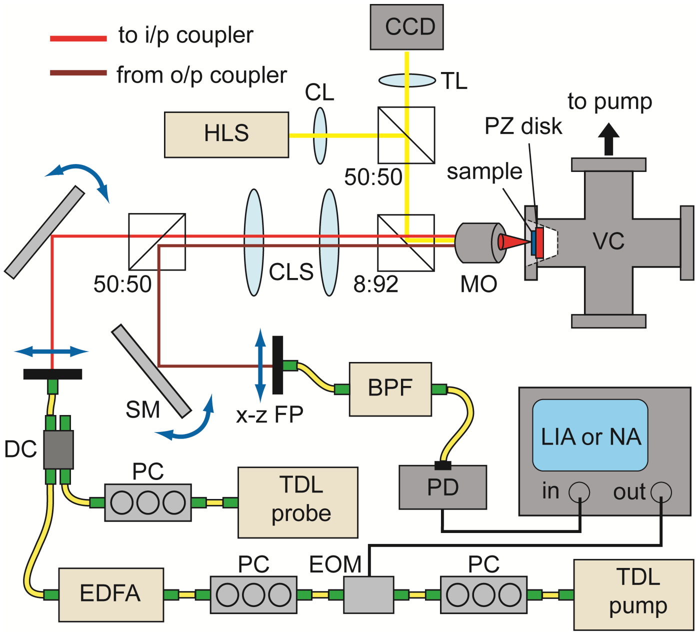

Figure 2.10: Schematic of the pump-and-probe experimental setup [69]. Image provided by Vincent Sauer, © IOP Publishing. Reproduced with permission. All rights reserved.

Although this setup has been detailed elsewhere [11, 118], we will describe it briefly here as well. The setup is pictured as a schematic in Figure 2.10, originally published in [69]. Our silicon-on-insulator chip is mounted inside the vacuum chamber (VC), which is connected to a turbo pump that pumps the chamber down to a pressure less than 1×10^{-5} torr to remove any viscous damping introduced by air. In the schematic, it is noted that the sample can be mounted on a piezoelectric (PZ) disc. Although this is a possibility to provide an alternative source of actuation [69, 168], it is not used in this thesis. Rather, we use optical actuation via the optical gradient force using the pump-and-probe approach detailed in Section 2.3.1.

There are two tunable diode lasers present in the setup, a probe laser for detecting the motion of the mechanical devices (TDL probe) and a pump laser for actuation (TDL pump). The probe laser is directed through a polarization controller (PC) and into a 50/50 directional coupler (DC). The pump laser is sent through an amplitude modulator, which consists of an electro-optic modulator (EOM) embedded within a Mach-Zehnder interferometer, and an erbium doped fiber amplifier (EDFA) before reaching the directional coupler. The EOM is connected to an AC voltage source such as a lock-in amplifier (LIA) or network analyzer (NA) to provide an AC drive signal at the desired frequency and amplitude. The EOM is also subject to a DC bias. The DC bias allows us to set the operating point of the modulator to provide the largest amplitude modulation and is optimized during each experiment to provide maximum output. The EOM permits the application of an AC optical force to the nanomechanical device. The AC component arises because of the amplitude modulation on the pump laser provided by the EOM. The optical AC power defined as the driving voltage, V_{drive}, applied to the EOM divided by its V_π. This ratio is then multiplied by the DC power in the bus waveguide, to determine the AC power present in the bus waveguide. This value can then be used to calculate the AC optical force, as described in Section 2.3.1.

Once the pump and probe are coupled together into a single fiber at the directional coupler, they are directed into the free space confocal lens system (CLS). Finally, the light reaches a microscope objective (MO) and is incident on the sample. The light is coupled into one grating coupler, and out of a second grating coupler. The output light re-enters the microscope objective and the confocal lens system. Finally, a 50/50 beam splitter is used to separate the output light from the input light and direct it into a fiber. The light passes through a band-pass filter (BPF), which is used to filter out the pump laser. This leaves only the probe laser to be detected at the photodiode (PD). The optical signal is converted to an electrical signal by the photodiode. The built-in low-pass filter in the photodiode separates the signal into DC and AC components. The AC signal is recorded by a lock-in amplifier, network analyzer, or spectrum analyzer. The DC signal is sent directly to a computer. The AC signal is used to measure the mechanical signals, whereas the DC signal is used to measure the optical response of the racetrack cavity.

To image the chip when it is in the vacuum chamber, a high-intensity white light source (HLS) is directed onto the chip with a series of beam splitters. The reflected light is directed back through the microscope objective and onto a CCD camera. Therefore, both the laser spots from the input and output grating couplers, as well as the devices themselves, can be imaged. This makes the system straightforward to align.

The tunability of the setup is largely due to the scanning mirrors (SM) and fiber positioners (FP). By adjusting the mirrors, we are able to adjust the incident angle of the light into the microscope objective. The fiber positioners alter the location of the laser spot on the microscope objective. Since the microscope objective acts to perform a Fourier transform on the incident light [83, 118], adjusting the scanning mirrors results in a change in the position of the spot on the chip's surface. Adjusting the fiber positioner results in changing the angle of the light incident on the chip. In this way, we are able to adjust the laser so that it can be received by a grating coupler in any orientation. The maximum angle that can be achieved with this setup is approximately 17°, which much larger than the typical incident angles required for grating couplers, which is usually closer to 10°.

This experimental setup has been used in all of the measurements described in the following chapters.

Chapter 3

Practical considerations for portable nano-optomechanical sensors

In this chapter we discuss several different methods to improve the overall device performance for mass sensors. In Section 3.1 we focus on the development of photonic and mechanical systems for use in fluidic environments. We also present a low-cost approach for packaging microfluidic sensors. The goal of this section is to make improvements in the technology with the application of health care diagnostic tools in mind.

Section 3.2 demonstrates a proof-of-concept fabrication process that allows for higher order modes to be detected in optomechanical systems. This technique allows for the improvement of the spatial resolution of nano-optomechanical mass sensors and provides a path to improve the accuracy of mass measurements.

In the final section, 3.3, we describe a measurement technique that permits the use of a low-frequency photodiode and a single drive laser to reduce the complexity of the surrounding electronics. This alternative measurement approach is beneficial for improving the portability of a mass sensing system.

3.1 Optomechanical Systems for Liquid Sensing

There is significant interest in developing mass sensors for use in fluidic environments, in addition to gaseous environments. There are many potential applications for fluid-based sensing including health care, for disease diagnosis or health monitoring, and environmental monitoring, to determine the concentrations of potentially hazardous compounds in water. Other applications include furthering basic scientific research, as chemical reactions could be monitored in situ with nanomechanical devices to determine reaction kinetics. These applications typically require that samples under test cannot be processed (i.e. dried or placed in vacuum) and the measurements are ideally done in fluid, in real time. Clearly, optical and mechanical components that can function in a fluidic environment are desirable. In the following sections, we discuss the design of photonic and nanomechanical components for use in water. The challenges with each design will be discussed.

3.1.1 Photonics for Use in Water

For optimal performance of optomechanics with photonic integrated circuits in water, there are three main concerns that must be addressed. First is that infrared light is strongly absorbed by water, with an absorption coefficient at $\lambda = 1550$ nm equal to approximately 10 cm^{-1} [169]. Therefore, we had to account for the high loss induced by the water. We also require a very high transduction coefficient, since any mechanical vibrations in water are strongly damped by the surrounding fluid (see Section 3.1.2 for more detail). Finally, water has a different index of refraction than air, which will alter the performance of the waveguides since the effective index changes when the cladding index changes (Section 2.2.1). In this section, we will address all three of these issues to formulate an effective design for optical racetrack resonators operating in water. We will show experimental evidence of the successful design and fabrication of these devices.

All of the photonic elements were simulated using commercial finite difference time domain simulations [170] or eigenmode solver simulations [171]. Grating coupler designs were provided by imec, the foundry we used to fabricate these devices. These grating couplers were not designed specifically for water. Rather, they were designed for oxide cladding. However, the grating couplers still perform well in air, as demonstrated in Chapters 4–5. Since the refractive index of water is 1.3, closer to the index of oxide than air, the grating couplers will actually perform slightly better in water than in air. Additionally, the tunability of our experimental setup (as described in Section 2.4) provided enough flexibility in the coupling angle to optimize the transmission through the grating couplers regardless of the cladding material.

To address the issue of absorption of near infrared light by water, the waveguide width was optimized. For wide waveguides, the effective index of the waveguide is higher and the majority of the electric field, and therefore the optical power, is confined within the silicon waveguide. As the waveguide width decreases, the effective index decreases and the electric field is less well-confined. More of the optical power is present near the waveguide edges and immediately outside of the waveguide, in the surrounding water. Wider waveguides are better for carrying light through water, as the light will be confined to the silicon waveguide and less energy will be absorbed by the water. Figure 3.1 shows the difference between the fundamental TE modes at a wavelength of 1550 nm traveling in (a) a narrow waveguide of 400 nm and (b) a wider waveguide of 500 nm. The fabricated waveguides had an average width of 502 nm with a standard deviation of 13 nm. These are the average dimensions measured from twelve scanning electron microscope (SEM) images of different waveguides. The performance changes significantly for a small variation in dimension. As discussed in Section 2.2.1, as the waveguide size decreases, the optical mode approaches cut-off, which is the mechanism for the field becoming less confined. By using the effective index method, we can estimate that cut-off will occur at approximately one-half of the wavelength in the silicon slab mode. The effective index of a TE silicon slab mode with air cladding is 2.8 [172], and so in this case cut-off will occur at a width of 1550/2.8/2 = 270 nm. The waveguide is multi-mode above 600 nm [95]. Clearly, the optical properties of the waveguide change quickly between 270 nm and 600 nm width, since the waveguide goes from cut-off to multi-mode over a 330 nm increment. Therefore, only small changes are required to significantly alter the behaviour of the waveguide mode.

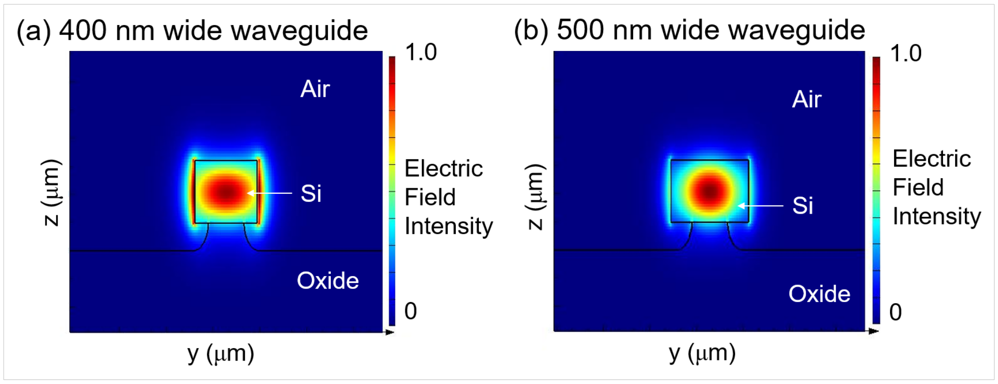

Figure 3.1: Simulated electric field profiles for (a) 400 nm wide waveguide and (b) 500 nm wide waveguide. The simulations used air cladding and are for the TE mode at a wavelength of 1550 nm. The waveguide thickness is 220 nm. The mode extends further outside silicon waveguide when the width is equal to 400 nm.

The other main design parameter for the photonic elements was the gap between the bus waveguide and the racetrack resonator. This gap determines whether the racetrack resonators are under, over, or critically coupled. For measuring mechanical devices in water, the steepest slope of the optical cavity transmission possible is desired to maximize the transduction coefficient (Eq. 2.42) and obtain the highest displacement sensitivity possible. This is because the mechanical devices will be strongly damped in liquid, and will have very small amplitudes of vibration [173]. Although the steepest slope is achieved in the under-coupled regime, the largest linear range (bandwidth) is obtained in the over-coupled regime [94]. To obtain a high slope while maintaining a reasonable linear range, we chose to use critical coupling.

We used the power coupling formalism described in Section 2.2 to determine the coupling coefficient and transmission coefficient required for the racetracks in water. Coupled mode theory, in conjunction with FDTD simulations, was used to calculate κ and τ. The simulated structures were SOI waveguides with a cladding index of 1.3, which is the index of water. The coupling length (L_{coupler}) was chosen to be 3 μm, as this provided an adequate interaction length for the adjacent mechanical devices. The cross-over length (L_{cross}, Eq. 2.20) was obtained from eigenmode solver simulations. From the cross-over length, we calculate the coupling coefficient from Eq. 2.21 [77]. Once κ, and therefore τ, is known for a variety of gaps, we can select the gaps that are the closest to achieving critical coupling. This is done by choosing a value of the transmission coefficient τ that is equal to a_{rt}. Based on past runs from imec, we were able to estimate the round-trip loss as approximately 0.99 for air-clad racetrack resonators. To obtain critical coupling in water, we fabricated coupling gaps from 130 nm to 250 nm. This was to ensure that even if the loss in the waveguides was high due to absorption by the surrounding water, some racetrack resonators would still perform well.

Figure 3.2 shows the measurement of two nominally identical racetrack resonators (from different chips) in both (a) air and (b) water. The measurement in air shows peak splitting, which is due to coherent backscattering in the racetrack resonator (see Section 2.2.6). To measure the racetrack resonators in water, we placed double sided tape with a thickness of 50 μm around the perimeter of the chip. A thin glass slide was placed on top of the SOI chip and held in place by the tape. A small space in the tape was left on each side of the chip. De-ionized (DI) water was then carefully dropped into the small gap, and wicked underneath the glass slide onto the racetrack resonators. This allowed for extremely quick prototyping of the photonics in water without the creation of a full fluid cell. The chips were placed on our experimental setup (Fig. 2.4) and characterized. In both measurements, 1.0 mW of optical power was incident on the grating coupler. Figure 3.2(b) shows that the backscattering vanishes when the racetrack resonator is measured in water. This is because the loss is greater when the racetrack resonator submerged in water, and therefore the backscattering is less visible. The extinction improves dramatically in water, reaching -25 dB. This measurement demonstrates successful design and fabrication of photonic racetrack resonators for use in water.

3.1.2 Designing Mechanics for Use in Water

The most significant issue in developing nanomechanical sensors for use in fluid is the damping that occurs due to the surrounding fluid. This damping can cause the quality factor of a typical resonator to decrease from a few hundred in air to 4 or 5 in liquid [173]. This damping makes it very difficult to detect nanomechanical devices such as cantilevers or doubly clamped beams in fluid due to the greatly reduced

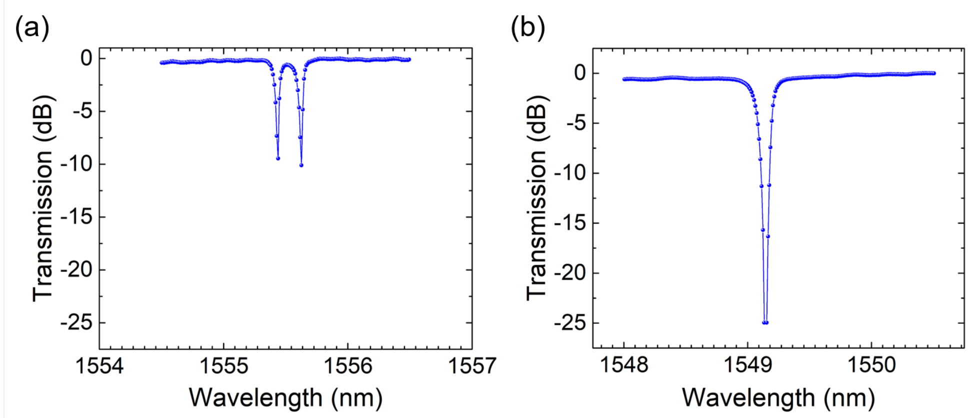

Figure 3.2: Experimental results of two racetracks with nominally identical dimensions, one measured in (a) air and the other measured in (b) water. The optical power input to the grating couplers was 1.0 mW. Coherent backscattering is present in air but not in water.

signal-to-noise ratio. For these reasons, many researchers have turned to other, atypical resonators for detection in fluid. One of the more successful is suspended micro- or nano-channel resonators. These are cantilevers or doubly clamped beams where the fluid is directed through the centre of the cantilever, instead of exterior to the cantilever. Mass sensing is accomplished by detecting the changes in the fluid within the cantilever. The main drawback of these devices is that they reach a limit in terms of scaling since the channels inside the resonator have to be large enough to permit fluid flow. For cantilever suspended nanochannel resonators, mass sensitivities of 0.85 ag have been measured by optimizing the cantilever and channel dimensions [174]. For doubly clamped suspended nanochannel resonators, the mass sensitivity is increased to 2 fg [175]. Other approaches include using high frequency breathing modes. Since these modes of vibration have a very high effective spring constant and a low amplitude of vibration, they are more robust to the damping induced by the fluid [176]. GaAs disk resonators in liquid had a theoretical mass sensitivity of 14 yoctograms [17]. Silicon nitride wheel resonators in water had a mass sensitivity of 1 ag [16]. The breathing mode of an optomechanical crystal in water had a theoretical mass sensitivity of 1.33 ag/Hz$^{1/2}$, and a measured noise floor of 9.33 am/Hz$^{1/2}$ [177].

To create a different type of nanomechanical resonator that would perform well in fluid, there were a few requirements to consider. The main requirement was to have a design that could easily be integrated into existing photonic circuits. A high spring constant and a high resonance frequency were also important factors, analogous to the breathing modes of disk resonators. The high spring constant is also important in preventing stiction. Stiction occurs when micro- or nanomechanical devices are exposed to liquids then dried. During the drying process, the capillary forces of liquids between the mechanical component and the substrate or adjacent structure (such as a waveguide) pull the mechanical component towards the substrate [178]. The mechanical device and the substrate adhere irreversibly due to the high forces between them. Ideally, the silicon photonic chips should be reusable due to their relatively high cost compared with plastic materials, however, stiction can make this impossible. Stiction can be reduced by drying devices from a solvent such as pentane rather than from water. However, commonly used microfluidic materials such as poly-methylmethacrylate (PMMA) are incompatible with these types of solvents [179]. This incompatibility is important to consider since the silicon chip may eventually be packaged into a microfluidic channel made from PMMA or a similar low-cost plastic material. To avoid stiction altogether, it is possible to use devices with a sufficiently high spring constant. This makes the devices better able to resist the capillary forces, reducing stiction. With these considerations in mind, we devised the concept of a 'fin' resonator. The fin is essentially an out-of-plane cantilever. A schematic of a fin resonator can be seen in Fig. 3.3. The fin is adjacent to the racetrack resonator. The base of the fin is attached to the oxide substrate. The top of the fin is the tip of the cantilever. The length of the device is defined by the thickness of the silicon device layer. The thickness, width, and gap are defined as in the bottom right panel of Fig. 3.3.

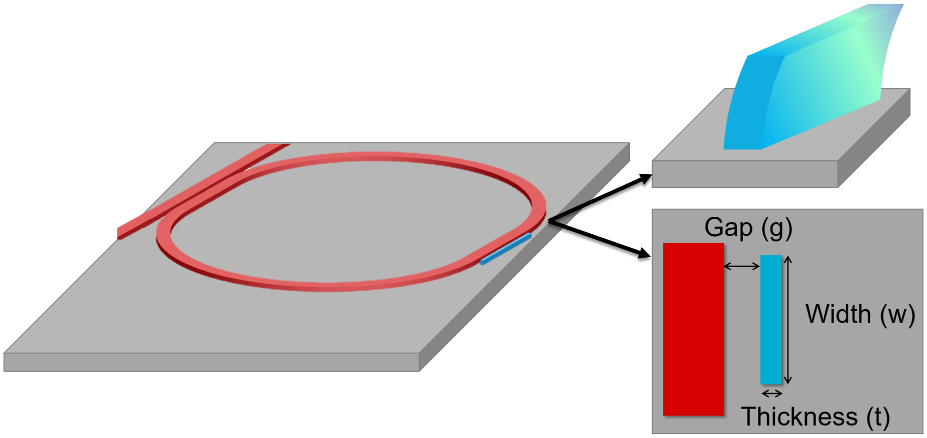

Figure 3.3: A schematic of the fin resonator. On the left-hand side, an image of the fin adjacent to a racetrack resonator. On the top right, a schematic of the fin's motion. On the bottom right, a top down view of the fin with the dimensions labeled.

The resonance frequencies of a simple cantilever can be estimated using Euler-Bernoulli beam theory. The fundamental resonance frequency, for example, is shown by

$$f_0 = \frac{0.162t}{l^2}\sqrt{\frac{E}{\rho}}, \tag{3.1}$$

where E is the Young's modulus and ρ is the density of the material, in this case silicon. The theoretical values from Euler Bernoulli beam theory for the first mode are shown by the red circles in Fig. 3.4. The second mode predictions are shown by the red diamonds. However, one of the primary approximations for this equation is that the beam should be thin compared to the length. Due to the fact that the fins are very short (220 nm), this condition is only met when the fin width is less than or equal to approximately 20 nm. More precise modeling of the resonance frequencies of the fins was completed with finite element analysis (COMSOL). The results of this modeling can be seen in Figure 3.4, which shows the resonance frequencies for (a) 1 μm width and (b) 3 μm width. The blue squares are the results from the finite element solver, and show that there are many modes present in each fin for a given dimension. Although the first two flexural modes are found by the finite element solver, many torsional-type modes are also observed. Examples of the (a) flexural and (b) torsional modes can be seen in Fig. 3.5. From Figure 3.4, it is clear that for a 1 μm wide fin, the Euler-Bernoulli predictions are not entirely accurate. However, for a 3 μm wide fin, the Euler Bernoulli model is much closer to the expected frequencies. Additionally, the wider device has more densely spaced modes compared to the narrower device. This makes sense intuitively, as the amount of strain energy added per node will be greater for the narrower device compared to the wider device. Since the addition of strain energy proportionally increases the resonance frequency, the resonance frequencies will have a larger spacing in the narrow device compared to the wider device.

Eq. (3.1) still provides a useful conceptual framework for the design of the fin resonators. Since the length of the fins is governed by the thickness of the silicon device layer, the only parameter we can vary to adjust the resonance frequency is the thickness. The spring constant k can be tuned by modifying both the thickness and the width, since $k = m_{\mathrm{eff}}\omega_0^2$. The resonance frequencies and spring constants of the fundamental mode of narrow fins with a length of 220 nm are shown in Fig. 3.6. For comparison, the spring constant of a cantilever with a length of 4 μm, thickness 160 nm and width of 220 nm is 0.4 N/m. The spring constants of the fin resonators are in the kN/m range. This difference in spring constant indicates that the fins will be resilient to stiction.

The width will also affect the transduction, according to Eq. 2.42. A larger width will improve the transduction for a given cavity length, which intuitively makes sense as the interaction length is increased for increasing width.

Very high frequency fins will be extremely difficult to detect, as the displacements will be very small and the frequencies are out of the range of our experimental setup.

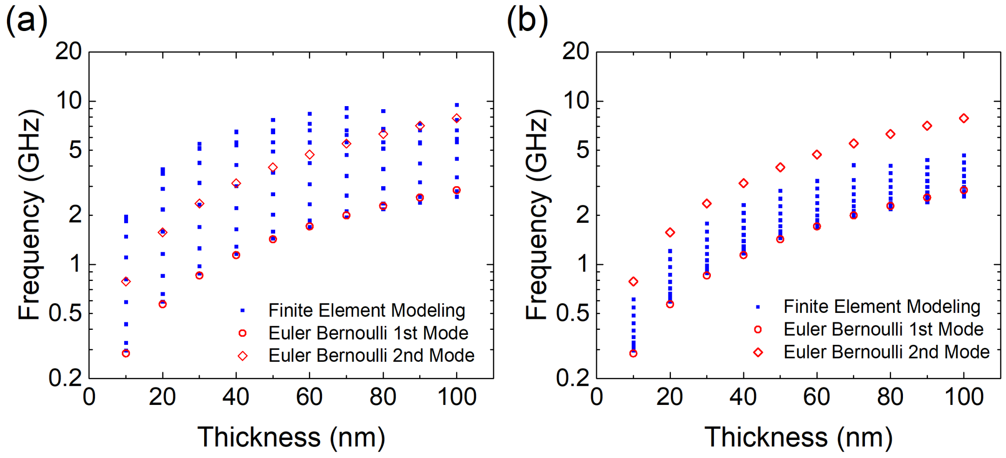

Figure 3.4: Finite element simulation results (blue squares) compared to Euler-Bernoulli beam theory (open red markers) for varying thicknesses of fins with a height of 220 nm and (a) 1 μm width and (b) 3 μm width. Many more modes are visible in the finite element simulations, as these calculations also produce the torsional modes of vibration instead of only the flexural. The standard Euler-Bernoulli beam theory is more accurate for the 3 μm wide fin shown in (b). It is less accurate for the smaller fin simulated in (a), however, the results are close enough that the standard Euler-Bernoulli beam theory may still be used as a design tool even at these small dimensions.

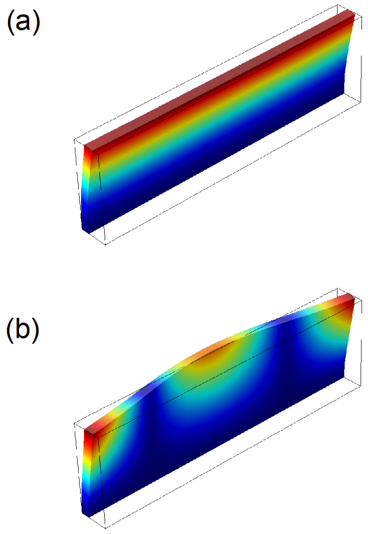

Figure 3.5: Finite element simulation simulation results showing (a) the first flexural mode and (b) the second torsional mode. The fins simulated are 220 nm tall, 1 μm wide, and 30 nm thick are anchored at the base (dark blue colour). The peak amplitude is represented by the red colour. These results highlight the difference in shape between the flexural and torsional modes, as the flexural modes always have peak displacements across the entire tip of the cantilever whereas the torsional modes have displacement nodes and anti-nodes along the width at the tip.

The frequency of the experimental setup is limited by the electronics that read out the mechanical motion; that is, the network analyzer or the lock-in amplifier. However, for thinner fins ($<$ 40 nm), the resonance frequency is close to 1 GHz, which is within the range of our experimental setup. We expect to observe driven mechanical resonances based on the fact that our displacement sensitivity is on the order of tens of fm/Hz$^{1/2}$ [69]. A fin with thickness equal to 40 nm and a width of 3 μm has a spring constant of 790 N/m. Let us assume a driving force of 3 pN, which is easily achievable with our setup as demonstrated in [21]. We will also estimate the quality factor to be no more than 100, given the potentially significant clamping losses in this structure. Using the simple equation $F = kx/Q$, this gives an estimated amplitude of 0.3 pm. We can also estimate the transduction coefficient $\mathrm{d}T/\mathrm{d}z$ using Eq. (2.42). Using the simulated value of $\partial n_{\text{eff}}/\partial x$ for a 40 nm thick fin and a gap between the fin and waveguide of 100 nm, we calculate the transduction coefficient to be 104 W/m. The expected signal size is therefore 104 W/m $\times$ 0.3 pm $=$ 35 pW. The noise floor of the photoreceiver sets limit on the signal size that we can detect. The noise floor of the photoreceiver with 1 GHz bandwidth (NewFocus 1611) is 20 pW/Hz$^{1/2}$. The signal is slightly above or close to the noise floor of the photodiode. The amplitude can be increased by decreasing the thickness of the fins, or by increasing the optical driving force. From this back-of-the-envelope calculation, we expect to see a response from fins with thicknesses less than 40 nm.

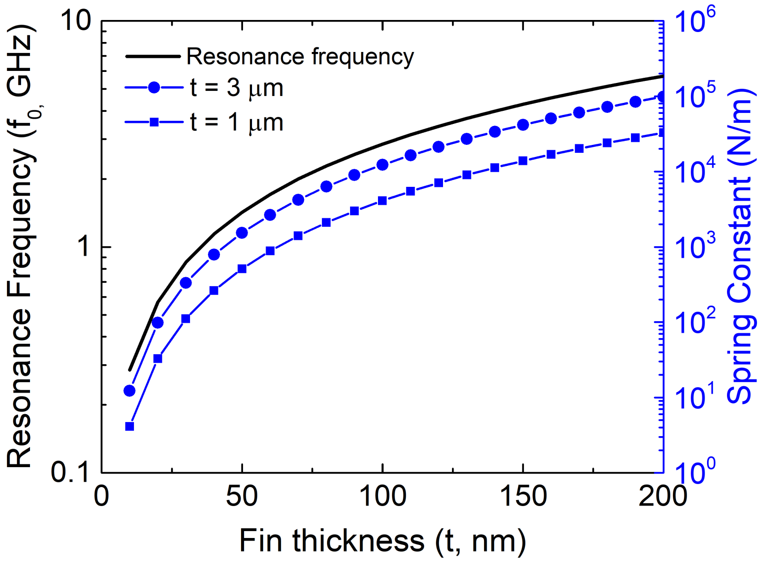

Figure 3.6: Predicted spring constants (blue lines with symbols) of fins with widths of 1 μm (blue squares) and 3 μm (blue circles). The fundamental resonance frequency is shown by the black line, and is calculated using Euler-Bernoulli beam theory.

We fabricated fins through the foundry imec. We coupled the fins to optical racetrack resonators with critical coupling. These fins had thicknesses of 130 nm and 150 nm, the minimum allowable dimensions from the foundry. An SEM image of the fins as-is from the foundry is shown in Fig. 3.7(a). Not surprisingly, mechanical signals from these devices could not be observed even under a large optical driving force, due to the very small expected displacement. In order to reduce the spring constant and increase the amplitude of vibration, post-processing was required. At first, ion milling using a focused ion beam was performed to reduce the thickness of the fins. This was done using a helium (He) ion microscope with a gallium (Ga) focused ion beam. The He ion beam was used to image the samples and the Ga beam was used to mill them. A sample image of a resulting device is shown in Fig. 3.7(b). These devices had thicknesses around 20–40 nm. However, when completing measurements of these devices it was observed that the optical response of the racetrack resonators was degraded. The significantly smaller slope of the optical transmission resulted in a reduced transduction sensitivity. Therefore, no mechanical signals from the ion-milled fins were observed. The change in the optical resonance is shown in Fig. 3.8.

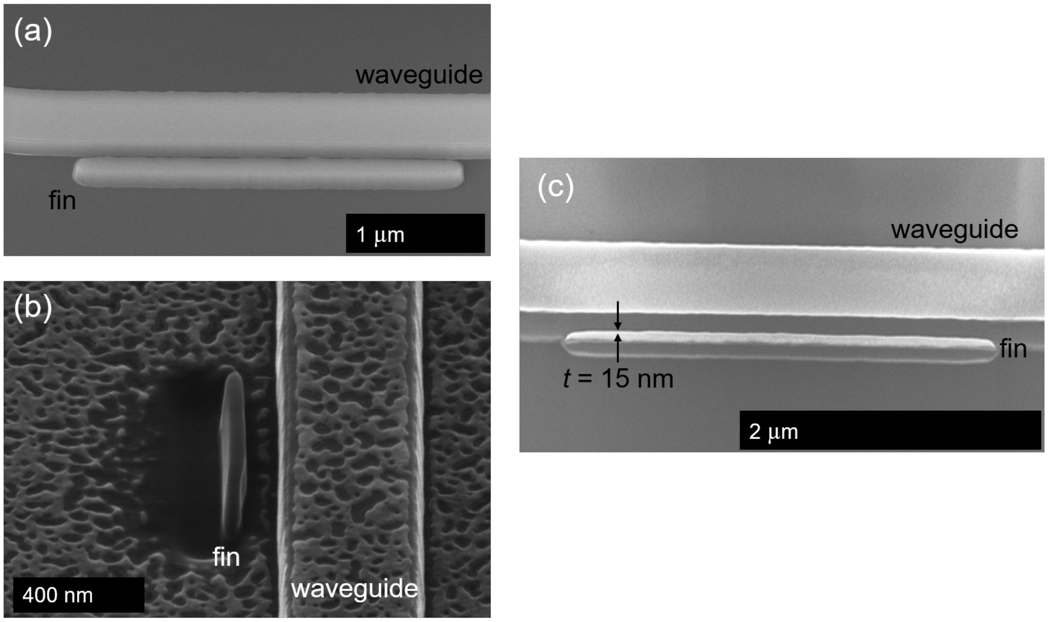

Figure 3.7: Images of different iterations of fins. (a) SEM image of fin as received from foundry, tilted at 30°. (b) Helium ion microscope image of a fin modified by FIB milling, with Au anti-charging layer still present on fin. (c) SEM image of fin from (a) after modification by electron beam lithography.

Next, we used electron beam lithography to reduce the thickness of the fins. ZEP-520A resist was spun onto the existing structures, and using the multilayer alignment capabilities of the Raith 150-TWO, a small opening in the resist was

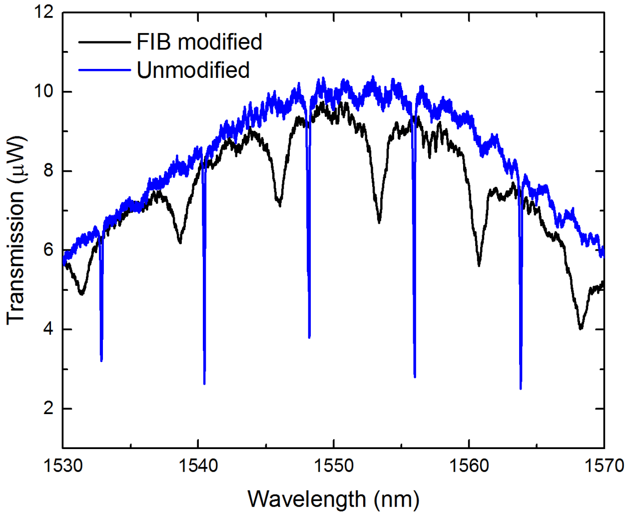

Figure 3.8: Optical ring resonances before (blue line) and after (black line) FIB modification. Before FIB modification, the optical quality factor was 11,000. After FIB modification, the optical quality factor was 2,000. The optical quality factor has been significantly degraded by the FIB process.

placed partially across the existing fins. This created an etch window, and all of the fin that was beneath the open window would be removed. The remainder of the fin was protected by the resist. The silicon was etched using reactive ion etching. Using this technique, fins ranging from 15–80 nm in thickness were produced (Fig. 3.7(c)). The resist was stripped by first performing a 20 minute flood UV exposure, followed by a short soak in Remover PG. The fins were resistant to stiction, as we were able to strip the resist from 15 nm fins with solvent, then rinse the devices in water and dry with nitrogen without stiction. Once the resist was removed and the device characterized by SEM, we measured the mechanical properties. Unlike the FIB process, the optical cavity properties were unchanged by this post-processing procedure. However, no mechanical signals were observed from even the smallest fins and with very high optical drive powers ($\approx$ 30 mW output from EDFA, compared to a typical output power of less than 10 mW). There are several potential reasons that the signal could not be observed. The signal strength of the fins is reduced as they become thinner, as there is simply less silicon to perturb the effective index of the optical cavity. Although simulations showed that very thin 10 nm thick fins should still affect the optical cavity, the perturbation simply may have been too small to resolve. The noise floor of the photodiode with a bandwidth greater than 1 GHz had a higher noise floor than the photodiode with a bandwidth of 125 MHz, increasing the measurement noise floor compared to the typical noise floor in the experimental setup. A rising noise floor may have been detrimental to the displacement sensitivity. Lastly, despite the fact that it appeared in SEM images that all of the resist had been removed, it is possible than some small residues were still present. Any extra residues could have caused damping that might reduce the signal quality factor and amplitude.

To increase the amplitude of vibration, we investigated using 300 nm SOI instead of 220 nm SOI. This would decrease the resonance frequencies substantially due to the $1/l^2$ dependence of the resonance frequency (Eq. (3.1)). For example, a 40 nm thick fin in 300 nm SOI has a resonance frequency closer to 600 MHz than 1 GHz. This would allow us to use our lock-in amplifier instead of the network analyzer, which is beneficial for decreasing the measurement bandwidth as much as possible. The increased amplitude would also allow for greater signal-to-noise. The drawback to this method is that waveguide design is not standardized for 300 nm SOI. All of the optical components, including grating couplers, had to be designed specifically for this application. We designed sub-wavelength grating couplers, where the grating couplers are fully etched and alternate a small, sub-wavelength grating with a grating larger than the wavelength [117]. We also designed waveguides that were 320 nm wide and ring resonators with a 5 μm radius. As we had not done previous work with this waveguide dimension, the coupling parameters could only be estimated. This is because the round trip loss was not known experimentally which, as described in Section 2.2.4, complicates the determination of the coupling coefficient κ and the transmission coefficient τ.

We had the devices fabricated using 100 keV electron beam lithography in 300 nm SOI by Applied Nanotools Inc (ANT) [180]. The thickness of fins achieved using this high-resolution lithography technique was approximately 40 nm (Fig. 3.9(a)). The ring resonators did not perform well as as required for our application. The quality factor was relatively low, indicating the loss was higher than expected. This loss may have been caused by the waveguides being too narrow, which may have resulted in unexpected bending loss or increased scattering loss. For this reason we were not able to measure any mechanical resonance frequencies in the 300 nm thick SOI devices. Figure 3.9(a) shows a 40 nm fin as fabricated from ANT. Figure 3.9(b) shows the ring resonance transmission from this design, with an optical quality factor of 2,000 and a slope $\mathrm{d}T/\mathrm{d}\lambda$ approximately 8 times shallower than the devices from in Section 3.1.1. According to Eq. (2.42), this indicated that our displacement sensitivity was 8 times worse. This explains why no mechanical signals were observed in these experiments.

In summary, we designed mechanical fin resonators specifically for use in a fluidic environment. Although these devices seemed promising for fluid sensing due to their stiction resistance, high resonance frequency, and straightforward design, the

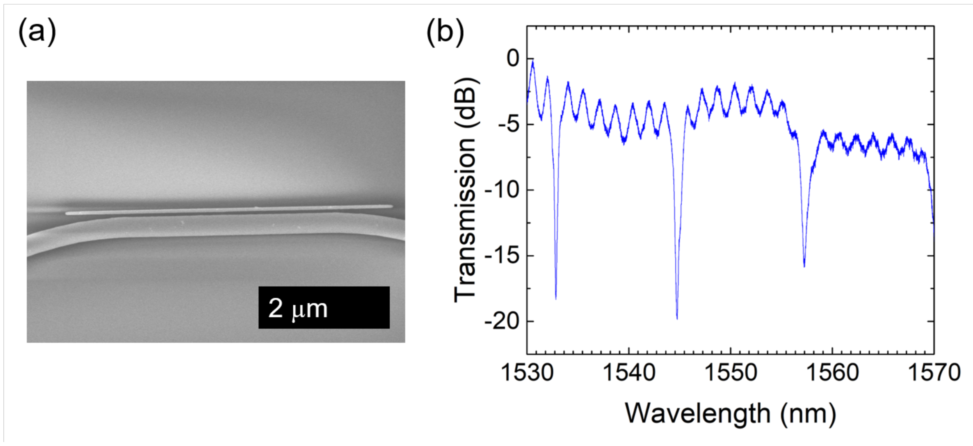

Figure 3.9: (a) SEM image of a 40 nm thick fin fabricated by 100 keV electron beam lithography. (b) Transmission through the 300 nm thick ring resonator. The optical quality factor is approximately 2,000, which is undesirable for optomechanical transduction.

signals were too small to be measured in our optomechanical setup. This makes them undesirable for sensing applications. Ideally, the sensor signal should be easy to resolve and track for robust performance outside of the lab. These devices did not meet this criteria, therefore we conclude that fin resonators coupled to racetrack resonators are not suitable for liquid sensing applications.

Recent work by Safavi-Naeini's group at Stanford has demonstrated fin resonators adjacent to photonic crystal cavities [181]. These are 340 nm tall, and 65 or 90 nm wide. They have resonance frequencies greater than 450 MHz. In this work, an EDFA is used to amplify the Brownian motion of their fin resonators for readout with a photodiode and spectrum analyzer. The mechanical quality factors are in the range of 40 to 180 and a peak signal-to-noise ratio of 15 dB. These devices have significantly higher optical quality factor and optomechanical coupling. Therefore, fin resonators are possible with high Q and large G optomechanical systems.

3.1.3 Photonic-based Temperature Stabilization for Microfluidic Chips

For a liquid sensing system, it is not only the sensor that is important. Packaging the sensor into a microfluidic chip is also important. The microfluidic chip should properly deliver liquid to the device and should also be temperature-stabilized. Temperature stabilization is especially important for biological applications, where cells must be kept at specific temperatures (often 37 °C). This packaging should be inexpensive, so that it could potentially be disposable. It should also be made from materials that are compatible with biological systems, as these would be the samples of interest in any health-care based applications. In conjunction with the Alberta

Centre for Advanced MNT (micro- and nanotechnology) Products (ACAMP) and Mitacs, we made strides towards developing a temperature-stabilized microfluidic chip that could be used for any liquid sensing application, including liquid sensing with nano-optomechanics.

The goal of this project was to simulate, design, fabricate, and test integrated photonics temperature sensors that can be directly integrated with a microfluidic cell. Integrated photonic devices were selected as temperature sensors for microfluidic devices, since electrical devices cannot be embedded in microfluidic channels without altering the flow of fluid in the channel [182]. However, standard integrated photonics are typically fabricated from silicon-on-insulator (SOI) substrates with typical silicon device layer thickness of 220 nm. These devices can have lateral dimensions on the order of 500 nm or less, which means advanced lithography techniques such as electron beam lithography or projection lithography must be used, and substantially drives up the cost. Since the intention of this device was to create a generalized, temperature-stabilized microfluidic system that could be used for many different applications, the cost should be kept low so that the chips could be disposable if the application called for it. Therefore, the entire device platform was created using inexpensive plastic materials. This choice of materials was intended to reduce cost and also improve the ease with which the temperature sensors could be integrated with microfluidics. Silicon-on-insulator substrates are not easily compatible with microfluidic systems. Microfluidic systems made from plastics such as poly-methylmethacrylate (PMMA) or cyclic olefin copolymer (COC) do not bond to silicon, reducing the ability of SOI-based integrated photonic sensors to be used in-situ for microfluidics monitoring as part of the microfluidic package. The main drawback to these materials is that they are not typically used for photolithographic patterning, which is required to create the small features required for integrated photonics. For this reason, the main focus of the project was to create a photolithographic process that could be used to create waveguides and other photonic structures using a fully plastic, microfluidic-compatible platform.

There are three main components necessary to create a waveguide: the substrate, the waveguiding material, and the cladding (see Figure 3.10). In order for light to travel in the waveguiding material, the refractive index of the waveguiding material must be higher than the substrate and cladding materials. The difference between the refractive indices of the waveguiding material and the cladding and substrate materials is referred to as the index contrast. Photonics based on plastic materials systems are usually low index contrast systems since the waveguiding material has an index close to that of the substrate and cladding. Silicon based photonics, alternatively, has a very high index contrast. We chose the negative resist KMPR for the waveguiding material. KMPR has been used in other works as a waveguiding material [74, 183]. The substrate and cladding materials we have studied are PMMA and COC. They are both materials commonly used for microfluidics, and have lower indices of refraction than KMPR. COC in particular is of interest as it is bio-compatible [184].

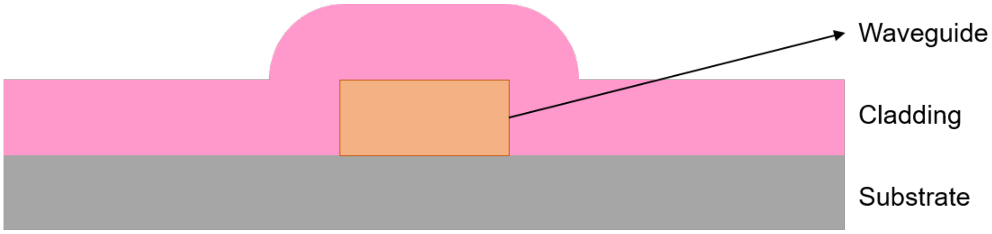

Figure 3.10: Schematic of a waveguide, including the substrate, waveguide core, and cladding layers. The waveguide has a higher refractive index than the cladding and substrate materials.

Another consideration was the wavelength of light to use for temperature sensing. Near infrared light (1500 to 1600 nm) was chosen because it typically does not interact with biological samples. Wavelengths in the visible range can interact with these samples, causing phenomena such as fluorescence [185, 186].

To create a photonic temperature sensor, we chose to fabricate racetrack resonators as the long coupling lengths should compensate for potentially large losses in the system, compared to microring resonators where only a point coupler is used. The temperature can be sensed due to the shift in the resonance wavelength that is induced by a temperature change [187];

$$\Delta\lambda_0 = \frac{\Delta T \lambda_0}{n_\mathrm{g}} \left(\frac{\partial n_\mathrm{eff}}{\partial T} + n_\mathrm{eff} \alpha_\mathrm{T} \right), \tag{3.2}$$

where T is the temperature, λ_0 is the resonance wavelength, n_g is the group index of the waveguide mode, n_eff is the effective index of the waveguide mode, α_T is the thermal expansion coefficient of the waveguide material, and $\partial n_\mathrm{eff}/\partial T$ is the thermo-optic coefficient of the waveguide.

The wavelength shift can be used to measure temperature in two ways. The first method is to position the laser at the edge of the optical resonance, similar to the probe laser in optomechanical measurements. The relative temperature shift can be determined by tracking the change in the power output. This is sometimes called the “side of the fringe” method. The second method is to scan the wavelength range repeatedly, and track the shift in the cavity resonance. Although this measurement is more time-consuming, it was found to have lower uncertainty than the “side of the fringe” technique [187].

Polarization was also an important consideration. In a high-contrast system, the TE and TM modes have very different electric field distributions, whereas in a low-contrast system the field distributions are fairly similar. The TE mode has an electric field discontinuity at the sides of the waveguide, resulting in a higher electric field at the sides of the waveguide compared to the top and bottom. The TM mode has the orthogonal distribution, where the discontinuity at the top and bottom results in a higher electric field compared to the sides of the waveguide. Since we are interested in temperature sensing, we chose to study the TE mode to reduce the cross-talk between the waveguide and the microfluidic channel, as the electric field will be largely confined in the cladding. For sensing applications where contact with the microfluidic channel is desirable, the TM mode should be used. This is because the electric field will extend further into the microfluidic channel since it has a higher electric field at the top of the waveguide, increasing the region of interaction with the analyte and therefore the sensitivity of the waveguide sensor.

Temperature Control with LabView

In addition to measuring the temperature, we would also like to control the temperature on a microfluidic chip. To accomplish this, a feedback loop is required. LabView software was used to write a proportional-integral-derivative (PID) feedback loop using the built-in PID functions in LabView. The feedback loop measures the temperature, and then activates or deactivates a heater as required to achieve the desired temperature set point. The temperature was measured using thermocouples and the heaters used were flexible, thin film heaters. These heaters were selected as they had a very uniform heat distribution and were supplied with a voltage supply that could reach up to 28 V. The PID loop successfully maintained the temperature at the desired set point to within 0.2 °C and could adapt to perturbations in the system.

Simulation and Design

To design the waveguides, Lumerical Solutions MODE was used [171]. The initial simulations and design were performed using values from the literature for the refractive indices of the COC, KMPR, and PMMA. When the initial experimental results did not match the simulations, experimental results for the indices of COC and KMPR were obtained using the VASE ellipsometer. More details on this experiment can be found in Section 3.1.3. The refractive index values used in the initial and final simulations are shown in Table 3.1.

Material	Literature Value (initial)	Measured Value (final)
KMPR	1.555	1.5678
COC	1.52	1.513
PMMA	1.49	NA

Table 3.1: Refractive Index Values for Simulations

First, the optimal size of the waveguides was determined. The size of the waveguides was important, as the dimensions determined whether the waveguide would be single- or multi-mode. To make the waveguides single-mode, they must be sufficiently small. However, the waveguide size had to be large enough to fabricate using photolithography. Photolithography was necessary to maintain the low cost of the device, compared to more expensive techniques such as electron beam lithography. To determine the optimal waveguide size, a KMPR waveguide was simulated with a PMMA substrate and cladding, and a COC substrate and cladding. The effective indices of the waveguide modes for several dimensions were found. Modes with effective indices greater than the refractive index of the substrate/cladding material will propagate. Modes with indices less than the index of the substrate/cladding will not propagate, as the loss will be too great. The line above which the modes will propagate is called cut-off. If multiple TE or TM modes are present above cut-off, the waveguide will be multi-mode. Single mode operation is ideal, as it greatly simplifies the racetrack resonator response. For PMMA cladding, the largest single mode waveguides were determined to be 2 μm x 2 μm. For COC cladding, the largest single mode waveguides were 3 μm x 3 μm. Waveguides with greater widths and heights were multi-mode. Figures 3.11, 3.12, and 3.13 show the detailed results of these simulations.

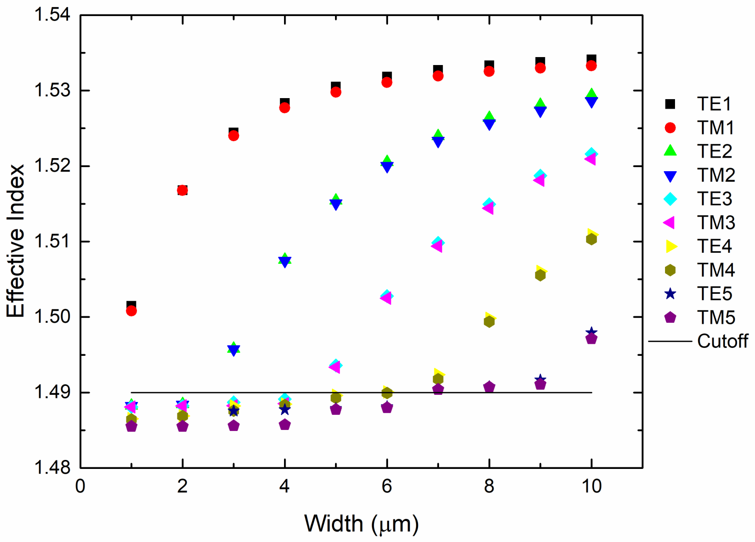

Figure 3.11: Modes in a 2 μm tall KMPR waveguide with PMMA substrate and PMMA cladding.

From these simulations, the three waveguide widths selected were 2 μm, 3 μm, and 5 μm. The 5 μm wide waveguides were included despite the fact that they were expected to be multi-mode to ensure some devices would be straightforward

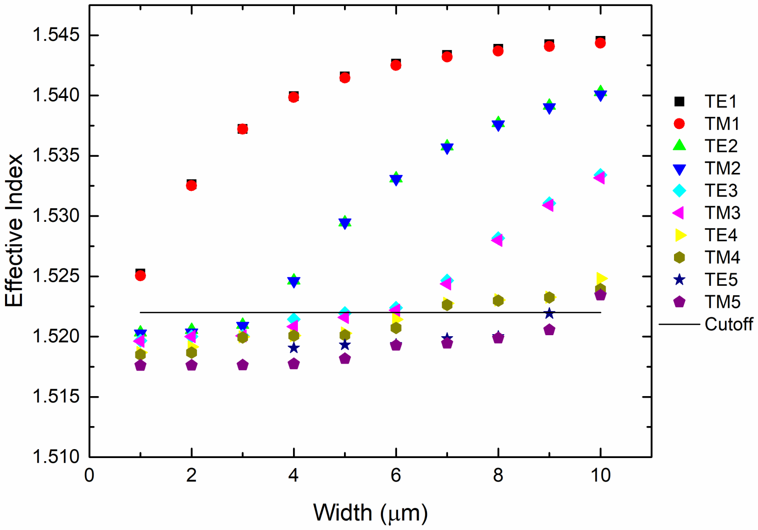

Figure 3.12: Modes in a 3 μm tall KMPR waveguide with COC substrate and COC cladding.

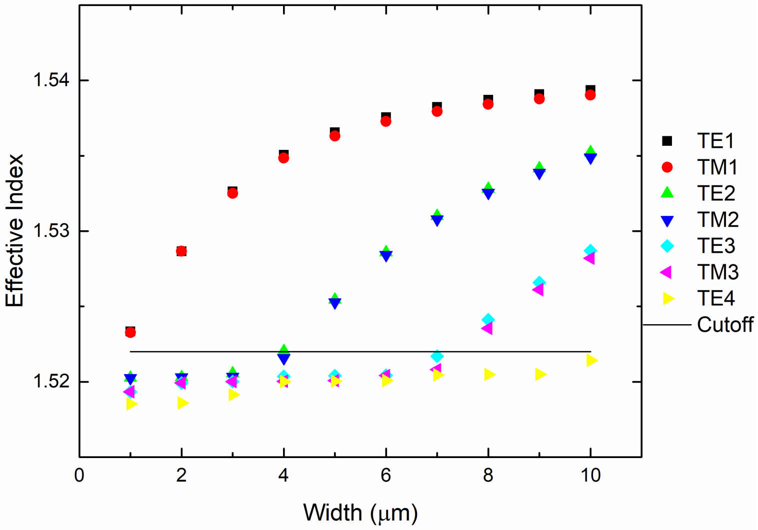

Figure 3.13: Modes in a 2 μm tall KMPR waveguide with COC substrate and COC cladding.

to fabricate, since the smaller waveguides widths were likely to be more challenging to fabricate. Since the ideal height for a PMMA surrounded waveguide was 2 μm, and the 2 μm waveguide surrounded in COC was still single mode and well above cut-off, 2 μm was selected as the ideal waveguide height. Figure 3.14 shows the final simulation of the first ten modes of the fabricated device using the measured values for the refractive indices (Table 3.1, column 3). Only two modes, the first TE mode and the first TM mode, are above cut-off. The final fabricated device was a 2 μm tall, 3 μm wide KMPR waveguide, with COC substrate and PMMA cladding.

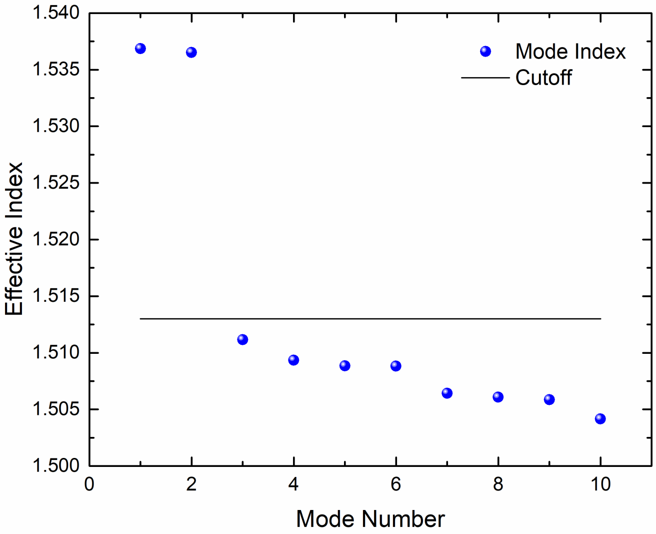

Figure 3.14: Modes in a 2 μm tall, 3 μm wide KMPR waveguide with COC substrate and PMMA cladding.

Once the dimensions of the waveguides were selected, the bending loss was calculated. The bending loss, measured in dB/cm, is a significant source of loss in low-contrast waveguides. In a curved waveguide, the mode is pushed towards the outer edge of the waveguide, and as a result the light travels closer to the outer edge of the curved waveguide than the inner edge. This variation in the mode profile introduces two loss mechanisms that can be grouped together to define the overall bending loss. The first loss mechanism is due to a spatial mismatch between the mode in the bent waveguide and the mode in the straight waveguide, resulting in inefficient conversion of power as the wave propagates from the straight section and into the bent section of the racetrack resonator. The second loss mechanism, which can be significantly greater than the mode mismatch loss in planar waveguides, is the radiative losses due to bending. Since the mode is pushed to the outer edge of the waveguide, the optical power tends to leak out of the waveguide as it travels around the bend. Attenuation due to radiative losses in the waveguide bend is

Waveguide Configuration	Bend Radius (μm)	First TE Mode Index	Loss (dB/cm)	First TM Mode Index	Loss (dB/cm)
2 μm x 2 μm KMPR waveguide surrounded by PMMA	100	1.520145	374.58	1.520129	369.1
	150	1.518409	88.11	1.518392	89.07
	200	1.517691	21.045	1.517687	22.693
	250	1.51735	4.8795	1.517349	5.8458
	300	1.517169	1.1038	1.517169	1.507
3 μm x 3 μm KMPR waveguide surrounded by COC	300	1.538746	103.44		
5 μm x 5 μm KMPR waveguide surrounded by PMMA	125	1.554242	7.1556	1.554514	6.8043
	150	1.551611	1.1604	1.551831	1.1118
	175	1.54992	0.17877	1.550101	0.17284
5 μm x 5 μm KMPR waveguide surrounded by COC	225	1.55135	102.99	1.551407	100.78
	250	1.55042	61.631	1.550471	60.521
	275	1.549704	36.482	1.549751	36.01

Table 3.2: Initial simulated bending loss

proportional to $exp(-\sigma R)$, where σ is a constant that depends on the waveguide geometry and the index contrast of the waveguide, and R is the radius of the curved waveguide [188]. For planar waveguides fabricated in silicon-on-insulator, bending radii on the order of a few microns can have very low loss [142]. For low-contrast waveguide systems such as silicon nitride waveguides with oxide cladding, the bending radii are typically on the order of tens of microns [189]. Since the contrast of the plastic photonic system fabricated here is less than the silicon nitride waveguides, we estimate that a low-loss bending radius will be achieved at radii greater than 100 μm. Since analytic approaches to calculating the bending loss are only approximations, we compute the bending loss using finite difference software [171]. Using a numerical approach, the smallest radius found to carry a mode was 100 μm, albeit with high loss. A radius of 300 μm was found to have very low loss. Therefore, 6 radii were chosen for the 2 μm and 3 μm wide waveguides: 100 μm, 150 μm, 200 μm, 250 μm, and 300 μm. In the case of the 5 μm wide waveguides, the bending loss was less so the larger radii were eliminated. The results of the initial bending loss simulations are shown in Table 3.2. The simulated bending loss for the final fabricated devices are shown in Table 3.3.

Once the bending loss was known, the directional couplers could be designed. Five different gaps were chosen for the directional couplers: 700 nm, 1 μm, 1.25 μm,

Bend Radius (μm)	First TE Mode Index	Loss (dB/cm)	First TM Mode Index	Loss (dB/cm)
100	1.541660	160.22	1.541489	162.80
150	1.539034	27.484	1.538784	31.592
200	1.538073	4.9843	1.537794	7.8406
250	1.537629	0.89101	1.537332	2.1592
300	1.537391	0.15845	1.537083	0.61742

Table 3.3: Bending loss for a 2 μm tall, 3 μm wide KMPR waveguide with COC substrate and PMMA cladding

1.5 μm, and 2 μm. The smaller gaps would provide better coupling, but were more difficult to fabricate. The larger gaps would provide less coupling, but would be simpler and more reliable for fabrication. For each gap, five coupling lengths were chosen.

The simulations for the directional couplers were done using 2D mode simulations using MODE Solutions. The simulations solved for the effective indices of the TE supermodes in a directional coupler. The coupling coefficient and the transmission coefficient were then solved for using the approach outlined in Section 2.2.4. The round-trip loss in each racetrack was calculated by assuming the bending loss was the only source of loss in the system. This is a reasonable assumption for low-contrast waveguides. By setting the transmission coefficient τ equal to the round-trip loss, an initial coupling length for each radius was chosen. Two shorter and two longer coupling lengths were then added in each case to cover a wide range of parameter space. Figure 3.15 shows a plot of the simulated transmission coefficient versus the coupling length for the three largest gaps for the final fabricated device.

The final simulation compiled all of these results to simulate the final response of the racetrack resonator. This was done by using MATLAB to solve for the transmission through a racetrack resonator circuit with a single bus waveguide using the Eq. (2.25). Figure 3.16 shows the expected response for the simulated values for a racetrack with a 400 μm long coupling length, a 100 μm radius, and 1.25 μm coupling gap. The waveguide dimensions were 2 μm tall and 3 μm wide. The waveguide was KMPR with a COC substrate and PMMA cladding. Figure 3.17 shows the expected response for the simulated values for a racetrack with a 200 μm long coupling length, a 300 μm radius and a 2 μm coupling gap, in the final fabricated configuration. The final design included 15 chips on a 4-inch wafer: 5 chips for 2 μm wide waveguides, 5 chips for 3 μm wide waveguides, and 5 chips for 5 μm wide waveguides.

Fabrication Process

The first fabrication process attempted was a transfer of the KMPR pattern from a silicon wafer to a PMMA wafer using a hot embossing tool (Jenoptik). Since

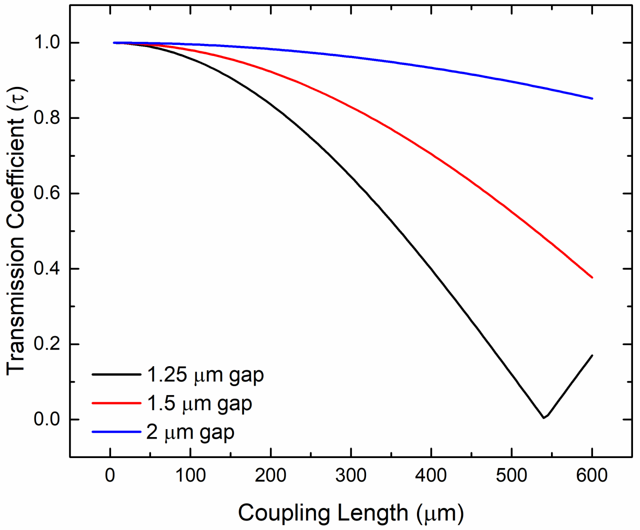

Figure 3.15: Coupling lengths in a 2 μm tall, 3 μm wide KMPR waveguide with COC substrate and PMMA cladding.

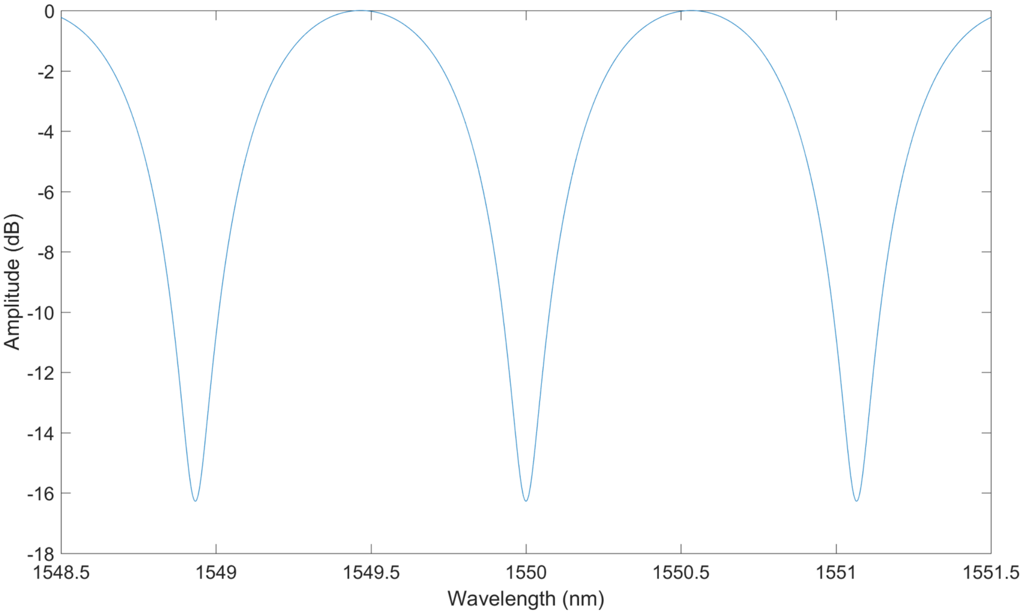

Figure 3.16: Expected racetrack resonator response for a radius of 100 μm, a coupling length of 400 μm, and a coupling gap of 1.25 μm. The waveguide is 2 μm tall, 3 μm wide KMPR waveguide with COC substrate and PMMA cladding

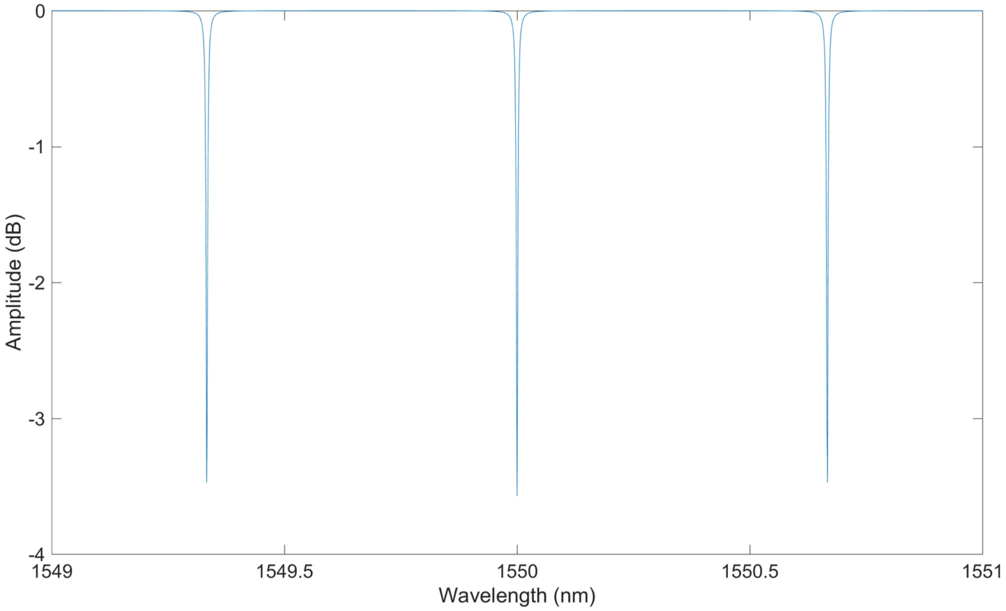

Figure 3.17: Expected racetrack resonator response for a radius of 300 μm, a coupling length of 200 μm, and a coupling gap of 2 μm. The waveguide is 2 μm tall, 3 μm wide KMPR waveguide with COC substrate and PMMA cladding.

adhesion between silicon and KMPR is relatively poor, it was thought that the pattern would transfer to the PMMA at the appropriate force and temperature. This did not succeed, despite varying ranges of forces and temperature tested.

The second fabrication process attempted was lithography with KMPR on PMMA substrates followed by encapsulation of the pattern by a top PMMA sheet using the hot embosser. The encapsulation of the KMPR pattern did not work, despite the range of temperatures tested and the extremely low force used. The aspect ratio of the KMPR features did not remain constant during this process.

The third fabrication process attempted was lithography on PMMA substrates to create KMPR waveguides with a spun-on PMMA cladding layer. However, adhesion of the KMPR features was consistently poor. Features less than 5 μm in width did not adhere well and were often wavy. One approach used to try to improve the adhesion was ramped bakes, which was found to be successful for a similar negative resist called SU-8 [190]. By increasing and decreasing the temperature slowly, the residual stress in the resist was reduced. However, this did not produce sufficient adhesion. We next worked towards developing a proprietary adhesion promotion technique to attempt to improve adhesion, with limited success. To characterize improvements in adhesion before and after performing this technique, contact angle measurements were carried out on the PMMA. High angles indicate adhesion will be poor due to increased hydrophobicity, whereas low angles indicate good adhesion as the surface has become more hydrophilic. The initial contact angle was 80.2°. The best contact angle achieved was 31.7°, which is not a substantial improvement. Poor adhesion also created issues when dicing, since the waveguide edges lifted up during dicing. Clean waveguide facets, necessary for edge coupling, were not achievable.

For these reasons, the substrate was switched to COC 5013. COC has improved adhesion over PMMA. Good adhesion was achieved by including the proprietary adhesion promoting technique before the KMPR was spun on. To confirm this technique would be a viable approach to improve the adhesion, contact angle measurements were performed. The initial contact angle was 99.7° and was reduced to 8.4°. This is a substantial improvement, and good adhesion was observed when spinning on the photoresist after treatment with our technique. Using ramped bakes were not necessary to achieve good adhesion with COC substrates. Long, ramped bakes were in fact detrimental as they caused significant debris on the wafers that was not removed during development.

To create wafers from COC sheets, two annealing steps were required, the first to flatten the COC sheet sufficiently so that it could be cut, and the second to fully flatten the wafer and smooth any roughness from the edges. Annealing was done using the hot embosser.

In addition to choosing an appropriate substrate, the KMPR resist had to be spun on to the correct thickness. According to the datasheet, KMPR 1005 spread with a thickness of 5 μm near 5000 rpm. Since the optimal thickness according to simulations was 2 μm, the KMPR had to be thinned. This was done by adding SU-8 thinner (cyclopentanone) to the KMPR in varying volumetric ratios until the correct ratio was achieved. The thickness varied from 1.8 – 2.2 μm depending on the batch. Once the desired resist thickness was achieved, the next step was to choose the appropriate bake steps and exposure levels. The hot plate could not be used as it caused the plastic wafers to distort due to the thermal mismatch between the bottom and top surface of the wafer. For this reason, the wafers were baked in an oven at 100 °C, the recommended temperature on the KMPR datasheet. Once the bake parameters were chosen, the exposure dose was determined using trial and error.

After the waveguide fabrication, the chips were diced to expose the waveguide edge facets for coupling the laser light in and out of the chip. The chips were diced so that the dicing time and the quality of the edge facet were optimized, allowing for edge facets that adhered to the wafer and were very clean.

To deposit the cladding on the waveguides, a thick layer of PMMA was spun onto the chips. The cladding layer was approximately 4.5 μm thick. According to the datasheet, PMMA should be baked at 180 °C on a hotplate. A hot plate could not be used as the chips distorted, and 180 °C was higher than the glass point of the COC wafer. Additionally, a reaction between the solvent in the PMMA and the

COC substrate occurred at elevated temperatures and so the PMMA could not be baked. The PMMA was air-dried instead.

The final fabrication run produced waveguides with gaps, heights, and widths that were close to the specified design, with the exception of the racetrack resonators with 700 nm gaps. These devices did not turn out, as the gaps did not expose properly and there was significant resist remaining in the gap. The dimensions were measured using an optical profilometer. Figure 3.18 shows sample results from the optical profilometer, showing the waveguide width, height, and gap were all close to the designed sizes. The waveguides tended to be slightly smaller (200–500 nm) than the designed dimensions. Scanning electron microscope (SEM) imaging could not be used without destroying the samples, as a metal coating was needed to prevent charging in the SEM. Figure 3.19 shows optical microscope images of the final devices after the application of the cladding.

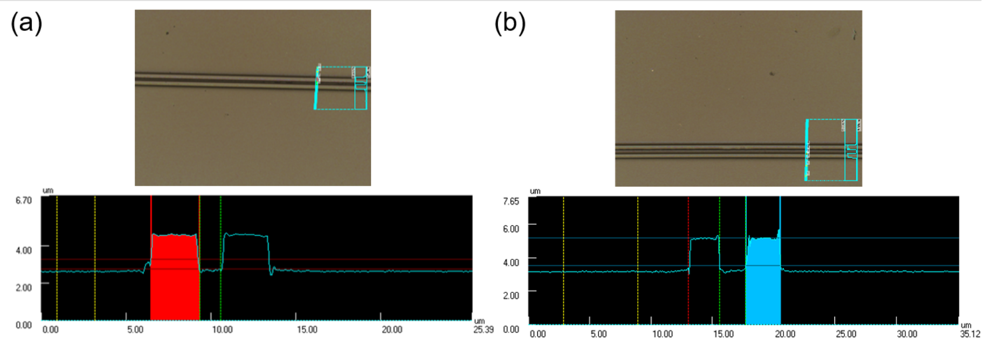

Figure 3.18: (a) Optical profilometer results for a 3 μm wide and 2 μm tall waveguide. The gap spacing was nominally 1.25 μm. The measured step height was 1.85 μm. (b) Optical profilometer results for a 3 μm wide and 2 μm tall waveguide. The gap spacing was nominally 2 μm. The measured step height was 1.81 μm.

Experimental Setup

To measure the photonic devices, a specialized setup is used. A schematic of the setup is shown in Figure 3.20. This setup is located in the Department of Electrical and Computer Engineering at the University of Alberta. The tunable diode laser has a wavelength range of 1510 nm to 1630 nm and can step in increments of 1 pm. The polarization controller sets the output polarization of the laser to either TE or TM mode. The polarization is calibrated using a polarization cube. Two 3-axis piezo stages are used to position the input and output fibers so they are aligned to the waveguide facets of the chip. This type of coupling is called edge coupling or butt coupling. The chip is stationary on a simple holder. The input and output fibers are lensed fibers to improve coupling into the waveguide. The output waveguide is directed to a photodetector where the signal is converted from an optical signal to

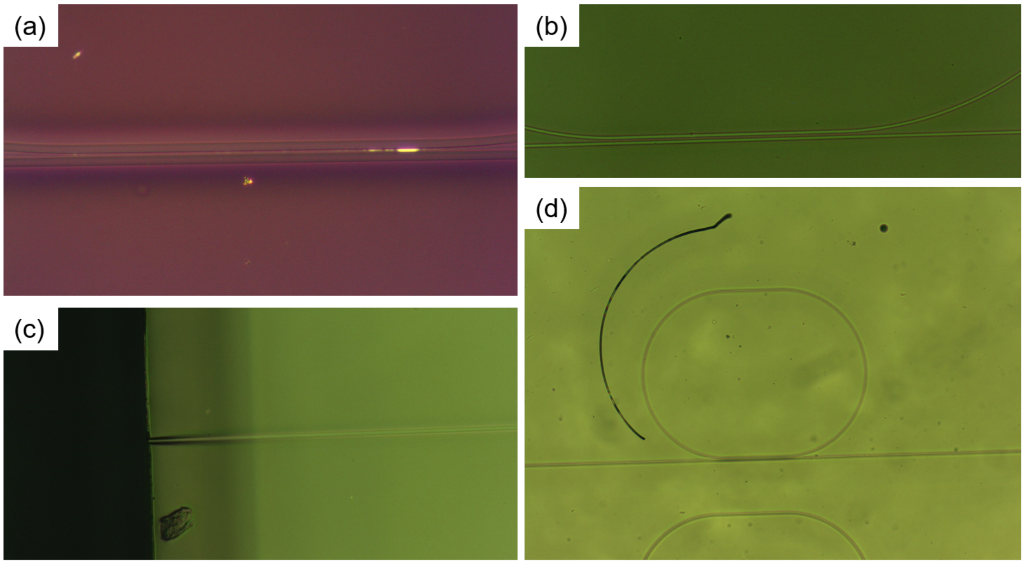

Figure 3.19: (a) Optical microscope image for a 3 μm wide and 2 μm tall waveguide after deposition of PMMA. The gap spacing was nominally 1 μm. The bright spot is likely an area not fully filled with PMMA. (b) Optical microscope image for a 3 μm wide and 2 μm tall waveguide after deposition of PMMA. The gap spacing was nominally 2 μm. (c) Optical microscope image of the edge of a 3 μm wide and 2 μm tall waveguide after deposition of PMMA. (d) Optical microscope image for a 3 μm wide and 2 μm tall waveguide after deposition of PMMA. The gap spacing was nominally 1.25 μm. This device is potentially damaged as it appears that the waveguide was broken during the application of the PMMA.

an electrical signal. To image the fiber tips and the sample, a white light source is directed through a microscope objective onto the chip. The live image is recorded with a CCD camera. This greatly improves the ease with which the sample can be aligned. A LabView program is used to sweep the laser wavelength through the desired range, and the device response is recorded at each wavelength.

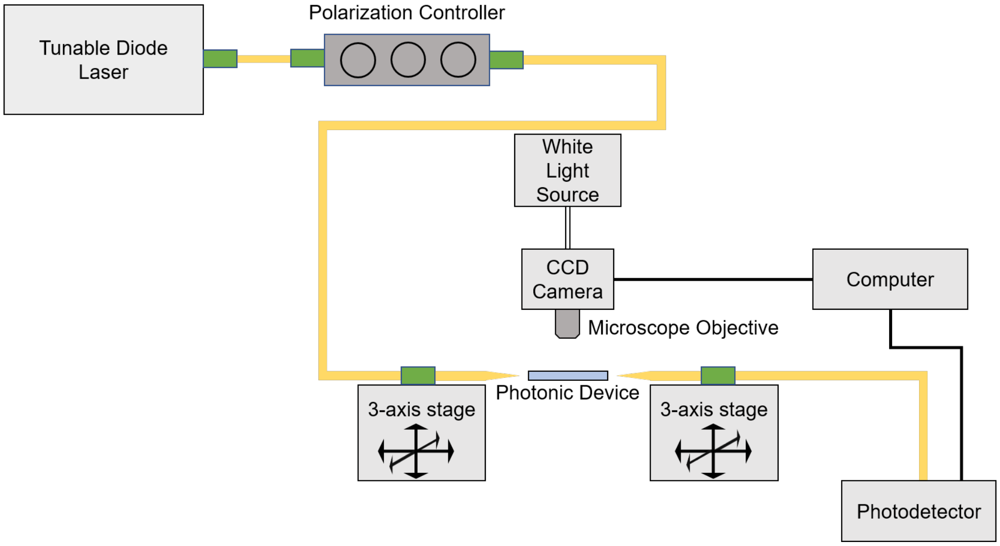

Figure 3.20: Schematic of the experimental setup used to measure the waveguides.

Refractive Index Measurements

To confirm the values for the refractive index used in simulations, ellipsometry was performed on the fabricated samples using the VASE ellipsometer. The samples measured were KMPR on silicon (approximately 2 μm thick), a bare COC substrate, and PMMA air-dried on silicon (approximately 4.5 μm thick). The measurements were done in the near infrared. The results were fit using the VASE analysis software. The results for the KMPR on silicon and COC were fit reasonably well with the models in the software, and converged to a singular value with good statistical correlation. For the PMMA, however, the model did not agree well with the measured data. Although visually the fit appears acceptable in Figure 3.21(b), similar results could be obtained by using different values for the percentage of non-uniformity of the PMMA and PMMA thickness. These different parameters gave the same statistical correlation, and therefore we concluded the fit did not converge to a singular value and the fitting results could not be used with confidence. The most likely cause of this was non-uniformity of the spun-on PMMA. The PMMA thickness varied significantly across the 1 cm x 1 cm sample, which affected the ellipsometry measurement. Since the measured values could not be fit with confidence, the experimental data was not used for the PMMA, and the values from the datasheet were used instead. Figure 3.21 shows the experimental results from the ellipsometry measurements, and compare the experimental results to the modeled results.

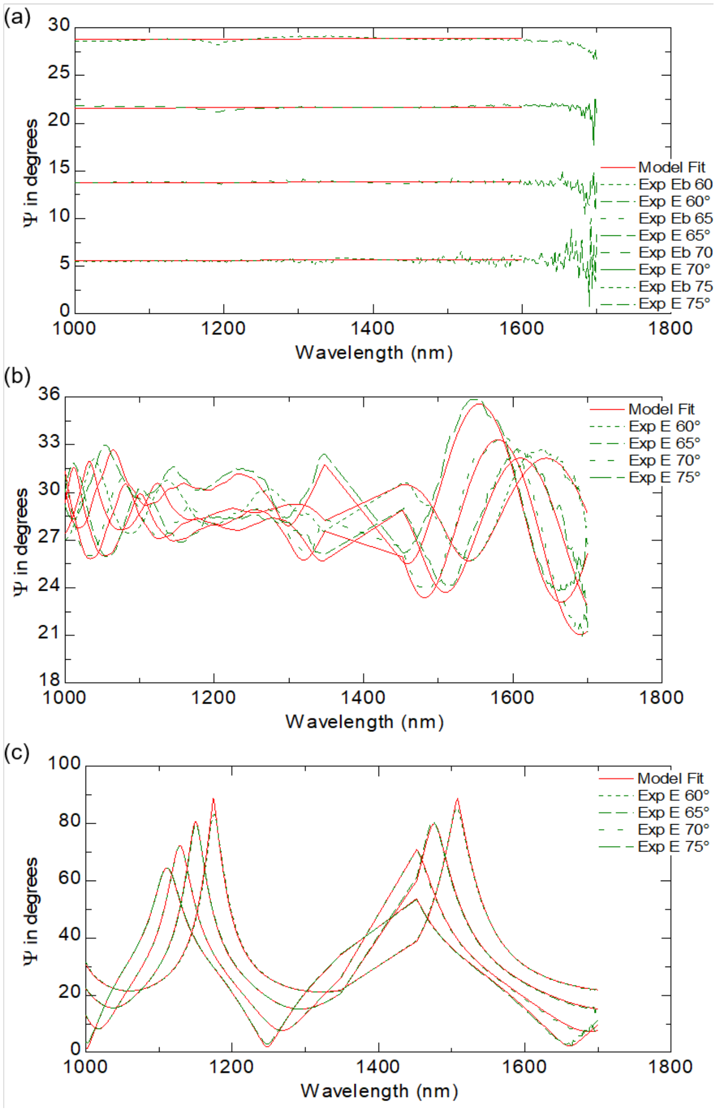

Figure 3.21: (a) Experimental and modeled ellipsometry results from the bare COC substrate. Reasonable agreement was obtained. (b) Experimental and modeled ellipsometry results from the air-dried PMMA on silicon. Visually, it is clear that the fit did not agree well with the experimental results. (c) Experimental and modeled ellipsometry results from the KMPR on silicon. Good agreement was obtained.

Waveguide Measurements

Measurements were carried out on the 3 μm wide waveguides, as they were determined to be the most promising. These devices should be single-mode, unlike the 5 μm wide waveguides. They should also have less loss than the 2 μm wide waveguides. The 3 μm wide waveguides also had a good range of coupling parameters on each chip. Finally, the 3 μm waveguides were more reliable in the final fabrication process, as the 2 μm devices had a lower yield.

Before testing, the devices were inspected using an optical microscope. Many of the devices had slight defects from the lithography, and so these devices were not tested. These defects could be due to debris on the mask or the wafer, or poor contact during lithography. The following devices were measured: 12 devices with gaps of 1 μm, 10 devices with gaps of 1.25 μm, 2 devices with gaps of 1.5 μm, and 8 devices with gaps of 2 μm, for a total of 32 measurements. The optical power output from the laser was 10 mW. Unfortunately, no resonances were observed for any devices. Figures 3.22 and 3.23 show two example measurements that are typical of the results obtained. Figure 3.22 is for a racetrack with a radius of 100 μm, a coupling length of 400 μm, and a gap of 1.25 μm. This curve is plotted in dB and does not show any significant drop in power that would indicate that there is a signal from the racetrack resonator. Additionally, free spectral range is approximately 5 nm. This is different than expected for a racetrack of this size, which should be closer to 1 nm as shown by Figure 3.16.

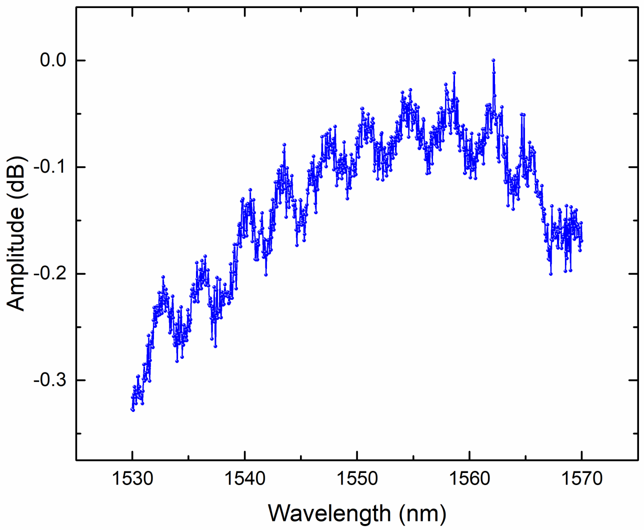

Figure 3.22: Measured racetrack resonator response for a radius of 100 μm, a coupling length of 400 μm, and a coupling gap of 1.25 μm.

One potential cause for the large deviation in the expected versus observed signal may be the presence of significantly higher loss than expected in the system. During the simulation and design phase, it was assumed that the main cause of loss would be due to bending in the racetrack resonator. However, other sources of loss may be contributing to increase the loss in the system. Other potential sources of loss could include surface roughness from the sides of the waveguide, material loss from the KMPR, or scattering loss from lithography defects. Although a significant increase in the loss (more than 4 times larger) would have to occur to produce results similar to what was observed in experiment, this is not completely unreasonable given the uncertainties in the material loss and the waveguide roughness. Another reason that resonances were not observed could be because the coupling between the bus waveguide and the racetrack was poor, potentially due to residual resist in the trench between the waveguide and the racetrack. SEM imaging would be helpful in the future to determine if this was the cause of poor coupling.

Figure 3.23 shows the response for a racetrack with a radius of 300 μm and a gap spacing of 2 μm. This response has a large signal at low wavelength (1500 nm) and drops to very small signal around -40 dB at high wavelength (1600 nm). This is not what is expected for a device of this type (see Figure 3.17 for expected signal). The most likely cause of this response is that the waveguide is approaching cut-off at higher wavelengths. This might occur if the waveguide was smaller than the designed dimensions, and therefore the light will propagate at low wavelengths but will become more lossy at higher wavelengths and cease to propagate. Another cause could be if the cladding index was higher than expected. Since the measurements of the cladding index were inconclusive, this could be another potential cause. Although the slope of this response could be used to sense temperature, it is a very shallow slope and would have very low sensitivity to fluctuations in temperature.

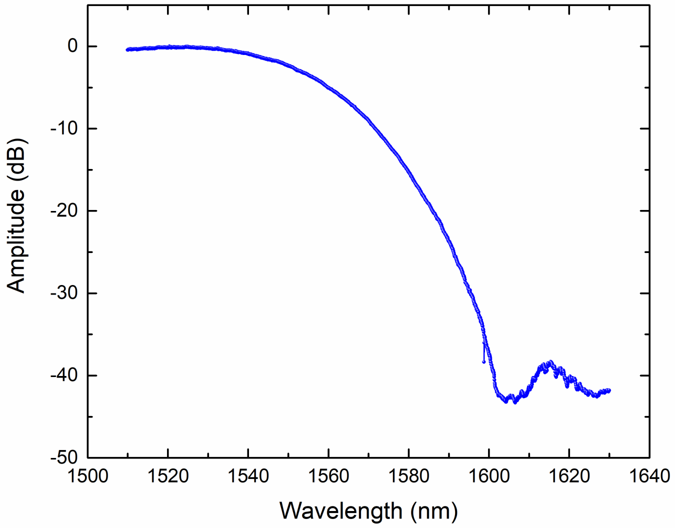

Figure 3.23: Measured racetrack resonator response for a radius of 300 μm, a coupling length of 200 μm, and a coupling gap of 2 μm.

Conclusions and Future Work

The goal of this project was to develop an on-chip temperature sensor compatible with microfluidic channels. Integrated photonics on an all-plastic platform was developed to accomplish this goal, and racetrack resonators were designed for the temperature sensing component. The fabrication of the photonic devices was challenging due to poor adhesion between the resist and the substrate. These challenges were overcome with a combination of changing materials systems and adding an adhesion promoting treatment before spinning on the photoresist. Although waveguides were successfully fabricated, the racetrack resonators did not function as anticipated. For this reason, temperature sensing was not achieved with these devices.

There are many potential directions for future work. One improvement to the fabrication process would be to select a different cladding layer that can be baked on, instead of dried at room temperature. This would improve the speed and reliability of fabrication. Potential cladding layers include PDMS, HSQ, or other glassy resists. To improve the racetrack resonators, one potential direction is to design multimode interference (MMI) couplers instead of directional couplers. This may permit stronger coupling into the racetracks to compensate for increased loss. Add/drop racetrack resonators could also be used and measured from the drop port to improve the signal-to-noise ratio. The waveguide loss could also be more accurately measured to improve optical cavity design. For example, the cut-back method could be used. Finally, alternative resonators such as Bragg gratings could be used instead of racetrack resonators.

3.2 Transduction of Even Modes in Doubly Clamped Beams

In the following sections, we will turn our focus towards nano-optomechanical systems fabricated on silicon-on-insulator substrates. Despite all of the advantages of nanophotonic transduction outlined in Chapter 1, there are some drawbacks as well. One of these disadvantages is that some modes of vibration in nano-optomechanical systems (NOMS) are not efficiently detected or actuated. For nanomechanical devices interacting evanescently with an optical cavity, nanomechanical displacement results in an oscillatory variation in the effective refractive index of the optical cavity. This results in an oscillation of the optical resonance and therefore an oscillatory optical power at the output. For some modes of vibration, the mode-averaged displacement is zero and therefore the effective index shift is zero. Similarly, the optical force averaged over the NOMS area is zero. Even modes in doubly clamped beams are an example of a set of modes that suffer from this effect, since they are symmetric about the midpoint of the beam. This effect is problematic because for mass sensing applications, additional information can be obtained when performing sensing experiments with multiple modes simultaneously. Accurate determination of both adsorbate mass and position on a nanomechanical beam can be determined by measuring multiple modes simultaneously [19, 191]. For these reasons, transduction of higher order modes is desirable for mass sensing applications.

In this section, we will discuss the design and fabrication of devices where symmetric modes can be detected. We will then detail the experiment where we tested the devices and demonstrate that we can measure symmetric modes. Finally, we will discuss another potential application of multi-mode sensing, which is the measurement of stress in the silicon device layer using the first and second modes of buckled doubly clamped beams.

3.2.1 Design and Fabrication

To allow for detection of these modes, we proposed a modification to the substrate with which the device is interacting [21]. The proof-of-concept work is done with a doubly clamped beam embedded in a racetrack resonator, which is coupled to the substrate beneath. To allow for the actuation and detection of even modes, we modify the size of the gap across the modal length of the beam. Stronger optomechanical coupling on one section of the beam length allows for efficient excitation and detection of the second flexural mode, while preserving coupling to the first and third flexural modes. To create a varying gap, we introduce a step in the substrate below a released section of a racetrack resonator. A schematic of this concept is shown in Figure 3.24(a) with the first three vibrational modes overlaid. The step in the substrate results in two different separation distances for the second mode, thus causing its effective index shift to be non-zero.

The photonic devices were fabricated on a silicon-on-insulator chip with 220 nm thick silicon device layer and a 2 μm buried oxide layer at the imec foundry. The racetrack resonator used was an add/drop racetrack resonator with a radius of 22.1 μm and an 18.3 μm long straight section, and was designed by another student [192]. Grating couplers were used to couple the light into and out of the system. To form a step in the substrate underneath the mechanical device, two electron beam lithography (EBL) steps were used to define the areas of the beam to be released. First, PMMA was spun on to the chip. Then, in the first EBL step, a small segment of the beam was exposed, opening an etch window. The device was then etched in buffered oxide etch (BOE) to undercut the Si waveguide and release the beam. The PMMA was removed using acetone, and then a fresh layer of PMMA was spun on for the second patterning step. In the second EBL step, the entire beam was exposed and etched. This created a two-step substrate beneath the doubly clamped beam. A scanning electron microscope (SEM) image taken at a 60° angle is shown

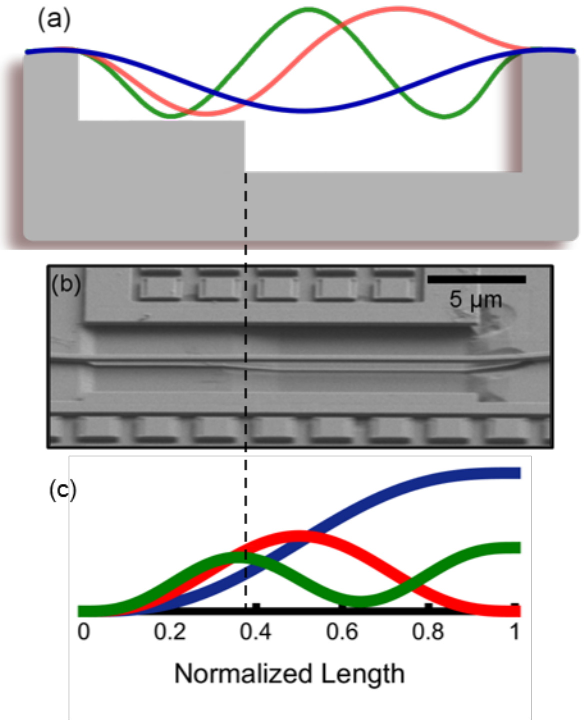

Figure 3.24: (a) Schematic of a two-step substrate designed to transduce the second flexural mode. The first three flexural modes are overlaid in blue (first mode), red (second mode), and green (third mode). (b) Scanning electron microscope image of the fabricated device, with the uneven substrate clearly visible. (c) Average displacement of the first three flexural modes (blue, red, and green respectively) integrated up to the step position as a function of that position. Reprinted from [21], with the permission of AIP Publishing.

in Figure 3.24(b). From this image, it can be seen that the step height did not change at the midpoint of the beam's length, but somewhere between one third and one half of the beam's total length. This is due to a slight misalignment in the two EBL steps and the isotropic nature of the BOE process.

Figure 3.24(c) plots the integral of the modal displacement as a function of integration length from one end of the beam over the full length of the beam. In other words, the length of the beam is normalized so that the maximum length of the beam is 1. The amplitude of each mode is also normalized to 1. These normalized mode shapes, as shown in Figure 3.24(a), are integrated at each position along the length of the beam. The result of this integration is what is plotted in Figure 3.24. For the first mode, the integration monotonically increases since the displacement of this mode is always positive (it is completely one-sided). The second mode increases until the midpoint of the beam where the normalized length equals 0.5, then decreases to zero at full length (since the whole mode average displacement is zero). The third mode reaches an integration node at about 2/3 of the length before increasing again. Figure 3.24(c) essentially shows the average displacement of the first three modes. A larger average displacement will result in an increased signal size due to the larger effect that the nanomechanical device will have on the effective index and therefore the optical resonance wavelength of the racetrack resonator. We can therefore say that the responsivity of the system depends on the step placement. The drive efficiency is also dependent on the step position, which we will describe in more detail in the following section. Figure 3.24(c) gives an estimate for the relative responsivity and drive efficiency that can be expected for the first three modes at a given step position along the full length of the beam. In the following section, it will be shown that this step location causes the transduction for the first three modes to be of comparable efficiency. Measurements of the first three modes are important for mass sensing applications. While the mass sensitivity (Eq. (2.7)) is improved at higher modes because higher order modes have reduced effective mass [193], the primary benefit to measuring higher order modes is in the spatial resolution provided by higher order modes. Measurement of the first two modes gives the analyte position and standard deviation. Measurement of the third mode adds information about the variance of the analyte [194]. Overall, the ability to simultaneously measure the first three modes increases the spatial resolution of the mass measurement.

3.2.2 Experiment and Results

The experimental setup described in Section 2.4 is used to measure the resonance frequencies of the NOMS. The optical cavity response was measured at the through port of the microring by sweeping the probe laser through a large wavelength span.

Subsequently, the probe laser was positioned at the point of maximum slope on the blue-detuned side of one of the racetrack resonators optical resonance dips. With only the probe laser activated, the thermomechanical Brownian motion of the devices was measured with a spectrum analyzer. We observed the thermomechanical motion of the first three modes of vibration, shown in Figure 3.25(a). These modes have resonance frequencies of 6.76 MHz, 18.93 MHz, and 37.34 MHz. The thermomechanical displacement was determined by converting the noise measurements recorded in volts per Hz$^{1/2}$, denoted as $S_{\mathrm{v}}^{1/2}$, to displacement spectral density ($S_{\mathrm{z}}^{1/2}$). We use the subscript z in this case because the motion of the beam is out-of-plane. This is accomplished using the method described in Section 2.1.1. The responsivity ($\Re$) in V/m obtained from this conversion provides a displacement calibration for driven measurements. We find that the responsivity increases slightly for each mode, resulting in the displacement sensitivity decreasing with mode number. This is partially consistent with Figure 3.24(c), as the second and third modes should be more responsive than the first with the step location at approximately 35% of the overall beam length. However, the second mode should be more responsive than the third, according to the model presented in Figure 3.24(c). This model assumes a step function underneath the beam, but sloped sidewalls from the BOE etch are clearly in the SEM image in Figure 3.24(b). When examining the effect of the sidewalls on the responsivity, we observe that they do slightly impact the responsivity. Although the sloped clamping point on the small-gap side would induce a similar effect for the second and third modes, the slope on the larger gap side (close to the full length of the beam, at a step position of 1) would induce a decrease in the responsivity for the second mode, but an increase for the first and third modes. Therefore, the sloped sidewalls are likely the reason that the responsivity for the third mode is higher than the second mode.

The noise floor of the displacement spectral density provides the displacement sensitivity of the measurement. The displacement sensitivity is the minimum detectable displacement, and can be used as a figure of merit to compare our device to others in the literature. The displacement sensitivity of our device is 228 fm/Hz$^{1/2}$, 153 fm/Hz$^{1/2}$, and 112 fm/Hz$^{1/2}$ for the first through third modes, respectively. Important for the present discussion is that the even (second) mode responsivity is comparable to the odd (first and third) modes, demonstrating the utility of our symmetry-breaking approach.

For sensing applications, it is beneficial to apply a driving force to nanomechanical devices. The reasoning for this is twofold. Firstly, it improves the signal-to-noise ratio (SNR) of the mechanical response. Secondly, when the mechanical devices are actuated, they have a coherent phase signal that can be tracked with a phase lock loop (PLL). This approach is common in many sensing applications [9, 195]. The

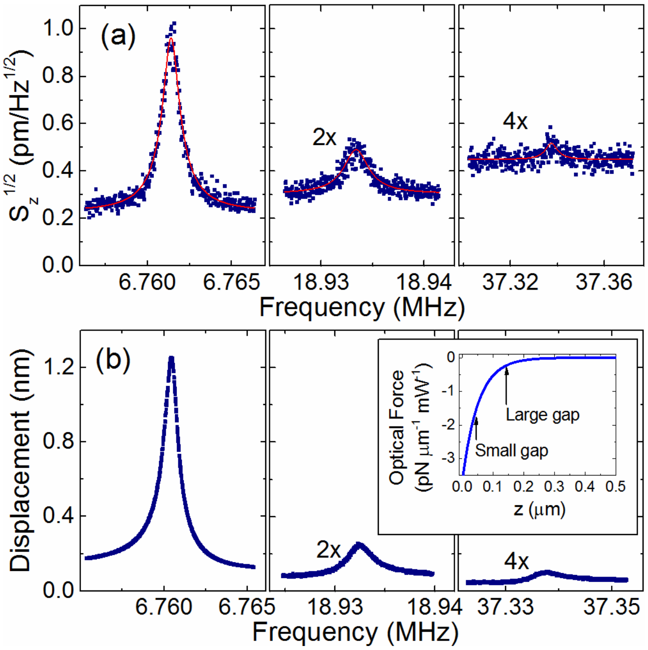

Figure 3.25: (a) Displacement spectral density of the first three flexural modes. The lines are fits to the measured data. (b) Measured displacements of the first three modes, as calibrated by the results in (a). The inset shows the simulated optical force as a function of the distance between the beam and the oxide substrate (z). The negative optical force is attractive force between the beam and the substrate. The arrows show the forces for the small and large gaps. The measurement of three mechanical modes can improve the spatial resolution of mass sensing measurements; the first and second mode give information on the location and standard deviation [19], whereas the third mode provides information about the analyte's spatial variance [194]. Reprinted from [21], with the permission of AIP Publishing.

devices were actuated using an amplitude-modulated pump laser positioned at the minimum of another optical resonance dip. This provided an AC actuation force at the mechanical resonance frequency via a varying optical gradient force. The details of this technique were described in Sections 2.3.1 and 2.4. The mechanical signal was read out with a network analyzer.

With the driving force applied, up to the fifth flexural mode was observed due to the improved SNR. The fourth mode is transduced because the step in the substrate is not exactly at the midpoint of the beam. Since the thermomechanical noise spectra could only be observed for the first three modes, we can only obtain the displacements for these modes. Dividing the data recorded in voltage by the responsivity in V/m, the displacement is calculated. The results of this calculation are seen in Figure 3.25(b). The peak displacements, z_{peak}, for the first through third modes are 1.26 nm, 0.12 nm, and 0.03 nm for the same applied driving force. The step in the substrate clearly allows actuation of both even and odd modes in the doubly clamped beam using an optical pumping technique. The next step is to determine how efficiently each mode is actuated, and compare the efficiencies to ensure that the actuation efficiency follows the trends predicted by the model shown in Figure 3.24(c).

From these peak displacements, we can calculate the total force on the beam using $F_{\text{drive}} = m_{\text{eff}}\Omega_0^2 z_{\text{peak}}/Q = k_{\text{eff}} z_{\text{peak}}/Q$ where k_{eff} is the effective spring constant of the mode and Q is the quality factor of the resonator. From these calculations we observe that F_{drive} is approximately constant at 0.4 pN for the first through third modes. The spring constant rises with each mode due to the increasing resonance frequency. Since the force is constant, the amplitude is reduced for the higher modes.

We can convert F_{drive} to an optical force to provide a meaningful comparison with simulated results shown in the inset of Figure 3.25. This can be done by normalizing the measured F_{drive} by the length of the beam (l) and the AC optical power in the device ($P_{\text{bus,AC}}$). The AC power is determined by driving voltage provided to the electro-optic modulator (EOM), which can then be converted to an optical power. The AC optical power output from the EOM was 0.4 mW_{rms}. Losses in the measurement system between the EOM output and the device must be taken into account. Multiplying by these losses gives the optical power entering the bus waveguide of $6.5 \pm 0.7\ \mu\text{W}_{\text{rms}}$ [118]. To determine how much optical power is in the ring resonator, and therefore how much optical force is acting on the beam, the power enhancement (PE) provided by the racetrack resonator should be included. Our racetrack resonators are subject to coherent backscattering effects, as can be observed by a small peak splitting at bottom of the resonance dip. These effects must be taken into account when calculating the PE. The average power enhancement on resonance is 10.6, which is calculated using Eqs. (2.36) and (2.37) for add-drop microrings from Section 2.2.6. This method will be described in more detail in Section 4.2.2. Multiplying the power entering the bus waveguide by 10.6, the average AC optical power in the racetrack resonator is $P_{\mathrm{bus,AC}} = 0.07 \pm 0.01$ mW. Finally, normalizing F_{drive} by $P_{\mathrm{bus,AC}}$ and l gives the total optical driving force, $F_{\mathrm{opt,AC}}$. This can be calculated for the first through third modes, giving values of $F_{\mathrm{opt,AC}} = 0.36 \pm 0.04$, 0.38 ± 0.04, and 0.39 ± 0.04 respectively.

The model shown in Figure 3.24(c) implies similar optical forces, however, the measured forces are much closer than the model suggests. We can improve the model by introducing a minor correction to account for the force from the larger gap section, as the current model only takes the force from the smaller gap into account. $F_{\mathrm{opt,AC}}$ can be described as the result of two contributions: one from the section with a small gap (F_{S}), and one from the section with the large gap (F_{L}). To simplify the integrations, we have modeled the position-dependent optical force $F_{\mathrm{opt,AC}}(x)$ as a step function with two step heights. We have neglected the sloped transitions between the gaps, which may introduce a small amount of error, as we saw in the case of the responsivity. Eq. (3.3) shows the expression for $F_{\mathrm{opt,AC}}(x)$, and accounts for the partial mode shape over which each force contribution acts:

$$F_{\mathrm{opt,AC}} = \int_0^1 F_{\mathrm{opt,AC}}(x)\mathrm{d}x = F_{\mathrm{S}} \int_0^{l_{\mathrm{s}}/l} \hat{u_{\mathrm{n}}}(x)\mathrm{d}x + F_{\mathrm{L}} \int_{l_{\mathrm{s}}/l}^1 \hat{u_{\mathrm{n}}}(x)\mathrm{d}x, \tag{3.3}$$

where l_{s} is the length of the beam interacting with the small gap. The normalized mode shape is described by the function $\hat{u_{\mathrm{n}}}$, where n is the mode number. The normalizations in Eq. (3.3) are consistent with those used for the thermomechanical noise calibration in Section 2.1.1. This function is a solution to the wave equation for the boundary conditions of a doubly clamped beam [22]. For clamped-clamped boundary conditions, $\hat{u_{\mathrm{n}}}$ is described by

$$\hat{u_{\mathrm{n}}} = a_{\mathrm{n}}(\cos(z_{\mathrm{n}}) - \cosh(z_{\mathrm{n}}) + b_{\mathrm{n}}(\sin(z_{\mathrm{n}}) - \sinh(z_{\mathrm{n}})), \tag{3.4}$$

with $z_{\mathrm{n}} = 4.7300, 7.8532, 10.9956...$ and $a_{\mathrm{n}}/b_{\mathrm{n}} = 1.0178, 0.9992, 1.0000....$

Since we know the experimental value for $F_{\mathrm{opt,AC}}$ and also the first three mode shapes, we have a system of equations to solve for F_{S}, F_{L} and l_{s}. Solving this system gives $F_{\mathrm{S}} = 1.86$ pN/μm mW, $F_{\mathrm{L}} = 0.24$ pN/μm mW, and $l_{\mathrm{s}}/l = 0.38$. We can compare F_{S} and F_{L} to those obtained via finite difference time domain simulations obtained with Lumerical Solutions (Figure 3.25(b), inset). The optical force between a waveguide and a substrate for varying separations (z) can be calculated with Eq. (3.5) [196], where the left hand side is optical force that has been normalized by the length of the mechanical resonator and the input optical power:

$$F_{\mathrm{opt}} = \frac{F_{\mathrm{drive}}}{P_{\mathrm{opt}} l} = \frac{n_{\mathrm{g}}}{n_{\mathrm{eff}} c} \frac{\partial n_{\mathrm{eff}}}{\partial z}. \tag{3.5}$$

If the force is negative, it is an attractive force that pulls the beam towards the substrate. If the force is positive, it is repulsive and pushes the beam away. By using the simulated values for $\partial n_{\text{eff}}/\partial z$ and n_{g}, we can calculate the simulated optical force as shown in the inset of Figure 3.25. We can then compare the simulated optical force to the measured values for optical force, F_{S} and F_{L}. These are shown by the arrows in the inset of Figure 3.25 and are comparable to other optical forces observed in the literature [54, 67]. F_{S} corresponds to a gap of 40 nm and F_{L} corresponds to a gap of 140 nm, which is reasonable on inspection of the SEM image in Figure 3.24(a).

Eq. (3.3) could also be used to design higher or lower transduction efficiency for various modes. A more complex pattern for the optomechanical gap would provide a function $F_{\text{opt}}(x)$ with shape that either maximizes or minimizes the integral for various mode shapes. For example, a high force on the first 25% of the beam's length and also on 50% to 75% of the beam's length would be fairly efficient at transducing the fourth mode. This could be attained with a series of alternating steps. This method could also be applied to actuate and transduce torsional paddles or to in-plane motion, to provide transduction for side-coupled doubly clamped beams. Essentially, this approach could be generalized to any choice of resonator, and would produce a specific pattern to provide comparable efficiency to the desired set of modes.

3.2.3 Duffing Amplitude of a Symmetry-Broken Beam

The critical amplitude is the point at which the mechanical resonator response transitions from linear to nonlinear behavior. For a doubly clamped beam, the first nonlinear effect typically observed is a stiffening Duffing nonlinearity and is caused by geometrical effects in the beam [197]. Experimentally, the critical amplitude is observed as an infinite slope on the falling edge of the resonance peak. The presence of the point of infinite slope on the falling edge indicates a stiffening nonlinearity, as opposed to the rising edge which would indicate a softening nonlinearity. By increasing the optical driving force to observe the critical amplitude, we can test whether the response due to increased driving power remains predictable in the symmetry-broken system.

For experimental determination of the critical amplitude (a_{cr}), the amplitude of the modulation on the optical driving force is increased by increasing the modulation voltage at the EOM. This provides a higher actuation force to the resonator. The mechanical response of the doubly clamped beam is measured at each driving voltage, and the driving voltage is increased until nonlinearity is observed. These results are shown in Figure 3.26, where the nonlinearity is evident at higher driving voltages and highlighted by the asymmetry observed in the mechanical response. To determine the critical amplitude, the amplitude at the centre frequency is recorded for each driving voltage, as plotted in the inset of Figure 3.26. Then, the amplitude at the 1 dB compression point ($a_{1\mathrm{dB}}$) is determined. $a_{1\mathrm{dB}}$ is the point where the amplitude at the resonance frequency is 1 dB less than predicted by the linear response. The 1 dB compression point is observed at a driving voltage of 0.16 $\mathrm{V}_{\mathrm{rms}}$, which corresponds to an optical power of 0.86 $\mathrm{mW}_{\mathrm{rms}}$. Then, the critical amplitude is related to the amplitude at the 1 dB compression point by [63]

$$a_{1\mathrm{dB}} = 0.745 a_{\mathrm{cr}}. \tag{3.6}$$

The amplitude at the 1 dB compression point is 3.1 nm, and so from Eq. (3.6) we calculate a critical amplitude of 4.2 nm. A theoretical value for the critical amplitude caused by a Duffing nonlinearity can be calculated using the following equation [197]:

$$a_{\mathrm{cr}} = \frac{1.685t}{Q^{1/2}}. \tag{3.7}$$

The theoretical critical amplitude is 3.9 nm, based on the experimentally measured quality factor for the driven measurements of the first mode, $Q = 9200$. t is the thickness of the beam, and in this case is equal to 220 nm, which is the thickness of the silicon device layer. The experimental value and theoretical value demonstrate very good agreement for the critical amplitude. This result highlights that the symmetry-breaking technique used to fabricate this device does not affect the functionality of the optical drive even at higher driving forces.

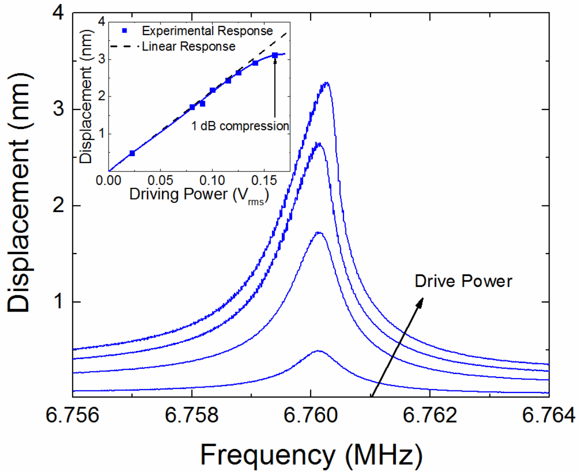

Figure 3.26: Amplitude of the first mode in nanometers as the drive power is increased. Inset: Experimental displacements at the centre resonance frequency compared to a linear response (black dashed line). The blue line is a guide to the eye. Reprinted from [21], with the permission of AIP Publishing.

3.2.4 Using Multiple Modes to Measure Stress

Thus far in the chapter, we have discussed the driving force and transduction of a doubly clamped beam with a step in the substrate. We have shown that the first three modes of a beam can be driven and detected effectively using this symmetry-breaking technique. Often when releasing doubly clamped beams from SOI wafers, as is done in this case, the beams can buckle due to the built-in stress in the silicon device layer [161]. We observed buckling in some of our longer doubly clamped beams. Due to the fact that we were able to detect even and odd modes in these devices, we are able to estimate the stress in the buckled Si device.

We fabricated a 17.85 μm long doubly clamped beam with a step in the substrate underneath using the approach described in Section 3.2.2. The device is pictured in Figure 3.27(a). The first two mechanical modes of vibration were measured using the previously described approach. The measured resonance frequencies of the first two modes are shown in Figure 3.27(b).

To extract the stress in the buckled beams, we need to compare the measured result to those predicted by theory. Using the approach described in [198], we can numerically solve the system of equations to determine the resonance frequencies of the n^{th} buckled mode in a doubly clamped beam, for different initial buckled deflections. In this theoretical description, the even modes are independent of stress and depend only on the length of the device. Therefore, we can determine the length of the device by setting the theoretical expression for the resonance frequency equal to the experimentally observed value and solving for the length. This calculation gives an exact length of 17.85 μm, which corresponds well to the SEM image in Figure 3.27(a). We would like to emphasize that this measurement would not be possible without the symmetry-breaking approach, as the second mode would not be visible.

Unlike the even modes, the odd modes depend on the stress in the beam. The stress in the beam can be related to the initial buckled deflection (z_{initial}) by

$$z_{\mathrm{initial}}^2 = \frac{4l^2(\sigma - \sigma_{\mathrm{c}})}{\pi^2 E}, \tag{3.8}$$

where σ is the stress in the device, E is the Young's modulus of silicon and is equal to 169 GPa, and $\sigma_{\mathrm{c}} = \pi^2 E t^2/3l^2$ is the critical buckling stress. In this equation, l is equal to 17.85 μm as determined by the second mode resonance frequency. We can determine the stress by plotting a range of values for z_{initial} versus the resonance frequency for the first mode. By comparing the experimental results for the fundamental resonance frequency to the theoretical curves, the initial buckled deflection can be determined. This approach is shown in Figure 3.27(b). From the initial buckled deflection, the stress in the device can be calculated using Eq. (3.8). From Figure 3.27(b), the initial buckled deflection is $z_{\mathrm{initial}} = 127$ nm. This value correlates well to the deflection observed in the SEM image in Figure 3.27(a). From Eq. (3.8), the stress in the buckled device is 106 MPa. This value is within the typical range for commercial SOI wafers [199].

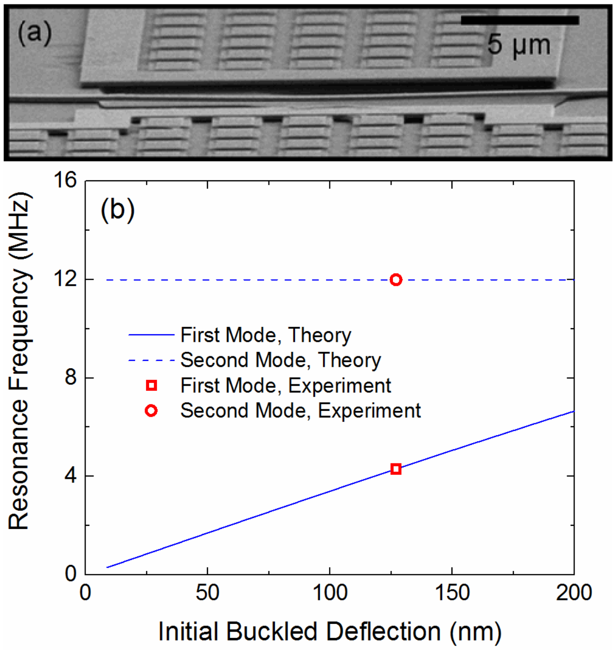

Figure 3.27: (a) SEM image of a 17.85 μm long buckled doubly clamped beam, taken at an 80° angle. (b) Experimental and theoretical resonance frequencies for the first two modes of a buckled doubly clamped beam. Experimental results for the first and second modes are an open square and open circle, respectively. Theoretically predicted results for the first and second modes are shown as solid and dashed lines, respectively. Reprinted from [21], with the permission of AIP Publishing.

3.2.5 Conclusion

We have demonstrated nanophotonic drive and readout of even vibrational modes in a doubly clamped beam. Transduction of the even modes is made possible by a step in the substrate underneath the mechanical device. This step breaks the substrate symmetry and allows for stronger coupling to one section of the beam. The symmetry-breaking process allows for straightforward measurement of the second mode while retaining strong a signal-to-noise in the odd modes. We use the thermomechanical noise signal to calibrate the displacement. From the peak displacement, we calculate the total optical force induced by the pump laser for the first three modes. By assuming different contributions from the small and large gap sections beneath the beam, we derived local optical forces that were consistent with photonic modeling. We also measured the observed critical amplitude of the first mode, which agrees well with the theoretically predicted critical amplitude for a mechanical nonlinearity. This agreement demonstrates that the beam with the symmetry broken behaves as expected under an applied optical driving force. Lastly, we have estimated the stress in the device layer to be 106 MPa by measuring the resonance frequency of the first two modes of a buckled doubly clamped beam. The technique of breaking the symmetry shown here may also be used in the design of other device geometries, such as side-coupled doubly clamped beams, to improve mass sensing for many different configurations.

3.3 Low-Frequency Single Laser Transduction

In an effort to further simplify our nano-optomechanical sensing platform, one option is to remove the pump laser from the system and use a single laser as both the drive and detection mechanism. This approach has been explored in [200]. In that work, it was demonstrated that a single laser with an amplitude modulation was sufficient to both drive and detect the nanomechanical device. The introduction of a constant background resulted in a Fano-like shape for the mechanical resonance. Despite the atypical lineshape, the signal could be tracked with a phase-locked loop (PLL), which meant the signal was suitable for sensing applications. The single laser reduces the complexity of the setup and may be more feasible for portable sensing applications.

To extend the work done in [200], and further simplify the experimental setup, it is desirable to create a signal that can be read out at low frequency. This would eliminate the need for expensive high-frequency photodiodes. For this reason, we would like to use a signal-mixing scheme to down-convert the high frequency mechanical signal (in the range of 1–100 MHz) to something on the order of tens of kHz. This signal could be easily read by an inexpensive DC photodiode. This type of photodiode would be straightforward to integrate onto a circuit board or even on-chip. Many down-conversion schemes exist in the literature, such as electronic [201] or optical [15] heterodyning, where a local oscillator signal is mixed with the measured signal to produce a down-converted output. Optical homodyning, where the local oscillator frequency is the same as the measured signal frequency, is also frequently used in optomechanics to obtain results with low noise [202, 203, 204]. Typically these techniques are used in optomechanics to detect the thermomechanical noise of the mechanical resonator. Distinct in the present scheme is the application of direct, controllable excitation power at the mechanical frequency, while also detecting response at low frequency.

Here, we use a single laser to drive and detect the mechanical signal at low frequency. We will discuss how the mechanical signal can be extracted with good signal-to-noise ratio. We will demonstrate low frequency phase locked operation of the high frequency nanomechanical sensor.

3.3.1 Theory

The power output from a device measured and actuated using the single-laser modulated drive and detection (SLMDD) method is described by $P_{\text{out}} = P_{\text{in}}(t)T(t)$. The input power can be expressed as the summation of the DC and AC components of the optical power, $P_{\text{in}}(t) = P_{\text{dc}} + P_{\text{1f}}\cos(\Omega t)$. The DC component is the laser power, and the AC modulation power is determined by the amplitude modulation introduced by an electro-optic modulator (EOM). The experimental details will be discussed further in the following section. The transduction function $T(t) = T_0 + x(t)\partial T/\partial x$ is an expansion of the optical transmission and includes a DC component (T_0), and a frequency dependent component $x(t)\partial T/\partial x$. This component has a frequency at $1f$, and sinusoidal time-dependence. The time dependence is sinusoidal since this component depends on $x(t) = B(2\pi f)\cos(2\pi ft - \varphi)$, which is the time-varying displacement of the nanomechanical device. $B(2\pi f)$ is the amplitude of the mechanical device as a function of frequency derived in Eq. (2.5). φ is the phase response of the mechanical device. The $1f$ component is the first order transduction coefficient that describes the modulation resulting from optomechanical effects. The transduction coefficient was previously described by Eq. (2.42). Substituting in these expressions and multiplying all terms gives results at DC, $1f$, and $2f$ frequency components. The DC and $1f$ results are shown in Eqs. (3.9) and (3.10) respectively;

$$P_{\text{out,dc}} = P_{\text{dc}}T_0 + \frac{P_{\text{1f}}}{2}B(2\pi f)\frac{\partial T}{\partial x}\cos\varphi, \tag{3.9}$$

$$P_{\text{out,1f}} = P_{\text{1f}}T_0\cos(2\pi ft) + P_{\text{dc}}B(2\pi f)\frac{\partial T}{\partial x}\cos(2\pi ft - \varphi). \tag{3.10}$$

The first term in Eq. (3.9) is the DC signal. It is very large in comparison to the second term, since the DC output from the optical cavity is much larger than the AC modulation of the cavity. The second term contains information about the mechanical signal. The Lorentzian amplitude of the mechanical signal is denoted by the function $B(2\pi f)$, and the phase shift of the mechanical signal is denoted by φ. Since the first term in Eq. (3.9) is significantly larger than the second, but the second term is where all of the information about the mechanical signal is located, the information is lost during measurements. If the full DC signal is observed, only the noisy first term is visible. However, the idea that we can extract amplitude and phase data at DC provides inspiration to find another way to observe the mechanical signal at very low frequencies, such that a DC photodiode can still read out the signal. To accomplish this, we can add a single sideband at a very low frequency (10–30 kHz) amplitude modulation onto the drive signal [205] such that

$$P_{\text{in}}(t) = P_{\text{dc}} + P_{\text{1f}}\cos(2\pi ft) + \frac{P_{\text{1f}}P_{\text{mod}}}{2}\cos(2\pi ft + 2\pi f_{\text{mod}}t), \tag{3.11}$$

where P_{mod} is the modulation power and f_{mod} is modulation frequency in the range of tens of kHz. To calculate P_{out}, we multiply P_{in} by the transduction function $T(t) = T_0 + x(t)\partial T/\partial x$ and substitute in $x(t) = B(2\pi f)\cos(2\pi f t - \varphi)$:

$$\begin{aligned} P_{\mathrm{out}}(t) = P_{\mathrm{in}}T(t) = \left[P_{\mathrm{dc}} + P_{\mathrm{1f}}\cos(2\pi f t) + \frac{P_{\mathrm{1f}}P_{\mathrm{mod}}}{2}\cos(2\pi f t + 2\pi f_{\mathrm{mod}}t)\right] \\ \left[T_0 + B(2\pi f)\cos(2\pi f t - \varphi)\partial T/\partial x\right]. \end{aligned} \tag{3.12}$$

We can expanding this equation and simplify it using trigonometric identities. This simplification process gives the following result:

$$\begin{aligned} P_{\mathrm{out}}(t) = P_{\mathrm{dc}}T_0 + \frac{P_{\mathrm{1f}}}{2}B(2\pi f)\frac{\partial T}{\partial x}\cos\varphi + \\ P_{\mathrm{1f}}T_0\cos(2\pi f t) + P_{\mathrm{dc}}B(2\pi f)\frac{\partial T}{\partial x}\cos(2\pi f t - \varphi) + \\ \frac{P_{\mathrm{1f}}}{2}B(2\pi f)\frac{\partial T}{\partial x}\cos(4\pi f t - \varphi) + \frac{T_0 P_{\mathrm{1f}}P_{\mathrm{mod}}}{2}\cos(2\pi f t + 2\pi f_{\mathrm{modt}}) + \\ \frac{P_{\mathrm{1f}}P_{\mathrm{mod}}B(2\pi f)}{2}\frac{\partial T}{\partial x}\left[\cos(2\pi f_{\mathrm{mod}}t - \varphi) - \cos(4\pi f t + 2\pi f_{\mathrm{mod}}t - \varphi)\right]. \end{aligned} \tag{3.13}$$

The first two terms are identical to Eq. (3.9), and are the DC terms. The third and fourth terms are identical to Eq. (3.10) and are the $1f$ terms. The fifth term is the $2f$ term generated by the power at $1f$ mixing with the mechanical signal. The sixth term is at $f + f_{\mathrm{mod}}$. The seventh term has a frequency only at f_{mod}. The final term has a frequency at $2f + f_{\mathrm{mod}}$. To summarize, the component solely at the modulation frequency f_{mod} is

$$P_{\mathrm{out,f_{mod}}} = \frac{\partial T}{\partial x}\frac{P_{\mathrm{1f}}P_{\mathrm{mod}}}{2}B(2\pi f)\cos(2\pi f_{\mathrm{mod}}t - \varphi). \tag{3.14}$$

This component at f_{mod} has the same form as the second term in Eq. (3.10). Notably, the mechanical amplitude B and phase φ are contained in this result. Therefore, we should be able to read out the mechanical signal at these very low frequencies by measuring the DC response from the photodiode at f_{mod}, eliminating the need for a high-frequency photodiode.

3.4 Experimental Results

To verify the theoretical prediction experimentally, we have used the experimental setup illustrated in Figure 3.28. The EOM is biased to provide the optimal signal-to-noise (SNR) at the output, as described in Section 2.4. The tunable laser is positioned on the side of the optical cavity slope to provide the maximum responsivity for the mechanical signal. Unless otherwise stated, the laser was positioned on the blue side of the optical cavity for all of the subsequent experiments. Polarization controllers (PCs) are set for TE polarization. Both the AC and DC signal outputs of the photodiode (PD) were connected to the lock-in amplifier (LIA). The AC signal was used for the SLMDD approach to verify that the results obtained are similar to those shown in [200]. The DC signal was used to measure the low-frequency data, to demonstrate that only a DC photodiode is necessary for these low-frequency measurements.

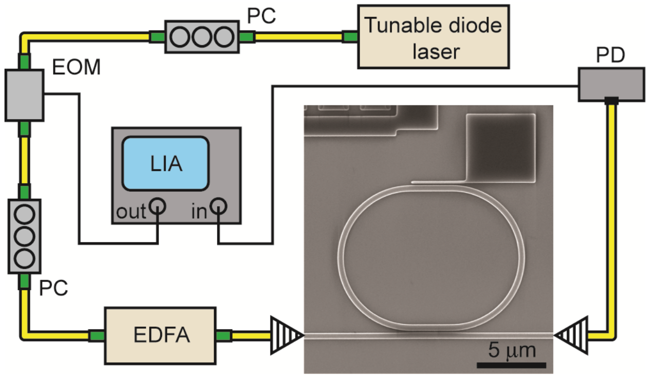

Figure 3.28: Schematic of the single-laser drive and detection system. Image courtesy of Vincent Sauer [200].

The device measured in these experiments is a 2.89 μm long, 130 nm wide cantilever with a fundamental resonance frequency at about 21.21 MHz. It is adjacent to a racetrack resonator with a 5 μm radius and 3 μm long straight section. The gap between the racetrack and the cantilever is approximately 90 nm and the optomechanical coupling is approximately 1 rad GHz/nm. To obtain the thermomechanical noise of this nanomechanical cantilever, the EOM was deactivated and the frequency response of the device was recorded using the AC signal from the photodiode. The result of this measurement is shown in Figure 3.29. As expected, a Lorentzian lineshape is observed.

To drive the device, the EOM was activated by applying the output driving voltage from the LIA. To set up the signal processing scheme, we have used many of the available capabilities of the Zurich UHF lock-in amplifier. Particularly, the modulation tab was used to add the amplitude modulation to the output signal from the lock-in amplifier. The carrier frequency was set to the mechanical resonance frequency, and the modulated component was added to the carrier as a single upper sideband. By sweeping the carrier frequency, we can sweep over the mechanical resonance to obtain a plot of amplitude versus frequency. To read the data, we set the AC output from the photodiode to one of the input demodulators of the lock-in amplifier to the carrier frequency and obtained the results from the AC component of the photodiode signal. This provides the SLMDD signal, and shows the

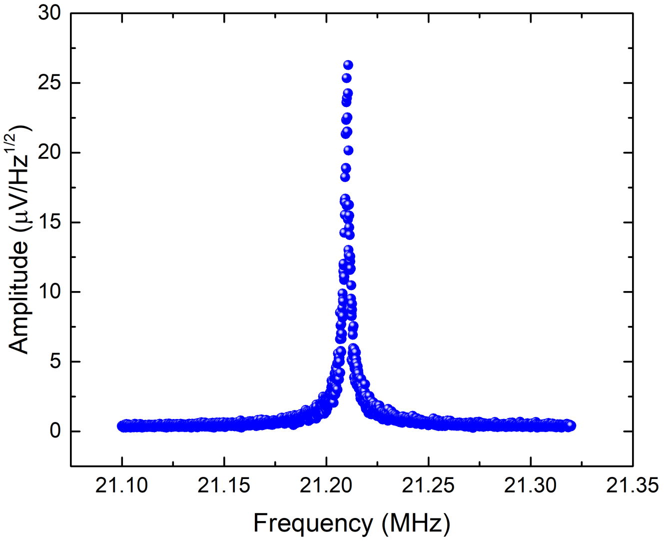

Figure 3.29: Thermomechanical noise of the cantilever device with the EOM deactivated.

amplitude and phase response as the frequency is swept over a range that includes the mechanical resonance. A second input demodulator was connected to the DC component of the photodiode signal, so only the low-frequency data was input to the LIA. This demodulator was set to a constant value of the modulation frequency f_{mod}. By setting the demodulator to this low-frequency value, we are measuring the change in the amplitude and phase of the mixed signal $P_{\mathrm{out,f_{mod}}}$ at f_{mod}. As the carrier frequency was swept over the mechanical response, the response at f_{mod} changes, and shows a signature of the mechanical signal. Although the response is read out at a constant low frequency value, the results obtained are still a function of the amplitude response of the mechanical device as the carrier frequency is swept over the frequency range of interest. For that reason, we have plotted the results as the mechanical signal amplitude $B(2\pi f)$ versus the carrier frequency.

It should be noted that the thermomechanical noise of the device cannot be observed using the low-frequency approach, as this technique requires that the carrier driving voltage is activated, that is, that P_{1f} is non-zero. This is one of the drawbacks of this technique, however, the benefits gained in terms of simplicity outweigh this drawback. Since mass sensing is done using a driven signal, the measurement of the thermomechanical noise is not required for a mass-sensing device.

To fully characterize our low-frequency detection technique, we have carried out a number of tests that show how different parameters affect the signal. The first parameter tested was the amplitude of the voltage of the carrier frequency as output from the LIA to the EOM. Essentially this parameter determines the amplitude of the driving signal output to the device, because as the driving voltage increases, the amplitude modulation provided by the EOM increases. In this test, the modulation frequency was set to 30 kHz and the optical power was set to 94 μW in the bus waveguide. The result of this test is shown in Figure 3.30, where (a) and (b) show the amplitude and phase response of the SLMDD signal, and (c) and (d) show the response of the low frequency signal. In part (e), the peak amplitude of the low-frequency signal is plotted versus the input carrier driving voltage.

There are several important results we observe from this data. The first observation is that the amplitude and phase of the SLMDD signal and the low frequency signal have the same shape, which is expected since Eq. (3.14) has the same form as the second term in Eq. (3.10). The second observation is that the low-frequency signal has two peaks, whereas the SLMDD signal has only one. This is because the carrier frequency plus the modulated frequency are being swept across the mechanical resonance. Therefore, the swept signal is equal to the mechanical resonance twice during the sweep; the first time is when $f_{\text{carrier}} + f_{\text{mod}} = f_0$ where f_0 is the mechanical resonance frequency in Hz. The second time is when $f_{\text{carrier}} = f_0$. Therefore, two peaks are measured while observing the output at the modulation frequency. The third observation is that the amplitude of both the SLMDD and low-frequency signal increase with increasing driving voltage, as expected. By examining Figure 3.30(e), we see that the rate at which the amplitude increases is not exactly as expected. We expect the peak amplitude to increase quadratically with the driving voltage according to Eq. (3.14), due to the $P_{1,\text{f}}B$ term, as both of these variables should increase linearly with increasing carrier drive voltage. However, the trend appears to be linear. The fourth observation is that both signals have a DC background that increases with driving voltage, and that the background is different for both signals. The DC background in the SLMDD signal is due to the first term in Eq. (3.10), and has been explored thoroughly in Ref. [200]. Essentially this is a coherent DC signal due to the DC transduction of the $1f$ signal. For the low-frequency signal, there is no DC term in the low-frequency model presented in Eq. (3.14) that would cause an equivalent DC background. Despite the fact that we are measuring at a specific, low modulation frequency, there is still clearly a coherent background signal from an unidentified source. The background level in the low-frequency signal increases with increasing carrier voltage in the amplitude domain (Figure 3.30(c)). There is also a constant phase background in Figure 3.30(d), which is different from the frequency-dependent phase background in the SLMDD signal, observed in Figure 3.30(b). We can conclude that the coherent background not frequency dependent, and as such is from a different source than the SLMDD signal. This coherent background may also explain why the increase in peak amplitude with input carrier voltage was linear as opposed to quadratic.

Interestingly, the random noise background decreases with increasing drive voltage in both the amplitude (Figure 3.30(c)) and the phase signal (Figure 3.30(d)).

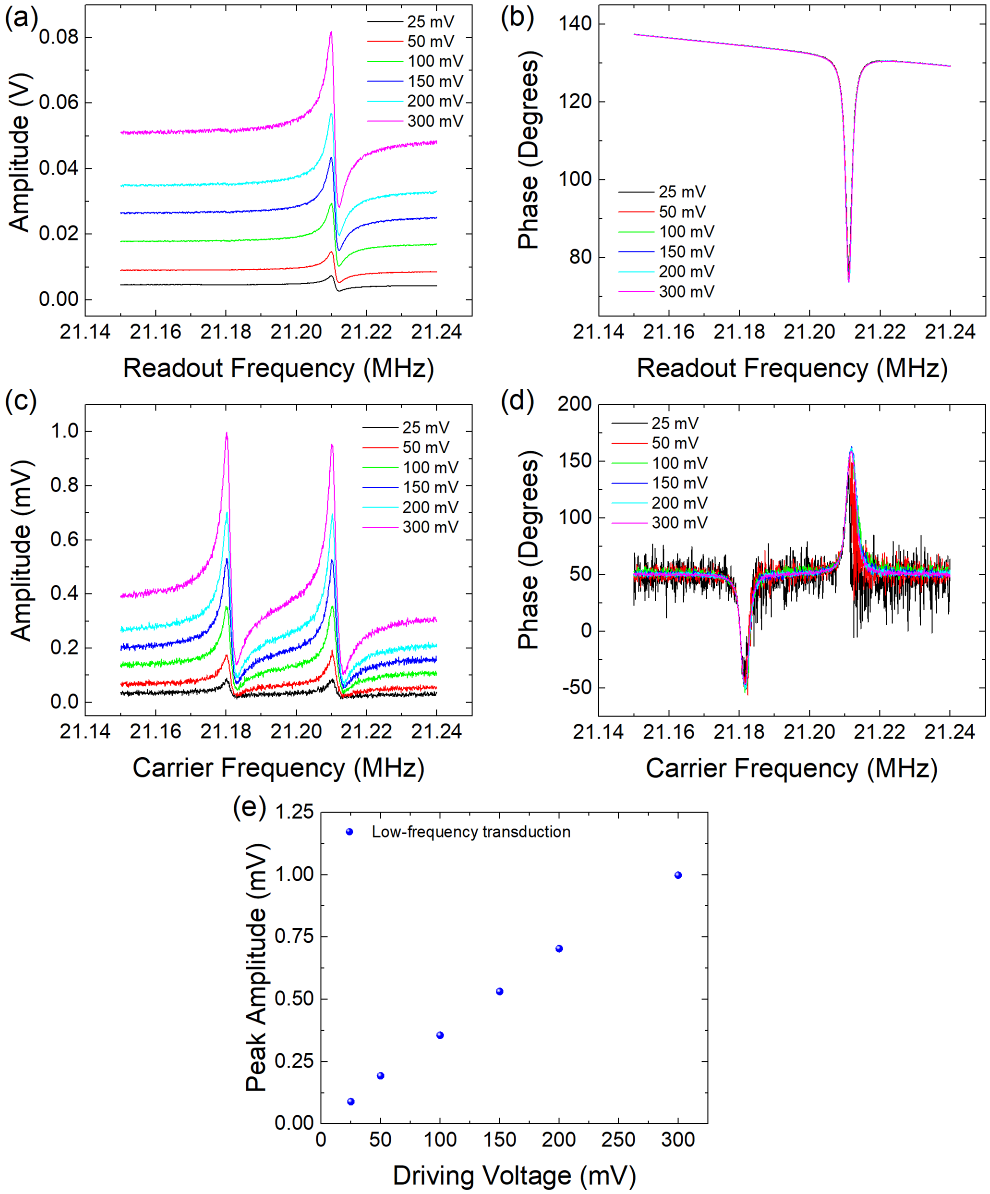

Figure 3.30: The results are recorded as the AC voltage of the high-frequency input carrier drive signal applied to the EOM is increased, with a constant DC laser power was set to 94 μW in the bus waveguide. (a) Amplitude and (b) phase signals plotted versus the readout frequency from the cantilever measured at 21 MHz using the SLMDD technique. (c) Amplitude and (d) phase signals from the same cantilever plotted versus the input carrier frequency using the low frequency single laser transduction technique using a 30 kHz modulation frequency, 100 mV modulation voltage. (e) Peak amplitude in mV of the results from (c) versus the AC input carrier voltage. We expect the peak amplitude to increase quadratically with the driving voltage according to Eq. (3.14), however the trend appears to be linear. This discrepancy may be due to the unexpected background present in (c).

Although the ratio between the peak amplitude signal and the average background level is constant as the carrier voltage is increased, the ratio between the peak amplitude signal and the height of the noise fluctuations decreases with increasing carrier voltage. This trend is especially noticeable in the phase signal, where the noise fluctuations are very large at the low carrier driving voltage of 25 mV. At the high carrier driving voltage of 300 mV, the noise fluctuations are reduced substantially. We can therefore conclude than the signal-to-noise ratio increases with increasing carrier driving voltage, which is a beneficial aspect of this transduction technique compared to the SLMDD technique.

The second experiment was to test the effect of the laser power on the low-frequency signal. Based on Eq. (3.14) we expect that as the laser power is increased, $P_{1\text{f}}$ and B are also increased, and therefore the amplitude of the signal increases accordingly in a quadratic fashion. We examined both the SLMDD and the low-frequency signals. The results of this experiment are shown in Figure 3.31. In this experiment, the amplitude of the signal increases with increasing laser power, as expected from the theoretical description in the previous section. Figure 3.31(e) highlights the fact that for the low-frequency transduction technique, the peak amplitude increases more rapidly compared to Figure 3.30(e) with increasing input power, but the increase is still not the expected quadratic trend. The main difference between the results highlighted in Figure 3.30 and Figure 3.31 is that the phase signal increases in amplitude for the latter as the power increases. This is true for both the SLMDD signal (Figure 3.31(b)) and the low-frequency signal (Figure 3.31(d)). This is expected for the SLMDD signal due to the fact that the DC background in the SLMDD signal is directly proportional to tanφ, as described in [200]. In the low-frequency signal, this is not expected from Eq. (3.14), since there is no DC component. However, this change in the phase is a strong argument for the fact that a background is present in the signal measured at f_{mod}, allowing the low-frequency signal to have many of the same characteristics of the SLMDD signal. By increasing the DC background, the phase shift changes significantly.

The next test was to determine the optimal value for f_{mod}. For this test, the frequency of the single sideband was varied between 10 kHz and 100 kHz, and the measurement was performed at each value of f_{mod}. The results of this test are shown in Figure 3.32. For the amplitude spectrum (Figure 3.32), as f_{mod} increases, the SNR in the amplitude spectrum decreases. From the amplitude spectrum, it would seem that the optimal choice for f_{mod} is as low as possible. However, the choice of f_{mod} also strongly affects the phase signal (Figure 3.32(b)). Since the goal of this application is to perform sensing experiments, which require the use of a phase-locked loop (PLL), the phase signal must show good SNR. The SNR of the phase signal is poor at both 10 kHz and at 50 kHz, and shows good SNR at

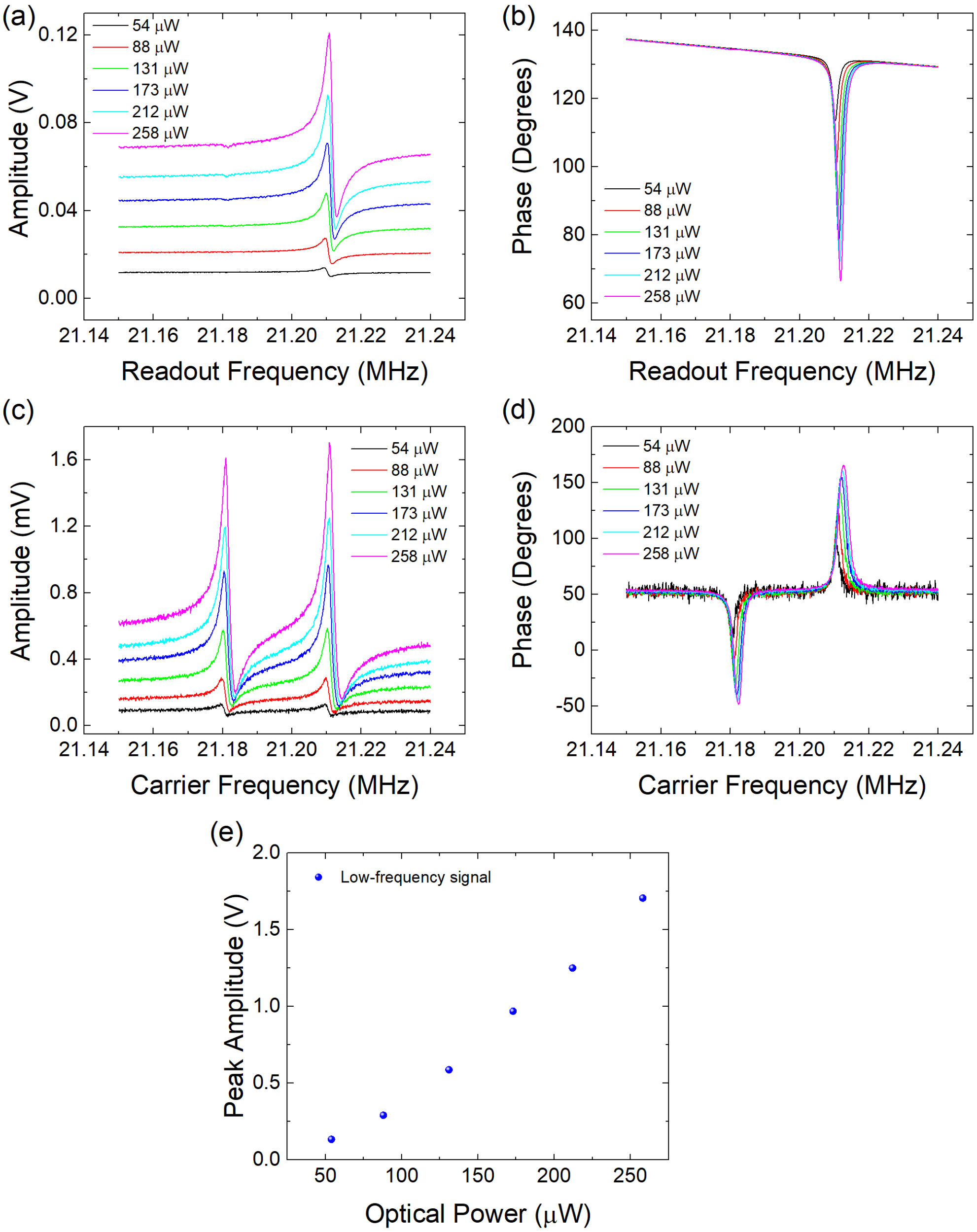

Figure 3.31: The mechanical response was recorded as the DC optical power was increased. The optical powers are defined as the power in the bus waveguide. The AC voltage of the input carrier signal applied at the EOM was 100 mV. (a) Amplitude and (b) phase signals from a cantilever plotted versus the readout frequency measured at different optical powers using the SLMDD technique. (c) Amplitude and (d) phase from the same cantilever plotted versus the carrier frequency using the low frequency single laser transduction technique with a 30 kHz modulation frequency and a modulation voltage of 100 mV. The results are plotted versus the carrier frequency signal as the readout frequency was constant at 30 kHz. (e) Peak amplitude from (c) plotted versus the optical power in the bus waveguide. The amplitude increases more rapidly than a linear trend predicts, but the increase is not as substantial as the expected quadratic trend would suggest. The discrepancy is likely due to the background signal.

30, 70, and 100 kHz. The optimal value for f_{mod} is then 30 kHz, as it has good SNR in the phase domain, and is the lowest frequency signal so the SNR in the amplitude domain is maximized. By changing the modulation frequency, the value of the background phase signal is changed in Figure 3.32. This means that the background signal that is affecting the low-frequency signal may be dependent on the modulation frequency. There is more noise at some frequencies (10, 50 kHz) than others, which may indicate a source of noise at a particular frequency. This may vary from setup to setup depending on the noise sources in the lab or in the equipment used, and so it is important to characterize the optimal f_{mod} for each experimental setup.

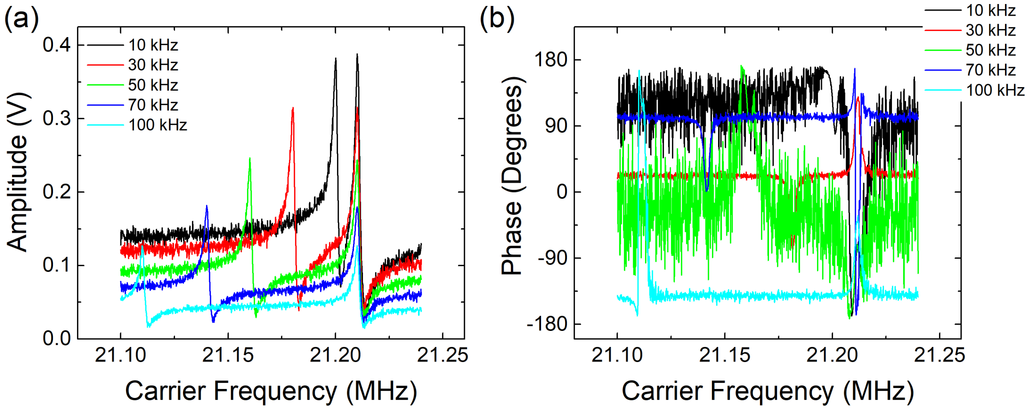

Figure 3.32: (a) Amplitude and (b) phase signals from a cantilever measured at different modulation frequencies. The optical power is set to 94 μW in the bus waveguide, the carrier voltage is set to 50 mV, and the centre driving voltage is set to 100 mV. The results are plotted versus the carrier frequency signal as the readout frequency for each measurement was constant at the frequency specified in the legend. For example, in (a), the amplitude signal was read out at a constant value of 10 kHz for the black curve, a constant value of 30 kHz for the red curve, and so on.

The final parameter varied was the voltage of the sideband signal, called the modulation voltage. This affects P_{mod}, but does not affect B, as shown in Eq. (3.14). Therefore, we expect peak amplitude of the observed signal to increase linearly with increasing modulation voltage. Instead of changing the voltage of the central carrier frequency, we modified the voltage of the sideband signal to determine the effect on the signal observed at low frequency. This also has no effect on the SLMDD signal, since it is not affected by the low-frequency modulation signal. The results of this experiment are shown in Figure 3.33 for the (a) amplitude and (b) phase signals. The peak amplitude of the observed mechanical signal is plotted versus the modulation voltage in Figure 3.33(c). As expected, the peak amplitude increases linearly with modulation voltage. Lastly, by increasing the carrier voltage, the SNR of the phase signals are improved as the noise is reduced. For the amplitude signal, the overall amplitude increases and the background level also increases.

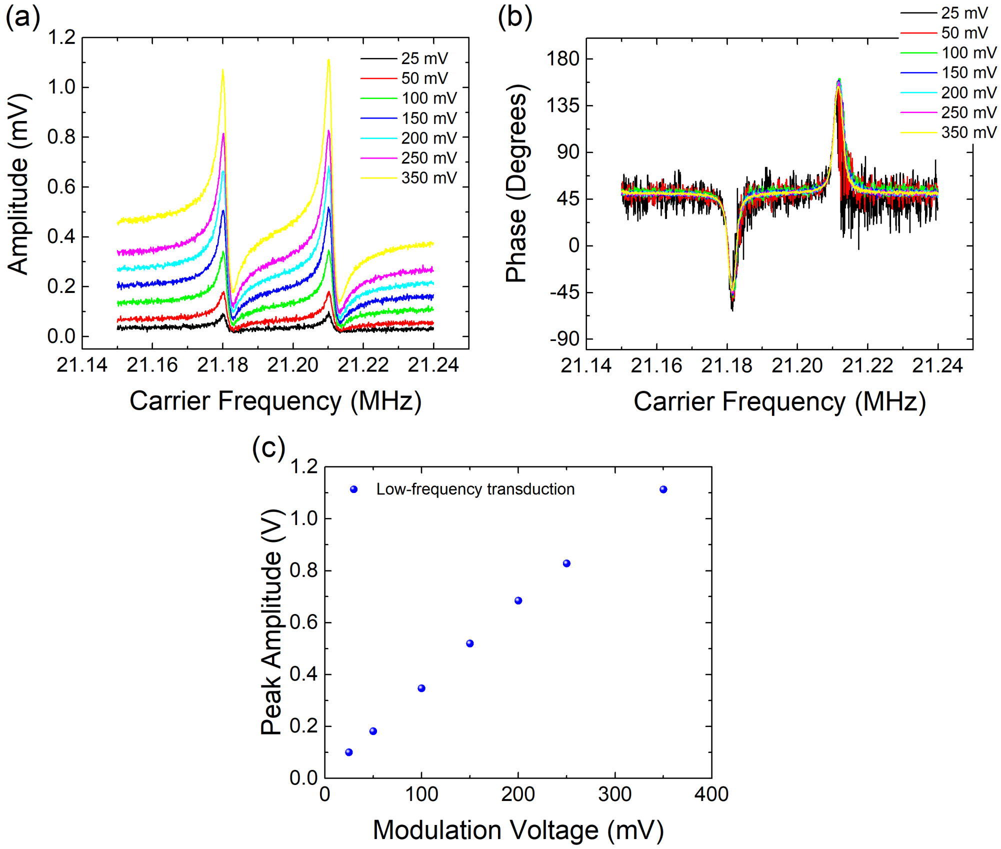

Figure 3.33: (a) Amplitude and (b) phase signals from the cantilever measured at different modulation voltages. The centre carrier driving voltage was set to 100 mV, and the optical power in the bus waveguide was set to 94 μW. The results are plotted versus the carrier frequency signal as the readout frequency was constant at 30 kHz. (c) The peak amplitude from (a) plotted versus the modulation voltage. The amplitude increases linearly with modulation voltage, as expected.

As a check to ensure that the signal measured at low frequency was in fact the mechanical signal of the cantilever, we moved the position of the laser from the blue side of the optical cavity to the red side, and monitored the response at both positions. This result is shown in Figure 3.34. As expected, the Fano-like shape changes its sign when the laser is moved from the blue to the red side due to the changing sign of the slope. This occurs for both the amplitude (Figure 3.34(a)) and phase (Figure 3.34(b)) signals. There is also a slight shift in the resonance frequency. As the cavity moves from blue to red, the mechanical resonance frequency decreases slightly. This is expected from the optical spring effect (Eq. (2.40)) since the blue side of the cavity induces a spring stiffening effect, whereas the red side induces a spring softening effect. The varying amplitudes in the signal are likely caused by a slightly different position on the optical cavity slope, causing a slightly improved transduction on the red side compared to the blue. As this optical cavity has a tendency towards optical bistability (see Section 5.2), the red side may be slightly steeper than the blue side and as a result the transduction is enhanced, providing larger voltage amplitudes.

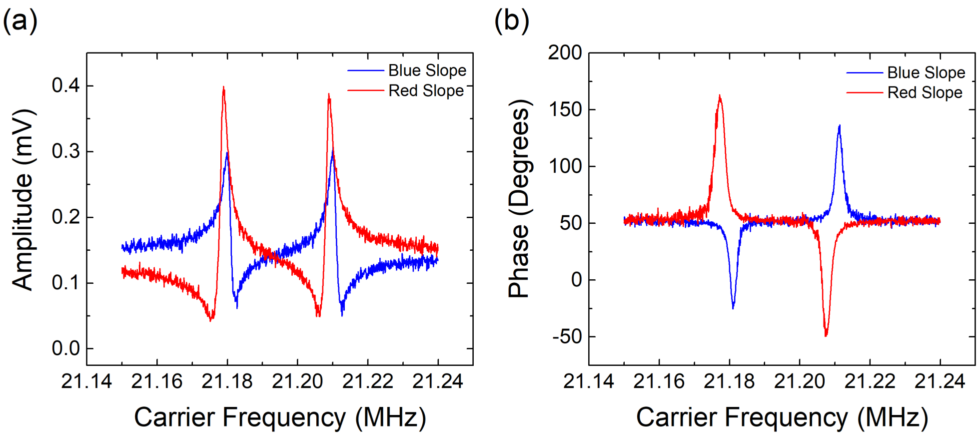

Figure 3.34: (a) Amplitude and (b) phase signals from a cantilever with measurements performed on each side of the optical cavity transmission. One measurement was performed on the red and one on the blue side of the cavity. As expected, due to the changing sign of the slope, the amplitude and phase are opposite signs for the red and blue sides. The results are plotted versus the carrier frequency signal as the readout frequency was constant at 30 kHz. The optical power in the bus waveguide was set to 94 μW.

To ensure that this technique is suitable for mass sensing applications, the final test is to lock the device using a phase lock loop (PLL). To use the low-frequency signal, we need to lock the PLL to a phase value at the frequency f_{mod}. As the resonance frequency of the device shifts due to mass loading effects, the phase signal will also shift and the PLL will track this shift. One way to demonstrate that the phase can be locked is to measure the Allan deviation. The Allan deviation provides information regarding the frequency stability of the device, and is a good indicator of whether or not the phase can be accurately locked for mass sensing experiments.

To lock the phase using our lock-in amplifier, the PLL was set to read in the phase at the frequency f_{mod}. The initial phase chosen was on the point of highest slope on the Lorentzian phase signal to maximize the sensitivity of the device. The PLL was set to drive at the carrier frequency, which was set to the mechanical resonance frequency f_0. In this way, we observe the signal at f_{mod}, but drive the device at the appropriate resonance frequency. As the frequency of the cantilever shifts, due to temperature or other external stimuli, the phase also shifts. This phase shift is read out in the low-frequency signal, and the PLL then adjusts the carrier frequency to compensate for the shift, such that the original phase setpoint is maintained, despite a shift in the mechanical frequency. This permits the low-frequency tracking of the high-frequency mechanical signal. The results of this experiment are shown in Figure 3.35(a)–(d) for four different bandwidths, 500 Hz, 100 Hz, 10 Hz, and 1 Hz, respectively. The Allan deviation decreases as the measurement bandwidth decreases. This is another benefit of locking to a low frequency signal. Smaller Allan deviations are typically better for mass sensing, as the minimum detectable mass is proportional to the Allan deviation [8]. Since a small Allan deviations can be obtained by shrinking the measurement bandwidth, it may be beneficial to use a small bandwidth during a mass sensing measurement. However, these small bandwidth measurements are harder to lock to at high frequency. With the low-frequency technique, we can easily lock using a smaller bandwidth, since the signal we are locking to is only 30 kHz.

(a) 500 Hz bandwidth (b) 100 Hz bandwidth

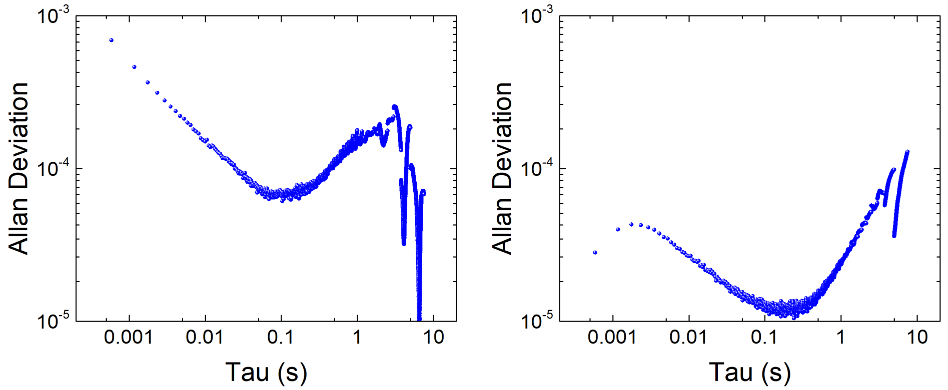

(c) 10 Hz bandwidth (d) 1 Hz bandwidth

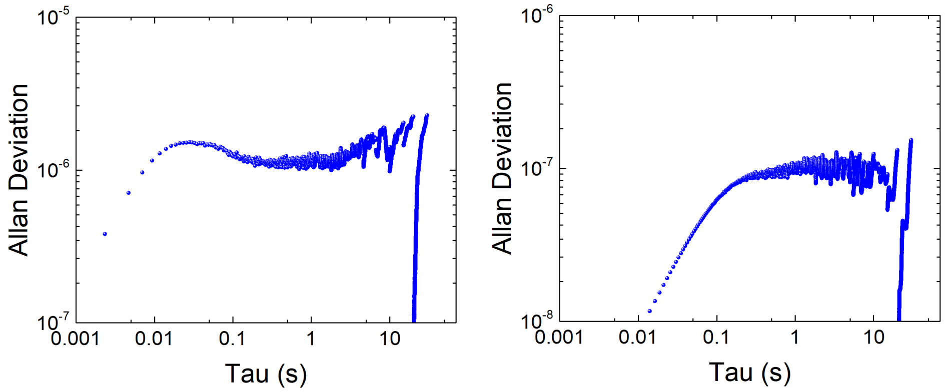

Figure 3.35: Allan deviation measurements using the low frequency single laser transduction signal at $f_{\mathrm{mod}} = 30$ kHz. These measurements were taken for four different bandwidths, (a) 500 Hz, (b) 100 Hz, (c) 10 Hz, and (d) 1 Hz.

3.4.1 Conclusion

In this section, we have examined a technique that allows us to down-mix a high-frequency mechanical signal at low frequency, in the range of 30 kHz. This technique uses a single laser for drive and detection, using the same approach as the SLMDD technique previously demonstrated in our lab. The benefits of this technique are that we can observe the signal using an inexpensive, low-frequency photodiode and that the phase locked loop can be set to a very low bandwidth for improved frequency stability. This is a simplified setup because only one laser is necessary. This simple measurement scheme could be used to more easily integrate our mass sensing device onto a small chip, since the laser and photodiode requirements are minimized.

Chapter 4

Optimization of Optical Driving Force

In Section 2.3.1, we discussed the difference between self-oscillation and optical actuation with an amplitude-modulated pump laser. In particular, we discussed that the pump and probe technique is beneficial for mass sensing because this technique can be used in conjunction with phase lock loop operation to reduce the phase noise of the system. We also mentioned that one of the advantages of the pump and probe approach was that the power could be increased to maximize the driven amplitude and therefore the dynamic range of the mass sensor. However, simply increasing the power to arbitrarily high levels is not practical for the portable mass-sensing device as described in Chapter 1. For this type of application, the overall power consumption of the system should be as low as possible. To achieve this, while still maintaining a high driven amplitude for the nanomechanical device, the actuation technique should be optimized to be as efficient as possible. Despite the fact that the pump and probe approach is often used in optomechanical systems [21, 67, 69], thorough design of optomechanical systems to optimize this actuation technique has never been studied.

To achieve maximum efficiency of the optical pump and probe actuation, we design optical cavities specifically optimized for pump-probe actuation. At first glance, an optimized design maximizes the optical power delivered to the nanomechanical device to apply the maximum driving force, which implies that excellent extinction and high quality factor are required [50]. However, there are several complications. Cantilevers are an example of a high amplitude device, and are known to have a higher mass sensitivity than doubly clamped beams due to their lower effective mass [20] and are therefore desirable for mass sensing. If the nanomechanical device has a large amplitude and optomechanical coupling coefficient G, the cavity will experience a significant shift in the detuning Δ during one period of vibration. The pump laser is therefore not at zero detuning for the entire period of oscillation, and so the maximum power is not consistently applied to the cantilever.

Additionally, silicon photonic microring resonators with good extinction and high quality factor often suffer from coherent backscattering [146], which may affect device actuation. One possible solution is to create a feedback loop to modulate the pump laser frequency so it is oscillating in phase with the mechanical device, such that the detuning is always zero. The large bandwidth required by this feedback loop makes it very difficult to implement. The bandwidth required is equal to the swing in the cavity response caused by the cantilever's large amplitude, and may be on the order of several GHz. Currently, the maximum bandwidth achieved for locking to these high finesse optical cavities is on the order of 3.5 MHz [206]. An improvement of three orders of magnitude is very challenging.

We suggest an alternative solution, wherein we design optical cavities specifically to compensate for the pump laser moving off the optical cavity resonance. In this way, the optical cavities are optimized for actuation of nanomechanical devices. In Section 4.1, we derive a simple model for designing optomechanical systems for optimal actuation using a pump-probe technique. The model accounts for optomechanical coupling, optical cavity loss rate, and the coupling loss rate and is applicable to any optomechanical system where the mechanical device behaves as a driven damped harmonic oscillator. For the specific example of a simple cantilever coupled to an optical racetrack resonator, we solve our numerical model for a wide range of input parameters to illustrate how the model can be used to determine the optimal cavity design. In Section 4.2, we discuss the fabrication and show experimental results from several different devices. We verify the model by comparing it to experimental results. Our experimental results also show that coherent backscattering affects only the actuation of the devices using an optical pump, while readout of the devices is unaffected. We verify experimentally a modification to the model to account for a pump optical cavity with coherent backscattering.

4.1 Theory

The peak amplitude of the AC optical force should be maximized to maximize the optical drive. Eq. (2.41) is a function of the detuning, which is in turn dependent on the position x of the mechanical resonator [157]. The pump laser is initially set at a detuning $\Delta = 0$, to maximize the optical power input to the cantilever and to ensure that the device is actuated solely through the amplitude modulated optical gradient force and not through self-oscillation. However, the pump laser is not constantly positioned at the optical resonance at all points in the mechanical measurement, since the cavity shifts as the mechanical device vibrates [158]. Consider, for example, the extreme case where the amplitude of the mechanical resonator is very large and the cavity linewidth is very small. In this example, the pump laser is rarely positioned on the optical resonance and may even be located outside of the optical resonance. Clearly, this will not produce efficient actuation as the power delivered to the cantilever is significantly reduced. The interaction of the mechanical device and the optical cavity must be optimized for efficient actuation to produce the largest amplitude mechanical displacement. With this large displacement we can make use of the full dynamic range of the cantilever, which is desirable for mass sensing.

To describe how much the optical cavity shifts for a given peak mechanical displacement, we approximate the detuning as a function of position such that $\Delta(x) = G_0 x$, where G_0 is the initial optomechanical coupling and x is the mechanical displacement. This relationship is obtained from the definition of the optomechanical coupling coefficient $G = \partial\omega/\partial x$. We define the Taylor series expansion of the optical frequency $\omega(x)$ about a mechanical displacement x_0 as

$$\omega(x) = \omega(x_0) + \omega'(x_0)(x - x_0) + \frac{\omega''(x_0)(x - x_0)^2}{2} + ... \tag{4.1}$$

We can define an approximation for $G(x_0)$ by rearranging Eq. (4.1) and solving for $\omega'(x_0)$. For the particular situation of driving with the optical gradient force using an amplitude modulation, the initial pump laser wavelength is set to $\Delta = 0$. Therefore, $\omega(x_0) = \omega_0$, where ω_0 is the resonance wavelength of the optical cavity. We can also define the initial mechanical displacement $x_0 = 0$. This is because the optical AC amplitude modulation will result in positive and negative deflections about the initial mechanical position. We therefore define the mechanical deflection as x, as referenced to the initial mechanical displacement. Combining all of these definitions and rearranging Eq. (4.1) results in the following equation for the variation in $\partial\omega/\partial x$ about the initial detuning $\Delta = 0$:

$$\omega'(0) = \frac{\omega(x) - \omega(0)}{x} - \frac{1}{x}\left(\frac{\omega''(0)x^2}{2} + ...\right). \tag{4.2}$$

Finally, we recall that the detuning is defined as $\Delta = \omega(x) - \omega_0 = \omega(x) - \omega(0)$. We use the definition of the optomechanical coupling $G = \partial\omega/\partial x$ to determine that the expansion for the optomechanical coupling about zero deflection $G(x_0) = G_0$ is

$$G_0 = \frac{\Delta(x)}{x} - \left(\frac{G_0' x}{2} + ...\right). \tag{4.3}$$

To first order, we can say that $\Delta = G_0 x$. The higher order terms in this expression represent the error in the approximation.

To derive a model to optimize the cavity performance for efficient actuation, we set Eq. (2.41), the equation for the optical gradient force, equal to $F(x) = -kx/Q$. This is the simple equation for the vibration amplitude on resonance of a driven damped harmonic oscillator, where k is the cantilever's effective spring constant. Re-writing this equality and moving all terms to one side gives

$$G_0^2 x^3 + \gamma^2 x - \frac{2 P_{\mathrm{bus}} V_{\mathrm{drive}} G_0 \gamma_{\mathrm{ex}} Q}{k \omega V_\pi} = 0, \tag{4.4}$$

which is a cubic polynomial in x and straightforward to solve numerically. Two imaginary solutions and one real solution are produced by the numerical solver. We use the real solution for our analysis. The model shown in Eq. (4.4) accounts for the fact that increasing mechanical amplitude reduces drive force efficiency. It produces an estimate of the maximum drive amplitude that can be achieved for a given set of experimental parameters, and can be used to optimize the optomechanical system to achieve the maximum amplitude of vibration. This simple model can be used for any dispersive optomechanical system where the mechanical device can be approximated by a driven damped harmonic oscillator.

To demonstrate the numerical model as a design tool for optimizing optomechanical systems for efficient actuation, we input experimentally relevant mechanical and optical parameters and solve Eq. (4.4). For this demonstration we use a cantilever with length = 3 μm, width = 130 nm, and thickness = 220 nm. It has $k = 0.8$ N/m and $Q = 10,000$. The cantilever is side-coupled to a racetrack resonator [69] with a radius of 5 μm and a 3 μm straight section. P_{bus} is 260 μW, a typical experimental value. The EOM has a $V_\pi = 1.5$ V. The intrinsic loss rate γ_0 is fixed at 16.4 rad GHz. This is an average value measured from several nominally identical optical cavities from the same foundry. If the racetrack has a sufficiently large radius, γ_0 is set only by the material loss and scattering loss in the waveguide as the bending loss is negligible in high contrast waveguides, such as those fabricated in SOI. Therefore, the intrinsic loss rate will remain relatively constant for the same racetrack dimensions if the same fabrication process is used. The coupling loss from the bus waveguide into the racetrack resonator, γ_{ex}, is used to tune the cavity linewidth γ, since $\gamma = \gamma_0 + \gamma_{\mathrm{ex}}$. The optomechanical coupling is adjusted by varying the distance between the cantilever and the racetrack resonator. We solve Eq. (4.4) for a wide range of optomechanical coupling and cavity linewidth values and for the mechanical parameters stated above to obtain a map of the possible cantilever amplitudes, which we will denote as the design amplitudes, created by these specific conditions.

We solve Eq. (4.4) for three different driving voltages, $V_{\mathrm{drive}} = 200$ mV, 500 mV, and 700 mV. Although we increase the driving voltage here, the same effect is achieved if P_{bus}, Q, or $1/k$ is increased. To increase Q or $1/k$, the initial mechanical design must be altered. During the experiment, V_{drive} or P_{bus} can be easily increased. Increasing V_{drive} is preferable as increasing P_{bus} is more likely to introduce optical nonlinearities that occur at higher DC input power. The results of solving Eq. (4.4) for the three voltage conditions are shown in Figure 4.1. The figure shows the range of optomechanical couplings and cavity linewidths where the maximum amplitude can be achieved. As the optomechanical coupling increases, the range of optimal cavity linewidths also increases. In a system with large optomechanical coupling, it is acceptable to have a so-called “bad” cavity and still achieve maximum mechanical amplitude. For higher optomechanical coupling, the cavity shifts more for a given amplitude of vibration. The pump laser will spend correspondingly less time near the bottom of the cavity where the power injected into the cavity is the greatest. This means less optical force is applied to the mechanical device as the average power enhancement is reduced off-resonance. However, if the cavity has a wider linewidth, the power decrease as the cavity moves off-resonance is reduced. For this reason, a wider cavity linewidth is beneficial for large optomechanical coupling. “Bad” cavities also become more optimal as the driving voltage increases. The envelope where the maximum amplitude is achieved grows larger as the driving voltage increases, including wider cavities for all optomechanical coupling values.

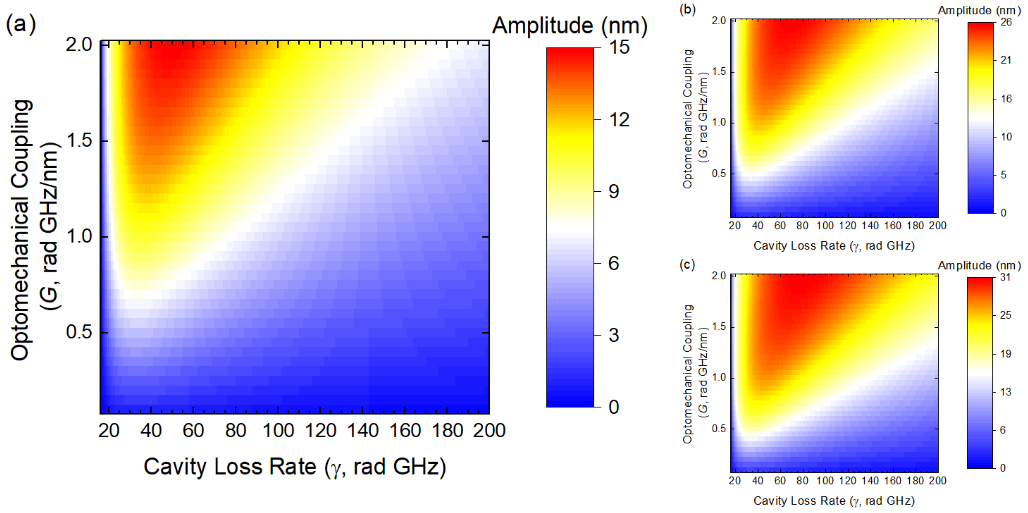

Figure 4.1: Optimization of the driven amplitude of a cantilever for a range of optical cavity linewidth and optomechanical coupling values. There is an envelope of maximum amplitude for a range of both optomechanical coupling and cavity linewidth. This envelope becomes larger as the driving voltage is increased from (a) 200 mV to (b) 500 mV to (c) 700 mV.

To check that this model’s validity at large amplitudes, we use the same parameters to calculate the error term from Eq. (4.3). For the largest amplitude calculated in Figure 4.1(c), the error in Eq. (4.3) is 17.7%. For the largest amplitude given in Figure 4.1(a), the error is 12.6%. We can therefore conclude that the error in the model increases with increasing amplitude. This result indicates that for amplitudes less than approximately 15 nm, the model derived in Eq. (4.4) will be an accurate estimate of the amplitude as the error will be less than 12.6%. For amplitudes greater than 15 nm, the exact amplitude produced by Eq. (4.4) may not compare as accurately to experimental data. However, the trends predicted by Eq. (4.4) will still hold true; therefore, we can still use this model as a general guideline to design optomechanical systems for efficient actuation at high amplitudes.

Our simple model shows the effects of the optical cavity linewidth, the optomechanical coupling, and the driving power on the peak amplitude of the nanomechanical resonator. In the next section, we demonstrate the design of an optomechanical system for efficient actuation using this model. We show the amplitude of the optomechanical system can be approximated by Eq. (4.4).

4.2 Experimental Validation

4.2.1 Device Parameters

To experimentally validate our model, we design and measure several cantilevers coupled to optical racetrack cavities with the same dimensions described in Section 4.1. Two optomechanical couplings were included to verify the effect of the optomechanical coupling on the amplitude. To create the two different optomechanical couplings, gaps between the racetrack resonator and the cantilever of 90 nm and 145 nm were fabricated. The optomechanical coupling should be made as high as possible to achieve the highest amplitude (Figure 4.1). 90 nm is the smallest gap we could fabricate given the practical restrictions of photolithography. We can simulate the optomechanical coupling using commercial eigenmode solver software [171]. We calculated the change in the effective index for a change in the gap spacing between the racetrack and the cantilever, $\partial n_{\text{neff}}/\partial x$. The optomechanical coupling is then calculated using Eq. (2.43) [69]. For a 90 nm gap, simulations showed the optomechanical coupling is expected to be 1.14 rad GHz/nm. This is smaller than ideal to achieve the highest amplitude from Figure 4.1(a) for a 200 mV drive voltage, but is in the ideal range for the higher driving voltages in Figure 4.1(b) and (c). The wide gap of 145 nm had a simulated optomechanical coupling of 0.32 rad GHz/nm, far from the optimal value.

To achieve the desired γ and obtain a cavity optimized for efficient actuation, the coupling gap between the bus waveguide and the racetrack resonator was adjusted. As previously mentioned, the intrinsic cavity loss is known to be approximately $\gamma_0 \approx$ 16.4 rad GHz. By using the directional coupler design principles from Section 2.2.4, we designed the coupling loss to be approximately equal to 10–20 rad GHz by choosing a coupling gap of 250 nm. When combined with the intrinsic cavity loss, this results in a cavity linewidth in the range of 25–35 rad GHz. This linewidth and optomechanical coupling places our device close to the maximum amplitude envelope for the low actuation voltage of 200 mV. For the 500 mV and 700 mV cases, the predicted amplitude is within the maximum amplitude envelope (Figure 4.1(b) and (c)). To obtain optical cavities with larger linewidths for comparison, we overcoupled several cavities by fabricating racetrack resonators with smaller coupling gaps, down to 130 nm. The overcoupled cavities are expected to have cavity linewidths up to 100 rad GHz, which means the amplitude will be very far from the optimal values shown in Figure 4.1.

The optomechanical systems were fabricated on SOI substrates at the silicon photonics foundry imec via CMC Microsystems. A timed maskless buffered oxide etch was completed to release the cantilever from the sacrificial oxide layer. All of the measurements were performed using the confocal microscope setup described in Section 2.4.

4.2.2 Effects of Coherent Backscattering

Five optical cavities with different coupling conditions were characterized by sweeping the probe laser through the appropriate wavelength range while the voltage was measured from the photodiode. Figure 4.2 is the response from one optical cavity, and shows two optical cavity resonances. Figure 4.2(a) is an example of peak splitting caused by coherent backscattering. We perform a fit of the transmission in Figure 4.2(a) using Eq. (2.36) to obtain the coupling parameters of our system. This fit directly produces τ and a_{rt}. These parameters can be related to the optomechanically relevant parameters γ_{ex} and γ_0 using Eqs. (2.28) and (2.30).

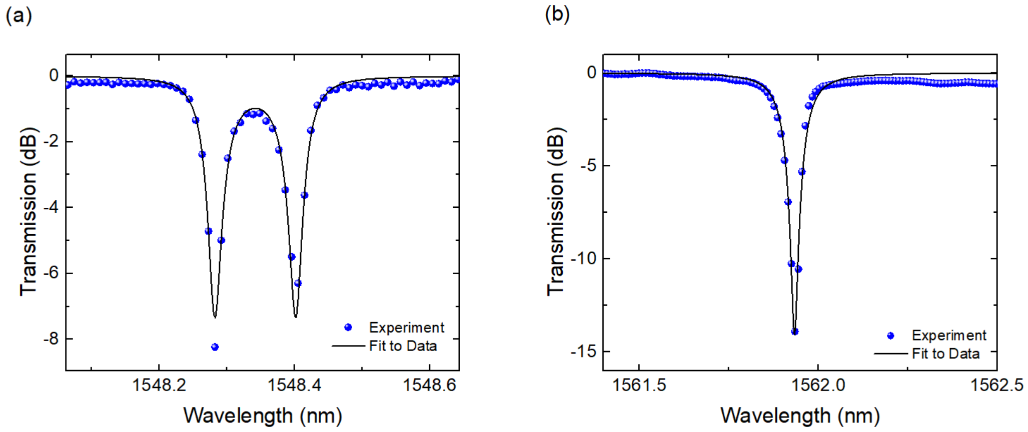

Figure 4.2: Optical response of one racetrack resonator. The resonance shown in (a) is used as the probe cavity, and suffers from coherent backscattering. The resonance shown in (b) is used as the pump cavity, and is not backscattered.

To experimentally determine the optomechanical coupling, we measured the thermomechanical noise of the cantilever across the entire cavity detuning. This result is shown in Figure 4.3(a). For this measurement, zero detuning is set to the highest point between the two resonance dips in Figure 4.2(a). Only the probe laser is activated. The optical spring effect causes the shift in mechanical resonance frequency when the probe wavelength changes from red to blue cavity detuning [162].

As described in Section 2.3, the optical spring effect can be used to directly measure G. The resonance frequency shift is extracted from each mechanical sweep in Figure 4.3(a) and plotted versus the detuning. This result is shown in Figure 4.3(b).

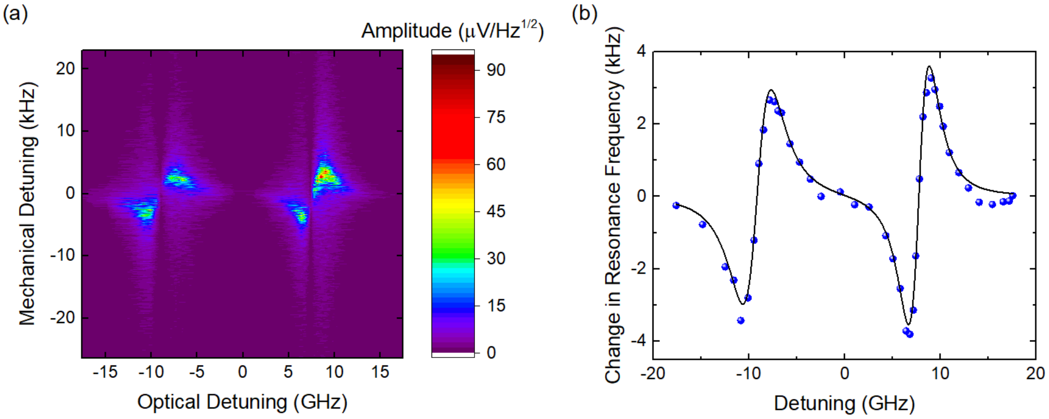

Figure 4.3: (a) Sweep of the thermomechanical noise along the full range of cavity detuning. The input power to the cavity was 77 μW. (b) Change in mechanical resonance frequency as a function of detuning caused by the optical spring effect. The circles are measured data and the black line is the fit with Eq. (4.5).

To fit this curve and extract the optomechanical coupling, we modify Eq. (2.40) to account for the split cavity. We regard the single split cavity as two uncoupled cavities, and add the optical spring equation for each cavity together. Lastly, we include an offset to account for the detuning of each cavity from zero. This is shown by Eq. (4.5), where δ is the offset of each individual resonance dip from zero detuning. The subscripts 1 and 2 indicate the red and blue detuned optical cavity resonances, respectively:

$$\delta\Omega_0 = \frac{4P_{\text{bus}}}{\hbar\omega}\left\{\frac{g_{0,1}^2\gamma_{\text{ex},1}(\Delta-\delta_1)}{[(\Delta-\delta_1)^2+\gamma_1^2]^2}+\frac{g_{0,2}^2\gamma_{\text{ex},2}(\Delta-\delta_2)}{[(\Delta-\delta_2)^2+\gamma_2^2]^2}\right\}. \tag{4.5}$$

We use Eq. (4.5) to fit the data in Figure 4.3(b) and extract the single-photon optomechanical coupling parameter for both the red and blue detuned cavities. We will use the blue-detuned cavity in the pump-and-probe experiments, and so we require $g_{0,2}$. From the fit, $g_{0,2} = 89.7$ rad kHz. We divide $g_{0,2}$ by x_{ZPF} to produce $G = 0.99 \pm 0.03$ rad GHz/nm. This is in good agreement with the simulated optomechanical coupling, demonstrating an optical resonance split by coherent backscattering is suitable for probing an optomechanical system, and that the standard optomechanical equations can be used with minimal modification in a backscattered system.

Since Figure 4.3 shows that the split optical resonance is suitable for probing the nanomechanical device, we can choose one side of the split cavity resonance as the probe laser position for our driven measurements. For driven measurements, the probe is set to the blue slope of one optical cavity, and the pump laser is set to the transmission minimum of the optical cavity resonance of another optical cavity (Figure 4.2(b)). Setting the laser to the optical cavity minimum ensures maximum force is delivered to the nanomechanical cantilever since the power enhancement is maximized on resonance, as shown by Eq. (2.26).

If the optical resonance used for pumping is backscattered, the power enhancement is more complex. Figure 4.4(a) shows the response of another racetrack resonator that suffers from coherent backscattering (top plot). This resonance is used as the pump cavity to actuate a second cantilever. Recall that the power enhancement for a backscattered cavity is dependent on the reflector position θ, as described by Eq. (2.37). The bottom plot in Figure 4.4(a) shows the power enhancement of the same cavity as a function of wavelength and θ. Clearly, the power enhancement varies significantly depending on the location of the reflector element. We plot the power enhancement at the pump laser position as a function of reflector position, shown by the dashed line in Figure 4.4(a) and the sinusoidal function in Figure 4.4(b). The lumped element model implies a single reflection at a single location. Experimentally, however, the scattering occurs at several locations within the racetrack. The power enhancement is the average value, shown by the blue line, of the sinusoid in Figure 4.4(b). This was experimentally verified in Section 3.2.

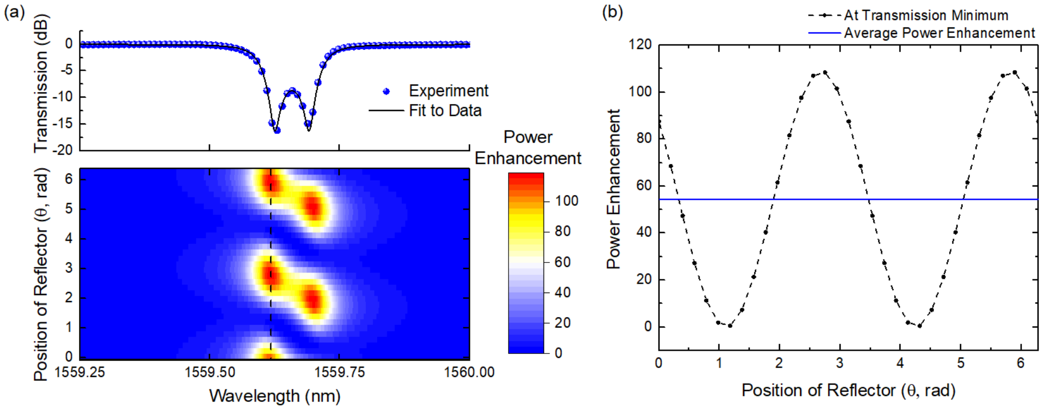

Figure 4.4: (a) Experimental measurement of a backscattered racetrack resonator cavity is shown in the top plot. The corresponding power enhancement is shown in the bottom plot. The power enhancement is plotted versus the wavelength and the reflector position θ. The dashed line indicates the pump laser position. (b) The black dashed line shows the power enhancement at the pump laser position, plotted versus the reflector position. The overall power enhancement for the device at the cavity minima is shown by the solid blue line, which is the average value of the sinusoid.

To account for backscattering in the optical cavity design model, the amplitude calculated via Eq. (4.4) is multiplied by the ratio of the average power enhancement of the backscattered cavity to the power enhancement of the same optical cavity with no backscattering. The subscript b is used to indicate a backscattered cavity:

$$x_{\mathrm{b}} = x\frac{PE_{\mathrm{b}}}{PE}. \tag{4.6}$$

The total force provided to the nanomechanical device is proportional to the power enhancement. The amplitude is directly proportional to the force since $F = kx/Q$. Eq. (4.6) shows that if the pump laser is positioned in a backscattered cavity, the amplitude of the cantilever will be reduced compared to an optical cavity that does not suffer from coherent backscattering. We conclude this discussion on coherent backscattering by emphasizing that a backscattered cavity may be used as the probe cavity with no additional modeling of optomechanical system. However, using an optical cavity resonance that suffers from coherent backscattering to drive a nanomechanical device reduces the driven amplitude and requires additional modeling. Since coherent backscattering is present in many photonic systems, it is important to understand its effects. Backscattering has been examined in both membrane-in-the-middle systems [207] and sideband-resolved regimes [208]. In both cases, including the effects of backscattering was necessary to accurately model the optomechanical systems.

4.2.3 Amplitude Calibration

To compare the results of the derived model to experiment for both backscattered and non-backscattered cavities, six measurements were taken of five different mechanical devices. To obtain the sixth measurement, we switched the position of the pump and probe lasers for one cantilever. The probe laser power in the bus waveguide was 108 μW. The DC pump laser power in the bus waveguide was initially set to 260 μW, then reduced to 100 μW for the remaining measurements after the observation of a readout nonlinearity. The applied AC voltage was 200 mV. The pump laser detuning was set to zero to ensure that the optical drive provided by the pump laser was solely through the amplitude modulation of the optical gradient force, and not by self-oscillation. The probe laser detuning was set to the maximum slope on the blue side of the optical cavity. The pump laser was filtered out before the photodiode by a narrow bandpass filter centered at the probe wavelength. The amplitude of the cantilevers was recorded in volts, then converted to watts using the conversion factor of the photodiode. For measurements that appeared to have linear readout, the amplitude was converted to metres using two techniques. The standard thermomechanical noise calibration, as described in Section 2.1.1, was performed. We also calibrated the data using the transduction coefficient $\mathrm{d}T/\mathrm{d}x$ in units of W/m, which was defined previously in Eq. (2.42). The amplitudes in watts are divided through by the transduction coefficient to give an amplitude in metres. These approaches provide experimental results to compare to the model, and to determine whether we have successfully optimized the optical cavities for efficient actuation.

The expected amplitude for the device designed for optimal actuation is greater than 10 nm for 260 μW of DC input power. Due to this high amplitude, we observed nonlinearities in the readout of the mechanical amplitude. These nonlinearities are due to the Lorentzian lineshape of the optical cavity and will be discussed in detail in Chapter 5. The outcome of the readout nonlinearity is that we cannot use the thermomechanical noise calibration or the transduction coefficient to determine the amplitude of the cantilever in metres. We confirm that a readout nonlinearity exists by observation of harmonics in the mechanical frequency spectrum [163] when the optical resonance shown in Figure 4.2(a) is used as the probe cavity and the resonance shown in Figure 4.2(b) was used as the pump laser cavity. For these measurements, zero detuning is redefined to the optical resonance of the blue side of the split cavity. To explore this result further, the pump laser was set at the optical resonance of Figure 4.2(b) and held fixed while the probe laser was swept across the blue half of the split cavity. At each wavelength, the mechanical response was measured at the fundamental resonance frequency (Figure 4.5(a)), as well as the second ($2f$), third ($3f$), and fourth ($4f$) harmonics (Figure 4.5(d)–(f), respectively).

In addition to the harmonics, a distortion in the peak shape as the probe laser detuning approaches zero is visible in Figure 4.5(a)–(c). This distortion, or dip, is caused by the probe laser crossing through the bottom of the optical resonance and moving from the blue side of the cavity to the red side during one mechanical period of vibration [165]. Since the cavity shift is related to the mechanical amplitude via the optomechanical coupling G, the location of the dip in the mechanical response allows for experimental estimation of the cantilever's amplitude. We note the detuning before a dip is observed and the detuning after a dip is observed, which correspond to the range of detunings where the cantilever starts to cross over the bottom of the optical resonance. The dip is first observed at $\Delta = 2\pi \times 1.88$ GHz. The optomechanical coupling is equal to 0.99 rad GHz/nm, and so this detuning corresponds to an amplitude of 11.95 nm, meaning the amplitude is equal to or greater than 11.95 nm. The last detuning before the dip is observed is $\Delta = 2\pi \times 2.00$ GHz, which gives an amplitude of 12.75 nm. The average value of these amplitudes is 12.3 ± 0.4 nm, thus providing an experimental estimate of the amplitude despite the readout nonlinearity.

We also experimentally confirm that the amplitude is generated by the optical force induced by the pump laser, and not by self-oscillation induced by the probe laser using the same high-amplitude device. For this test, the pump laser was deactivated and the probe laser was positioned at the point of maximum slope on the blue side of the optical cavity. To account for heating in the optical cavity introduced

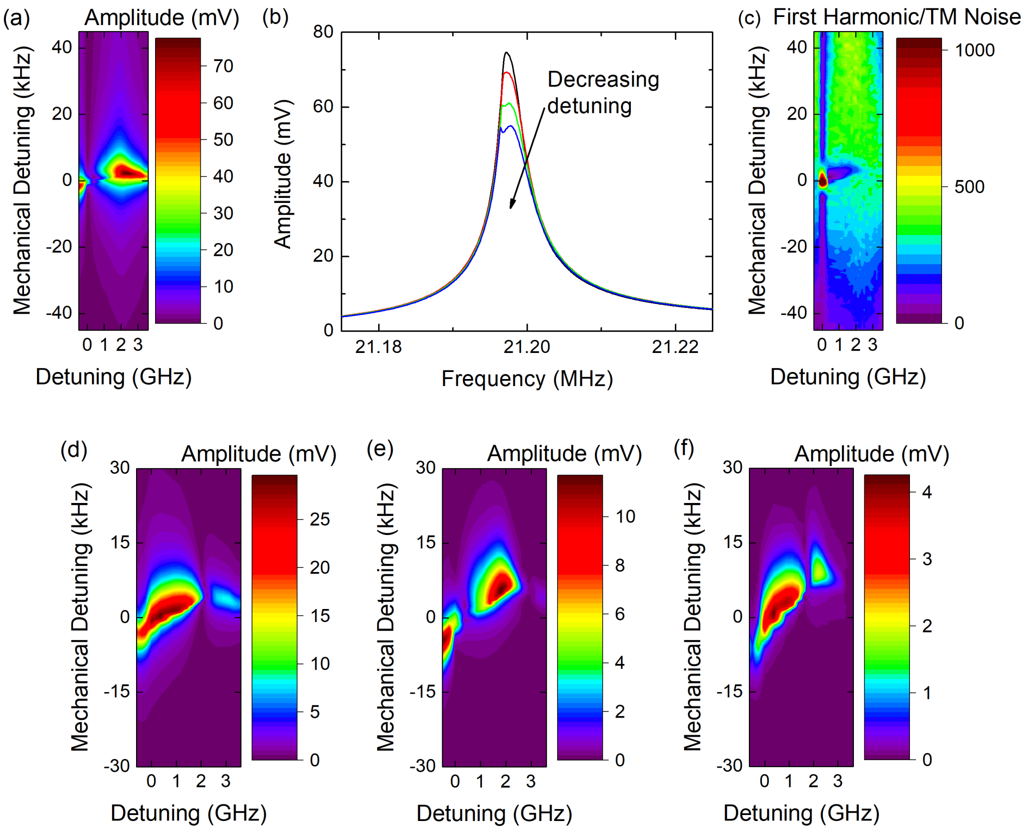

Figure 4.5: The mechanical response as the probe laser is swept through the cavity detuning, with the pump laser held at a constant wavelength and DC power with a 200 mV amplitude modulation applied at the EOM. The probe laser power in the bus waveguide is 108 μW and the pump laser power in the bus waveguide is 260 μW. The responses are shown as contour maps. The fundamental resonance frequency is shown in (a). Visible in these contour maps are dips in the response as the detuning is decreased. These dips are shown in more detail in (b) and (c) and are the result of the probe laser crossing the minimum of the optical resonance. (b) shows the specific mechanical sweeps before and after the appearance of the dips as the probe detuning is decreased. (c) shows the contour map in (a) divided by the thermomechanical noise. The dips are present in this figure as the horizontal purple line near zero mechanical detuning. Contour maps for (d) the second harmonic, (e) the third harmonic, and (f) the fourth harmonic are also shown.

by increased laser power, and the thermo-optic induced shift of the optical resonance, the position of the probe laser was verified and shifted for each measurement to ensure that the probe laser was positioned at the point of maximum slope. The power in the probe laser was initially set to 77 μW and increased to 293 μW. The results for this test are shown in Figure 4.6. The square root of the power spectral density $S_{\mathrm{v}}^{1/2}$ is shown versus the mechanical frequency for increasing optical power in Figure 4.6(a). The quality factor of the mechanical measurement versus the optical power is shown in Figure 4.6(b).

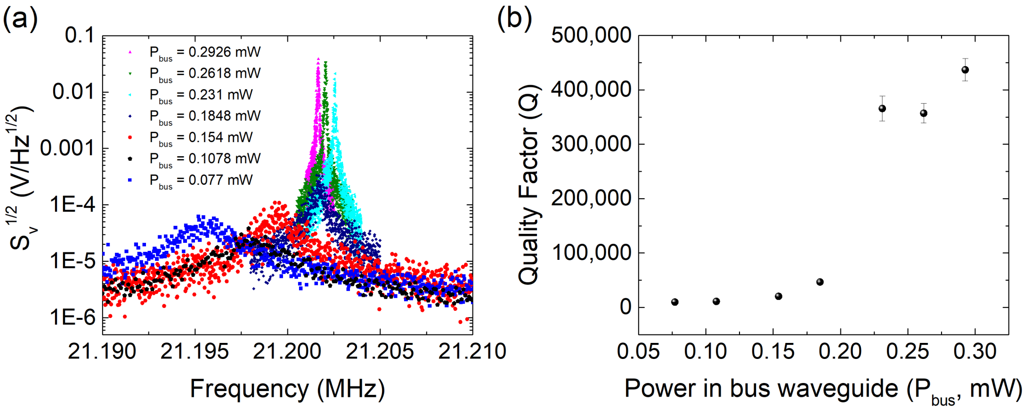

Figure 4.6: Characterization of the self-oscillation behaviour of the optomechanical system. The input power is increased from 77 μW to almost 300 μW with the probe laser set to the point of maximum slope on the blue side of the optical cavity. The power spectral density was recorded at each input power. The square root of the power spectral density $S_{\mathrm{v}}^{1/2}$ is recorded at each optical power and plotted in (a). The mechanical quality factor from each measurement is extracted from a curve fit to the data in (b). From both (a) and (b), we can determine that the threshold for self-oscillation is above 200 μW, because there is a sudden and substantial increase in both $S_{\mathrm{v}}^{1/2}$ and the quality factor above this input power. Below this threshold, the device has not entered self-oscillation. The probe input power must be kept below this threshold to ensure that all measurements are not affected by the presence of self-oscillation.

When the optical power is below 200 μW, the quality factor of the mechanical resonance slowly increases for increasing power and the peak height of $S_{\mathrm{v}}^{1/2}$ also slowly increases but is less than 4×10^{-4} V/Hz$^{1/2}$. The slight increase in quality factor and peak height is expected, since the optical damping is proportional to the input optical power. Above 200 μW, the peak height and quality factor abruptly increase to 2×10^{-2} V/Hz$^{1/2}$ and 366,000 respectively. This sudden and significant increase in both the amplitude and quality factor indicates that the threshold for self-oscillation has been surpassed, and that the optical power of the blue-detuned probe laser is now driving the mechanical device into self-oscillation. This occurs for optical powers greater than 200 μW. We can therefore conclude that self-oscillation is not a contributing factor to our previous measurements, and that the optical gradient force is the cause of the device actuation, since the probe power in our previous measurements was set to 108 μW. This value is well below the threshold optical power required for self-oscillation, as demonstrated by Figure 4.6. We can also use the quality factors observed in Figure 4.6(b) to confirm in our future measurements whether we have surpassed the threshold for self-oscillation. If the quality factor remains in the range of 10,000 to 50,000, as observed for the optical powers below 200 μW, we can confirm that self-oscillation is not the dominant actuation mechanism.

4.2.4 Comparison of Experimental Amplitudes to Theoretical Model

The experimentally measured and calibrated amplitudes are shown in Figure 4.7, where (a) shows the data for devices with higher optomechanical coupling, and (b) shows the data for devices with lower optomechanical coupling. The result calibrated using the dip in the mechanical spectrum is the largest observed amplitude. The other five measurements were calibrated using both the thermomechanical noise and the transduction coefficient. The amplitudes calibrated by using the thermomechanical noise are shown by the squares. The error bars are smaller than the symbol size for all thermomechanically calibrated amplitudes, and the error is obtained from the curve fit of Eq. (2.8) to the thermomechanical noise. The amplitudes calibrated by the transduction coefficient are shown by black stars. Vertical error bars account for errors in determining the optomechanical coupling and the cavity slope. The error bars are large because the optomechanical coupling was directly measured only for one device, shown in Figure 4.3. From that measurement, the optomechanical coupling for the remaining devices was calculated based on the exponential relationship between the optomechanical coupling and the gap between the device and waveguide using Eq. (2.43). The gaps were measured directly from scanning electron microscope images. Horizontal error bars account for errors in determining the cavity linewidth from curve fits to the measured optical cavity transmission. The solid lines are theoretical amplitudes calculated using Eq. (4.4). These amplitudes are obtained by inputting the experimentally measured values for each device, such as the cantilever lengths, resonance frequencies, mechanical quality factors, calculated optomechanical couplings, and cavity linewidths. These calculations also account for the different DC optical pump power used in each measurement. Recall that during the experiment, the power was reduced to eliminate readout nonlinearities. Therefore, this change in power must be accounted for in each measurement.

First, we compare the design and experiment for the case where the optomechanical coupling is high, approximately equal to 1 rad GHz/nm. The device with a low cavity linewidth, on the order of 25 rad GHz, has an optimized design. As a result,

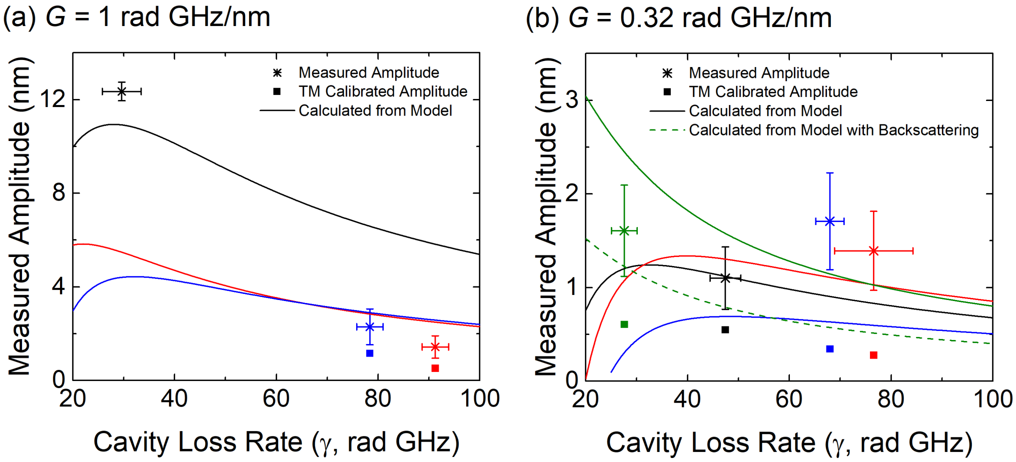

Figure 4.7: Comparison of the experimental amplitude to the amplitudes calculated with the theoretical model. The stars are the experimental amplitude calibrated using the transduction coefficient. The squares are the experimental amplitude calibrated using the thermomechanical noise. The solid lines are the theoretical amplitudes calculated using Eq. (4.4) that account for the experimentally measured properties of the optomechanical system and the pump power in the bus waveguide. The results for each device are grouped by colour; for example, the measured amplitude, TM calibrated amplitude, and theoretically calculated amplitudes for the same device are all shown by the same colour. (a) shows the results for high optomechanical coupling, close to 1 rad GHz/nm. (b) shows the results for low optomechanical coupling, approximately 0.32 rad GHz/nm. (b) also includes one device where the pump was placed on a backscattered peak. The green dashed line shows the theoretical amplitude after the model has been corrected with Eq. (4.6). The probe laser power in all cases was 108 μW.

the amplitude is very large and reaches 12.3 ± 0.4 nm. This result demonstrates successful optical cavity design using Eq. (4.4) to achieve a high output amplitude. The drawback is that this cantilever suffers from readout nonlinearities due to the high amplitude. Another important result is that Eq. (4.4) is accurate despite the presence of coherent backscattering in the probe optical cavity. The other two devices, driven with low DC input power, have large γ, and therefore the amplitudes are lower than ideal. The experimentally measured amplitudes, calibrated using both the thermomechanical noise and the transduction coefficient, are below the predicted amplitude. The result from the thermomechanical noise calibration is also smaller than the transduction coefficient calibration.

The results for devices with low optomechanical coupling are shown in Figure 4.7(b). The experimental results calibrated with the thermomechanical noise are lower than the experimental amplitudes calibrated with the transduction coefficient. The experimental values calibrated with the transduction coefficient are close to within error of the values calculated using Eq. (4.4) with the exception of the narrowest cavity linewidth. For the narrowest linewidth, the predicted amplitude is approximately a factor of 1.5 greater than the measured amplitude. For this device, the pump laser was placed on the backscattered cavity shown in Figure 4.4(a). Therefore, the power enhancement in the optical cavity is reduced, providing less driving force to the cantilever. We apply Eq. (4.6) to the original calculation of Eq. (4.4) to account for the reduction in power enhancement. This correction produces the green dashed line seen in Figure 4.7(b). This updated theoretical value is within error of the measured value. To correctly estimate the amplitude, the power enhancement reduction when the pump is placed in a backscattered cavity is important to include in the model.

For both the high and low optomechanical coupling coefficients, the amplitude calibrated with the thermomechanical noise is smaller than the amplitude calibrated with the transduction coefficient. There are some potential causes for this. For some devices, the mechanical resonance had a slight background signal when the AC modulation was activated, which may affect the calibration. Some devices also had a slightly higher noise floor at $2f$, although no clear signals were observed. It is possible that this is an indicator of a slight readout nonlinearity. As we will discuss in Chapter 5, a readout nonlinearity would significantly impact the accuracy of the thermomechanical noise calibration as the energy of the mechanical signal may become spread out over several higher order harmonics instead of remaining localized in the signal at the fundamental mechanical resonance frequency. The calibration using the transduction coefficient would be affected to a lesser extent, since that calibration depends mainly on the properties of the optical cavity. However, this calibration is also somewhat suspect for large amplitudes, since the slope of the optical cavity and the term $\partial n_{\text{eff}}/\partial x$ are only linear for small deflections x. Clearly, precise determination of the mechanical amplitude, especially when large amplitudes are achieved, is not a straightforward issue. The model we have presented in Eq. (4.4) provides yet another avenue to estimate the amplitude. Corroborating the model with the data presented in Figure 4.7, we can conclude that the transduction coefficient may be a better estimate of the amplitude than calibration with the thermomechanical noise at large amplitudes of vibration.

Regardless of the method of amplitude calibration, we can see from examination of Figure 4.7 that the model presented in Eq. (4.4) provides an excellent path forward for the design of optomechanical systems for efficient actuation. In comparing Figure 4.7(a) and (b), we clearly see that higher optomechanical coupling is beneficial for increasing the amplitude of vibration, as the unoptimized designs with high optomechanical coupling had amplitudes comparable to the best designs with low optomechanical coupling. This trend was predicted by Eq (4.4) and demonstrated in Figure 4.1. We also see that there is an optimal range for the cavity loss rate, which leads to an improved amplitude of vibration. This trend was also suggested by the model we derived. The amplitude decreases quickly if the cavity loss rate is too low, and more slowly if the cavity loss rate is higher than optimal. It is therefore not beneficial for the cavity loss rate to be too low, and so slightly lower Q optical cavities are more desirable for this application.

Finally, we would like to quantify the improvement that the optimized optomechanical system designed using this model provides over an unoptimized design. To accomplish this, we can compute the amount of optical power used experimentally to achieve the peak amplitude shown by the black star in Figure 4.7(a). The AC optical power in the bus waveguide required to actuate this device to 12.3 nm was 34 μW. We can use Eq.(4.4) to calculate the equivalent amount of power required to achieve the same amplitude for the unoptimized cavity shown by the red star in Figure 4.7(b). This device is does not have an optimized optomechanical coupling or cavity linewidth. To achieve the same amplitude with this device, an AC optical power of 133 μW would be required. This is a 3.85 times increase in the AC optical power. This calculation demonstrates that an optimized optomechanical system designed using Eq. (4.4) is approximately four times more efficient than an unoptimized design. Therefore, our model successfully reduces the power requirements for an optomechanical mass sensor.

4.3 Conclusion

We have derived and tested a simple model to design optomechanical systems for efficient optical actuation via the optical gradient force. Efficient actuation is important in sensor applications to reach the maximum dynamic range of the optomechanical system, while keeping overall power consumption as small as possible. By comparing experimental results to the theoretical model, we use the model to successfully design optomechanical systems that have high amplitudes of vibration. We demonstrate that a driven amplitude of 12 nm is achieved by optimizing the optomechanical coupling and the optical cavity linewidth. To achieve the same amplitude with an unoptimized cavity, the AC optical power must be increased by approximately four times.

We have also explored the effect of coherent backscattering on optomechanical systems. If the probe cavity is backscattered, the split optical cavity behaves as two independent cavities and no further modeling is needed. If the pump cavity is backscattered, additional modeling is required to account for coherent backscattering. Backscattering reduces the amount of driving force delivered to the cantilever as the power enhancement is reduced. To avoid the reduction in efficiency caused by coherent backscattering, the pump laser should be positioned at a non-backscattered optical resonance.

Our simple model predicts that higher optomechanical coupling produces more efficient actuation via the optical gradient force. The cavity loss rate is also an important consideration; a cavity loss rate that is too low reduces the efficiency of the technique, however, a high optical cavity loss rate is also not beneficial. There is an optimal range for the cavity loss rate the must be considered in the design of the optomechanical system. We verify this result experimentally and confirm the model's validity for designing optomechanical systems for efficient actuation. By following the design rules set in our model, we can increase the amplitude of the nanomechanical mass sensor and therefore increase the dynamic range for a given input power. In this case, we have demonstrated that the maximum dynamic range of the cantilever has been reached, since we have observed a nonlinearity in the output. This represents an improvement on previous cantilever designs [69], which had mass sensitivity in the zeptogram range without reaching the full dynamic range of the mechanical sensor.

Chapter 5

Transduction of Large Amplitudes with Racetrack Resonators

Nonlinear behaviour in micro- and nanomechanical devices is important for many reasons. If the mechanical device is used as a sensor, nonlinearities are detrimental and much work has been devoted to eliminating or avoiding the nonlinearities in order to increase the dynamic range of the sensors [18, 209, 210]. For other applications, such as in quantum optics or oscillator circuits, nonlinearities are essential. For example, it has been shown that mechanical Duffing nonlinearities can help prepare squeezed mechanical states [211], and can also help form autonomous oscillators [212]. Regardless of the application of the nanomechanical device, understanding its nonlinear behaviour is crucial. For these reasons, it is important to understand how the actuation and readout methods can introduce nonlinearities into a nanomechanical system. For some actuation and readout techniques, nonlinearities are well understood. One example is in capacitive transduction, where nonlinear effects due to pull-in are well studied and the effects can be quantified and tuned [213, 214]. When the actuation and readout is optomechanical, however, nonlinearities in the transduction are not as well explored [43, 154, 166, 215, 216]. In optomechanics, the complex interaction between the nanomechanical device and the optical cavity can lead to a wide range of nonlinear effects. In addition to the purely mechanical nonlinearities observed such as stiffening and softening mechanical nonlinearities, such as those seen in Section 3.2, nonlinear coupling between the mechanical device and the optical cavity can be achieved [217], and both radiation pressure force and dispersive optical forces are inherently nonlinear [218, 219].

For mass sensing nanomechanical devices, the nonlinearities of interest are those that limit the dynamic range of the sensor [20]. For doubly clamped beams, this nonlinearity is typically the mechanical Duffing nonlinearity. Cantilevers, however, have a significantly higher threshold for mechanical nonlinearity, since the onset of mechanical nonlinearity is proportional to the length of the cantilever, instead of the thickness [197, 209]. Therefore, the type of nonlinearity that a cantilever will encounter at the peak of its dynamic range in an optomechanical system is much more likely to be from another source. In this chapter, we explore the sources of nonlinearity affecting the dynamic range of a cantilever that is both actuated and read out optomechanically. We examine both a readout nonlinearity and optical force nonlinearities caused by the large amplitude of the cantilever. We present a numerical model that separates both the mechanical and optical outputs from the system, allowing us to understand the dynamics of the system even when readout nonlinearities obscure the experimental results.

In this chapter we will study the simultaneous effects of both a pump and probe laser on the nonlinear behaviour of a nanomechanical cantilever coupled to a racetrack resonator. Previous work has studied the effects of a single pump laser actuating a nanomechanical cantilever via the optical gradient force [219]. The addition of the probe laser into the system greatly increases the complexity and produces unexpected behaviour. We first describe the mathematical background for nonlinear mechanical resonators in Section 5.1. In Section 5.2, we provide details on the fabrication and initial characterization of the optomechanical system. In Section 5.3 we show the experimental results, beginning with the experimental observation that positioning the probe laser on the blue side of the optical cavity results in a softening effect, and that positioning the probe laser on the red side of the cavity results in a stiffening effect. This is directly opposite to what is described in Section 2.3 for a typical optomechanical system. We also demonstrate experimentally that the thermomechanical noise calibration described in Section 2.1.1 does not hold for our optomechanical system under our experimental conditions. We attribute this to a readout nonlinearity, which also introduces harmonics into the mechanical frequency spectrum. We observe these harmonics experimentally and discuss how they are linked to the readout nonlinearity. We will then explore in depth the cause of the unexpected stiffening and softening behaviour. By utilizing an analytical model for the optical force nonlinearity previously demonstrated in [219], we can begin to explain some of our experimental observations. This model incompletely describes our system, leaving the optomechanical system behaviour at zero detuning unexplained. To model our pump-and-probe optomechanical system, we derive a numerical model that includes both lasers and can be used to account for the optical force nonlinearity introduced by the probe laser position in the optical cavity. To describe the optomechanical system, including the behaviour at zero detuning, we demonstrate that the optical force nonlinearity introduced by the evanescent field outside of the waveguide is crucial to include in the numerical model. By including this additional source of nonlinearity in the numerical model, we can correctly identify the softening and stiffening behaviour at every detuning. This numerical model also allows us to estimate the amplitude of the mechanical device, which is beneficial since the thermomechanical noise calibration is ineffective in this case. In Section 5.4 we discuss the results in further detail, highlighting the three different contributions to the nonlinearity; the readout, the optical cavity force, and the optical evanescent force. We conclude in Section 5.5 and determine that unexpected experimental results caused by our pump-and-probe transduction technique, and the numerical model we derive to help explain these results, forms a unique contribution to the study of optomechanical nonlinearities.

5.1 Theoretical Description of Nonlinear Resonators

To determine the upper bound on the dynamic range of a sensor, one experimental approach is to gradually increase the driving power until a nonlinearity is observed. Previous studies have demonstrated that there are several potential sources of nonlinearity for nanomechanical resonators. As shown in Section 3.2, geometric or mechanical nonlinearities can dominate the performance of doubly clamped beams. In the case of cantilevers, the onset of geometric nonlinearity is proportional to the device length according to $a_{\mathrm{cr,mech}} = 6.3 l_{\mathrm{m}}/Q^{1/2}$ [209]. Using this relation, the mechanical critical amplitude for the cantilever measured here, with a length of 2.89 μm, is expected to be approximately 180 nm. This amplitude is double the size of the gap between the cantilever and the waveguide and therefore we reasonably expect that another source of nonlinearity will occur before the mechanical nonlinearity is reached. Our goal with these measurements is to find the onset of nonlinearity, and to determine the source of this nonlinearity. Once we know the source of the nonlinearity, we may be able to design future devices with higher linear ranges to improve the performance of the mass sensing devices. Other potential sources of nonlinearity include actuation nonlinearity, which has been observed in cantilevers under electrostatic actuation [213, 220]. This type of nonlinearity affects the amplitude that can be attained with a given actuation method. Another type of nonlinearity is a readout nonlinearity. This type of nonlinearity can result in a nonlinear relationship between the amplitude of the nanomechanical device and the output signal that is measured [38], but does not affect the actual amplitude of the device.

The behaviour of a nonlinear resonator, regardless of the source of nonlinearity [221], can be described by a similar differential equation to Eq. (2.4). Two additional terms are included in the differential equation to account for the quadratic and cubic nonlinearities, as shown in the following differential equation [219, 222]:

$$m_{\text{eff}}\frac{\mathrm{d}^2x}{\mathrm{d}t^2}+\frac{m_{\text{eff}}\Omega_0}{Q}\frac{\mathrm{d}x}{\mathrm{d}t}+k_{\text{eff}}x+m_{\text{eff}}\alpha_2x^2+m_{\text{eff}}\alpha_3x^3=F(t), \tag{5.1}$$

where x is the amplitude of the mechanical device, t is time, m_{eff} is the effective mass, Ω_0 is the fundamental resonance frequency, Q is the mechanical quality factor, k_{eff} is the effective spring constant, α_2 is the second-order or quadratic nonlinearity coefficient, and α_3 is the third-order or cubic nonlinearity coefficient, and $F(t)$ is the applied driving force. A nonlinear resonator with α_3 as the dominant nonlinearity term is usually referred to as a Duffing resonator. Experimentally, a Duffing resonator has a frequency resonance curve with a shark-fin shape and exhibits bistability.

The onset of nonlinearity, called the critical amplitude a_{cr}, is generally considered to be the upper bound on a sensor's dynamic range [20, 21, 197, 214, 219]. The critical amplitude is the point at which the Lorentzian lineshape of the mechanical signal begins to exhibit the shark-fin shape. Mathematically, this can be described as $\mathrm{d}^2\Omega/(\mathrm{d}B_{\text{NL}}^2)^2=0$, where B_{NL} is the frequency-dependent nonlinear amplitude of the resonator. The critical amplitude is described as [222]

$$a_{\text{cr}}=\left(\frac{8\Omega_0^2}{3\sqrt{3}Q\alpha}\right)^{1/2}, \tag{5.2}$$

where α is the combined quadratic and cubic nonlinearity terms. To combine the two nonlinearity terms into a single term describing the nonlinearity of the resonator, we can use the expression [223]:

$$\alpha=\alpha_3-10\alpha_2^2/9\Omega_0^2. \tag{5.3}$$

The critical amplitude can be calculated as long as the total nonlinearity is known. Eq. (5.2) gives a detuning-dependent critical amplitude, since α is a function of the detuning Δ.

The experimental procedure for determining the critical amplitude is to increase the drive power linearly, and record the peak amplitude and frequency of the mechanical device. The results of this experiment produce a plot of amplitude versus frequency that is often referred to as the "backbone" curve of a nonlinear device. To extract the nonlinearity coefficient from this curve, we use the following expression [222]:

$$a_{\text{peak}}=\sqrt{\frac{8}{3}\frac{\Omega_0(\Omega_{\text{peak}}-\Omega_0)}{\alpha}}, \tag{5.4}$$

where α is positive for a stiffening nonlinearity and negative for a softening nonlinearity.

Another approach to determining the critical amplitude is using the 1 dB compression point. This technique was used in Section 3.2 for a doubly clamped beam.

The 1 dB compression point is where the amplitude falls to 1 dB below the linearly expected trend. The 1 dB compression point is related to the critical amplitude via Eq. (3.6). The same experimental procedure of obtaining the peak amplitude for increasing drive power described in the previous paragraph is used. In this case, however, the peak amplitude is plotted versus the input drive power. A linear trend can be determined from the results at low drive power. At the drive power increases, the amplitude no longer follows the linear trend, and is smaller than predicted by the linear trend. The 1 dB compression point is obtained from comparing the peak amplitudes at high drive power to the linearly expected tend. This is a straightforward method to experimentally determine the critical amplitude, although not as mathematically rigorous as the previously described approach.

With this description of nonlinear resonators in mind, we can begin characterization of the pump-and-probe optomechanical system to determine the sources of nonlinearity and therefore the upper bound on the dynamic range of the device for mass sensing.

5.2 Optomechanical System Fabrication and Characterization

The optomechanical system was fabricated on a silicon-on-insulator chip with a 220 nm thick device layer and a 2 μm thick sacrificial oxide layer. The mechanical device has a length of 2.89 μm, which is coupled to an optical racetrack cavity. The cantilever was 220 nm wide and 130 nm thick and the gap between the racetrack resonator and the cantilever was approximately 90 nm. The racetrack resonator had 5 μm radius with a straight coupling section 3 μm long. The waveguides width was 500 nm and the coupling gap between the bus waveguide and the racetrack resonator was 250 nm. Grating couplers were used to couple the incident light into the bus waveguide. The optomechanical system was fabricated at imec. Post-processing to release the devices was completed at the University of Alberta NanoFab. The only post-processing required was a buffered oxide etch to release the cantilever. This was a timed, maskless process to release the narrow waveguides while keeping the waveguides attached to the oxide layer. A scanning electron microscope (SEM) image of the mechanical cantilever device before release is shown in Figure 5.1.

For characterization, we use the free-space confocal microscope setup described in Section 2.4. The DC component of the signal is used to characterize the optical cavity, while the AC component is sent to a digital lock-in amplifier and used to characterize the mechanics of the system. To actuate the devices, we use the optical driving technique described in Chapter 4. The driving frequency is set by the lock-in amplifier.

First, we characterize the response of the optical racetrack cavity. The pump

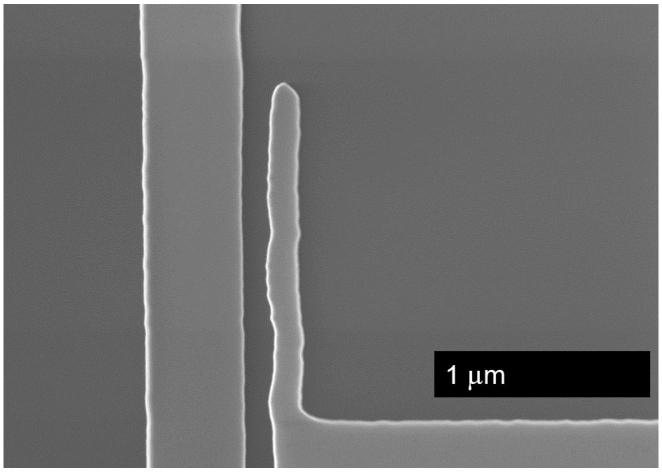

Figure 5.1: Scanning electron microscope (SEM) image of the nanomechanical cantilever adjacent to an optical racetrack resonator.

laser is deactivated and the wavelength of the probe laser is swept to measure the optical response over a wide wavelength range from 1530 nm to 1570 nm, as shown in Figure 5.2(a). Three optical cavity resonances are observed, with an FSR of approximately 14.5 nm. The first two optical cavity resonances show peak splitting, which is caused by coherent backscattering. For the following experiments, the pump laser is placed at the bottom of the highest wavelength resonance unless otherwise specified. The probe wavelength is positioned on the side of the centre optical cavity, close to 1548 nm.

A fine scan is used to provide detailed information about the blue half of the split optical cavity, as it is the optical cavity used to measure the optomechanical interaction. The scan was first performed at low power, with approximately 77 μW in the bus waveguide (Figure 5.2(c), blue circles). The response begins at 0 dB on the blue side of the cavity, but does not reach 0 dB on the red side due to the peak splitting effect. The power was then increased to 108 μW (Figure 5.2(c), red circles). As the power increased, asymmetry in the optical cavity was observed and the optical resonance increased in wavelength.

Potential sources of nonlinearity in silicon photonic integrated circuits include thermal nonlinearities and free carrier effects such as free carrier dispersion [224, 225, 226, 227, 228]. Free carriers are generated through two-photon absorption. Two-photon absorption can occur when the bandgap energy is less than two times the photon energy. For example, the bandgap of silicon is 1.12 eV. The energy of a photon at 1550 nm is 0.8 eV. Therefore, the combined energy of two photons is larger than the bandgap of silicon. This means that two photons can combine to excite an electron from the valence band to the conduction band, generating free carriers in the silicon waveguide. Two-photon absorption is an intensity-dependent

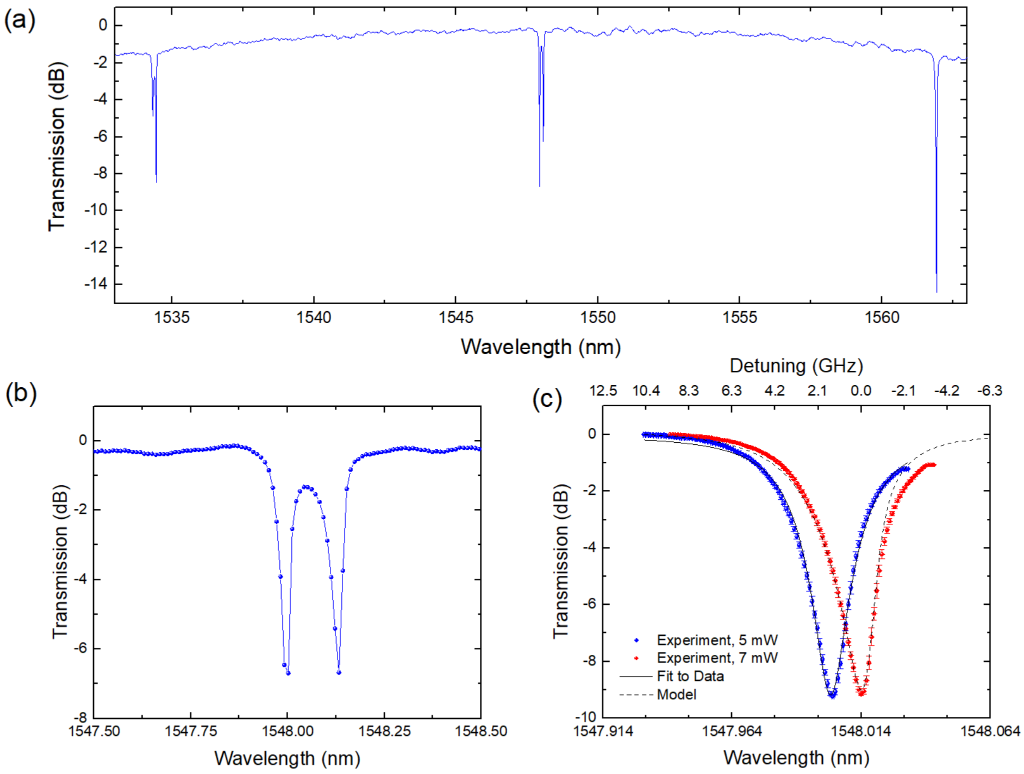

Figure 5.2: (a) Sweep of the optical cavity response over a wide wavelength range. Three resonances are observed. The two lowest wavelength resonances exhibit peak splitting, but the highest wavelength response has no splitting and shows good extinction. For the following experiments, the probe is set to the side of the slope in the middle cavity. The pump is set to the bottom of the third resonance unless stated otherwise. (b) Coarse sweep of the probe optical cavity. Peak splitting is observed. (c) Fine sweep of the probe optical cavity at 77 μW (blue circles) and the corresponding curve fit (solid line). The experimental cavity data does not reach 0 dB on the red side because of the peak splitting. A second sweep at 108 μW (red circles) is also shown, with a theoretical model approximating the behaviour of the optical cavity (dashed line).

process, and therefore we would expect this to increase as the input laser power increases [229]. The free carriers generated as a result of two-photon absorption can have two effects, free carrier absorption (FCA) and free carrier dispersion (FCD). FCA leads to increased absorption in the silicon waveguide but does not alter the resonance wavelength of the racetrack resonator. The resonance wavelength is, however, affected by FCD. FCD induces a decrease in the refractive index proportional to the number of free carriers [230]. A decreasing silicon refractive index results in an overall decrease in the effective index of the silicon waveguide. The optical path length also decreases, and the resonance wavelength decreases. Therefore, a blue shift in the racetrack resonance wavelength is expected for nonlinearities introduced by FCD.

Thermal nonlinearities in microring or racetrack resonators arise because of the large thermo-optic coefficient in silicon. The thermo-optic coefficient, or how much the refractive index of a material shifts with temperature, is 1.8×10^{-4} K^{-1} at room temperature [231]. Processes such as FCA can lead to increased heating in the silicon waveguide due to phonons that are generated when electrons and holes recombine. Two-photon absorption is also a source of additional heat. Heating effects are amplified in racetrack resonators near resonance because of the high power enhancement. As the wavelength is swept from the blue side of resonance to the red side, the power in the racetrack increases as the wavelength approaches resonance and also maximum power enhancement. Absorption and heating also increase. This results in an increase in the refractive index because the thermo-optic coefficient in silicon is positive, and therefore an increase in the effective index of the waveguide. The path length of the cavity effectively increases, causing an increase in the resonance wavelength. Therefore, a thermal nonlinearity produces a red shift in the racetrack resonance wavelength. As the wavelength is swept past the optical resonance, the power enhancement in the racetrack resonator decreases and the heating effects also decrease. The index changes induced by the thermo-optic effect will reduce as well, and the resonance shifts back to its original position. This produces an asymmetric optical resonance, where the blue side of the resonance is elongated, and the red side of the resonance exhibits a sharp decrease. At high powers, this effect can result in hysteresis in the measurement of the optical spectrum [232].

The asymmetry and red shift observed in our data indicate that the dominant source of nonlinearity is a thermal nonlinearity. There may simultaneously be FCD occurring in the racetrack resonator, however, the blue shift expected from that effect is obscured by the large red shift introduced by the thermal nonlinearity. To account for this effect, we first fit the data recorded at low input power using Eq. (2.25), the standard power coupling equation for an all-pass microring resonator. Using the values obtained for τ and a_{rt}, we can develop a model for the nonlinearities in the higher power sweeps. The equation for nonlinear transmission through an all-pass racetrack resonator can be derived using the power coupling formalism [94]. The result of this derivation is the inclusion of a nonlinear phase ϕ_{NL} to Eq. (2.25), such that the total round trip phase is equal to $\phi + \phi_{\mathrm{NL}}$. However, this equation cannot be used alone to perform a curve fit to the experimental data because the nonlinear phase changes throughout the entire wavelength sweep, depending on the proximity to the optical resonance. To solve for the nonlinear phase at each point in the optical resonance, we use the expression for the nonlinear amplitude inside the optical cavity. By taking the square of the absolute value of the amplitude in the racetrack resonator and simplifying the result we obtain the following expression [94]:

$$\frac{1}{1 + F\sin^2(\frac{\phi+\phi_{\mathrm{NL}}}{2})} = -\frac{c\phi_{\mathrm{NL}} n_{\mathrm{eff}}^2 A_{\mathrm{eff}}}{n^2 n_2 \omega P_{\max} L_{\mathrm{eff}}}, \tag{5.5}$$

where F is the contrast of the racetrack resonator and is defined as $F = 4\tau a_{\mathrm{rt}}/(1 - \tau a_{\mathrm{rt}})^2$ for a racetrack in the all-pass configuration, n is the bulk index of the silicon and is equal to 3.45, n_2 is the nonlinear index of the silicon waveguides, $P_{\max}$ is the peak power inside the racetrack on resonance, and A_{eff} is the effective modal area of the waveguide. Both n_{eff} and A_{eff} can be obtained using commercial mode solver software [171]. Finally, $L_{\mathrm{eff}} = (1 - e^{-\alpha_0 L_{\mathrm{c}}})/\alpha_0$ is the effective length of the racetrack resonator, which accounts for the optical loss of the waveguide α_0 in units of 1/m, and L_{c} is the physical cavity length. All of these parameters are known or can be solved for using simulation, with the exception of n_2. This nonlinear index describes how the effective index of the waveguide changes as a function of intensity. This parameter is not known for this specific racetrack resonator configuration. Although it is possible to measure this value experimentally [224], it is sufficient in our case to use this value to tune the nonlinear index. Essentially, we can use n_2 as a free parameter, and vary it to produce a range of nonlinear phase shifts from Eq. (5.5). Then the nonlinear phase is substituted back into Eq. (2.25) to produce a model of the optical transmission. To determine the correct value for n_2, we extract the wavelength shift observed when the power is increased from 77 μW to 108 μW from the experimental data. We can then adjust n_2 in the model until the correct shift is observed between the curve fit to the 77 μW data and the model. The model for the higher power data is shown in Figure 5.2. Although this model is not a curve fit, it does provide a good estimate of the curve shape. The properties of the probe and pump optical resonances are summarized in Tables 5.1, 5.2, and 5.3. The probe laser is maintained below the threshold for self-oscillation determined experimentally in Chapter 4. The pump laser is always positioned at zero detuning to avoid introducing self-oscillation.

Once the optical cavity parameters have been determined, the mechanical properties of the system can be studied. Based on the dimensions observed in the SEM

Table 5.1: List of probe optical cavity properties ($\lambda \approx 1548$ nm)

Parameter	Value	Unit
a_{rt}	0.9977	-
τ	0.9952	-
γ	12.8	rad GHz
γ_{ex}	8.6	rad GHz
P_{bus}	107.8	μW
ω_0	$2\pi \times 193.8$	rad THz

Table 5.2: List of pump optical cavity properties ($\lambda \approx 1560$ nm)

Parameter	Value	Unit
a_{rt}	0.9934	-
τ	0.9902	-
γ	26.2	rad GHz
γ_{ex}	17.6	rad GHz
$P_{\mathrm{bus,DC}}$	258.2	μW
$P_{\mathrm{bus,AC}}$	34.4	μW
ω_0	$2\pi \times 192.2$	rad THz

Table 5.3: List of pump optical cavity properties ($\lambda \approx 1535$ nm)

Parameter	Value	Unit
a_{rt}	0.9936	-
τ	0.9952	-
γ	20.3	rad GHz
γ_{ex}	8.75	rad GHz
$P_{\mathrm{bus,DC}}$	170	μW
$P_{\mathrm{bus,AC,minimum}}(Simulation)$	1.13	μW
$P_{\mathrm{bus,AC,maximum}}(Simulation)$	22.7	μW
ω_0	$2\pi \times 195.8$	rad THz

image in Figure 5.1, we can calculate the effective mass of the cantilever as 48 fg (1 fg= 10^{-15}g). We can also determine the noise floor of the system, which in turn can be used to establish the bottom of the dynamic range of the sensor [18, 20]. This noise floor is established by the thermomechanical noise of the cantilever, which is measured by setting the pump laser modulation off and measuring the mechanical response with the lock-in amplifier. The result of this measurement can be seen in Figure 5.3, and is expressed in terms of the detuning from cavity resonance. In this case, the optical cavity resonance ω_0 is set to the bottom of the optical resonance curve at the higher power of 108 μW (red dots in Figure 5.2(c)). The data has been smoothed to reduce the vibrational noise introduced by the vacuum pump. From Figure 5.3, we can determine that centre mechanical resonance frequency is $\Omega_0 = 2\pi \times 21.1956$ rad MHz, which is the frequency at zero detuning where the optical spring effect vanishes. The observation of the thermomechanical noise shows that we can access the noise floor of our device even at large detunings where the mechanical transduction by the optical cavity is not efficient. The average quality factor of the measurements in Figure 5.3 is 10,000, and therefore we set the mechanical $Q = 10,000$.

The final characterization is the optomechanical interaction. One of the most important parameters defining the optomechanical interaction is the optomechanical coupling coefficient $G = \partial\omega/\partial x$, which describes the strength of the interaction between the mechanical resonator and the optical cavity. There are several ways to determine the optomechanical coupling coefficient, one of which is by measuring the thermomechanical noise of the mechanical resonator at a variety of detunings. If the optomechanical coupling is sufficiently large, frequency shifts caused by the optical spring are observed. These shifts can be used to calculate the optomechanical coupling. This procedure is described in detail in Chapter 4. From Figure 5.3, we can extract the peak values of the mechanical response at each detuning and use this to calculate the optomechanical coupling coefficient. The resulting value is $G = 0.987$ rad GHz/nm. The mechanical properties of the system are summarized in Table 5.4.

Table 5.4: List of mechanical properties

Parameter	Value	Unit
G	0.987	rad GHz/nm
Ω_0	$2\pi \times 21.1956$	rad MHz
Q	10,000	-
m_{eff}	47.7	fg

With the optical, mechanical, and optomechanical properties of the system without a driving force known, we can introduce the pump laser to provide actuation through the optical gradient force. This increases the complexity of the system, as

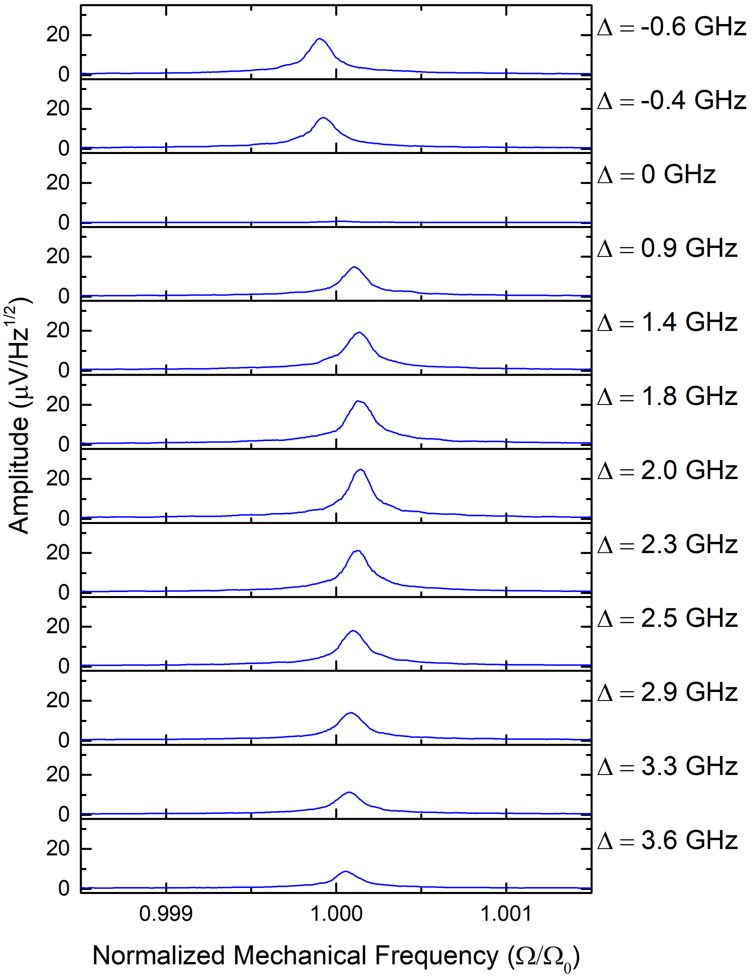

Figure 5.3: Experimental measurement of the thermomechanical noise of the cantilever, smoothed to eliminate noise introduced by vacuum pump vibrations. This result can be used to extract the optomechanical coupling coefficient.

we will see in the following section.

5.3 Large Amplitude Nonlinearities

To characterize the nonlinear behaviour of the optomechanical system using a pump-and-probe actuation and detection approach, we gradually increase the applied AC optical force and measure the mechanical amplitude response. We set the pump laser wavelength to the lowest point of the first optical resonance in Figure 5.2(a), and therefore the values listed in Table 5.3 apply. We activate our amplitude EOM and use the lock-in amplifier to increase the voltage applied to the EOM, thereby increasing the AC amplitude of the actuation power applied to the cantilever. The probe laser was positioned at the point of maximum slope on both the red and blue side of the optical cavity transmission from Figure 5.2(c), to maximize the signal-to-noise ratio of the mechanical signal. This corresponds to a detuning of approximately ±0.61 GHz. The lock-in amplifier was used to sweep the frequency of the voltage drive across the mechanical frequency spectrum to obtain driven measurements of the mechanical device. As the applied AC optical force was increased, nonlinearity was observed for both red and blue detuning. A stiffening nonlinearity was observed in the red-detuned measurements, whereas a softening nonlinearity was observed in the blue-detuned measurements. This is opposite to the behaviour described by the optical spring effect in Section 2.3. We will investigate the cause of this result in Section 5.3.1. To determine the critical amplitude, the data recorded in voltage by the lock-in amplifier must be converted to metres. The thermomechanical noise is used to calculate the responsivity for use as a calibration factor, using the method from Section 2.1.1. We have performed the conversion using the responsivity from volts to metres on the data to produce Figure 5.4. Using the 1 dB compression point approach described in Section 5.1, we can use Figure 5.4 to determine that the critical amplitude for the mechanical device measured with a blue-detuned probe laser is 1.9 nm. The critical amplitude for the same device measured with a red-detuned probe laser is 3.6 nm.

The amplitudes shown in Figure 5.4 are significantly smaller than expected for the driving force input to the system. The driving force F_{opt} applied to the device is calculated using Eq. (2.41). All of these parameters are known experimentally from the measured optical cavity responses. The force calculated from this expression can be converted to a corresponding amplitude using the simple relation for a damped harmonic oscillator, $F_{\text{opt}} = kx/Q$, where $k = m_{\text{eff}}\Omega_0^2$ is the spring constant, x is the amplitude, and Q is the quality factor. These values are known from the characterization of the mechanical device in the previous section. Using these well-known relationships, we can estimate that the largest amplitude in Figure 5.4(a) should be 6.3 nm. The largest amplitude in Figure 5.4(b) should be 20.7 nm,

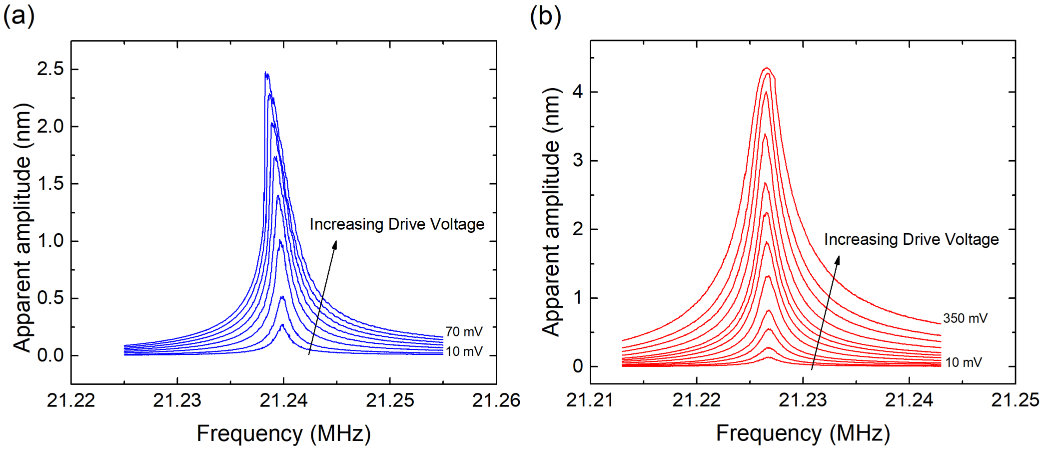

Figure 5.4: The frequency response of the cantilever in nanometres as the driving voltage is increased with the probe laser positioned on the (a) blue and (b) red sides of the optical cavity. The apparent amplitude is calculated using the thermomechanical noise calibration and assumes there is no readout nonlinearity. The power of the probe laser in the bus waveguide is 154 μW. The DC power of the pump laser in the bus waveguide is 170 μW. For (a), the AC power is increased from 1.13 μW to 7.93 μW. For (b), the AC optical power is increased from 1.13 μW to 39.7 μW. The pump laser frequency is held constant for both measurements. When the probe laser is positioned on the blue side, a softening effect is observed. When the probe laser is positioned on the red side, a stiffening effect is observed. This is opposite to the expected result in optomechanical systems.

as a significantly larger voltage was applied to this measurement. The expected amplitudes are a factor of 2.5–4.5 times larger than the observed amplitudes, which is the first indication that there may be an issue with the calibration using the responsivity obtained from thermomechanical noise.

To obtain more information about the driven optomechanical system, we can perform a sweep of the mechanical signal at different detuning points in the optical cavity. We move the pump laser to the highest wavelength optical resonance in Figure 5.2(a), to improve the efficiency of the driving laser power by moving it to a non-backscattered peak. It also eliminates any possibility that the drive laser could shift from one minimum of the split cavity to the next, since the highest wavelength optical resonance does not exhibit any peak splitting. The pump laser power was set to a DC value of $P_{\text{bus,pump}} = 258\ \mu\text{W}$. A constant voltage of 200 mV was applied to the EOM, producing an AC power of 34 μW in the bus waveguide. The probe laser was activated and set to $P_{\text{bus,probe}} = 108\ \mu\text{W}$. Next, the probe laser wavelength was swept through the optical cavity, starting at the far blue-detuned side and increasing the wavelength to sweep through the cavity. At each wavelength position, the frequency response of the cantilever was measured using the lock-in amplifier. The frequency response at the fundamental resonance frequency was recorded, as well as data from higher harmonics ($2\Omega/2\pi$, $3\Omega/2\pi$, and $4\Omega/2\pi$). The results of these sweeps are shown in Figure 5.5. There are clear signals at all of the higher harmonics measured, which is indicative of a readout nonlinearity. This readout nonlinearity is apparent when a driving force is applied, since the thermomechanical noise only has a component at the fundamental resonance frequency. This indicates that the nonlinearities are induced by the large amplitude of oscillation of the cantilever device, and are most likely related to a readout nonlinearity as opposed to an optomechanical nonlinearity induced by the optical force as observed in [219]. However, a softening effect appears as the probe laser wavelength approaches the cavity centre from the blue side in Figure 5.5(e). A stiffening effect is visible as the probe laser wavelength moves past zero detuning and onto the red side. These effects are consistent with Figure 5.4, and are not observed in other reports of nonlinearities caused purely by readout [163, 233, 234]. From this result, we conclude that there are at least two sources of nonlinearity present in the system; a readout nonlinearity and another source of nonlinearity.

To confirm that the harmonic components observed in Figure 5.5 are caused by a readout nonlinearity, and not another source of nonlinearity that induces higher order harmonics such as second-order optomechanical coupling [215], we examine the relationship between the harmonics and the optical cavity. If the optomechanical nonlinearity observed is caused mainly by a nonlinearity in the transduction, the shape of the optical cavity and its derivatives will correspond to the peaks of the

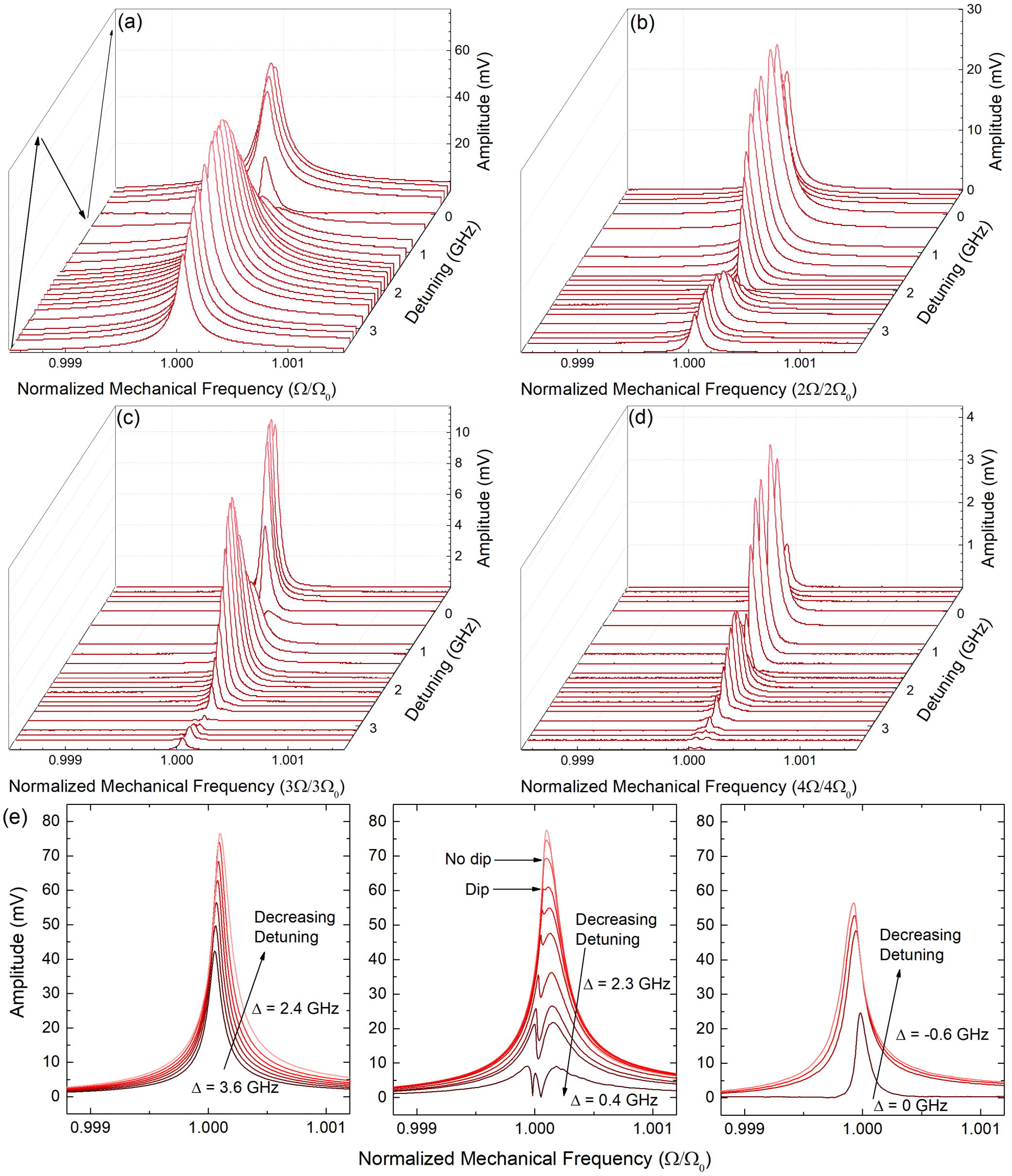

Figure 5.5: The frequency response of the cantilever as the probe laser is swept through the optical cavity. In the bus waveguide, the probe power is 108 μW, the DC pump power is 258 μW, and the AC pump power is 34 μW. (a) The response at the fundamental resonance frequency. The black arrows show the peak height trend as the detuning is decreased. (b)–(d) The harmonic components at $2\Omega/2\pi$, $3\Omega/2\pi$, and $4\Omega/2\pi$, respectively. The harmonics are indicative of a readout nonlinearity. (e) The fundamental response is re-plotted to show the changing nonlinearity as the detuning is decreased. In the first panel, very little nonlinearity is observed for large positive (blue) detuning. In the second panel the detuning approaches zero. A softening nonlinearity is observed and the peaks begin to have dips. The last peak without a dip is at $\Delta = 2.0$ GHz and the first peak with a dip is at $\Delta = 1.88$ GHz. The frequency difference between these peaks and $\Delta = 0$ can be used to estimate that the amplitude is 12.3 ± 0.4 nm. In the third panel, a stiffening nonlinearity is seen for negative detuning. The stiffening and softening nonlinearities are not caused by a readout nonlinearity.

harmonics observed in Figure 5.5. The voltage peaks are extracted from Figure 5.5 for the first and second harmonic, then normalized to one. The normalized values are plotted versus the detuning. The voltages where the mechanical phase is shifted by π are denoted as negative voltages. The result of this calculation is shown in Figure 5.6, where the fundamental peaks are represented by the blue circles, and the second harmonic peaks are represented by the red circles. We can then compare these curves to the derivatives of the nonlinear optical cavity model shown by the dashed line in Figure 5.2(c) and plotting the results versus the detuning. The first and second derivatives are shown in Figure 5.6 and are represented by the blue and red dashed lines, respectively.

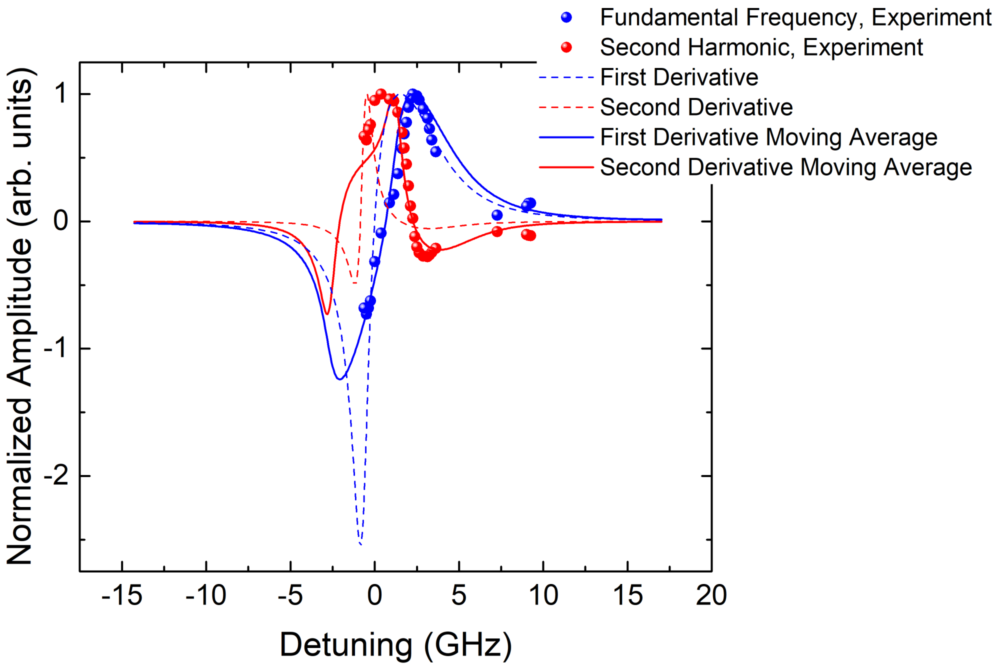

Figure 5.6: The peak value of the mechanical signal is shown for the fundamental frequency (blue circles) and second harmonic (red circles). These peaks are extracted from Figure 5.5(a) and (b). The first (blue) and second (red) derivatives of the nonlinear optical cavity are shown by the dashed lines. A moving average of the first (blue) and second (red) derivatives with a window size equal to the peak-to-peak amplitude of the nanomechanical cantilever is shown by the solid lines. There is excellent agreement between the experimental peaks and the moving average of the first and second derivatives. This demonstrates that the harmonics in the mechanical frequency spectrum are directly related to the shape of the optical cavity and are a result of a readout nonlinearity. The large window of the moving average indicates that the readout is also directly affected by the large amplitude of the cantilever.

The derivatives represent the slope and curvature of the cavity at an instantaneous point along the optical resonance. However, the large-amplitude cantilever in this experiment samples significantly more than a single point during one period of vibration. The optical cavity slope may be an accurate measure of the transduction for small amplitude vibrations such as the thermomechanical noise or doubly clamped beams [67, 69], but this does not hold for a driven cantilever where the amplitudes are large enough to move past the approximately linear section of the Lorentzian optical resonance. To more accurately map the slope and curvature that the cantilever samples as it moves through one period of vibration with a large amplitude, we take a moving average of the first and second derivatives of the optical cavity. The window size of this moving average is the peak-to-peak amplitude of the nanomechanical device converted to a detuning using the optomechanical coupling coefficient. The peak amplitude is estimated from observing the detuning at which the dips in the mechanical spectrum appear, since those dips arise from the probe laser crossing over the optical cavity resonance minimum, resulting in a change in slope and an abrupt change in the signal [165]. This is the same method used to estimate the amplitude in Chapter 4. We can use the first detuning that exhibits a dip and the last detuning without a dip as reference points to estimate the amplitude of the cantilever, and therefore also the window size for the integration. At the detuning where the first dip occurs, we know that the optical cavity is moving from its initial detuning position to the other side of the optical cavity slope. This gives a minimum shift that the optical cavity is experiencing at the cantilever's peak amplitude. On the other hand, at the detuning immediately before the first dip, the probe laser does not complete the shift to the other side of the optical cavity. This detuning value gives a maximum amount of shift that the optical cavity is experiencing during the peak of the cantilever's vibration. By averaging the maximum and minimum shifts, we can obtain an estimate of the appropriate window size for the integration. The average shift is a substantial 1.95 GHz at the cantilever's peak amplitude. Therefore, the window for the integration should be twice this value, 3.9 GHz, to account for the peak-to-peak amplitude of the cantilever. Using the peak-to-peak amplitude is necessary to account for the full range of the optical cavity that the cantilever samples during one period of vibration. To confirm that this estimate makes sense, we can convert the average shift to an amplitude using the optomechanical coupling coefficient $G = \partial\omega/\partial x \approx \Delta\omega/\Delta x$. The resulting amplitude is 12.3 ± 0.4 nm, which is close to the expected amplitude of 11.0 nm given the optical force applied during the experiment.

This approximate approach to finding the window size and amplitude is necessary because of the large discrepancy between the expected and observed amplitudes in Figure 5.4, where the responsivity obtained from the thermomechanical noise was used to calibrate the amplitudes. This result indicates that the thermomechanically calibrated amplitudes may not be accurate. The result of applying a 3.9 GHz wide moving average window to the first and second derivatives of the optical cavity is shown by the solid blue and red lines respectively in Figure 5.6. These curves agree very well to the peaks obtained from the mechanical sweeps for the first and second harmonics shown by the circles in Figure 5.6. This close agreement shows that the shape of the optical cavity is closely linked to the harmonics observed in the mechanical frequency spectrum. This is a strong indicator that the harmonics we have observed in the experiment are caused mainly by a readout nonlinearity, which is purely due to the nonlinear nature of the Lorentzian transfer function of the optical cavity instead of another mechanism. The nonlinear readout also provides some understanding as to why the amplitude calculated using the thermomechanical noise responsivity (Figure 5.4) gave such erroneous results. With nonlinear readout, there is no longer a linear relationship between the driven amplitude and the thermomechanical noise, rendering the calibration inaccurate. The significant number and high signal-to-noise (SNR) of the harmonics present in the mechanical spectrum in Figure 5.5 indicate that much of the energy of the driven signal is shifted from the fundamental resonance frequency to the higher order harmonics. Calculating the amplitude using the thermomechanical responsivity does not take this energy loss and nonlinearity into account.

Although the cause of the harmonics in the mechanical frequency spectrum is a readout nonlinearity resulting from the Lorentzian shape of the optical cavity, the mechanical resonances in Figures 5.4 and 5.5(e) show softening and stiffening distortions that are similar to a Duffing nonlinearity. A readout nonlinearity alone is insufficient to explain these nonlinear effects. As mentioned in Section 5.1, a readout nonlinearity may result in incorrect conversion between the observed and actual amplitudes, however, it does not alter the left-to-right symmetry of the mechanical peak shape. In the following sections, we examine the other sources of nonlinearity in the optomechanical system. Since driving the devices to high amplitude is crucial to reaching a high dynamic range for our mass sensing cantilevers, we must understand what factors affect the nonlinear behaviour of the system.

5.3.1 Optical Force Nonlinearity

Other types of optomechanical nonlinearities have been previously observed, including an optomechanical nonlinearity caused by the optical force [219]. The optical force nonlinearity can be further divided into two components; nonlinearity introduced by the Lorentzian line shape of the optical cavity, and nonlinearity introduced by the exponential decay of the evanescent field outside of the waveguide. The first type of optical force nonlinearity is a function of detuning, since the optical force applied will vary with the detuning according to Eq. (2.41). The second type of nonlinearity is only relevant for optomechanical devices where the optical cavity is physically separated from the mechanical resonator, as in our case since the cantilever adjacent to the racetrack resonator. For clarity, we will label these different sources of nonlinear optical force as the optical cavity force nonlinearity and the evanescent force nonlinearity, respectively. For small amplitudes of vibration, both optical forces are approximately linear. The evanescent force strongly depends on the gap between the optical cavity and the mechanical element, and for larger gaps will be linear over a larger range.

To obtain a first-order approximation of the nonlinearity and to see whether the unexpected stiffening and softening behaviour observed in Figure 5.4 could be explained by these optical force nonlinearities, we use the model derived in [219]. This model produces the total nonlinearity coefficient α described in Eq. (5.3). It includes both the optical cavity force and the evanescent force, and shows how the softening and stiffening nonlinearities depend on the probe laser position in the optomechanical system. To calculate the total nonlinearity, the quadratic and cubic nonlinearities α_2 and α_3 are calculated from the second and third order spring constants k_2 and k_3 via $\alpha_2 = -k_2/m_{\mathrm{eff}}$ and $\alpha_3 = -k_3/m_{\mathrm{eff}}$. The detuning Δ and optomechanical coupling G in the expression for the dispersive optical force, Eq. (2.41), are expanded about $x = 0$ to obtain an expression of the form $k_1x+k_2x^2+k_3x^3+\ldots = F(x)$. Using this expansion, the terms proportional to x, x^2, and x^3 are grouped together and the coefficients extracted to obtain expressions for k_1, k_2, and k_3, respectively. We modify the model to account for the nonlinearity of the optical cavity observed in Figure 5.2(c). This can be done by converting the nonlinear phase used to model the optical cavity in Section 5.2 to a nonlinear detuning. The relationship between the phase and the frequency shift is $\omega_{\mathrm{NL}} = -c\phi_{\mathrm{NL}}/L_{\mathrm{c}}n_{\mathrm{g}}$. Using the same approach described in [108], we can add this nonlinear detuning to the standard detuning in the equations for the spring constants k_1, k_2, and k_3 to produce the following equations:

$$k_1 = \frac{4P_{\mathrm{bus}}\gamma_{\mathrm{ex}}G}{\omega}\frac{\zeta(\gamma^2+(\Delta_0+\omega_{\mathrm{NL}})^2) - G(\Delta_0+\omega_{\mathrm{NL}})}{(\gamma^2+(\Delta_0+\omega_{\mathrm{NL}})^2)^2}, \tag{5.6}$$

$$\begin{aligned} k_2 = \frac{P_{\mathrm{bus}}\gamma_{\mathrm{ex}}}{\omega(\gamma^2+(\Delta_0+\omega_{\mathrm{NL}})^2)^3}&[2G^2\gamma^2 - 4\zeta^2\gamma^4 + 12G\zeta(\Delta_0+\omega_{\mathrm{NL}})\gamma^2 \\ -(6G^2+8\zeta\gamma^2)(\Delta_0+\omega_{\mathrm{NL}})^2 &+ 12G\zeta(\Delta_0+\omega_{\mathrm{NL}})^3 - 4\zeta^2(\Delta_0+\omega_{\mathrm{NL}})^4], \end{aligned} \tag{5.7}$$

$$\begin{aligned} k_3 = \frac{P_{\mathrm{bus}}\gamma_{\mathrm{ex}}G}{\omega(\gamma^2+(\Delta_0+\omega_{\mathrm{NL}})^2)^4}&[-8G^2\zeta\gamma^4 + \frac{8}{3}\zeta^3\gamma^6 + (8G^3\gamma^2 - \frac{56}{3}G\zeta\gamma^4)(\Delta_0+\omega_{\mathrm{NL}}) + \\ &(16G^2\zeta\gamma^2 + 8\zeta^3\gamma^4)(\Delta_0+\omega_{\mathrm{NL}})^2 - (8G^3 + \frac{112}{3}G\zeta^2\gamma^2)(\Delta_0+\omega_{\mathrm{NL}})^3 \\ +(24G^2\zeta + 8\zeta^3\gamma^2)(\Delta_0+\omega_{\mathrm{NL}})^4 &- \frac{56}{3}G\zeta^2(\Delta_0+\omega_{\mathrm{NL}})^5 + \frac{8}{3}\zeta^3(\Delta_0+\omega_{\mathrm{NL}})^6]. \end{aligned} \tag{5.8}$$

In these equations, all terms have been previously defined except ζ. ζ is the field amplitude decay constant for the racetrack resonator. This parameter describes the decay length of the amplitude of the evanescent field outside the optical waveguide. It can be calculated using the approach described in Section 2.2.1 and Eq. (2.11). ζ can also be calculated numerically using finite difference simulations and solving for the electric fields of the optical mode in the waveguide. To obtain this parameter, we use mode solver simulations [171] to calculate the field decay outside the waveguide. For our waveguides, this value is equal to $\zeta = 1/83\ \text{nm}^{-1}$. Once ζ is obtained, we can calculate k_2 and k_3 using Eqs. (5.7) and (5.8), and finally solve for the total nonlinearity α by substituting α_2 and α_3 into Eq. (5.3).

The total nonlinearity for the probe laser is solved for a wide range of detunings, using the values in Tables 5.1 and 5.4. The total nonlinearity of the pump laser is solved only at $\Delta = 0$ using the values in Tables 5.2 and 5.4, and the resulting value of $0.092\ \text{MHz}^2/\text{nm}^2$ is summed with the total nonlinearity for the probe laser. The nonlinearity of the pump laser essentially acts as a DC offset since the detuning is constant. The combined nonlinearity is plotted in Figure 5.7. The result shows that for $\Delta = 0.4 - 2.3$ GHz the nonlinearity is negative and therefore a softening effect is expected. All other detunings have a positive nonlinearity and a stiffening effect is expected.

This approach correctly predicts that a stiffening effect occurs for a red-detuned probe laser, and that a softening effect occurs for a blue detuned laser. Therefore, we can conclude that these nonlinearities, opposite to what is expected from the optical spring effect, are introduced by the optical force of the probe laser on the nanomechanical device. This occurs despite the fact that the probe laser power is well below the threshold for self oscillation, as discussed in Chapter 4.

When we examine the results more closely, however, we see that the model correctly predicts the sign of the nonlinearity observed in experiments at all detunings, except at $\Delta = 0$ GHz. At zero detuning, a softening is observed (Figure 5.5(e), third panel) when a stiffening is predicted. To better quantify the agreement between the model and the experimental results, we can apply Eq. (5.2) to calculate a critical amplitude for the nonlinearity. The result for the critical amplitude as a function of detuning for the optical force nonlinearity is shown on the second axis in Figure 5.7, for both the case of the cavity with and without optical nonlinearity. The model shown in Figure 5.7 predicts that for the values of Δ close to zero, the critical amplitude is less than 10 nm. This agrees with the experimental results obtained in Figure 5.5, since all of the mechanical data recorded between $\Delta = -0.5$ GHz and $\Delta = 0.5$ GHz exhibit nonlinear behaviour. This is as expected, because the critical amplitude is less than 10 nm, but the amplitude for this nanomechanical device was previously estimated to be 12.3 nm. However, the model does not hold at a detuning

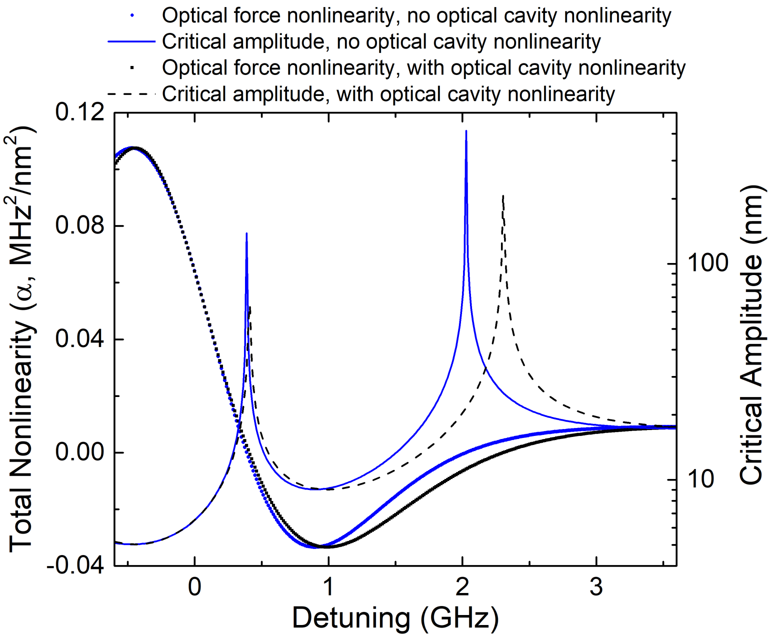

Figure 5.7: The theoretically calculated nonlinearity coefficient α of the combined pump and probe system plotted versus the detuning in units of GHz. The result for a linear optical cavity is shown by the blue circles, and the theoretically calculated α including an optically nonlinear cavity is shown by the black squares. The addition of the optical nonlinearity produces the expected result, with a narrowed linewidth on the red side and a broadened linewidth on the blue side. The blue solid line is the critical amplitude for the optical cavity with no optical nonlinearity, and the black dashed line is the critical amplitude for the optical cavity with nonlinearity.

of $\Delta = 2.0$ GHz. At this detuning, we experimentally observe nonlinear behaviour as shown by Figure 5.5(a) and highest peak in the centre panel of Figure 5.5(e). The critical amplitude at $\Delta = 2.0$ GHz predicted in Figure 5.7 is 20.5 nm when the optical cavity nonlinearity is included in the model. At this detuning, the model presented in Figure 5.7 disagrees with the experimental result.

Although the model shown in Figure 5.7 does indicate that the source of the stiffening and softening nonlinearities observed in experiment are due to an optical force nonlinearity, there are several discrepancies that indicate that the model does not sufficiently describe our optomechanical system. These discrepancies include the incorrect prediction of the sign of the nonlinearity at $\Delta = 0$ GHz, and the incorrect prediction of the critical amplitude at $\Delta = 2$ GHz. These discrepancies may be caused by the very large amplitudes of our cantilever, or the additional complexities introduced by the optical forces of the pump laser, which were only modeled as a DC offset. This model also does not provide any way to incorporate the readout nonlinearity, and therefore cannot predict the non-Lorentzian peak shapes observed in the centre panel of Figure 5.5(e). Additionally, this model does not provide a mechanism to estimate the displacement, which would be useful since the amplitude cannot be correctly measured because of the readout nonlinearity. Finally, we cannot easily separate the optical cavity force and the evanescent force nonlinearities, as they are tied together in this model.

To fully understand our optomechanical system and provide better agreement to experimental results, we must derive an alternative model. This model must model the effects of the pump laser, account for the very large amplitudes of the cantilever, and should also include the readout nonlinearity in order to accurately describe the optomechanical system.

5.3.2 Numerical Model

We have demonstrated that existing models of optomechanical nonlinearities do not sufficiently describe our optomechanical system, likely due to the complexity of the second pump laser in the system and the large amplitudes achieved by the cantilever using the pump-and-probe technique. To accurately model the behaviour of our optomechanical system we use a numerical approach. We solve a set of coupled differential equations that describe the interaction between the probe laser optical resonance, the pump laser optical resonance, and the mechanical resonator. This approach is derived using the energy coupling formalism for the optical cavity described in Section 2.2.5. Recall that the energy coupling formalism describes the coupling of optical power in time, and therefore we describe the evolution of the optical cavity amplitude as a function of time, $a(t)$. The amplitude in the ring is dependent on the loss rate γ, the external loss rate γ_{ex}, the power in the bus waveguide P_{bus}, and the detuning $\Delta = \omega - \omega_0$. The optomechanical coupling coefficient G describes the interaction of the optical cavity with the nanomechanical device. To describe the rate of change of the optical cavity amplitude as the mechanical device oscillates, we can derive the optomechanical Hamiltonians. This procedure has been previously presented for the interaction between a mechanical resonator and a single optical cavity [143]. The additional complication in our system arises due to the presence of the pump laser to drive the nanomechanical device. The pump laser adds a second, time-varying optical cavity to the system of equations. By following the approach used in [143], we can write a system of equations for the optomechanical pump-and-probe system. The equations for the probe optical cavity (subscripts 1), pump optical cavity (subscripts 2), and mechanical resonators are as follows:

$$\dot{a}_1(t) = -\gamma_1 a_1(t) + i(\Delta_1 + Gx(t))a_1(t) + \sqrt{2\gamma_{\text{ex},1}P_{\text{bus},1}/\hbar\omega_1}, \tag{5.9}$$

$$\dot{a}_2(t) = -\gamma_2 a_2(t) + i(\Delta_2 + Gx(t))a_2(t) + \sqrt{2\gamma_{\text{ex},2}P_{\text{bus},2}/\hbar\omega_2}, \tag{5.10}$$

$$m_{\text{eff}}[\ddot{x}(t) + \Omega_0\dot{x}(t)/Q + \Omega_0^2 x(t)] = \hbar G|a_1(t)|^2 + \hbar G|a_2(t)|^2, \tag{5.11}$$

where $a(t)$ is the normalized (unitless) time-dependent optical cavity amplitude, and all other parameters have been previously defined. The main difference between Eqs. (5.9) and (5.10) are the functional forms of P_{in}, the input power to the system. $P_{\text{in},1}$ is a DC optical power determined by the probe laser power input to the system, and the detuning Δ_1 varies to mimic the probe laser sweep in Figure 5.5. The pump input power, $P_{\text{in},2}$, has both a DC and an AC component, to mimic the experimental conditions provided by the EOM. The form of the pump power is $P_{\text{in},2} = P_{\text{in},2}^{\text{DC}} + P_{\text{in},2}^{\text{AC}}\cos(\xi\Omega_0 t)$. The pump laser has a constant detuning of $\Delta_2 = 0$ GHz, as it is always set at the cavity minima. The probe and pump input powers have both been normalized by $\hbar\omega$ such that the units for the input power are in Hz. The variable ξ is used to calculate the response off-resonance, and is defined as Ω/Ω_0. By setting ξ to a range of values between $\xi = 0.999$ and $\xi = 1.001$, we can effectively sweep the mechanical frequency in the equations, thereby mimicking the experimental results. The evanescent force is not initially included in the model, as we wish to determine which of the two optical force nonlinearities is the most significant contributing factor. By simultaneously solving these three equations numerically for a range of values for Δ_1 and ξ, we can determine a solution for $x(t)$ and $a(t)$ at various optical detunings and mechanical frequencies close to resonance. The coupled set of equations is solved simultaneously for time steps increasing from 100 ns to 1 ms. Once the time domain results are obtained, they are transformed to the frequency domain using a numerical fast Fourier transform. We select only the steady state data from the end of the simulations for our analysis. The values input to the simulation are listed in Tables 5.1, 5.2, and 5.4.

We compare the simulated optical cavity data $a_1(t)$, which is the optical resonance in which the probe laser is positioned, to the experimentally obtained results. To make this comparison, we start with the simulated value $a_1(t)$, which is the normalized, time-averaged complex amplitude inside the racetrack resonator cavity. To convert this value to the optical power inside the bus waveguide, we must convert the amplitude from a normalized value to an optical amplitude by multiplying the amplitude by $(\hbar\omega_1)^{1/2}$. Then, we re-write Eq. (2.27) in terms of the input power and cavity amplitude to obtain

$$P_{\text{out},1} = |\sqrt{P_{\text{in},1}} - \sqrt{2\gamma_{\text{ex},1}\hbar\omega}a_1(t)|^2, \tag{5.12}$$

where $P_{\text{out},1}$ is the output power in the bus waveguide from the racetrack resonator and includes the signal at the fundamental resonance frequency, as well as all of the higher order harmonics. It also includes a DC component. The DC component is comprised of the DC output from the optical cavity in the absence of modulation, which is the typical output observed in Figure 5.2, and a DC signal formed from the self-beating of the harmonics, which downmixes to a DC signal. By taking the Fourier transform of $P_{\text{out},1}$, we can filter out the DC component at 0 Hz. The Fourier transform also allows us to separate the simulated results by frequency, allowing for results at the fundamental frequency and all of the higher order harmonics. We extract the peaks from the frequency spectrum for each detuning, normalized mechanical frequency ξ, and at the first four harmonics in the frequency spectrum. The simulated results at the fundamental resonance frequency are shown in Figure 5.8. The results for the second through fourth harmonics are shown in Figure 5.9(a)–(f). The simulated results (open points) are compared to the experimental results (solid lines). To compare the experimental results at the same point in the experimental setup, we take the results from the lock-in amplifier (recorded in volts), and use the responsivity of the photodetector (in W/V) to convert the results to an optical power. By accounting for the losses in the experimental setup between the bus waveguide and the photodiode, we convert the experimental results in volts to an optical power in the bus waveguide for direct comparison to the simulated results. We also normalize the experimentally recorded frequencies by $\Omega_0 = 2\pi \times 21.1956$ MHz, which is the resonance frequency of the thermomechanical noise at zero detuning (Figure 5.3). One potential source of error in this conversion is imperfect alignment of the laser spot on the grating couplers, which may result in improved or reduced optical power measured at the photodiode, which would then change the calculated power in the bus waveguide. For this reason, comparison between the shape of the peaks, instead of the peak heights, is of greater importance in this analysis. Correct agreement in the peak shape indicates that we have successfully modeled the source of nonlinearity in the system.

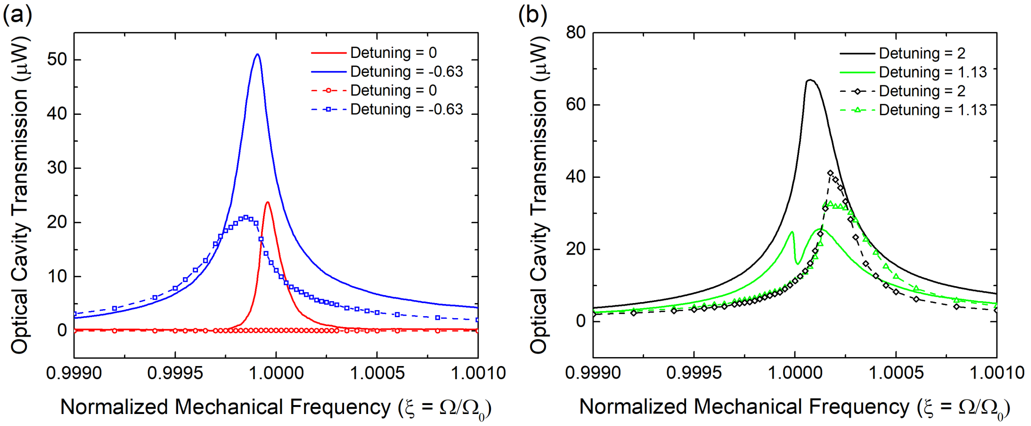

Figure 5.8: Comparing the numerically modeled results (dashed lines with open symbols) to the experimental data (solid lines) for the fundamental mechanical resonance frequency. The results for $\Delta = 0$ GHz and $\Delta = -0.63$ GHz are shown in (a), and the results for $\Delta = 1.13$ GHz and $\Delta = 2$ GHz are shown in (b). The correct stiffening and softening behaviour is identified in all cases except $\Delta = 0$, where a signal of zero is predicted by simulation. Although the correct directions of stiffening and softening are predicted, the simulated peak shapes do not closely match experimental results, which indicates that this model is incomplete.

In addition to the optical cavity data, we can also extract the results for the mechanical amplitude x from the simulation. This result is shown in Figure 5.10 for four different detunings. The calculated mechanical displacement had components only at the fundamental resonance frequency and no signals at higher frequency components, confirming that the harmonics are generated by the readout and not by the mechanical device itself. The same analysis procedure used to extract the frequency components of the simulated optical cavity data was used to extract the mechanical amplitude. The steady state time domain data was Fourier-transformed to frequency data, and the peak value extracted at each Δ and ξ. The simulated results show that the amplitudes achieved by the nanomechanical cantilever are significantly higher than those calculated using the responsivity obtained from the thermomechanical noise. The peak simulated amplitudes range from 12.1 nm at a detuning of $\Delta = -0.63$ GHz, up to a maximum of 13.1 nm at a detuning of $\Delta = 2.0$ GHz. These amplitudes are very close to the 12.3 ± 0.4 nm estimated from Figure 5.5. The peak heights of the simulations are as expected based on the optical damping and amplification discussed in Section 2.3. The amplitude of the cantilever measured by a red-detuned probe laser is slightly damped compared to the amplitude measured by a blue-detuned probe laser.

One of the most important features in Figure 5.10 is that the detuned results show nonlinear behaviour, where blue-detuned peaks show softening behaviour and the red-detuned peaks show stiffening behaviour. At zero detuning, the stiffening

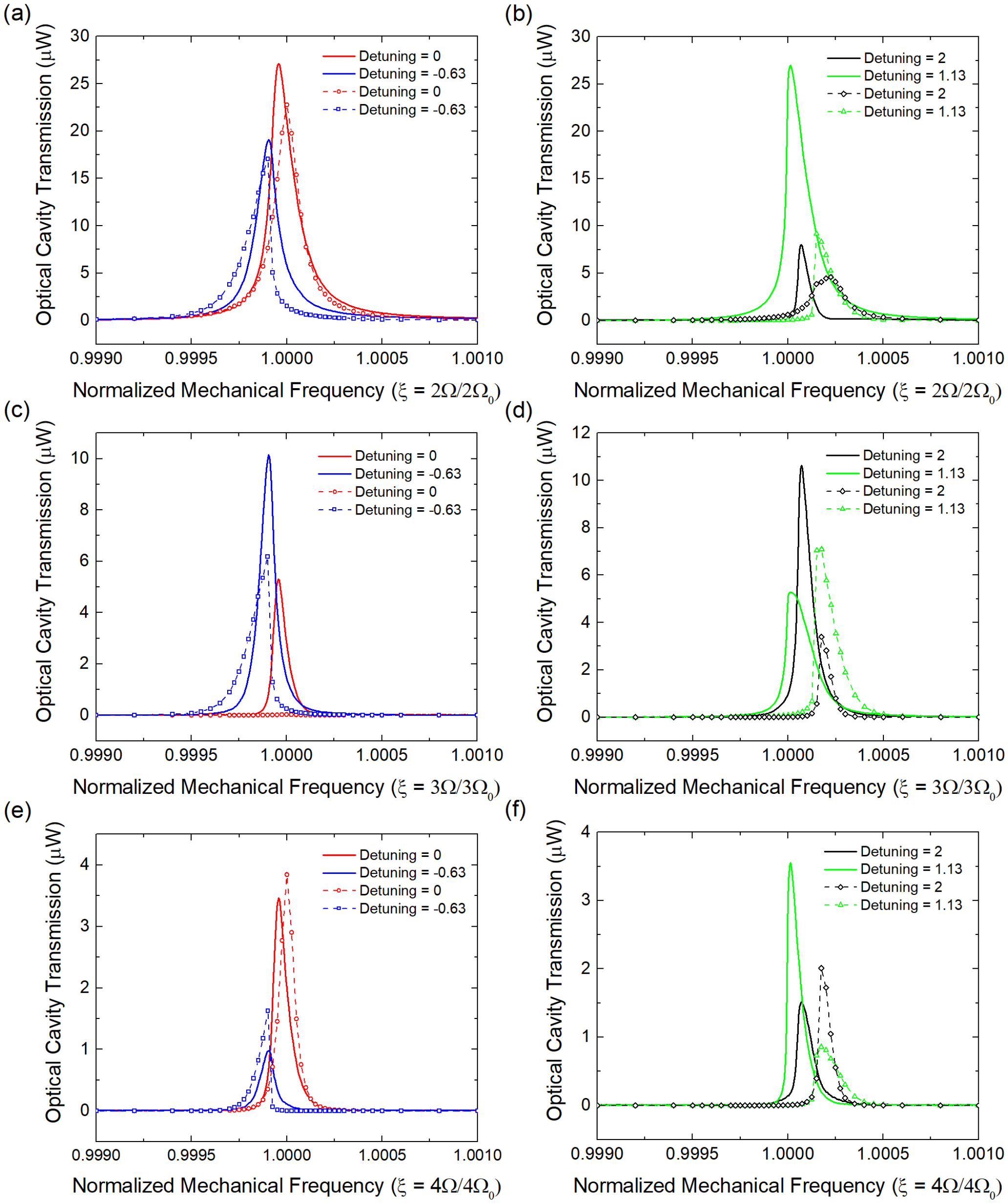

Figure 5.9: Comparing the results from the numerical model (dashed lines with open symbols) to the experimental data (solid lines) for the second, third, and fourth harmonics. The results for $\Delta = 0$ GHz and $\Delta = -0.63$ GHz are shown for (a) the second harmonic, (c) the third harmonic, and (e) the fourth harmonic. The results for $\Delta = 1.13$ GHz and $\Delta = 2$ GHz are shown in for (b) the second harmonic, (d) the third harmonic, and (f) the fourth harmonic. The correct directions for the stiffening and softening are predicted for every detuning except $\Delta = 0$ GHz.

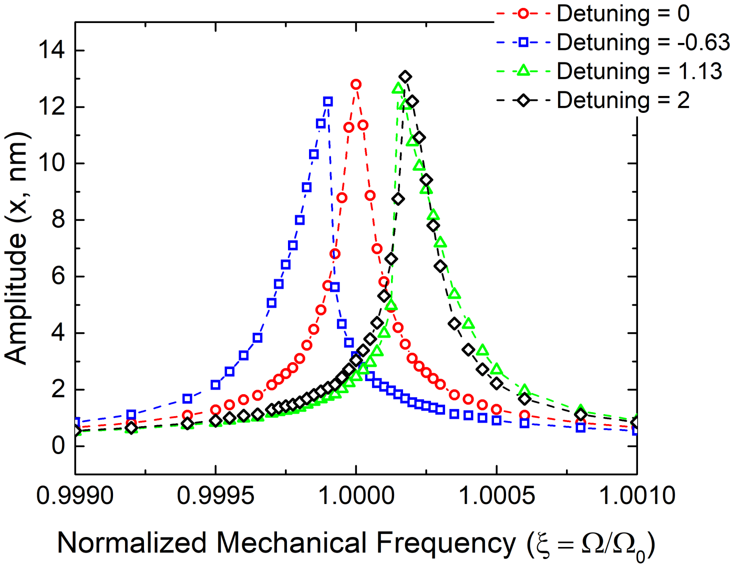

Figure 5.10: Calculated mechanical amplitude x obtained from simultaneous numerical solutions of Eqs. (5.9)–(5.11) for four different detunings. The dashed lines are a guide to the eye. The amplitudes are close to the experimental result of 12.3 ± 0.4 nm. This graph demonstrates that the amplitude is fairly consistent for each detuning, which is as expected since the pump-and-probe approach applies the same pumping force at each detuning. The effect of the probe laser is evidenced by the slight damping of the red-detuned result compared to the blue-detuned results.

and softening nonlinearities vanish, causing the amplitude to be symmetric. This indicates that the stiffening and softening nonlinearities are induced by the position of the probe laser in the system, as that is the only parameter changing in the simulations. From this we confirm that the optomechanical force nonlinearity affects the mechanical device itself, and is separate from the readout nonlinearity and its associated harmonic frequencies. The nonlinearity in this case is purely the optical cavity force nonlinearity induced by the probe and pump lasers, as the evanescent force was not included in these simulations.

One difference between the simulated and experimental results is immediately obvious. In Figures 5.8 and 5.9(c), which show the results for the first and third harmonics, the simulated result is zero for all mechanical frequencies when $\Delta = 0$ GHz. This is because the simulation is based on a perfectly symmetric optical cavity, thus the transduction at zero detuning is zero. However, for the experimental result, there is a peak when $\Delta = 0$ GHz. The presence of a signal at $\Delta = 0$ GHz in the experiment may be due in part to the asymmetry in the optical cavity from Figure 5.2(c). Since the optical peak is asymmetric, the signal will be greater on one side than the other, producing a signal at $\Delta = 0$ GHz. The cavity asymmetry does not, however, account for the slight softening of the experimentally observed signal at zero detuning, as that is a mechanical effect and not caused by the readout. From this, we conclude that the evanescent force is an important factor in this optomechanical system. Since the cantilever is external to the optical cavity, the optical gradient force interacting with the cantilever is an evanescent force with an exponential form. Typically, the amplitudes of the cantilevers are sufficiently small that the exponential force can be linearized about the initial displacement point of the beam. In this case, however, the amplitudes are very large, and the exponential form of the evanescent field must be accounted for. To introduce an exponential dependence in Eqs. (5.9) to (5.11), we modify the optomechanical coupling term to include an exponential decay. The optomechanical coupling has been previously demonstrated to have an exponential form [219], and can be written as

$$G = G_0 \exp(-2\zeta x), \tag{5.13}$$

where G_0 is the optomechanical coupling of the stationary device, x is the amplitude of the mechanical device, and ζ is the exponential decay constant of the evanescent field outside the waveguide. x is referenced to the initial, stationary position of the cantilever and is permitted to be positive or negative in the simulations. ζ is the same value previously calculated to be $1/83\ \text{nm}^{-1}$ using mode solver simulations. By substituting Eq. (5.13) into the set of coupled equations (5.9)–(5.11), we create a set of equations where the result x is dependent on the exponential decay of the evanescent field outside the waveguide, therefore accounting for the fact that the cantilever is external to the waveguide. We solve this set of equations numerically using the same approach as before. The data is extracted from the simulation using the same technique. The results for the optical cavity output at the fundamental mechanical frequency are shown by Figure 5.11. The experimental results are plotted in the same graphs for straightforward comparison. The results for the second, third, and fourth harmonics are plotted in Figure 5.12.

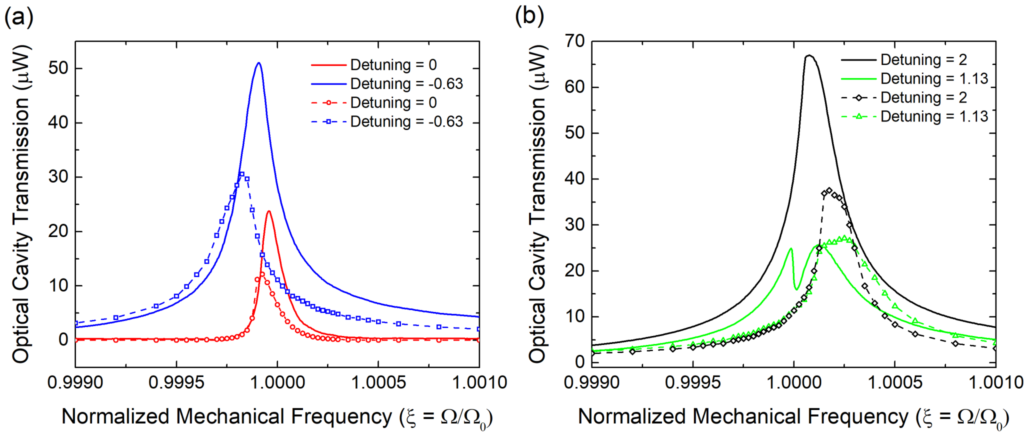

Figure 5.11: Comparing the results from the numerical model (dashed lines with open symbols) to the experimental data (solid lines) for the fundamental mechanical resonance frequency, where the model includes a displacement-dependent G caused by the evanescent force. The results for $\Delta = 0$ GHz and $\Delta = -0.63$ GHz are shown in (a), and the results for $\Delta = 1.13$ GHz and $\Delta = 2$ GHz are shown in (b). The correct stiffening and softening behaviour is identified by the numerical model for each detuning. The simulated peak shapes agree well with the experimental shapes, including at zero detuning. The slight dip in the result at $\Delta = 1.13$ GHz is also predicted by the simulation. The difference in the size of the dip may be explained by the asymmetry in the optical cavity, which is not modeled by these simulations. Overall the agreement between the experimental and predicted peak shapes is excellent, and indicates that we have successfully modeled the sources of nonlinearity in the model.

By including the exponential decay of the evanescent field in the optomechanical coupling coefficient, a signal is now visible at zero detuning. The signal at zero detuning also shows a softening effect, and matches well with the measured data. The signals at other detunings also have similar curve shapes to the measured data. Notably, the signal at $\Delta = 1.13$ GHz at the fundamental harmonic (Figure 5.11(b)) has a slight dip in the response, and while not as dramatic as the dip in the experimentally measured response, this demonstrates the model is able to reproduce the experimental results well. The remaining discrepancies may be a result of the slight optical nonlinearity in the optical cavity, error in extracting the exact optical power in the measured value since the coupling into the grating couplers is not known precisely, and small errors in experimentally determining the detuning. Overall,

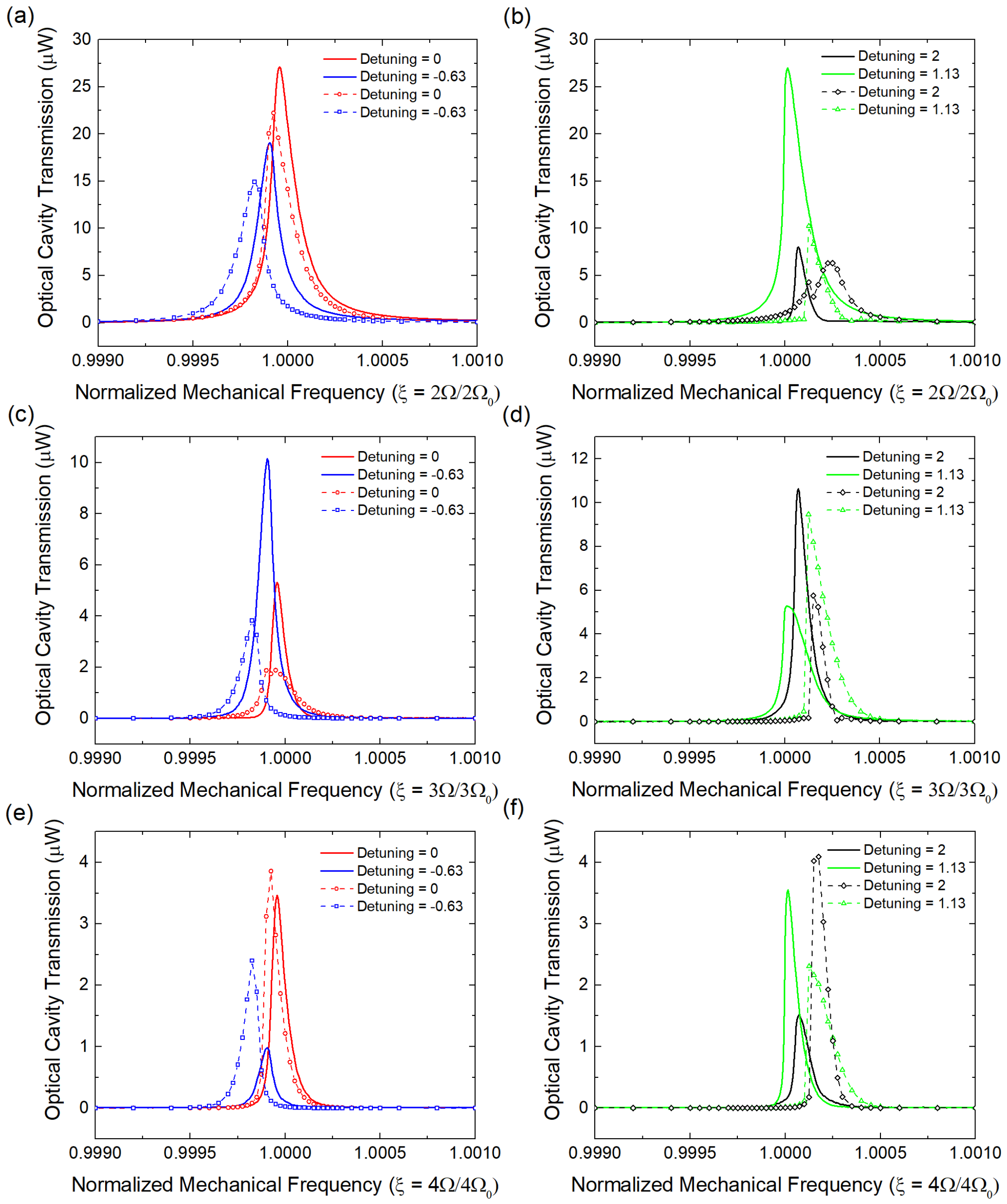

Figure 5.12: Comparing the numerically modeled results (dashed lines with open symbols) to the experimental data (solid lines) for the second, third, and fourth harmonics, where the model includes a displacement-dependent G caused by the evanescent force. The results for $\Delta = 0$ GHz and $\Delta = -0.63$ GHz are shown for (a) the second harmonic, (c) the third harmonic, and (e) the fourth harmonic. The results for $\Delta = 1.13$ GHz and $\Delta = 2$ GHz are shown in for (b) the second harmonic, (d) the third harmonic, and (f) the fourth harmonic. The correct directions for the stiffening and softening are predicted for all detunings.

the addition of the evanescent force into the simulations significantly improves the prediction of the curve shape in comparison to the results of Figures 5.8 and 5.9. From this we can conclude that the evanescent force nonlinearity adds distortions in the signal shape that must be accounted for, and that it also causes asymmetry in the signal that permits the signal at zero detuning to be observed.

We can also examine the effects of the evanescent force nonlinearity directly on the mechanical amplitude, which is shown in Figure 5.13. The main difference between the results in Figures 5.10 and 5.13 is that the mechanical signal at zero detuning exhibits softening in the latter figure. This is because of the extra nonlinearity included in this simulation, caused by the exponential form of the evanescent force. The amplitudes are fairly similar, although slightly smaller in the case where the evanescent force is included. The amplitudes for the evanescent force case are 12.5 nm for $\Delta = 2$ GHz, 11.5 nm for $\Delta = 1.13$ GHz, 11.9 nm for $\Delta = 0$ GHz, and 12.1 nm for $\Delta = -0.63$ GHz. All of these values are within error of the experimentally estimated value of 12.3 ± 0.4 nm, with the exception of the value at $\Delta = 1.13$ GHz, which is slightly below the expected value. Although the amplitude peak shapes are different when comparing the results from the simulations with and without the evanescent force included, the overall heights are not significantly different.

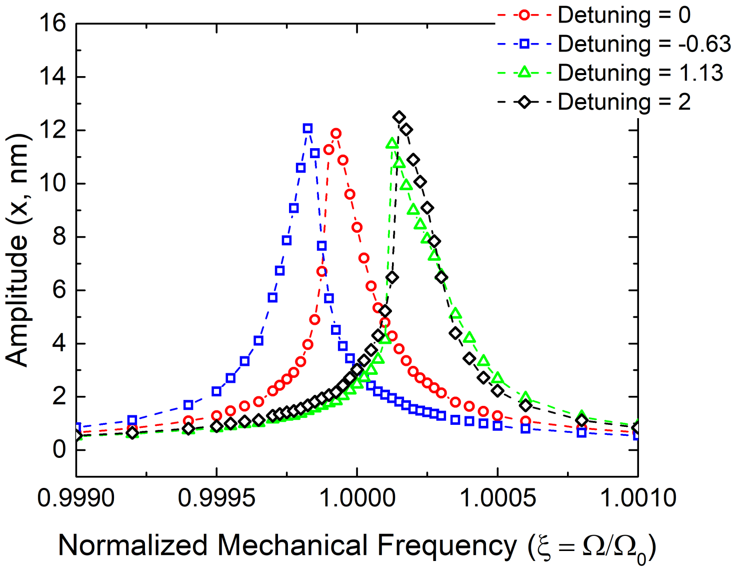

Figure 5.13: Calculated amplitudes obtained from simultaneous solutions of Eqs. (5.9)–(5.11), with the exponential form of the optomechanical coupling included. The dashed lines are a guide to the eye. All the simulated results are within error of the experimental result except the value at $\Delta = 1.13$ GHz.

The result obtained in Figure 5.13 is also important because it demonstrates that the amplitude of the mechanical signal does not change significantly throughout the range of detunings. The change in the amplitude between detunings in Figure 5.13 is less than 10%. The optical force nonlinearities induced by the pump and probe lasers clearly alter the peak shape and the nonlinear behaviour of the optomechanical signal, but do not substantially alter the amplitude of the mechanical device over the simulated detuning range. This indicates that the assumption that we made to calculate the moving average of the optical cavity derivatives in Figure 5.6 holds true; that is, using a window of constant size to calculate the moving averages is a reasonable approximation. Since the agreement between the optical cavity derivatives and the peaks of mechanical signals depends only on the window size, as demonstrated in Figure 5.6, we can conclude that the nonlinearity introduced by the probe laser does not substantially affect the harmonic content of the mechanical signal. In other words, the amplitude of the harmonics observed in the experiment are indeed purely a readout nonlinearity, and are not strongly affected by the optical force nonlinearity present in the system.

5.3.3 Simulating the Critical Amplitude

One final comparison that can be made between these numerical results and the model presented in the previous section is a comparison of the critical amplitude. To test the critical amplitude using simulated values, we return to the modeling without the evanescent force. This decreases the computation time and complexity, and is an acceptable substitution for an estimate of the critical amplitude since the mechanical amplitudes from Figures 5.10 and 5.13 are very close. By increasing the AC component of $P_{\text{in},2}$ in the model, we increase the driving power in the model to mimic the experimental conditions used in the experimental measurement of Figure 5.4. We perform these computations at detunings of $\Delta = \pm 0.61$ GHz and use the cavity parameters for the lowest wavelength curve from Figure 5.2 (Table 5.3) to provide further similarity to the experimental conditions used to obtain Figure 5.4. The resulting amplitudes in nanometres are shown in Figure 5.14(a) for a range of input powers.

The critical amplitude is extracted using "backbone" approach detailed in Section 5.1. The backbone method is preferred in the case of simulated results compared to the 1 dB compression point approach. In the 1 dB compression point approach, several peaks at low power with linearly increasing amplitude are required to obtain the linear trend. The exact peak height is also necessary, requiring very high resolution in ξ. This makes this approach an experimentally straightforward one, but a numerically challenging one as the required resolution in both frequency and input power is computationally expensive.

To extract the critical amplitude, we find the peak of each mechanical resonance

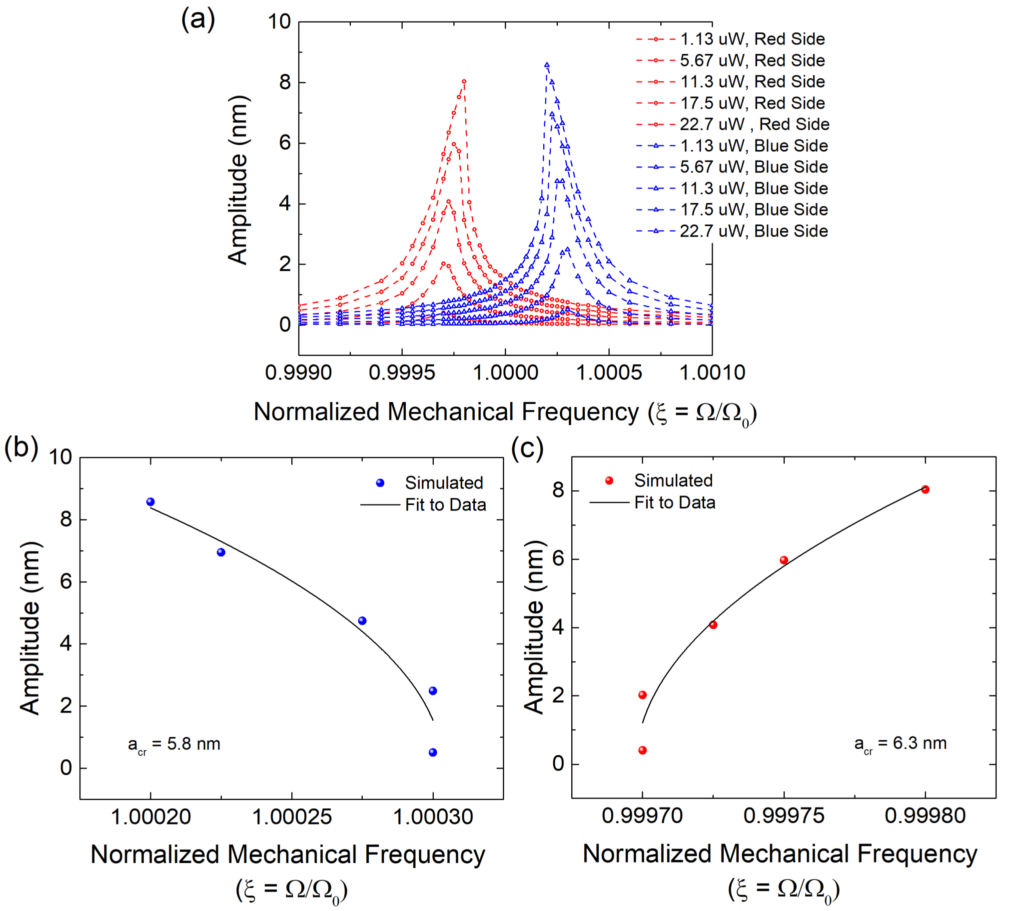

Figure 5.14: (a) Modeled amplitudes with increasing input AC pump power. The optical cavity data input to the simulation were the same as the experimental results in Figure 5.4; the pump laser was positioned at the lowest-wavelength optical cavity resonance (Table 5.3), and the probe laser was positioned at the point of steepest slope on the centre optical cavity transmission. (b) Critical amplitude extraction using the backbone curve technique for the blue side model. The critical amplitude is 5.8 nm. (c) Critical amplitude extraction using the backbone technique for the red side model. The critical amplitude is 6.3 nm. The simulated result that the critical amplitude is larger for red probe detuning compared to blue probe detuning matches the experimentally observed result in Figure 5.4.

in Figure 5.14(a) and plot it versus the peak frequency to obtain the plots shown in Figure 5.14(b) and (c), for the blue and red detuned probe laser positions respectively. We fit these curves using Eq. (5.4) to obtain the nonlinearity coefficient α. Finally, we input α into Eq. (5.2) to calculate the critical amplitude for each detuning. The critical amplitude when the laser is blue-detuned is 5.8 nm, and the critical amplitude when the laser is red-detuned is 6.3 nm. This result indicates that the red side is more difficult to drive into nonlinearity, which agrees with the result found experimentally in Figure 5.4. In contrast, the analytical model summarized by Figure 5.7 incorrectly predicts that the critical amplitude should be lower on the red side compared to the blue side for $\Delta = \pm 0.61$ GHz. That our numerical model correctly produces this asymmetry in the critical amplitude is a notable accomplishment.

The original experimental critical amplitudes from Figure 5.4 were 1.9 nm for the blue detuned probe laser, and 3.6 nm for the red detuned probe laser. The numerical model predicts significantly higher critical amplitudes, 3 times higher for the blue-detuned case and 1.75 times higher for the red-detuned case. This again suggests that the calculation of the amplitude using the thermomechanical noise responsivity is not accurate as a result of the readout nonlinearity. Recall that the expected amplitude of the largest mechanical signal in Figure 5.4(a) is 6.3 nm based on the applied optical force and Eq. (4.4). The simulated critical amplitude of 5.8 nm is much closer to this value than the thermomechanically calibrated critical amplitude of 1.9 nm. This indicates that we may use the simulated critical amplitude as a calibration technique for the amplitude when a readout nonlinearity is present, if the critical amplitude can be determined both experimentally and numerically and the input parameters to the model such as optical cavity properties and optical power are known.

5.4 Discussion

This analysis demonstrates that even if the readout nonlinearity is eliminated, optomechanical nonlinearities induced by the force of the pump and probe lasers still exist in the system. This implies that we have multiple simultaneous nonlinearities; readout nonlinearity, optical cavity force nonlinearity, and evanescent force nonlinearity. Without numerical modeling, we would not be able to separate them. With the modeling, however, we are able to see that the harmonics in the mechanical frequency spectrum are generated by the readout nonlinearity. This is caused by the Lorentzian lineshape of the optical cavity. The readout nonlinearity is what prevents proper calibration using the thermomechanical noise. The softening and stiffening behaviour observed in the experiment are a result of the optomechanical force nonlinearities, the optical cavity force nonlinearity caused by the pump and probe lasers moving through the Lorentzian lineshape of the optical cavity and the evanescent force nonlinearity caused by the cantilever moving towards and away from the racetrack resonator. The readout nonlinearity cannot cause this type of mechanical peak asymmetry, as it does not affect the movement of the mechanical device. Finally, our detailed numerical approach is important to ensure that the effects of both the pump and probe are modeled accurately. Previously published models studying optomechanical nonlinearities do not include a strong, amplitude modulated pump laser. Since the power of this laser is high, it is important that the optical force nonlinearities generated by this laser are taken into consideration as well. Table 5.5 summarizes different approaches used to model the optomechanical nonlinearity in the literature. This table demonstrates that our numerical model occupies a unique niche. It is the only model that accounts for nonlinearities using a pump-and-probe approach with an AC amplitude modulation on the pump laser.

Table 5.5: Summary of Approaches to Optomechanical Nonlinearity

Type of Nonlinearity	Experiment	Bessel Function Expansion [216]	Optical Force Expansion [219]	Numerical Model, Constant G	Numerical Model, Exponential G
Readout	Yes	Yes	No	Yes	Yes
Optical cavity force, DC	Yes	Yes	Yes	Yes	Yes
Evanescent force, DC	Yes	No	Yes	No	Yes
Optical cavity force, AC	Yes	No	No	Yes	Yes
Evanescent force, AC	Yes	No	No	No	Yes

By comparing the information from experiments and the detailed numerical modeling with and without the exponential form of the optomechanical coupling included, we are able to fully understand the source of nonlinearities in our optomechanical system. This is important so that we can design future optomechanical systems for reduced nonlinearity to improve the dynamic range of our sensor. To reduce the readout nonlinearity, we can design optical cavities with longer linear ranges or smaller optomechanical coupling. Smaller optomechanical coupling will result in a smaller optical cavity shift for a given nanomechanical amplitude. To reduce the optical cavity force nonlinearity, the optomechanical coupling could be reduced, or the optical input power could be reduced. The detuning is also an important point to choose experimentally, as the detuning impacts the amount of nonlinearity caused by the optical cavity force. To reduce the evanescent force nonlinearity, the optomechanical coupling could be decreased yet again, so that the operation point of the optomechanical system is in the more linear region of the exponential curve. Clearly, a higher optomechanical coupling is not necessarily ideal for optomechanical systems to be used as mass sensors. The downside of decreasing the optomechanical coupling is a decrease in the signal-to-noise ratio and the efficiency of the optical driving force, as the readout and actuation are both proportional to the optomechanical coupling.

Clearly many possibilities exist to improving the dynamic range of the optomechanical system, however, they come at a cost. A trade-off in the design must be made to optimize both the linearity of the system and the signal to noise ratio. With the knowledge of the source of the nonlinearity, and the ability to simulate the different types of nonlinearity individually, we can determine the best designs to maximize the linear range while maintaining a suitable signal to noise ratio in future designs.

5.5 Conclusion

We have demonstrated that several optomechanical nonlinearities occur simultaneously when a mechanical device such as a cantilever is undergoing large amplitude vibrations induced by a coherent driving force. The nano-optomechanical pump-and-probe system produces harmonics in the mechanical frequency spectrum, which are a signature of a readout nonlinearity. The system also exhibits a stiffening nonlinearity when the probe is red-detuned and a softening nonlinearity when the probe laser is blue detuned, which is opposite to the expected result introduced by the optical spring effect. These nonlinearities are caused by an optical cavity force nonlinearity induced by the detuning of the probe laser in the system. The third nonlinearity, caused by the evanescent force outside of the racetrack resonator cavity, results in a signal at zero detuning that exhibits a softening nonlinearity. These types of nonlinearity cannot be separated and understood only by looking at the experimental results or by previous models in the literature due to the added complexity of the pump laser in the system. We have used full numerical modeling to study the system and determine the differences between these two sources of nonlinearity. The numerical models also aid in the determination of the mechanical amplitude, since the typical thermomechanical noise responsivity cannot be used to calibrate the amplitude when the readout is nonlinear.

Numerical modeling of our pump-and-probe optomechanical system provides a much better understanding of the dynamics of the system, and allows us to separate the readout nonlinearity from the two optical force nonlinearities. In the future, these results could allow for better optical cavity design for optimization of linear operation for both the force and the transduction. The full understanding of the nonlinearities in the system may also be useful for applications where nonlinearities are required, and in determining whether a sensor is in the linear or nonlinear regime.

Chapter 6

Transduction of Large Amplitudes with Racetrack-Loaded Mach Zehnder Interferometers

In this section we discuss the design and measurement of an optomechanical system to increase the range of linear operation of a nanomechanical sensor with large amplitude. In Chapters 4 and 5, cantilevers with very large amplitudes produced nonlinear readout, which is detrimental to sensor performance. Ideally, an optomechanical sensor will reach large amplitudes of vibration with linear readout to maximize the dynamic range of the sensor.

To solve this issue, we design a photonic circuit with a larger linear readout range. In Section 6.1, we create a definition of the linear range using the transmission of the photonic circuit. This definition is based on our experimental procedure. We apply this definition to the racetrack resonators used in previous chapters to create a baseline linear range. The next section, Section 6.2, take this definition and applies it to a new photonic circuit, the racetrack-loaded Mach Zehnder interferometer. In this section we demonstrate the design of this new circuit including the derivation of the transfer function of the circuit. Our analysis suggests that this circuit will allow the cantilever to reach larger vibrational amplitudes with linear readout, without compromising the high sensitivity of optomechanical transduction, and is robust to fabrication imperfections. As this design converts a phase measurement to an amplitude measurement, it may allow for a greater flexibility in applications such as on-chip homodyne detection. We fabricate a variety of design with different coupling conditions to fully explore the parameter space of this photonic circuit. We then characterize the optical and mechanical performance of these optomechanical systems in Section 6.3. The optical results demonstrate that for most coupling conditions, the racetrack-loaded MZI provides an enhancement in both the linear range and the sensitivity compared to a racetrack resonator only. The mechanical measurements confirm that the linear range and sensitivity is improved for certain coupling conditions. In Section 6.4, we discuss the results in detail and determine that by switching to the racetrack-loaded MZI architecture, that a 2.8 times improvement in mass sensitivity may be gained. In Section 6.5, we summarize and conclude that these results provide a good parameter space for future work, and highlight the best designs to use moving forward.

6.1 Defining the Linear Range

Compared to doubly clamped beams, cantilevers are better mass sensors due to their smaller effective mass. They also have a larger dynamic range, which is beneficial for mass sensing applications in ambient or fluidic conditions where the quality factor is relatively low [18]. This improvement in dynamic range is useless, however, if the readout does not remain linear throughout the entire amplitude of vibration. As demonstrated in Chapter 5, optical cavities with reasonably good finesse (≈400) close to critical coupling do not have enough range for linear readout. Other racetrack resonators, such as over-coupled cavities with lower finesse (50–70) also do not have enough linear range [235], although higher amplitudes can be reached. Based on this experimental evidence, we can conclude that although racetrack resonators are very sensitive photonic elements, they lack the linear range required to measure the large amplitudes of vibration produced by cantilevers.

We would like to design an alternative photonic circuit with a higher linear range for mass sensing applications. To determine whether the linear range is enhanced, we require a definition for the linear range that can be compared to the racetrack resonator response. Ideally, the linear range should be determined from the optical properties of the photonic circuit so that we can obtain an estimate of the linear range from analytic equations of the photonic circuit transmission response, and easily compare it to the racetrack resonator response. Defining the linear range based on the optical response is not a straightforward process, as there are many potential definitions that could be used. We will be begin by defining a linear range for the racetrack resonators that is based on our experimental limitations. The linear range is defined in nanometres, and represents the linear wavelength span of the photonic circuit. We can then apply this definition to new designs to determine whether the linear range has been enhanced.

During the optomechanical measurements, we place the probe laser at the position of largest absolute value of the slope of the optical cavity transmission. This measurement point produces the largest transduction coefficient, as shown by the term $\mathrm{d}T/\mathrm{d}\lambda$ in Eq. (2.42), and therefore the signal with the largest signal-to-noise ratio (SNR). We will define this point as the mid-point of the linear range because the increase or decrease in optical cavity transmission induced by the mechanical vibration are measured with reference to this point. It is the point of zero deflection for the cantilever. We also saw in Chapters 4 and 5 that when the cantilever amplitude becomes too large, the cavity shifts sufficiently that the probe laser moves from one side of the optical cavity to the other. This produces dips in the mechanical signal readout (Figures 4.5 and 5.5). The dips are a result of nonlinearity in the signal readout, and as such represent a limitation on the linear range of the readout. The maximum cavity shift that produces a linear readout is therefore limited to the distance in wavelength between the initial probe position and the resonance wavelength of the racetrack resonator. The maximum linear cavity shift is introduced by the mechanical device moving from a deflection of zero to a point of maximum positive (or negative) deflection. Therefore, the total linear range is two times the maximum cavity shift, to account for the cantilever moving from zero deflection to a point of maximum negative (or positive) deflection, shown visually in Figure 6.1.

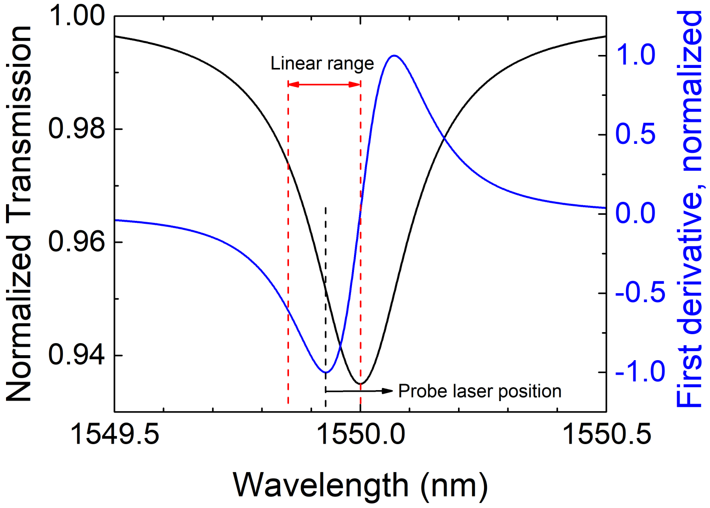

Figure 6.1: Graphical representation of the linear range, using the racetrack resonator transmission function as an example. The racetrack resonator response plotted here has a round trip loss $a_{\mathrm{rt}} = 0.9991$ and a transmission coefficient $\tau = 0.95$. The probe is positioned at the point of minimum (or maximum) slope, denoted by the dashed black line. The linear range is defined as two times the wavelength distance between the point of minimum (or maximum) slope, and cavity minimum where the slope is equal to zero. The edges of the linear range are denoted by the dashed red lines. The linear range is spanned by the solid red arrow. For this example case, the linear range is 0.14 nm.

To generalize this result, we define the linear range as two times the distance between the cavity minimum and the point of maximum slope. Expressed in terms of the first derivative of the optical cavity transmission, this is two times the distance between the first derivative minimum or maximum, and the point where the first derivative equals zero. This is shown graphically in Figure 6.1. This graph is produced by calculating the optical cavity transmission using Eq. (2.25) for a round trip loss $a_{\mathrm{rt}} = 0.9991$ and a transmission coefficient $\tau = 0.95$. The slope is calculated by taking the first derivative of the optical cavity transmission. This definition is based on the experimental procedure of choosing the point of highest slope as the operating point of the measurement, and accounts for the fact that the probe cannot cross over the cavity minimum without producing a readout nonlinearity.

6.2 Design of Racetrack-Loaded Mach Zehnder Interferometers

To improve the linear range of the optical readout, we can more closely examine the transfer function of the all-pass racetrack resonator. In Eq. (2.25, we describe the transmission of the all-pass racetrack resonator by taking the square of the absolute value of the transfer function. However, the transfer function also has a phase component Φ that is described by [94]:

$$\Phi(\phi) = \arctan\left(\frac{\sin\phi}{\tau/a_{\mathrm{rt}} - \cos\phi}\right) - \arctan\left(\frac{\sin\phi}{1/\tau a_{\mathrm{rt}} - \cos\phi}\right), \qquad (6.1)$$

where ϕ is the round trip phase, τ is the transmission coefficient, and a_{rt} is the round trip loss. These parameters are defined in detail in Section 2.2.4. We calculate the phase for the three coupling conditions; over-coupled, under-coupled, and critically coupled. This result is plotted in Figure 6.2. The transmission for each case is also plotted.

For the over-coupled case, shown in Figure 6.2(a), we see there is a slowly increasing phase shift from zero to 2π. The phase does not change sign or slope on resonance, and is linear across the optical cavity resonance. The transmission is clearly not linear across the optical cavity resonance, as the slope changes sign. This difference between the phase and the transmission observed in Figure 6.2(a) indicates that the phase has an enhanced linear range compared to the transmission for over-coupled racetrack resonators. However, the criteria established in the previous section cannot be used to precisely determine the linear range for the phase, as there is no point of zero slope to use as an end-point for the linear range. For this case, we estimate that the linear range of the phase is likely approximately two times greater than the linear range of the transmission, because the phase is linear across the optical resonance and is a slowly-varying function.

For the under-coupled case, it appears visually in Figure 6.2(b) that the phase may have a larger linear range than the transmission. The criteria established in the previous section can be used to determine the linear range of both the transmission and the phase in this case. The transmission has a linear range of 2.5 pm, whereas the

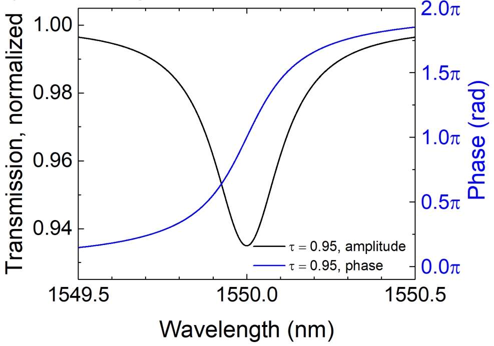

(a) Over-coupled

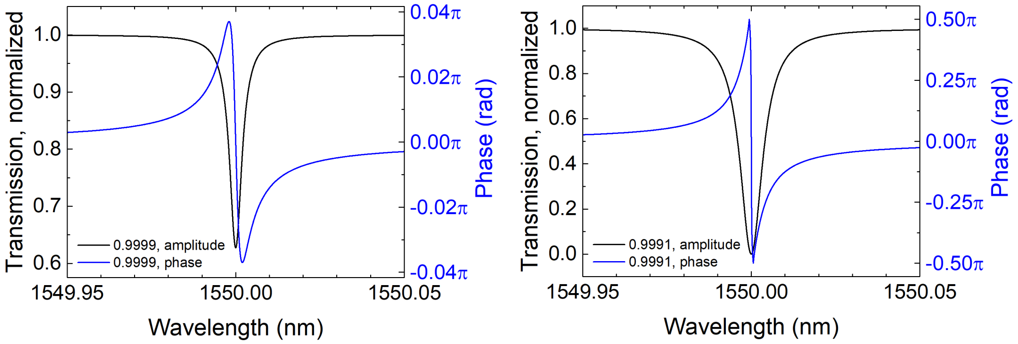

(b) Under-coupled

(c) Critically coupled

Figure 6.2: The normalized transmission (solid black lines) and phase (solid blue lines) for a racetrack resonator under three different coupling conditions; (a) over-coupled, (b) under-coupled, and (c) critically coupled. The phase shift for an over-coupled cavity has a slowly increasing phase shift from 0 to 2π. In this case, we can see that the linear range of the phase is approximately two times that of the transmission, as the slope of the phase does not change sign on resonance and there is no sharp transition. The phase shift for the under-coupled cavity is very small and returns to zero off resonance. The under-coupled cavity has a linear range of 2.5 pm for the amplitude, but a linear range of 3.9 pm for the phase. The phase shift for the critically coupled cavity also returns to zero off resonance, but completes a sharp shift from -0.5π to 0.5π across the racetrack resonance. In this case, the phase does not visually appear to provide a linear range improvement over the transmission.

phase has a linear range of 3.9 pm. This result suggests that the phase has a slightly larger linear range than the transmission for under-coupled racetrack resonators.

For the critically coupled case, it is unclear what the linear range of the phase is because there is a sharp transition on-resonance. In Figure 6.2(c), we see that the slope at the transition from maximum to minimum phase (0.5π to -0.5π) is nearly infinite. Therefore, the linear range for this phase signal is approximately zero using the criteria established in the previous section. For the critically coupled case, it is not immediately obvious that the phase signal produces a benefit in the linear range when compared to the transmission.

This analysis of the transfer function suggests detecting nanomechanical motion through the phase may produce a larger linear range compared to the transmission. Optical homodyne detection, commonly used in the field of optomechanics [14, 203, 204, 218, 236], provides access to the optical phase of the cavity signal. To implement homodyne detection on chip, and to convert the phase of the racetrack resonator into a signal that we can observe at the photodiode, we look to the field of silicon photonics. By using the silicon photonics literature as inspiration, we observe that ring resonators or racetrack resonators can be combined with Mach Zehnder interferometers (MZIs) to produce spectra that have a Fano-like shape [237, 238, 239, 240]. An MZI measures the phase difference between the two interferometer arms. Assuming that the optical power is equally split between the two interferometer arms, the transfer function T_{MZI} of an MZI is described by

$$T_{\mathrm{MZI}} = \left| \frac{1}{2}\left(1 + e^{i\theta}\right) \right|^2, \tag{6.2}$$

where θ is the phase difference between the two arms. From this expression, we see that the output of the MZI depends only on the phase difference between the two arms, and converts the phase difference to a measurable power change in the transmission T_{MZI}. Therefore, we should be able to use the MZI to detect the phase of the racetrack resonator and convert that phase to a power change that can be measured with a photodiode.

We adopt the device architecture used in [237] and [238]. This photonic integrated circuit consists of an MZI loaded with a racetrack resonator on one arm. A schematic of this structure is shown in Figure 6.3. The amplitude of the field input to the system is labeled s_{i}. This input is split by a 50/50 coupler and directed to each arm. The bottom arm in the schematic is loaded with a ring resonator. The ring resonator is coupled to the MZI arm using a directional coupler with coupling parameters κ and τ. The upper arm is the reference arm, and has a phase shift of θ relative to the second arm. The signals from the two arms are recombined at the output coupler again at a 50/50 ratio. Finally, the signal amplitude output from the system is s_{t}.

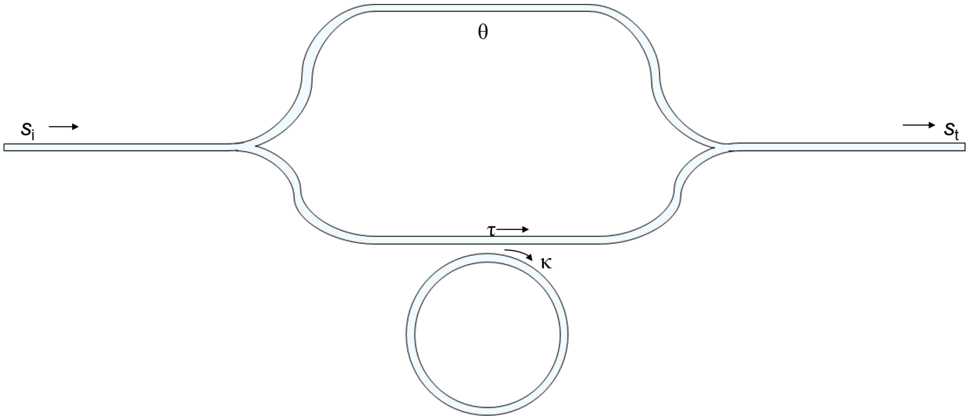

Figure 6.3: Schematic of the racetrack resonator loaded Mach-Zehnder interferometer (MZI). A racetrack resonator is placed adjacent to one arm of the MZI, and has coupling parameters τ and κ. The phase shift of the reference arm, θ, is also indicated on the schematic. The input signal s_i is split 50/50 to each arm. The amplitude in each arm is recombined at 50/50 to produce the output signal s_t.

In this work, we implement homodyne detection on-chip using the SOI platform with the device architecture shown in Figure 6.3. The homodyne measurement approach used by many in the optomechanics field [204, 218, 241] is generally implemented using optical fibers and discrete external components. In a homodyne measurement, the initial input signal is split to form a local oscillator signal and a detection signal. These two signals are mixed at a splitter, and the phase difference between the two signals is detected. Two detectors are used for balanced optical homodyning. One of the downsides of traditional homodyne detection is the complexity of the experimental setups required to implement homodyne detection, as many other components are required such as fibre stretchers. Polarization and perfect mode overlap are key concerns for these types of setups, and a mismatch in polarization or incomplete interference can be detrimental to the detection efficiency [236]. In our on-chip implementation, only one polarization exists as the grating couplers are polarization-sensitive and admit only either TE or TM polarization, and the interfering optical modes are essentially perfectly pre-aligned by the integrated photonics. The on-chip implementation is simple and compact, and could potentially simplify the setup of a homodyne measurement [242, 243]. One of the benefits of a homodyne measurement is that the power of the local oscillator signal can be increased, thereby increasing the signal-to-noise ratio (SNR) of the mixed signal even if the detection signal is small. In this chapter we demonstrate 50/50 splitting of the optical power into the two arms of the on-chip MZI, and therefore do not take advantage of the potential SNR enhancement of a usual homodyne approach. However, in future implementations the power could be split to any ratio desired by replacing the 50/50 splitter with a directional coupler designed to split the power in whatever ratio is desired. In addition, balanced homodyne detection could be easily incorporated by modifying the MZI output coupler to be a 2:2 coupler, instead of 2:1.

The transfer function of the racetrack-loaded MZI can be expressed as $|s_{\mathrm{t}}/s_{\mathrm{i}}|^2$ and is derived by following the progress of s_{i} through the photonic circuit and keeping track of the phase changes carefully, as an MZI is a phase-sensitive device. We assume the optical amplitude is split equally between the two arms. By summing the two outputs where they recombine at the splitter, we obtain an expression for the output amplitude of the overall photonic circuit. To express the result as an output power, we square the amplitude result and take the absolute value. Half of the optical power will enter the ring-loaded arm, which has a transfer function of an all-pass ring resonator, as described in Section 2.2.4 (Eq. (2.25)). The phase information is contained in this transfer function via the round-trip phase ϕ. The final expression for the transmission of the ring-loaded MZI is:

$$T_{\mathrm{R-MZI}} = \left|\frac{s_{\mathrm{t}}}{s_{\mathrm{i}}}\right|^2 = \left|\frac{1}{2}\left(\frac{\tau - a_{\mathrm{rt}}e^{i\phi}}{1-\tau a_{\mathrm{rt}}e^{i\phi}} + e^{i\theta}\right)\right|^2. \tag{6.3}$$

We see from Eq. (6.3) that the transmission of the racetrack-loaded MZI is dependent on the phase difference between the racetrack resonator and the phase of the reference arm θ. The phase of the reference arm is defined as [77]

$$\theta = \frac{2\pi n_{\mathrm{eff}} L_{\mathrm{arm}}}{n\lambda}, \tag{6.4}$$

where n is an integer, L_{arm} is the arm length, and λ is the design wavelength. The fact that the phase shift depends on the effective index of the waveguide indicates that the MZI phase will not be constant across all wavelengths. This is because the effective index depends on the wavelength, as discussed in Section 2.2.1 and defined in Eq. (2.17). Therefore, an MZI fabricated using planar waveguide technology will have a sinusoidal output, as the phase varies across the wavelength [68].

Let us assume that we are operating the device near 1550 nm, and that the variation in the effective index is small over full width of one optical racetrack resonance. In this small wavelength region, the effective index is approximately constant. Therefore, we can set the phase shift θ by choosing an appropriate arm length. If theta is equal to $m\pi$, where m = 0,1,2,..., then the output from the racetrack-loaded MZI will be a Lorentzian response superimposed on the MZI sinusoid. This is because the phase difference between the reference arm and the racetrack-loaded arm is simply the phase of the racetrack resonator. If, however, the phase is set to $\pi/2$, the phase difference between the two arms off-resonance is $\pi/2$. As we approach the resonance, the racetrack resonator phase increases and therefore the difference decreases. When the racetrack resonator phase reaches $\pi/2$, the phase difference is zero and therefore the transmission is equal to zero. The transmission increases as the phase moves away from $\pi/2$, and eventually returns to the initial value off-resonance. We will show the effect of the phase change mathematically later in the section, but for now we see that setting the phase of the reference arm to $\pi/2$ produces a much different response in the transmission function than the typical racetrack resonator response. If we use Eq. (6.3) to plot the transmission of the racetrack-loaded MZI with $\theta = \pi/2$, we see that the transmission is a Fano-like shape very similar to the phase of the racetrack resonator [237], as shown in Figure 6.4.

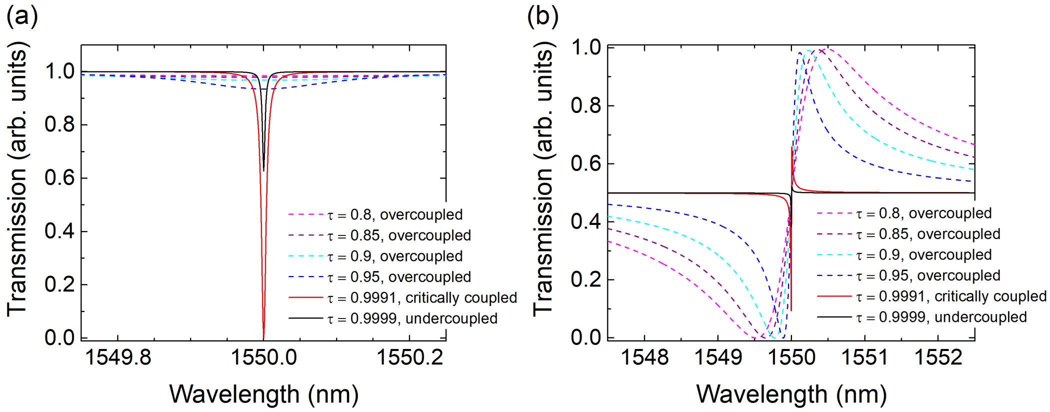

Figure 6.4: The calculated transmission of a (a) racetrack resonator and (b) racetrack-loaded Mach Zehnder interferometer with a $\pi/2$ phase shift. Both results are calculated for over-coupled ($\tau = 0.8, 0.85, 0.90.95$), critically coupled ($\tau = 0.9991$) and under-coupled ($\tau = 0.9999$) conditions. Visually, the linear range is improved for over-coupled devices.

We can use the definition provided in the previous section to establish the linear range of the racetrack-loaded MZIs. By using the same criteria as in Section 6.1, the point of maximum slope occurs at the midpoint between the maximum and minimum of the Fano-like response, making this the optimum operating point for any experimental measurements. The linear range is defined as two times the wavelength spacing between the minimum of the Fano-like response and the midpoint. The linear range of the Fano-like response from the racetrack-loaded MZI is shown graphically in Figure 6.5.

By varying τ to change the coupling of the racetrack resonator to the MZI, it is possible to tune the linear range of this photonic circuit to produce superior linear ranges when compared to racetrack resonators or MZIs alone. We use Eq. (6.3) to begin the design process. The phase shift in the reference arm is set to $\theta = \pi/2$, which produces a symmetric Fano-shaped response as discussed previously. The parameters we examine for each case are the optical linear range and the slope of the optical curve. Both of these parameters are compared to a racetrack resonator with the same coupling parameters to determine whether the racetrack-loaded MZI im-

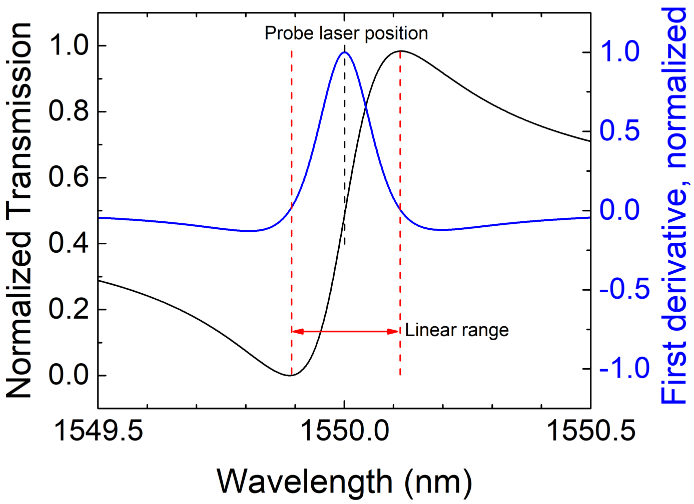

Figure 6.5: The solid black line shows the transmission of the racetrack-loaded MZI. The solid blue line shows the first derivative of the transmission. The probe laser is positioned at the point of maximum slope, at the midpoint of the Fano-like response. This position is shown by the black dashed line. The linear range is defined as two times the wavelength span between the point of maximum slope and the point of zero slope, and is shown by the red arrow between the red dashed lines. In the case of a symmetric Fano-like response, this definition means that the linear range is simply the wavelength span between the maximum and minimum of the Fano-like transmission.

proves on the racetrack resonator design. The linear range is as defined in Figure 6.5. The second parameter is the slope, which is of interest because it helps to determine the signal-to-noise ratio of the optomechanical system. This is demonstrated by the fact that the transduction coefficient (Eq. (2.42)) is proportional to the slope of the optical cavity. As the slope increases, the transduction also increases.

The first design parameter we examine is the transmission coefficient of the ring, τ. It is important to know the round trip loss (a_{rt}) to determine whether the device is over-, under-, or critically coupled for a given transmission coefficient. The round trip loss of the device is set by the fabrication process, and varies depending on the foundry and processes used. The foundry used to fabricate these devices, IME, has been shown to have a loss for strip waveguides of approximately 2 dB/cm [244]. For the racetrack resonator geometry of a 5 μm radius and 3 μm straight sections (total length of 37 μm), this results in a round trip loss $a_{\mathrm{rt}} = 0.9991$. We vary the coupling parameter τ from 0.8 to 0.9999 to determine the effects of under-, over-, and critically coupling the racetrack-loaded MZI. We compare these results to those obtained from a standard racetrack resonator with the same loss and coupling parameters. The transmission from both of these device architectures is shown in Figure 6.4, where (a) shows the response from a racetrack resonator, and (b) shows the response from a racetrack-loaded MZI. The response for the over-coupled racetrack resonator is very shallow, especially when compared to the critically coupled racetrack resonator. The shape of the curve changes dramatically over the various coupling conditions; the resonance of the strongly over-coupled racetracks are almost flattened into the background. This highlights the fact that the racetrack resonators are very sensitive to the coupling conditions, especially when strongly over-coupled. In Figure 6.4(b), we see that for the over-coupled devices ($\tau < a_{\mathrm{rt}}$), the Fano-like response is not very sharp and has a very large variation in slope across the coupling conditions. This follows the trend of the phase of the racetrack resonator shown in Figure 6.2(a). Unlike the racetrack resonator alone, an extremely over-coupled device does not result in the signal vanishing, but rather a shallower slope. This indicates that the racetrack-loaded MZI is more robust with regards to over-coupled conditions. The under-coupled and critically coupled devices in this case are very sharp curves with a very steep slope at resonance. This is as expected based on the phase response of the racetrack resonator when under- and critically coupled as shown in Figure 6.2(b) and (c).

To analyze these responses in more detail, and in particular the linear range and slopes, we extract both the linear range and slope from each curve in Figure 6.4(a) and (b). This summary results in Figure 6.6, where the linear range is shown in (a) and the slope is shown in (b) for both the racetrack alone (red stars) and the racetrack-loaded MZI (blue circles). For over-coupled devices, the racetrack-loaded MZI has a linear range approximately double that of a racetrack resonator alone. This is the same result we obtained from analyzing the phase response in Figure 6.2(a). As expected, the linear range increases as the devices become more over-coupled and the phase changes more slowly. The critically coupled and under-coupled devices have significantly lower linear ranges than the over-coupled devices, as expected from the phase shown in Figure 6.2(b) and (c). However, the racetrack-loaded MZI still outperforms the racetrack resonator in these instances as well. Interestingly, the linear range of the critically coupled device has a higher linear range than the under-coupled device, despite the nearly infinite slope in the phase from Figure 6.2(c).

In terms of the slope, as the coupling shifts from over- to under-coupled, the racetrack resonator slope dramatically increases. The slope for the critically coupled and under-coupled devices is more than 400 times greater than the slopes for the over-coupled racetrack resonators. Although the slopes are higher for the critically coupled and under-coupled racetrack-loaded MZIs compared to the over-coupled devices, the difference is not as significant. The slopes for the critically coupled and under-coupled devices are greater than the over-coupled devices by approximately a factor of 16. According to Eq. (6.3), the racetrack-loaded MZI is a more sensitive device for detecting the small motion of the nanomechanical devices in the case

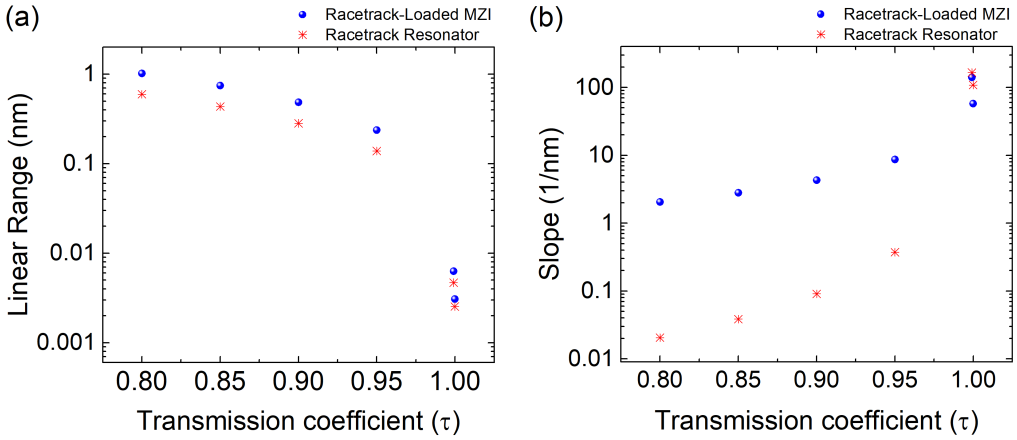

Figure 6.6: The simulated (a) linear range and (b) slope are shown for both racetrack resonators only (red stars) and racetrack-loaded Mach Zehnder interferometers (blue circles). Devices with τ between 0.8 and 0.95 are over-coupled. Devices with $\tau = 0.9991$ are critically coupled, and with $\tau = 0.9999$ are under-coupled. The over-coupled racetrack-loaded MZIs show an improvement over the racetrack resonators in the case of both the linear range and the slope. The under- and critically coupled racetrack-loaded MZIs show an improvement in the linear range, however, the slope is higher for the racetrack resonators.

of over-coupling, but racetrack resonators are more sensitive at critical and under-coupling.

By examining Figure 6.6, we see there is a trade-off between maximizing the linear range and the slope. Since the slope determines the sensitivity of the transduction, it is important to keep the slope relatively large. However, the thermomechanical noise has been observed previously using over-coupled racetracks [69], and so it is acceptable to have a slightly lower slope in favour of a higher linear range. For this reason, the optimal coupling range for the racetrack-loaded MZIs is over-coupled. For the final design, we choose $\tau = 0.999$, 0.995, 0.987, and 0.948. Ideally, we would like to increase the coupling further to have values closer to $\tau = 0.8$, however, the smallest gap spacing between two waveguides permitted by the foundry was 200 nm, which limited our ability to choose stronger coupling. To try to achieve coupling as large as $\tau = 0.948$, the racetrack resonators have been made with 10 μm coupling lengths instead of 3 μm coupling lengths, which increases the round trip loss slightly. If a very large linear range is required, fabrication by electron beam lithography may be required to decrease the gap spacing and create very over-coupled devices.

The final parameter to examine in our design of the racetrack-loaded MZI is the phase shift θ. We have already determined that a phase near $\pi/2$ produces a symmetric Fano-like response. Figure 6.7 shows the response of the photonic circuit under various phase shifts. In this calculation, the round trip loss is set to 0.9991 and τ is set to 0.95. By varying the phase shift θ from 0 to $\pi/2$, we see the effect θ has on the signal shape. If the phase shift is set to 0, the output is a Lorentzian similar to the through port response of a microring resonator. A phase shift of $\pi/2$ produces a symmetric Fano-like lineshape. The phases between 0 and $\pi/2$ produce Fano-like shapes with varying asymmetry. This is the same result observed in [237]. Interestingly, the linear range (Figure 6.7(b)) for all cases except $\theta = 0$ is greater than the equivalent racetrack resonator only. For $\theta = 0$, the linear range is the same for the racetrack resonator and the racetrack-loaded MZI. The linear range is largest for $\theta = \pi/2$. Therefore, even if the phase shift is not perfectly equal to $\pi/2$, the design is an improvement over the racetrack resonator alone. This improves the robustness of the design to fabrication variations. The slope is also largest for $\theta = \pi/2$ and decreases as the phase shift decreases, as shown in Figure 6.7(b). Based on the linear range and slope, we conclude that a phase shift of $\theta = \pi/2$ is the best choice for the design. However, the racetrack-loaded MZI design is robust to design flaws or fabrication imperfections, since the linear range and slope are improved for all phase shifts greater than $\theta = 0$ compared to a racetrack resonator. This robustness is a beneficial feature since silicon photonics can be strongly affected by fabrication process variations [245, 246].

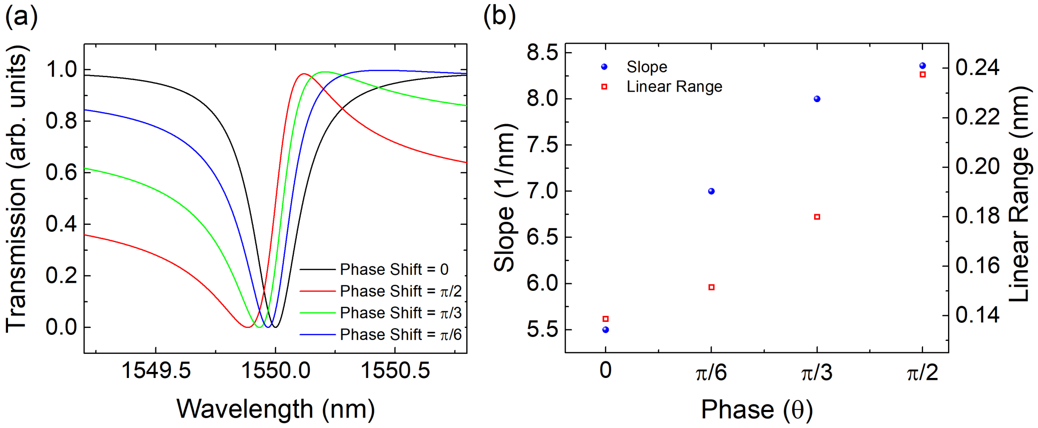

Figure 6.7: (a) The effect of varying the phase shift in the reference arm of the Mach Zehnder interferometer on the transmission of the photonic circuit. As the phase is increased from zero to $\pi/2$, the transmission shifts from a Lorentzian lineshape to a Fano-like lineshape. (b) The effect of varying the phase shift on the slope (blue circles) and linear range (open red squares). In both plots, $a_{\mathrm{rt}} = 0.9991$ and $\tau = 0.95$, and so the device is over-coupled. A phase shift of $\pi/2$ produces the best linear range and slope.

To design for a phase shift of $\theta = \pi/2$, we need to add the correct length to the reference arm. To determine the length required, the effective index is required. This is obtained from simulation using Lumerical MODE simulations [171]. The structure is a 500 nm wide, 220 nm tall silicon waveguide surrounded by oxide cladding. The effective index at a wavelength of 1550 nm is $n_{\text{eff}} = 2.3487$. To determine the arm length, we set $\theta = \pi/2$ and solve for L_{arm} in Eq. (6.4). We set n to a large value such that the path length is on the order of tens of microns to simplify the layout process. The final path length difference is $L_{\text{arm}} = 33$ μm.

The design was submitted for fabrication at the IME foundry in Singapore. In addition to the racetrack-loaded MZI circuits, as in Figure 6.3, single racetrack resonators with identical coupling properties were also fabricated as reference devices. The mechanical cantilevers in the design were all 220 nm tall, as that is the thickness of the silicon device layer. The cantilever dimensions were 2 μm long and 200 nm wide, 3.5 μm long and 180 nm wide, and 5 μm long and 180 nm wide. The gaps between the cantilever and racetrack resonators were 100 nm, 160 nm, and 200 nm. The smaller gaps were designed to maximize the optomechanical coupling, however, the minimum device spacing specified by the foundry was 200 nm. Placing these devices on the four different coupling conditions gave a total of 36 racetrack resonators, and 36 racetrack-loaded MZIs.

Additionally, active racetrack-loaded MZIs were also designed and fabricated. An active device means that the optical transmission of the device can be modified after fabrication by the application of a voltage. The active device used here was an electro-optic MZI. Active interferometric devices such as this are often used as modulators [247, 248, 249]. The MZI was designed by Xu Wang and Han Yun, students from the University of British Columbia [250]. This device operates on the principle of the free carrier effect. Recall that the free carrier effect, discussed in detail in Section 5.2, induces a change in the refractive index, and therefore the optical path length, of the silicon waveguide. When this effect is applied to one arm of an MZI device, the change in path length corresponds to a change in the phase shift in the arm according to Eq. (6.4), where n_{eff} is modified by the free carrier effect. The transmission of the MZI spectrum will then shift in wavelength to reflect this phase change. Controlling the phase shift is useful in our application to obtain an exact $\pi/2$ phase shift, to obtain a symmetric Fano-like response as shown in Figure 6.7(a).

The MZI arms were comprised of rib waveguides. Rib waveguides, as described in Section 2.2.1 and Figure 2.1, have thin silicon slabs adjacent to the central waveguide. The central waveguide has a height of 220 nm. The benefit of the rib waveguide for electro-optic devices is that the rib portions can be doped with high levels of n and p type ions. The exact doping level is protected intellectual property of the IME foundry. For this active MZI device, one side of the rib waveguide was doped with n-type ions and the other side of the rib waveguide was doped with p-type ions. Metal vias were used to connect the doped sections of the rib waveguide to aluminum traces on top of a thick cladding oxide. Vias are vertical features on a chip created by etching holes in a layer, such as the oxide cladding layer. The holes are then filled with metal to create an electrical connection from the top of the chip to features buried below other layers. The aluminum traces were connected to bond pads at the edge of the chip. Using the bond pads, a voltage can be applied across the n and p doped sections of the waveguide to generate free carriers. Therefore, the entire chip, including the simple passive devices, was covered in a thick oxide cladding layer with exposed aluminum pads at the edge of the chip. This active MZI device will ideally be beneficial in helping to compensate for thermal drift in the circuit, or for any fabrication imperfections or dispersion that causes the phase shift to be greater or less than $\pi/2$.

The only remaining issue is determining where to set the pump laser for pump-and-probe operation, and how the force applied by the racetrack-loaded MZI compares to the racetrack resonators alone studied in Chapter 4. To determine the best placement of the optical pump laser in the racetrack-loaded MZI system, we examine the power enhancement. Since the cantilever is placed adjacent to the racetrack resonator, the cantilever experiences an optical force proportional to the power enhancement of the racetrack resonator, and is unaffected by the remainder of the MZI circuit. The power enhancement can be calculated using Eq. (2.26) for various coupling conditions. The result is shown in Figure 6.8, and indicates that the power enhancement is maximized at the optical resonance, which is at the midpoint of the steepest point of the Fano-like lineshape from Figure 6.4(b). The figure also highlights a trade-off between the linear range (Figure 6.6(a)) and the power enhancement. As the transmission coefficient decreases, the power enhancement also decreases. Therefore, the force applied to the cantilever will also decrease. The force is maximized for critical coupling, where the linear range is smaller. Although this trade-off is not ideal, we can increase the pumping power by increasing the optical input power and the modulation voltage (Eq. (2.41)). This will help to counteract the driving force that is lost as the linear range improves.

The analysis from Chapter 4 is used to determine the efficiency of the driving force. Unfortunately, the optomechanical coupling for these devices is significantly lower than those from Chapter 4 because the gap between the racetrack and the cantilever is larger due to the limitations from the foundry. From Eq. (2.43), we calculate the optomechanical coupling for the devices with the lowest optomechanical coupling, the 2 μm long cantilevers. For these cantilevers, the optomechanical coupling is at most 0.6 rad GHz/nm and at least 0.06 rad GHz/nm, for gaps of 100 nm and gaps of 200 nm respectively. Using Eq. (4.4), we calculate the optimal cavity linewidth for these optomechanical couplings to obtain the highest amplitude. Unfortunately, for the smaller optomechanical coupling coefficient of 0.06 rad GHz/nm, the device is outside the optimal range for optical pumping for all transmission co-

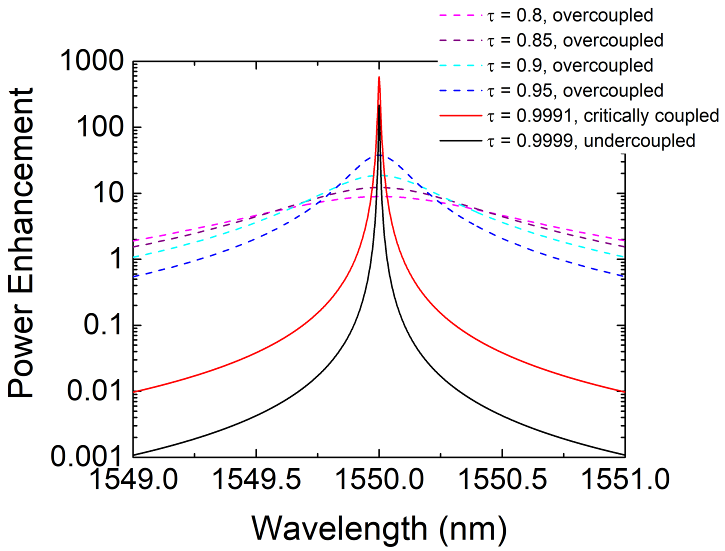

Figure 6.8: The power enhancement the cantilever will experience from the racetrack resonator in the racetrack-loaded MZI photonic circuit. The black line is an undercoupled racetrack, the red line is a critically coupled racetrack, and the dashed lines are over-coupled racetracks. The power enhancement decreases as the transmission coefficient decreases.

efficients and driving powers. For the larger optomechanical coupling coefficient, the optimal driving range can be achieved for transmission coefficients greater than 0.995, but only when the optical input power or the modulation voltage is increased sufficiently. Therefore, the optical driving force cannot be properly optimized with the low optomechanical coupling resulting from the large gap spacing required by the foundry. To successfully drive the devices to maximum amplitude, the optical power and modulation voltage must be increased significantly.

We have described the design process for the racetrack-loaded MZIs in detail, and have provided many reasons why they are an improvement over single racetrack resonators for large-amplitude nanomechanical sensors such as cantilevers. The over-coupled racetrack-loaded MZI has a larger linear range and slope, and the design is robust to fabrication imperfections.

6.3 Experimental Results

The racetrack-loaded MZIs are measured using the confocal microscope setup described in Section 2.4. First, the optical properties of the system are characterized in detail. The characterization was done with the cladding oxide still in place; that is, before the mechanical devices were released from the sacrificial oxide layer. The optical results are detailed in the first section below.

In the second section, the results from mechanical measurements are described.

The mechanical characterization includes both thermomechanical and driven measurements to test the mechanical linear range and displacement sensitivity of the nano-optomechanical system.

6.3.1 Optical Results

To find the optical properties of the system, the reference racetrack resonators are characterized first. The response of each racetrack is measured using only the probe laser for a wide wavelength range of 1520–1580 nm for a total of 36 measurements, resulting in nine measurements of each coupling configuration which are then averaged to provide an estimate of the round trip loss and the transmission coefficient for each configuration. For all measurements, the optical power incident on the grating coupler was 1.0 mW. The experimental measurements are fit with either Eq. (2.25) or Eq. (2.36) depending on the amount of backscattering in the system. The results of these measurements are shown in Figure 6.8. The transmission coefficients and round trip loss values are plotted versus the cantilever device number. The cantilevers are sorted by increasing length then increasing gap, and then numbered accordingly. For example, Device 1 has a length of 2 μm and a gap of 100 nm. Device 6 has a length of 3.5 μm and a gap of 200 nm.

From Figure 6.9, we see that all of the devices with gaps of 100 nm (Devices 1, 4, and 7) did not have optical resonances, and are therefore missing data, or that a_{rt} is substantially less than the other racetrack resonators with the same coupling condition. This indicates that the cantilever gaps may not have cleared properly during the lithography step, most likely due to the fact that the gap was significantly smaller than the minimum gap suggested by the foundry. In this case, the cantilever is most likely stuck to the racetrack resonator, causing significantly more loss than expected. To confirm this hypothesis, focused ion beam (FIB) was used to image the devices. By using an ion beam to mill through the oxide cladding, the devices can be imaged. Figure 6.10(a) shows an image of the smallest gap device where the cantilever is joined to the waveguide, indicating that these small gaps did not resolve properly in the photolithography process and will not produce functional devices. For this reason, the devices with the smallest gaps are excluded from future analysis. Figure 6.10(b) shows a device with a properly resolved gap of approximately 160 nm, confirming that the devices with larger gaps were fabricated as expected.

The remainder of the devices show reasonably good agreement between the designed values (bottom right corner of Figure 6.8(a)–(d)) and the experimental values. In all cases the transmission coefficient is slightly lower than the designed value, likely because there was more coupling than anticipated at the curved sections of the racetrack resonators. Despite this, the coupling is close to the designed value in each case, providing a good range of transmission coefficients. To compare these

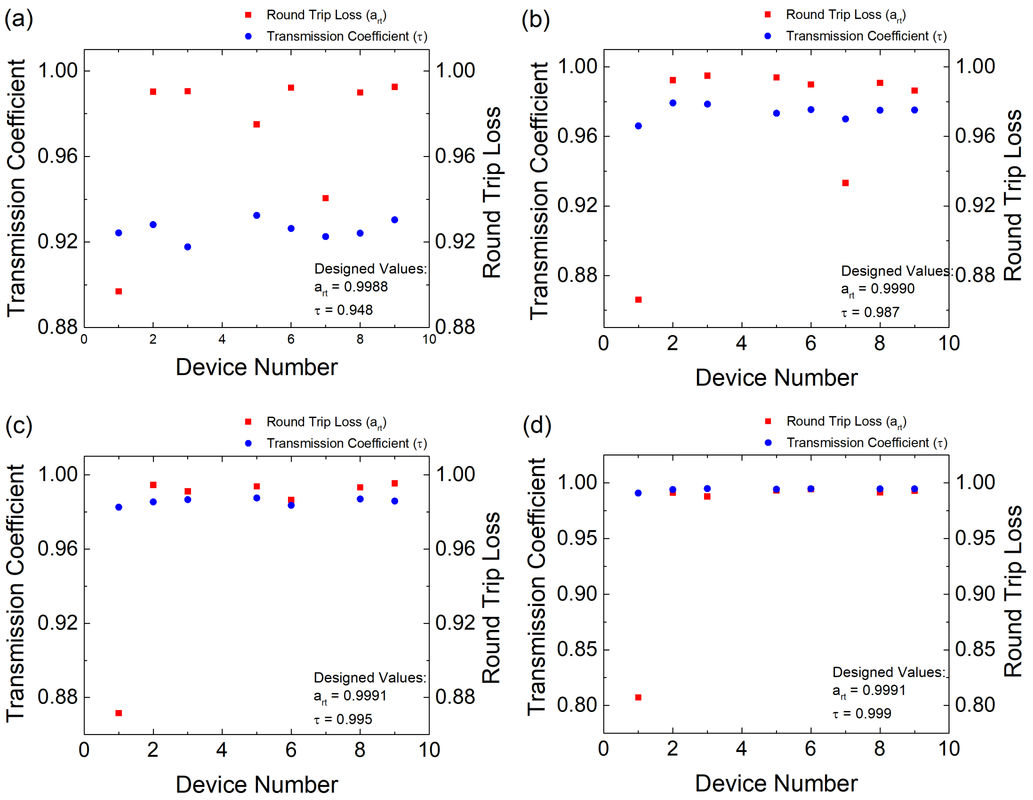

Figure 6.9: The round trip loss (red squares) and transmission coefficient (blue circles) are shown for each coupling configuration starting with the most over-coupled (a) and ending with the closest to under-coupling (d). The designed parameters are shown in the bottom right corner of each graph. In all four graphs, Device Numbers 1, 4, and 7 are often missing or have substantially different round trip loss values compared to the other designs. These devices had the smallest gaps between the mechanical device and the racetrack (100 nm), which indicates the mechanical devices may be attached to the racetrack resonator and increased the loss in the optical cavity substantially.

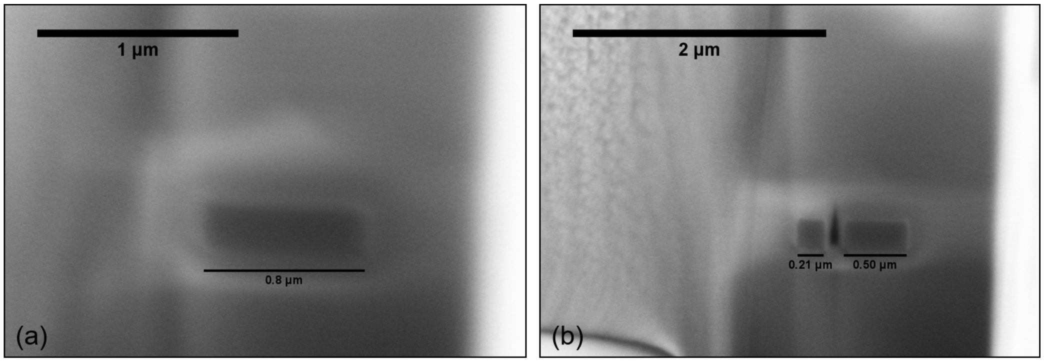

Figure 6.10: Focused ion beam images of the cantilevers coupled to racetrack-loaded MZIs. The device in (a) had the smallest gap. This gap did not resolve, as the measured size of the waveguide in this image is approximately 800 nm. The 800 nm feature is the total length of the 500 nm waveguide plus the 200 nm beam plus the 100 nm gap. Devices with these gaps were excluded from the analysis. The device shown in (b) is the mid-sized gap of 160 nm, where it is clear that the cantilever is separate from the waveguide. The waveguide is 500 nm wide as expected. At 210 nm, the cantilever is slightly wider than the 200 nm design width.

results to the racetrack-loaded MZIs and the simulated results from Figure 6.6, the slope and linear range were extracted from the curve fits to the racetrack resonators. The linear range was obtained using the same criteria described in Section 6.1. The experimental linear range and slope are shown in Figure 6.11(a) and (b) respectively. In both cases, the single point is the average linear range of six measured devices with the same coupling coefficient. The error bars are the standard deviation of the six measurements.

Measurements of the racetrack-loaded MZIs revealed that the response required a slightly different model to describe the results than the ideal model presented in Eq. (6.3). The experimental results across a large wavelength spectrum are shown by the black dots in Figure 6.12. The racetrack resonator response is superimposed on the sine wave response of the MZI, which is clearly visible in Figure 6.12. Additionally, we observe that the shape of the on-resonance response changes as the wavelength increased. In some cases, the shape is Fano-like, as expected. However, there are also resonances that have a purely Lorentzian transmission. To account for the variation in the resonance shape, we can include several factors as fitting parameters. The first parameter that we include as a fitting parameter is the length of the MZI reference arm L_{arm}. This parameter is present in the variable θ, as shown in Eq. (6.4). Including this parameter as a fit parameter accounts for variations in the fabrication of the devices.

Another variable that influences the transmission function is the effective index. Recall that Eq. (6.4) is dependent on the wavelength through the variable n_{eff}. We discussed previously that the change in the effective index results in a sinusoidal

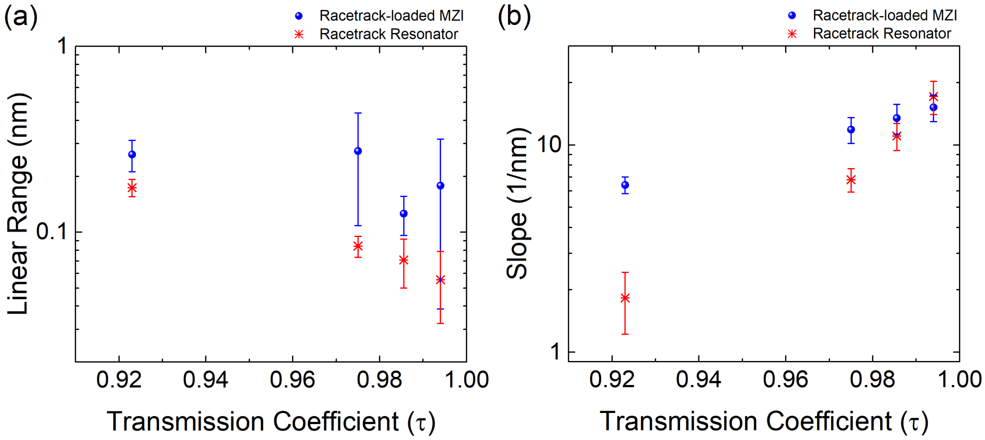

Figure 6.11: The experimental (a) linear range and (b) slope are shown for both racetrack resonators only (red stars) and racetrack-loaded Mach Zehnder interferometers (blue circles). The single point is the average linear range of six measured devices with the same coupling coefficient, with the exception of the racetrack-loaded MZIs at $\tau = 0.994$ where only four measurements were taken since only four working devices were observed. The error bars are the standard deviation of the measurements. The racetrack-loaded MZIs show a distinct improvement over the racetrack resonators for the case of the linear range. When $\tau = 0.994$, the improvement is less clear as the variability in the linear range is very high for the racetrack-loaded MZIs. The slopes are higher for the racetrack-loaded MZIs compared to the racetrack resonators except when $\tau = 0.994$. For all measurements, the optical power input incident on the grating coupler was 1.0 mW.

output for a silicon photonic MZI. We can account for the wavelength dependence of the effective index by assuming that the variation of the effective index is approximately linear over our wavelength range of interest. This assumption can be verified using Eq. (2.17) or by numerical methods. By including a linear wavelength dependence of the effective index in θ, we obtain a more accurate fit to the experimental data.

The change in the effective index also affects the racetrack resonator response. In Section 2.2.1, we defined the free spectral range, or FSR, of the racetrack resonator as

$$\mathcal{F} = \frac{\lambda^2}{L_\mathrm{c} n_\mathrm{g}}, \tag{6.5}$$

where n_g is the group index of the waveguide and L_c is the cavity length. The FSR is therefore also dependent on the effective index via Eq. (2.19). The variation of the FSR with wavelength is accounted for in the expression for the round trip phase, which we defined in Section 2.2.4 as $\phi = (\lambda - \lambda_0)/\mathcal{F}$, where λ is the measurement wavelength and λ_0 is the resonance wavelength. However, according to simulations [171], the variation of the group index is less than 2% over the wavelength range of 1550–1600 nm. In comparison, the simulated effective index has a variation greater than 6% over the same wavelength range. To simplify the already complicated fitting function, we set the group index as a fit parameter that does not vary with wavelength, instead of using Eq. (2.19) as yet another fitting equation.

The final parameter in our fitting function accounts for a power difference in the arms when the two signals recombine. Although the power in the arms is theoretically identical, the splitting may not be ideal and more power may be lost as the light travels through the racetrack resonator arm than through the reference arm. This results in a slight power imbalance when the signals from the two arms recombine, and therefore the destructive and constructive interference is not perfect. We will account for this using the value b, which is between zero and one, where one represents perfect cancellation at the output. The final expression for the experimental power transmission is

$$T_\mathrm{R-MZI,exp} = \left| \frac{1}{2} \left(b \frac{\tau - a_\mathrm{rt} e^{i(\lambda-\lambda_0)L_\mathrm{c} n_\mathrm{g}/\lambda^2}}{1 - \tau a_\mathrm{rt} e^{i(\lambda-\lambda_0)L_\mathrm{c} n_\mathrm{g}/\lambda^2}} + e^{i2\pi n_\mathrm{eff}(\lambda) L_\mathrm{arm}/\lambda} \right) \right|^2, \tag{6.6}$$

where the fitting parameters are b, n_g, $n_\mathrm{eff}(\lambda) = m\lambda + n_\mathrm{eff,0}$, τ, a_rt, λ_0, and L_arm. m is the slope of the linear relationship between the effective index and the wavelength. We use Eq. (6.6) to fit the experimental data. The experimental data is obtained by activating the probe laser and observing the transmission of the photonic integrated circuit as the wavelength is increased from 1520 – 1580 nm. For all measurements, the optical power incident on the grating coupler was 1.0 mW. Four fits, one for each designed value of τ, are shown in Figure 6.12. The data is normalized to one, allowing for a better fit by subtracting the effect of the grating coupler envelope on the low and high wavelength portions of the data. The fits show reasonably good agreement with the model in Eq. (6.6). The arm length varied between 0.2% and 2.7% of the designed value of 33 μm, which is a reasonable variation similar to that observed in the literature [246].

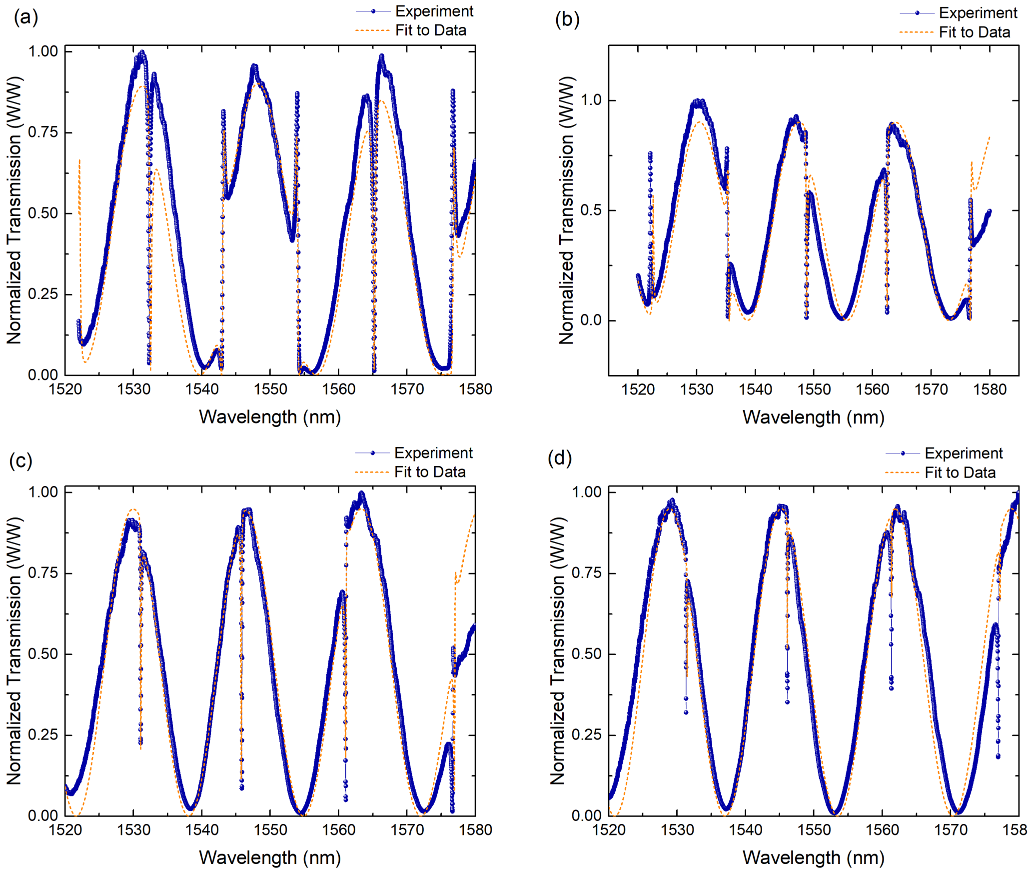

Figure 6.12: Experimental racetrack-loaded MZI data. The MZI peaks are normalized to one to remove the envelope introduced by the grating coupler and allow for a better fit. The fits are shown for 2 μm long cantilevers with 200 nm gaps for the four different coupling conditions. The transmission coefficients in each case are (a) $\tau = 0.923$, (b) $\tau = 0.975$, (c) $\tau = 0.986$, and (d) $\tau = 0.994$ as measured from the ring resonator data. The transmission coefficients obtained from the fits were very similar to the ones measured from the racetrack resonators. The largest variation was for the fit shown in (b), which had a 1.3% difference. For all measurements, the optical power incident on the grating coupler was 1.0 mW.

The next step in the analysis is to compare the performance of the racetrack-loaded MZIs to the racetrack resonators. The linear range and slopes are extracted directly from the experimental results using the approach detailed in Section 6.1.

Since the shape of the response varied over the wavelength spectrum as seen in Figure 6.12, the most Fano-like shape is chosen from each spectrum to perform the linear range and slope analysis. The single blue points in Figure 6.11 are the average linear range of six measured devices with the same coupling coefficient, with the exception of the racetrack-loaded MZIs at $\tau = 0.994$ where only four measurements were taken since only four working devices were observed. The error bars are the standard deviation of the measurements. When compared to the racetrack resonators alone, the racetrack-loaded MZIs have a larger average linear range for all transmission coefficients. The standard deviation is, however, very large for the result at $\tau = 0.994$, putting the results from the racetrack-loaded MZI and the racetrack resonator alone within error of each other for this transmission coefficient. Overall, the results match the trends predicted by the simulated results from Figure 6.6. The linear range is lower than predicted by simulation for the smallest transmission coefficient of 0.923, approximately 0.26 nm compared to 1 nm. For the higher transmission coefficients, including those close to critical coupling, the linear range is substantially higher than predicted by simulation, by more than a factor of ten. The slopes for both the racetrack resonators and racetrack-loaded MZIs are higher than predicted by simulation for the smallest transmission coefficient of 0.923. For the transmission coefficient of 0.975, the slopes were higher for the racetrack-loaded MZIs than the racetrack resonators. As the transmission coefficients approached the critical coupling condition, the slopes for the racetracks alone were higher than the racetrack-loaded MZIs, which was predicted in the initial model.

From these plots, the coupling configuration that maximizes both the linear range and the slope simultaneously is $\tau = 0.975$. This transmission coefficient provides the highest average linear range, and the slope of the transmission is only 1.5 times smaller than the maximum achieved by any device, and only 1.3 times smaller than the maximum value achieved by the racetrack-loaded MZIs. This coupling coefficient also provides an improved situation for optically pumping the devices, since the power enhancement increases as the transmission coefficient approaches the round trip loss and critical coupling is achieved. To test these conclusions, the mechanical properties of these devices are characterized in the following section.

6.3.2 Mechanical Results

Although the optical properties indicate that the racetrack-loaded MZIs have increased linear range and sensitivity, the results must be verified experimentally by measuring the mechanical cantilever adjacent to the racetrack resonator. To measure the mechanical devices, they must first be released from the thermal oxide underneath the silicon device layer and the cladding oxide above the cantilever.

The cladding oxide could not simply be removed in a maskless release, because of the presence of the aluminum bond pads and electrical traces on top of the oxide cladding layer that were required for the active MZI design. A masking layer was used to protect the aluminum features while allowing release of the cantilevers. First, the chip was treated with HMDS, an adhesion promoter, to ensure improved adhesion of the photoresist to the chip. Then, HPR504 photoresist was spun onto the chip. Photolithography was used to pattern the masking layer. The resist was developed and windows in the photoresist around the mechanical components were created on the chip. The optical components, such as the racetrack resonators and grating couplers, were protected with photoresist. The chip was then etched using BOE for five minutes to ensure a full etch of the thermal oxide underneath the cantilevers. The photoresist was removed and the chip was critical point dried to prevent stiction. This process resulted in successful release of the mechanical cantilevers, while protecting the aluminum features elsewhere on the chip. Optical microscope images of the chip post-release are shown in Figure 6.13 for both (a) racetrack resonators and (b) racetrack-loaded MZIs. The etch was inconsistent across the surface of the chip, as is evidenced by the differing etch patterns around the racetracks compared to the racetrack-loaded MZIs. This is potentially due to inconsistencies in the cladding oxide density or stoichiometric composition across the chip.

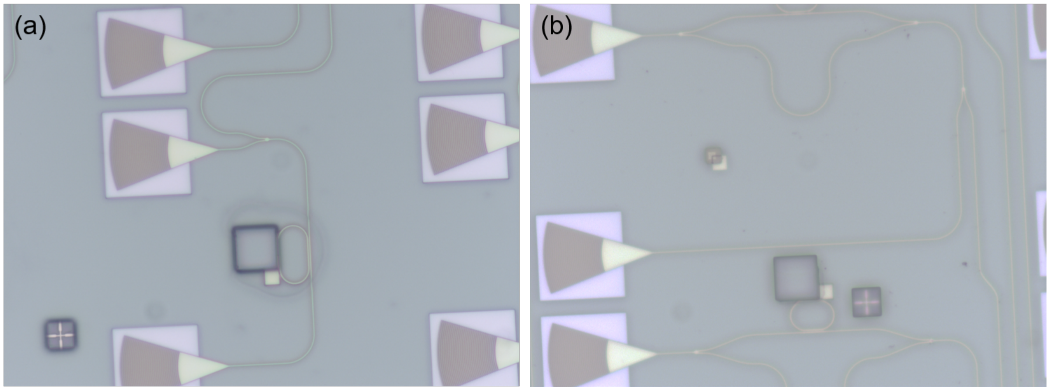

Figure 6.13: Optical microscope images of (a) a racetrack resonator and (b) a racetrack-loaded MZI after device release. The inconsistent etch pattern around the devices is indicative of an uneven etch of the cladding oxide.

Once the mechanical devices were released, they could be measured using the lock-in amplifier. The devices measured were 3.5 μm long cantilevers with a 160 nm gap, the smallest gap available since the 100 nm gaps did not pattern correctly. Due to this large gap, the optomechanical coupling for the devices was very low and as a result the signal-to-noise ratio of the mechanical measurements was also low. For the racetrack-loaded MZIs, all four coupling conditions had functional mechanical devices. For the racetracks alone, resonances for only three out of the four mechanical devices were observed. The data for the coupling condition $\tau = 0.975$, was not observed. The device either stictioned during the release process, or was not fully released.

To set up the mechanical measurements, the following procedure was followed for each device. First, the probe laser was activated and positioned at the point of maximum slope of each optical resonance. The probe power was set such that the optical power incident on the grating coupler was 1 mW at the probe wavelength. Then, the pump laser was activated. The wavelength of the drive laser was positioned such that the output power of the mechanical signal was maximized, which indicates that the pump laser is positioned at the resonance frequency of the racetrack resonator. This eliminates any potential accidental actuation via self-oscillation. For the racetrack-loaded MZIs, the maximum drive power was found manually for each device by maximizing the signal observed on the lock-in amplifier. This was because the phase differed across the optical spectrum causing some resonances to be more Lorentzian than Fano-like. For the initial setup, the AC voltage to the amplitude modulator was disabled so that the pump was only providing DC optical power. The pump power was set such that the optical power incident on the grating coupler was 1 mW at the pump wavelength.

First, the thermomechanical noise of the cantilevers was measured with the amplitude modulation deactivated. The thermomechanical noise is useful for two reasons. First, it allows for conversion of the data to an amplitude in meters using the responsivity as described in Section 2.1.1. Second, the tails of the thermomechanical noise are used to find the displacement sensitivity of each photonic circuit, which is a figure of merit used to establish the overall sensitivity. The smaller the displacement sensitivity, the better the circuit sensitivity, and so a smaller displacement sensitivity is more ideal. The displacement sensitivity is obtained by fitting a Lorentzian to the thermomechanical noise, and converting the thermomechanical noise to a displacement via the responsivity as per Section 2.1.1. Once the displacement spectral density is obtained, the displacement sensitivity can be extracted from the noise floor of the Lorentzian fit in units of $\mathrm{m/Hz^{1/2}}$. The displacement sensitivities for the different coupling conditions and photonic circuits are shown in Figure 6.14.

In Figure 6.14, we see the displacement sensitivity is smallest for the racetrack resonators with the largest transmission coefficient. This is in agreement with Figures 6.6(b) and 6.11(b), which predict the highest sensitivity for the highest transmission coefficient. In most cases, the racetrack resonators have better displacement sensitivity than the racetrack-loaded MZIs. This is expected from Figure 6.6(b) for the highest transmission coefficient, where the cavity is under-coupled. For the second-highest τ (close to critical coupling), the displacement sensitivity is again

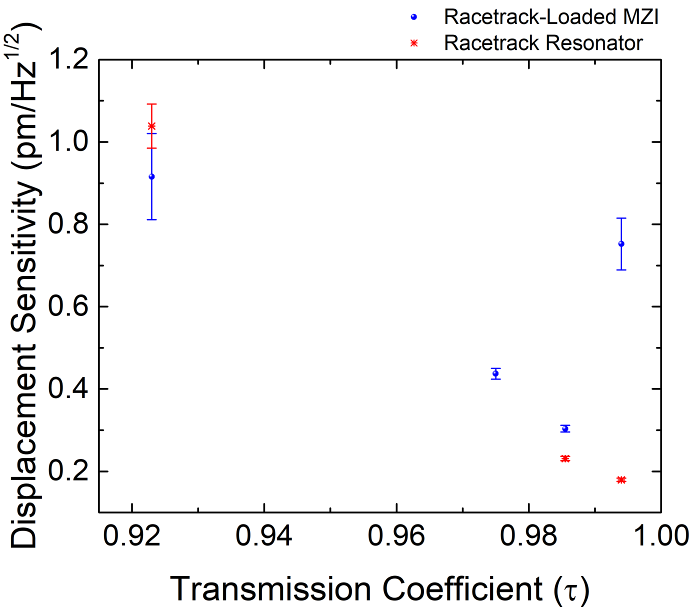

Figure 6.14: Displacement sensitivities of the different photonic circuits and coupling conditions. The racetracks are shown by the red stars, and the racetrack-loaded MZIs are shown by the blue dots.

better for the racetrack resonator. This is opposite to the result from simulation, but not unexpected given the close measurement of the slopes in Figure 6.11(b). For the smallest value of τ, the expected trend is observed, with the racetrack-loaded MZI showing a better displacement sensitivity compared to the racetrack resonator alone. Since the displacement sensitivity for both device architectures improves as τ increases, the ideal design for minimizing the displacement sensitivity is somewhere in the range of slightly over-coupled to critically coupled. This corresponds to $\tau = 0.97 - 0.99$.

After the thermomechanical measurements were recorded and the displacement sensitivity obtained, the amplitude modulation was activated for driven measurements. The driven measurements were recorded for increasing drive voltage amplitudes output from the lock in amplifier to the electro-optic modulator. The first and second harmonic signals ($1f$ and $2f$ signals) were recorded for each photonic circuit. A large background was present in all of the driven mechanical measurements. The large background resulted in a mechanical signal that was not a Lorentzian shape, but rather a Fano-like shape for both the racetracks and the racetrack-loaded MZIs. To subtract this background and return the mechanical signal to the expected Lorentzian lineshape, the following transformation was used. The measured data, taken in polar coordinates, was transformed to Cartesian coordinates using the typical equations $x = r\cos\theta$ and $y = r\sin\theta$. Then, x and y were plotted. A mechanical signal with no background is centered on the origin. However, it is clear from our data that a background is present as the data is always centered off the origin. The first and last 75 points in each dataset were averaged to determine the average start and end point. The midpoint of these start and end points was found to determine the overall background signal in Cartesian coordinates. This background was subtracted from the x and y data to re-center the data to the origin. Finally, the data was converted back to the usual polar coordinates for analysis. This procedure is shown graphically in Figure 6.15. The exact cause of the background is uncertain, but as it was a frequency-dependent background it may have been due to noise processes in the optical racetrack resonators that are dependent on frequency, such as a thermal effect. It is also possible that the pump laser was leaking through the filter and causing a frequency-dependent signal. Determining the cause of the background is a source of future work.

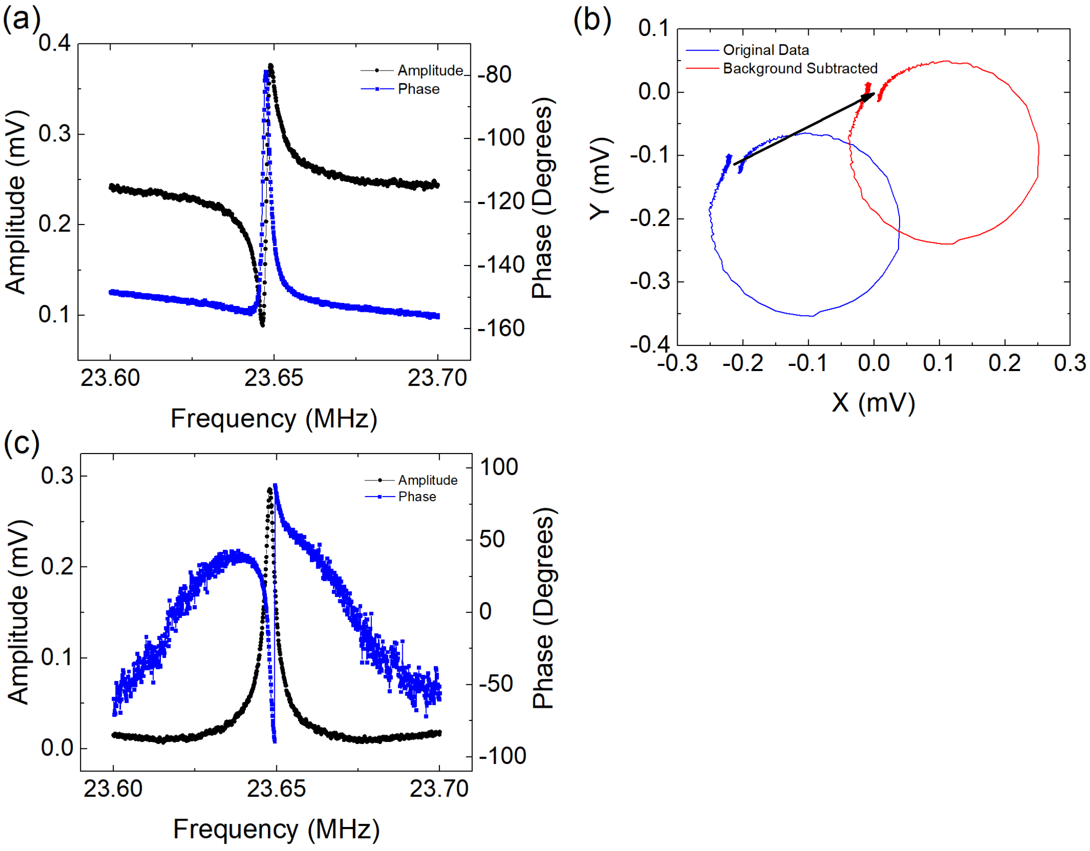

Figure 6.15: Visual description of the procedure used to subtract the frequency dependent background from the Fano-like signals. (a) The original recorded data in polar coordinates. (b) The original data converted to Cartesian coordinates is shown by the blue line, and the red line shows the transformed data where the background has been subtracted. The signal is now centered at the origin. (c) The transformed data in polar coordinates.

Once the fundamental and $2f$ peaks have been converted to Lorentzians and the background has been removed, we proceed with the analysis. The fundamental and $2f$ responses were fit with a Lorentzian to determine the peak value for each device and driving voltage. Many of the $2f$ signals with lower driving voltages could not be fit with a Lorentzian, since the signal was indistinguishable from the noise floor. This is expected, as the harmonic contribution will be negligible at low driving voltages. The peak voltages for the fundamental response were then converted to metres via the thermomechanical noise. By converting the fundamental response to metres, we are able to directly compare the results from different devices, as slight differences in driving power are automatically accounted for. Differences in driving power may be caused by different power enhancements in the optical cavity, slight changes in the alignment of the free-space optics to the grating couplers, or differences in the frequencies of the various cantilevers. The $2f$ peaks were extracted in units of μV. To compare the linear ranges of the racetracks to the racetrack-loaded MZIs, the $2f$ signal was plotted versus the fundamental displacement for each coupling condition. This result is shown in Figure 6.16.

For the most over-coupled case, shown in Figure 6.16(a), the racetrack resonator begins to show $2f$ components when the amplitude of the cantilever reaches approximately 0.9 nm. This is the largest linear range seen in any of the various coupling conditions. This trend agrees with results from simulation and the optical measurements of the devices shown in Figures 6.6(a) and 6.11(a) respectively. The racetrack-loaded MZI in this case did not reach a large enough amplitude to produce a signal at the $2f$ harmonic. The amplitude reached was only 0.2 nm. The optical drive for this device was clearly inefficient and did not drive the cantilever to a significant amplitude. The same optical power and voltage were input to the racetrack-loaded MZI as the racetrack resonator alone, however, only half of the input power reaches the cantilever in the racetrack-loaded MZI photonic circuit. The frequency of the cantilever on the racetrack-loaded MZI was also approximately 2 MHz higher than the cantilever on the racetrack. The higher frequency leads to a higher stiffness, and correspondingly a higher force is required to drive it to the same amplitude. For $\tau = 0.975$, we cannot make a direct comparison between the racetrack and racetrack-loaded MZI, since only the data from the racetrack-loaded MZI is available for that coupling condition. However, we can observe that the amplitude at which the $2f$ signal becomes apparent in Figure 6.16(b) is approximately 0.9 nm, the same as the racetrack in (a). Therefore, we determine that the linear range for the strongly over-coupled racetrack resonator is roughly equivalent to the linear range for the slightly over-coupled racetrack-loaded MZI. However, the racetrack-loaded MZI has significantly improved displacement sensitivity, suggesting that this architecture is in fact an improvement over the racetrack alone for transmission coefficients in the range of $0.925 - 0.975$.

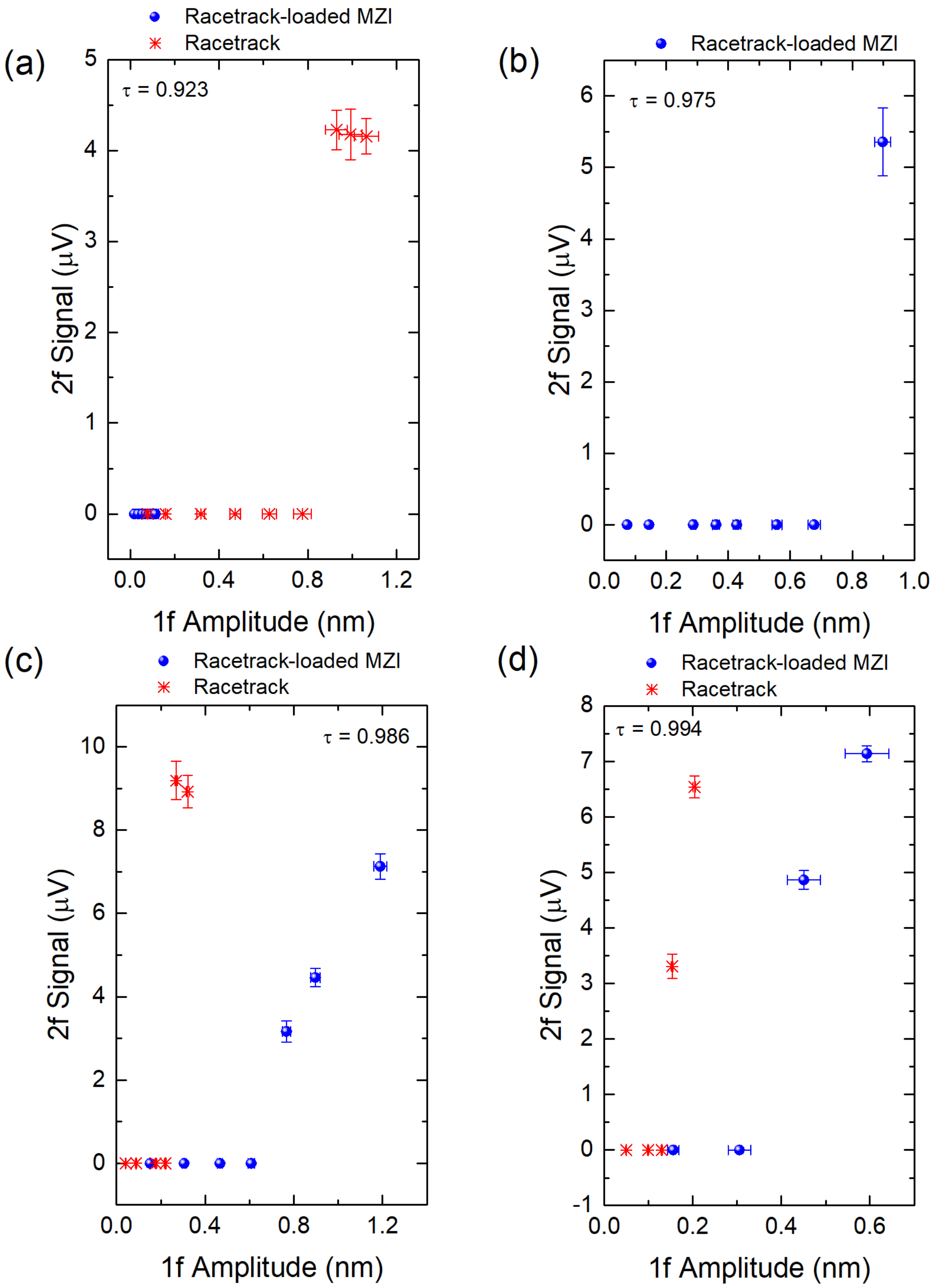

Figure 6.16: Amplitude of the fundamental mechanical signal in metres plotted versus the $2f$ signal in volts. The data for the racetrack resonators is shown by the red stars and the data for the racetrack-loaded MZIs is shown by the blue circles. The results are plotted for four coupling conditions; (a) strongly over-coupled, $\tau = 0.923$, (b) slightly over-coupled, $\tau = 0.975$, (c) close to critically coupled, $\tau = 0.986$, and (d) under-coupled, $\tau = 0.994$. The results demonstrate that the linear range is always greater for the racetrack-loaded MZIs, as the threshold for the onset of the $2f$ signal occurs at a lower mechanical amplitude for the racetracks compared to the racetrack-loaded MZIs.

We can compare more directly the cases for the critically coupled and under-coupled devices (Figure 6.16(c) and (d), respectively). For the critically coupled devices, the racetrack resonator has $2f$ components at a fundamental amplitude of 0.3 nm. The racetrack-loaded MZI has $2f$ components at a fundamental amplitude of 0.8 nm, which is a linear range improvement of 2.7 times. Furthermore, the amplitude of the $2f$ components for the racetrack-loaded MZI do not reach the same levels as the racetrack until the fundamental amplitude is close to 1.2 nm, which is a linear range improvement of 4 times. For the under-coupled case, the racetrack resonator has $2f$ components at a fundamental amplitude of 0.15 nm, and the racetrack-loaded MZI has $2f$ components at a fundamental amplitude of 0.45 nm, for a factor of 3 improvement in the linear range. Clearly, the racetrack-loaded MZIs allow for a larger fundamental amplitude to be reached before the $2f$ components become significant. This indicates that a larger linear readout of nanomechanical motion is achieved by the racetrack-loaded MZIs than by the racetracks alone, for all coupling conditions.

6.4 Discussion

From experimental results of both optical and mechanical measurements of racetrack resonators and racetrack-loaded MZIs, we conclude that racetrack-loaded MZIs have a longer linear range than racetrack resonators alone. The improvement in linear range is substantial; an improvement of 3–4 times is observed in both the optical and mechanical results when the coupling is close to critical. As the devices become more over-coupled, the performance of the racetrack resonator improves more quickly than the racetrack-loaded MZI, and so the benefit provided by the racetrack-loaded MZI is smaller. These results match the expected trends from simulation. In terms of the transduction sensitivity, the racetracks outperform the racetrack-loaded MZIs close to critical coupling. The racetracks become less sensitive than the racetrack-loaded MZIs as τ decreases. Again, this is the expected result from simulation.

Both simulations and experimental results demonstrate that the linear range is largest when τ is smallest, but the sensitivity worsens as τ decreases. These are both important factors in the consideration of the overall photonic circuit design. Another factor is the driving force applied through an optical pump to the devices. For the racetrack-loaded MZIs, the optical power delivered to the cantilever is halved compared to the racetrack resonator alone, decreasing the driving power. The results of Chapter 4 indicate that the driving force is reduced for over-coupled cavities where γ is large. Figure 6.16(a) shows that the reduced drive results in a very small driven amplitude. For the cavity in Figure 6.16(a), $\tau = 0.923$, $\gamma \approx 200$ rad GHz and $G \approx 0.2$ rad GHz/nm. Comparing these values to Figure 4.1 we see that the expected amplitude, and therefore the driving force, is very low. To compensate for the reduced drive power, the power in the drive laser can be increased or the driving voltage can be increased. Alternatively, the optomechanical coupling can be increased to provide higher driving force. The latter is a trade-off, however, since increasing the optomechanical coupling will increase the required linear range.

The increase in linear range obtained by using the racetrack-loaded MZI results in an increase in the dynamic range of the optomechanical system. This is beneficial for mass sensing. As described in Section 2.1, the mass sensitivity is proportional to the frequency fluctuations $\delta\Omega_0/\Omega_0$. This term is proportional to $a_{\text{noise}}/a_{\text{driven}} = 1/SNR$, where SNR is the signal-to-noise ratio. We can calculate the SNR for both the racetrack-loaded MZI and for the racetrack for the case where the coupling coefficient $\tau = 0.986$. a_{driven} is defined as the amplitude of the $1f$ signal before the onset of the $2f$ readout nonlinearity. For the racetrack-loaded MZI, $a_{\text{driven}} = 0.61$ nm. For the racetrack, $a_{\text{driven}} = 0.22$ nm. The amplitude of a_{noise} in each case is extracted from the thermomechanical noise, and is equal to 87.4 pm/Hz$^{1/2}$ for the racetrack-loaded MZI, and equal to 87.6 pm/Hz$^{1/2}$ for the racetrack. The SNR for the racetrack-loaded MZI is therefore 698 m/m Hz$^{1/2}$, and the SNR for the racetrack is 251 m/m Hz$^{1/2}$. This means that $\delta\Omega_0/\Omega_0 \propto a_{\text{noise}}/a_{\text{driven}}$ improves by a factor of 2.8 for the racetrack-loaded MZI compared to the racetrack resonator. Therefore, the mass sensitivity also improves by a factor of 2.8 with the new photonic architecture.

Overall, there are three main considerations to choosing the appropriate coupling condition for future designs; the linear range, the sensitivity, and the drive power. The choice of coupling condition will depend on the properties of the mechanical device. If the device has a very high frequency, for example, the sensitivity and drive power should be increased by designing a cavity close to critical coupling. The linear range can be sacrificed somewhat in this regard, as the stiffer cantilever will have a smaller amplitude of vibration. A low frequency device will naturally have a larger amplitude, and so a larger linear range is necessary. For a cantilever with low resonance frequency, the required optical drive power and sensitivity are reduced, and so the cavity can be strongly over-coupled. Regardless of the coupling condition is chosen, using a racetrack-loaded MZI will improve the linear range of the mechanical readout.

6.5 Conclusion

To reduce the readout nonlinearity observed in racetrack resonator coupled optomechanical systems, we have designed, fabricated, and tested racetrack-loaded Mach Zehnder interferometers. A racetrack resonator is coupled to one arm of a MZI, while the reference arm has a phase shift set to $\pi/2$ at a wavelength of 1550 nm. Although in this case we have used this photonic circuit to improve the linear range for optomechanical mass sensors, this phase-sensitive photonic integrated circuit may also enable on-chip homodyne measurements for other optomechanical applications. The Fano-like resonance shape of the racetrack-loaded MZI increases the linear response of the transfer function of the photonic circuit by between 3–4 times, depending on how strongly the racetrack resonator is coupled to the MZI arm. The improvements in the linear range were observed in both the optical spectra and the mechanical signal. To determine the mechanical linear range, the mechanical signal was recorded at the fundamental resonance frequency as well as higher harmonics. The mechanical linear range was specified by the fundamental amplitude in metres where the $2f$ signal was greater than zero. The linear range was highest for the most over-coupled optical cavities, and smallest for under-coupled cavities. The displacement sensitivity of the racetrack-loaded MZIs was slightly worse than racetrack resonators close to critical coupling. When the cavities were strongly over-coupled, the racetrack-loaded MZIs had better displacement sensitivity.

The linear range of the racetrack-loaded MZIs was greater than the racetrack resonators in all cases. By converting the improvement in linear range to an improvement in signal-to-noise ratio, we are able to determine than the SNR of the racetrack-loaded MZI is improved by 2.8 times compared to the racetrack. This should lead to an improvement in mass sensitivity by a factor of 2.8. This photonic circuit architecture will be very valuable for reducing the readout nonlinearity of photonic transduction when using cantilevers or other high amplitude nanomechanical devices, and improving their performance as mass sensors.

Chapter 7

Conclusions

Nanomechanical devices are very promising mass sensors due to their low limit of detection. When combined with integrated photonic transducers to create nano-optomechanical systems, a number of desirable properties such as excellent signal-to-noise ratio, high bandwidth, and CMOS compatibility are attained. In this thesis, we have studied nanomechanical cantilevers coupled to optical racetrack resonators. The end goal in mind is low-cost, portable mass sensing technology that could be used in applications such as health care diagnostic tools and gas analysis. The nanomechanical cantilevers are actuated using an all-optical pump-and-probe approach. The nano-optomechanical system is fabricated using silicon-on-insulator substrates and operates at near-infrared wavelengths.

An important consideration for portable sensor technology is power consumption. We derived a unique design methodology specifically for the pump-and-probe approach that improves the efficiency of the integrated photonic transduction scheme. By adhering to these design principles, the AC optical power required to reach the upper bound on the cantilever's dynamic range was reduced by approximately four times compared to an unoptimized system. By using the optimized optomechanical system, we were able to achieve large amplitudes greater than 12 nm. This large amplitude was sufficient to introduce nonlinearity into the system and thereby reach the upper end of the dynamic range of the cantilever. Reaching the full dynamic range while reducing power consumption by 4 compared to previous nano-optomechanical system designs represents a significant improvement.

Once we reached the upper bound on the dynamic range of the nano-optomechanical system, we performed in-depth experimental characterization of the device, while it was driven into nonlinearity. To extend the dynamic range of the nano-optomechanical system, and improve the detection limit of the system for use as a mass sensor, we must first understand the sources of nonlinearity. By studying the effects of pump laser drive power and probe laser detuning on the nano-optomechanical system, we experimentally observed a stiffening nonlinearity when the probe laser was red-detuned, a softening nonlinearity when the probe laser was blue-detuned, and a softening nonlinearity at zero detuning. This counterintuitive result could not be fully explained by any existing models in the literature. We adapted an existing analytical model to include the pump laser, and this approach was able to reproduce the softening observed at blue detuning and the stiffening observed at red detuning. The model could not explain the softening at zero detuning. Furthermore, no other existing model accounted for an AC amplitude modulated pump laser, or for the large amplitudes of vibration experienced by the cantilever in our optomechanical system. We derived and solved a numerical model to account for the effects of the pump laser and the large amplitudes of vibration. By using the numerical model we were able to ascertain that there were three sources of nonlinearity in the nano-optomechanical system; a readout nonlinearity, an optical cavity force nonlinearity, and an evanescent force nonlinearity. Using the numerical model, we could separate the different types of nonlinearity and determine the impact that each one had on the nanomechanical system. The amplitude of the mechanical device could also be modeled directly, which allowed for approximation of the amplitude. This is an important benefit, as the amplitude could not be obtained experimentally due to the readout nonlinearity. The model successfully accounted for the stiffening and softening effects observed red, blue, and zero detuning.

It was evident that the readout nonlinearity posed the most significant challenge for using these devices as mass sensors, as the amplitude could not be correctly calibrated and the onset of this nonlinearity was earlier than the other types of nonlinearity. For this reason, in the final chapter we studied an alternative integrated photonic circuit for transduction of the nanomechanical device. This circuit, a racetrack-loaded Mach Zehnder interferometer (MZI), is a phase-sensitive circuit and has a Fano-like lineshape and constitutes an integrated photonics implementation of optical homodyning. For these reasons, the circuit was expected to have a larger linear range than the racetrack resonator alone. Many different aspects of the circuit were modeled in the design process, including the coupling conditions of the racetrack resonator to the MZI and the phase difference between two arms of the racetrack-loaded MZI. The design process for on-chip, phase-sensitive detection of optomechanical systems has not been previously explored and may find use in other applications, such as on-chip homodyne detection. Experimental testing of the optical and mechanical properties of the racetrack-loaded MZIs resulted in a linear range improvement compared to the racetrack resonators, regardless of the coupling condition of the racetrack-loaded MZI. We demonstrate that improvement in the linear range results in an improvement in the dynamic range, and therefore the mass sensitivity, by a factor of 2.8.

This work has demonstrated approximately a four times reduction in the power consumption and approximately three times improvement to the mass sensitivity of nano-optomechanical systems, improving the overall performance of these devices as mass sensors. However, the primary contribution of this work is in improving the understanding of the source of nonlinearities in nano-optomechanical systems when used with a pump-and-probe transduction scheme. The model derived here can be used to design future systems and characterize existing systems, and occupies a previously unexplored niche in the complex realm of nano-optomechanical nonlinearity.

All of these improvements have contributed to a greater understanding of nano-optomechanical systems for use in mass sensing applications. These improvements are important strides to make optomechanical mass sensing more practical and portable. In the following section, we provide suggestions on how to build on the work presented here, to continue to make improvements for mass sensing technology based on nano-optomechanical mass sensors.

The end goal for this technology is to combine the remarkable sensitivity of the nanomechanical sensor, integrated photonic transducer, and all of the necessary electronics to create a portable, low-cost mass analysis system. The sensor and transducer already have a low limit of detection, a small footprint, and low cost due to the fact that they are both simultaneously fabricated using CMOS processes. This is an excellent starting point for the overall technology. To create a portable system, the surrounding lasers and electronics are an important consideration. The large, tunable diode laser could be replaced with a small on-chip laser. The bulky chambers used to hold the chips could be replaced with smaller, gas-tight packages. However, the biggest hurdle for creating a portable device is the electronics used for analysis. The lock-in amplifier, currently used for phase-lock loop operation, is not portable. However, creative solutions such as using a wireless connection on the chip or package may be incorporated. The chip and package would then be small and portable, with a larger, less portable "reader" elsewhere for data analysis. This approach, used in conjunction with the sensor and transducer improvements suggested in this thesis, would help propel the technology forward. With each improvement to the sensor, transducer, electronics, or packaging, the dream of a portable mass analysis system for health care, environmental monitoring, or gas analysis becomes closer to reality.

7.1 Directions for Future Work

One area for future development is in developing nano-optomechanical mass sensing technology for operation in liquid. Future development should focus on the fin resonators, which despite the difficulties observed in this work still have significant potential for liquid sensing. The fin response may be seen if the noise floor of the measurement of fins could be reduced by modifying the experimental setup. Lower noise photodiodes, amplifiers at the output, or a mixing technique to reduce the overall noise may all be useful directions to explore. The sensitivity of the transduction could be improved by using high quality factor optical cavities such as photonic crystals.

When considering the dynamic range of the mass sensor, the next step is to combine the optimized drive with the racetrack-loaded MZI circuit. To achieve this goal, devices defined using electron beam lithography will likely be required to obtain the small gap between the cantilever and the optical cavity required to achieve the desired optomechanical coupling coefficients. This design should be modeled numerically to determine the sources of nonlinearity, so that they may be reduced as much as possible. A future design that accounts for all of these aspects will represent a substantial improvement in the on-chip mass sensing architecture. These improvements to the overall sensor technology are crucial to moving nano-optomechanical mass sensors forward to enable our vision of a portable, inexpensive mass analysis technology.

Bibliography

[1] J. Chaste, A. Eichler, J. Moser, G. Ceballos, R. Rurali, and A. Bachtold. "A nanomechanical mass sensor with yoctogram resolution." Nat. Nanotechnol., **7** (5), 301–304, 2012. [Cited on page 1.]

[2] K. S. Hwang, J. H. Lee, J. Park, D. S. Yoon, J. H. Park, and T. S. Kim. "In-situ quantitative analysis of a prostate-specific antigen (PSA) using a nanomechanical PZT cantilever." Lab Chip, **4**, 547–552, 2004. [Cited on page 1.]

[3] N. V. Lavrik, M. Sepaniak, and P. G. Datskos. "Cantilever transducers as a platform for chemical and biological sensors." Rev. Sci. Instrum., **75** (7), 2229–2253, 2004. [Cited on page 1.]

[4] J. L. Arlett, E. B. Myers, and M. L. Roukes. "Comparative advantages of mechanical biosensors." Nat. Nanotechnol., **6** (4), 203–215, 2011. [Cited on page 1.]

[5] J. Tamayo, P. M. Kosaka, J. J. Ruz, Á. San Paulo, and M. Calleja. "Biosensors based on nanomechanical systems." Chem. Soc. Rev., **42** (3), 1287–311, 2013. [Cited on page 1.]

[6] X. M. H. Huang, M. Manolidis, S. C. Jun, and J. Hone. "Nanomechanical hydrogen sensing." Appl. Phys. Lett., **86** (14), 143104, 2005. [Cited on page 1.]

[7] M. Li, E. B. Myers, H. X. Tang, S. J. Aldridge, H. C. McCaig, J. J. Whiting, R. J. Simonson, N. S. Lewis, and M. L. Roukes. "Nanoelectromechanical resonator arrays for ultrafast, gas-phase chromatographic chemical analysis." Nano Lett., **10** (10), 3899–903, 2010. [Cited on page 1.]

[8] S. Fanget, S. Hentz, P. Puget, J. Arcamone, M. Matheron, E. Colinet, P. Andreucci, L. Duraffourg, E. Myers, and M. Roukes. "Gas sensors based on gravimetric detectionA review." Sensors Actuators B Chem., **160** (1), 804–821, 2011. [Cited on pages 1 and 98.]

[9] A. Venkatasubramanian, V. T. K. Sauer, S. K. Roy, M. Xia, D. S. Wishart, and W. K. Hiebert. "Nano-optomechanical systems for gas chromatography." Nano Lett., **16**, 69756981, 2016. [Cited on pages 1, 2, 9, 37, and 78.]

[10] K. De Vos, I. Bartolozzi, E. Schacht, P. Bienstman, and R. Baets. "Silicon-on-Insulator microring resonator for sensitive and label-free biosensing." Opt. Express, **15** (12), 7610–5, 2007. [Cited on page 2.]

[11] V. Sauer. *Nanophotonic detection of nanomechanical structures for use toward mass sensing applications.* Ph.D. thesis, 2014. [Cited on pages 2 and 41.]

[12] I. Bargatin, E. B. Myers, J. S. Aldridge, C. Marcoux, P. Brianceau, L. Duraffourg, E. Colinet, S. Hentz, P. Andreucci, and M. L. Roukes. "Large-scale integration of nanoelectromechanical systems for gas sensing applications." Nano Lett., **12** (3), 1269–74, 2012. [Cited on page 2.]

[13] J. D. Teufel, D. Li, M. S. Allman, K. Cicak, A. J. Sirois, J. D. Whittaker, and R. W. Simmonds. "Circuit cavity electromechanics in the strong-coupling regime." Nature, **471** (7337), 204–208, 2011. [Cited on page 2.]

[14] J. Bochmann, A. Vainsencher, D. D. Awschalom, and A. N. Cleland. "Nanomechanical coupling between microwave and optical photons." Nat. Phys., **9** (11), 712–716, 2013. [Cited on pages 2 and 160.]

[15] S. M. Meenehan, J. D. Cohen, S. Gröblacher, J. T. Hill, A. H. Safavi-Naeini, M. Aspelmeyer, and O. Painter. "Silicon optomechanical crystal resonator at millikelvin temperatures." Phys. Rev. A, **90** (1), 1–5, 2014. [Cited on pages 2 and 86.]

[16] K. Y. Fong, M. Poot, and H. X. Tang. "Nano-Optomechanical Resonators in Microfluidics." Nano Lett., **15** (9), 6116–6120, 2015. [Cited on pages 2, 37, and 48.]

[17] E. Gil-Santos, C. Baker, D. T. Nguyen, W. Hease, C. Gomez, A. Lemaître, S. Ducci, G. Leo, and I. Favero. "High-frequency nano-optomechanical disk resonators in liquids." Nat. Nanotechnol., **10** (9), 810–816, 2015. [Cited on pages 2, 36, and 48.]

[18] S. K. Roy, V. T. K. Sauer, J. N. Westwood-Bachman, A. Venkatasubramanian, and W. K. Hiebert. "Improving mechanical sensor performance through larger damping." Science, **360**, eaar5220, 2018. [Cited on pages 2, 8, 9, 37, 38, 118, 128, and 156.]

[19] M. S. Hanay, S. I. Kelber, C. D. O'Connell, P. Mulvaney, J. E. Sader, and M. L. Roukes. "Inertial imaging with nanomechanical systems." Nat. Nanotechnol., **10** (4), 339–344, 2015. [Cited on pages xiii, 3, 9, 75, and 79.]

[20] K. L. Ekinci, Y. T. Yang, and M. L. Roukes. "Ultimate limits to inertial mass sensing based upon nanoelectromechanical systems." J. Appl. Phys., **95** (5), 2682–2689, 2004. [Cited on pages 3, 9, 37, 100, 118, 121, and 128.]

[21] J. N. Westwood-Bachman, Z. Diao, V. T. K. Sauer, D. Bachman, and W. K. Hiebert. "Even nanomechanical modes transduced by integrated photonics." Appl. Phys. Lett., **108**, 061103, 2016. [Cited on pages xiii, 4, 52, 75, 76, 79, 83, 85, 100, and 121.]

[22] A. N. Cleland. *Foundations of Nanomechanics*. Springer New York, 2002. [Cited on pages 7 and 81.]

[23] J. N. Westwood. *High Surface Area Nanoelectromechanical Systems via the Integration of Glancing Angle Deposition Thin Films*. Ph.D. thesis, University of Alberta, 2013. [Cited on page 7.]

[24] M. V. Salapaka, H. S. Bergh, J. Lai, A. Majumdar, and E. McFarland. "Multi-mode noise analysis of cantilevers for scanning probe microscopy." J. Appl. Phys., **81** (6), 2480, 1997. [Cited on page 7.]

[25] B. D. Hauer, C. Doolin, K. S. D. Beach, and J. P. Davis. "A general procedure for thermomechanical calibration of nano/micro-mechanical resonators." Ann. Phys. (N. Y)., **339**, 181–207, 2013. [Cited on page 7.]

[26] K. Y. Yasumura, T. D. Stowe, E. M. Chow, T. Pfafman, T. W. Kenny, B. C. Stipe, and D. Rugar. "Quality factors in micron-and submicron-thick cantilevers." J. Microelectromechanical Syst., **9** (1), 117–125, 2000. [Cited on page 7.]

[27] M. Li, H. X. Tang, and M. L. Roukes. "Ultra-sensitive NEMS-based cantilevers for sensing, scanned probe and very high-frequency applications." Nat. Nanotechnol., **2** (2), 114–20, 2007. [Cited on pages 8 and 10.]

[28] M. Bao and H. Yang. "Squeeze film air damping in MEMS." Sensors Actuators A Phys., **136** (1), 3–27, 2007. [Cited on page 8.]

[29] R. Lifshitz and M. L. Roukes. "Thermoelastic damping in micro- and nanomechanical systems." Phys. Rev. B, **61** (8), 5600–5609, 2000. [Cited on page 8.]

[30] P. Mohanty, D. Harrington, K. Ekinci, Y. Yang, M. Murphy, and M. L. Roukes. "Intrinsic dissipation in high-frequency micromechanical resonators." Phys. Rev. B, **66** (8), 085416, 2002. [Cited on page 8.]

[31] I. Wilson-Rae. "Intrinsic dissipation in nanomechanical resonators due to phonon tunneling." Phys. Rev. B, **77** (24), 245418, 2008. [Cited on page 8.]

[32] I. Wilson-Rae, R. A. Barton, S. S. Verbridge, D. R. Southworth, B. Ilic, H. G. Craighead, and J. M. Parpia. "High-Q Nanomechanics via Destructive Interference of Elastic Waves." Phys. Rev. Lett., **106** (4), 047205, 2011. [Cited on page 8.]

[33] I. Voiculescu, M. E. Zaghloul, and R. A. McGill. "Electrostatically actuated resonant microcantilever beam in CMOS technology for the detection of chemical weapons." Sensors J., **5** (4), 641–647, 2005. [Cited on page 8.]

[34] A. M. Elshurafa, K. Khirallah, H. H. Tawfik, A. Emira, A. K. S. Abdel Aziz, and S. M. Sedky. "Nonlinear dynamics of spring softening and hardening in folded-mems comb drive resonators." J. Microelectromechanical Syst., **20** (4), 943–958, 2011. [Cited on page 8.]

[35] O. Svitelskiy, V. Sauer, D. Vick, K.-M. Cheng, N. Liu, M. R. Freeman, and W. K. Hiebert. "Nanoelectromechanical devices in a fluidic environment." Phys. Rev. E, **85** (5), 056313, 2012. [Cited on page 8.]

[36] A. Prak, M. Elwenspoek, and J. H. J. Fluitman. "Selective mode excitation and detection of micromachined resonators." J. Microelectromechanical Syst., **1** (2), 179–186, 1992. [Cited on page 8.]

[37] A. G. Krause, M. Winger, T. D. Blasius, Q. Lin, and O. Painter. "A high-resolution microchip optomechanical accelerometer." Nat. Photonics, **6**, 2012. [Cited on page 8.]

[38] L. G. Villanueva, R. B. Karabalin, M. H. Matheny, D. Chi, J. E. Sader, and M. L. Roukes. "Nonlinearity in nanomechanical cantilevers." Phys. Rev. B, **87** (2), 024304, 2013. [Cited on pages 8 and 120.]

[39] A. Kumar, S. Rajauria, H. Huo, O. Ozsun, K. Rykaczewski, J. Kumar, and K. L. Ekinci. "Surface area enhancement of microcantilevers by femto-second laser irradiation." Appl. Phys. Lett., **100** (14), 141607, 2012. [Cited on page 8.]

[40] J. D. Thompson, B. M. Zwickl, A. M. Jayich, F. Marquardt, S. M. Girvin, and J. G. E. Harris. "Strong dispersive coupling of a high-finesse cavity to a micromechanical membrane." Nature, **452** (7183), 72–5, 2008. [Cited on pages 8 and 33.]

[41] R. B. Karabalin, M. H. Matheny, X. L. Feng, E. Defay, G. Le Rhun, C. Marcoux, S. Hentz, P. Andreucci, and M. L. Roukes. "Piezoelectric nanoelectromechanical resonators based on aluminum nitride thin films." Appl. Phys. Lett., **95** (10), 103111, 2009. [Cited on page 8.]

[42] R. B. Karabalin, S. C. Masmanidis, and M. L. Roukes. "Efficient parametric amplification in high and very high frequency piezoelectric nanoelectromechanical systems." Appl. Phys. Lett., **97** (18), 183101, 2010. [Cited on page 8.]

[43] K. Y. Fong, L. Fan, L. Jiang, X. Han, and H. X. Tang. “Microwave-assisted coherent and nonlinear control in cavity piezo-optomechanical systems.” Phys. Rev. A, **90** (5), 1–5, 2014. [Cited on pages 8 and 118.]

[44] H. Li and B. Balachandran. “Buckling and free oscillations of composite microresonators.” J. Microelectromechanical Syst., **15** (1), 42–51, 2006. [Cited on page 8.]

[45] B. Ilic, S. Krylov, K. Aubin, R. Reichenbach, and H. G. Craighead. “Optical excitation of nanoelectromechanical oscillators.” Appl. Phys. Lett., **86** (19), 193114, 2005. [Cited on page 8.]

[46] R. De Alba, T. S. Abhilash, R. Rand, H. G. Craighead, and J. M. Parpia. “Low-power photothermal self-oscillation of bimetallic nanowires.” **0** (c), 1–7, 2016. [Cited on page 8.]

[47] H. Fu, C. Liu, Y. Liu, J. Chu, and G. Cao. “Selective photothermal self-excitation of mechanical modes of a micro-cantilever for force microscopy.” Appl. Phys. Lett., **99** (17), 173501, 2011. [Cited on page 8.]

[48] D. Ramos, J. Tamayo, J. Mertens, and M. Calleja. “Photothermal excitation of microcantilevers in liquids.” J. Appl. Phys., **99** (12), 0–8, 2006. [Cited on page 8.]

[49] D. Ramos, J. Mertens, M. Calleja, and J. Tamayo. “Phototermal self-excitation of nanomechanical resonators in liquids.” Appl. Phys. Lett., **92** (17), 2006–2009, 2008. [Cited on page 8.]

[50] Q. Lin, J. Rosenberg, X. Jiang, K. J. Vahala, and O. Painter. “Mechanical oscillation and cooling actuated by the optical gradient force.” Phys. Rev. Lett., **103** (10), 1–4, 2009. [Cited on pages 8, 33, 37, and 100.]

[51] J. Roels, I. De Vlaminck, L. Lagae, B. Maes, D. Van Thourhout, and R. Baets. “Tunable optical forces between nanophotonic waveguides.” Nat. Nanotechnol., **4** (8), 510–3, 2009. [Cited on pages 8 and 33.]

[52] M. Eichenfield, R. Camacho, J. Chan, K. J. Vahala, and O. Painter. “A picogram- and nanometre-scale photonic-crystal optomechanical cavity.” Nature, **459** (7246), 550–5, 2009. [Cited on pages 8 and 33.]

[53] Q. Lin, J. Rosenberg, D. Chang, R. Camacho, M. Eichenfield, K. J. Vahala, and O. Painter. “Coherent mixing of mechanical excitations in nano-optomechanical structures.” Nat. Photonics, **4** (April), 236—-242, 2010. [Cited on pages 8 and 33.]

[54] D. Van Thourhout and J. Roels. “Optomechanical device actuation through the optical gradient force.” Nat. Photonics, **4** (4), 211–217, 2010. [Cited on pages 8, 33, and 82.]

[55] N. Kacem and S. Hentz. “Bifurcation topology tuning of a mixed behavior in nonlinear micromechanical resonators.” Appl. Phys. Lett., **95** (18), 183104, 2009. [Cited on page 8.]

[56] V. Sazonova, Y. Yaish, H. Ustünel, D. Roundy, T. A. Arias, and P. L. McEuen. “A tunable carbon nanotube electromechanical oscillator.” Nature, **431**, 284–7, 2004. [Cited on page 8.]

[57] P. A. Truitt, J. B. Hertzberg, E. Altunkaya, and K. C. Schwab. “Linear and nonlinear coupling between transverse modes of a nanomechanical resonator.” J. Appl. Phys., **114** (11), 114307, 2013. [Cited on page 8.]

[58] P. Ivaldi, J. Abergel, M. H. Matheny, L. G. Villanueva, R. B. Karabalin, M. L. Roukes, P. Andreucci, S. Hentz, and E. Defaÿ. "50 nm thick AlN film-based piezoelectric cantilevers for gravimetric detection." J. Micromechanics Microengineering, **21** (8), 085023, 2011. [Cited on page 8.]

[59] M. H. Matheny, L. G. Villanueva, R. B. Karabalin, J. E. Sader, and M. L. Roukes. "Nonlinear Mode-Coupling in Nanomechanical Systems." Nano Lett., **13**, 1622–1626, 2013. [Cited on page 8.]

[60] H. Guo, X. Chen, Y. Yao, G. Du, and H. Li. "Detection of ethanol and methanol vapors using polymer-coated piezoresistive Si bridge." Sensors Actuators B Chem., **155** (2), 519–523, 2011. [Cited on page 8.]

[61] P. Li and X. Li. "A single-sided micromachined piezoresistive SiO 2 cantilever sensor for ultra-sensitive detection of gaseous chemicals." J. Micromechanics Microengineering, **16** (12), 2539–2546, 2006. [Cited on page 8.]

[62] P. R. Wilkinson, W. S. Klug, B. Van Leer, and J. K. Gimzewski. "Nanomechanical properties of piezoresistive cantilevers: Theory and experiment." J. Appl. Phys., **104** (10), 103527, 2008. [Cited on page 8.]

[63] W. K. Hiebert, D. Vick, V. T. K. Sauer, and M. R. Freeman. "Optical interferometric displacement calibration and thermomechanical noise detection in bulk focused ion beam-fabricated nanoelectromechanical systems." J. Micromechanics Microengineering, **20** (11), 115038, 2010. [Cited on pages 8 and 83.]

[64] K. L. Ekinci. "Electromechanical transducers at the nanoscale: actuation and sensing of motion in nanoelectromechanical systems (NEMS)." Small, **1** (8-9), 786–797, 2005. [Cited on page 8.]

[65] T. Larsen, S. Schmid, S. Dohn, J. E. Sader, A. Boisen, and L. G. Villanueva. "Position and mode dependent optical detection back-action in cantilever beam resonators." J. Micromechanics Microengineering, **27** (3), 035006, 2017. [Cited on page 8.]

[66] T. Larsen, S. Schmid, L. G. Villanueva, and A. Boisen. "Photothermal analysis of individual nanoparticulate samples using micromechanical resonators." ACS Nano, **7** (7), 6188–93, 2013. [Cited on page 8.]

[67] M. Li, W. H. P. Pernice, C. Xiong, T. Baehr-Jones, M. Hochberg, and H. X. Tang. "Harnessing optical forces in integrated photonic circuits." Nature, **456**, 480–4, 2008. [Cited on pages 8, 33, 82, 100, and 135.]

[68] V. T. K. Sauer, Z. Diao, M. R. Freeman, and W. K. Hiebert. "Nanophotonic detection of side-coupled nanomechanical cantilevers." Appl. Phys. Lett., **100** (26), 261102, 2012. [Cited on pages 8, 39, and 162.]

[69] V. T. K. Sauer, Z. Diao, M. R. Freeman, and W. K. Hiebert. "Optical racetrack resonator transduction of nanomechanical cantilevers." Nanotechnology, **25** (5), 055202, 2014. doi:10.1088/0957-4484/25/5/055202.
URL `https://doi.org/10.1088/0957-4484/25/5/055202` [Cited on pages x, 8, 38, 39, 40, 41, 42, 52, 100, 103, 105, 117, 135, and 166.]

[70] S. Dohn, S. Schmid, F. Amiot, and A. Boisen. "Position and mass determination of multiple particles using cantilever based mass sensors." Appl. Phys. Lett., **97** (04), 044103, 2010. [Cited on page 9.]

[71] H. W. C. Postma, I. Kozinsky, A. Husain, and M. L. Roukes. "Dynamic range of nanotube- and nanowire-based electromechanical systems." Appl. Phys. Lett., **86** (22), 223105, 2005. [Cited on page 9.]

[72] A. Mekis, S. Gloeckner, G. Masini, A. Narasimha, T. Pinguet, S. Sahni, and P. De Dobbelaere. "A Grating-Coupler-Enabled CMOS Photonics Platform." IEEE J. Sel. Top. Quantum Electron., **17** (3), 597–608, 2011. [Cited on pages 10, 19, and 41.]

[73] X. Chen and H. K. Tsang. "Polarization-independent grating couplers for silicon-on-insulator nanophotonic waveguides." Opt. Lett., **36** (6), 796–8, 2011. [Cited on pages 10 and 19.]

[74] G. Beaudin, E. Grondin, A. Belarouci, P. G. Charette, and V. Aimez. "Evanescent field coupler optimized for high refractive index differences (ECHRID) - A platform for a soi photonics optical interface." IEEE J. Sel. Top. Quantum Electron., **22** (6), 8200509, 2016. [Cited on pages 10, 18, and 58.]

[75] D. Bachman, Z. Chen, and R. Fedosejevs. "Permanent fine tuning of silicon microring devices by femtosecond laser surface amorphization and ablation." Opt. Express, **21** (9), 3738–3743, 2013. [Cited on pages 10 and 18.]

[76] A. Yariv. "Coupled-Mode theory for guided-wave optics." IEEE J. Quantum Electron., **9** (9), 919–933, 1973. [Cited on pages 10 and 23.]

[77] L. Chrostowski. "CMC Passives Workshop.", 2014. [Cited on pages 10, 20, 23, 41, 47, and 162.]

[78] B. E. A. Saleh and M. C. Teich. *Fundamentals of photonics*, volume 22. Wiley New York, 1991. [Cited on page 12.]

[79] K. Kawano and T. Kitoh. *Introduction to Optical Waveguide Analysis: Solving Maxwell's Equation and the Schrödinger Equation*. John Wiley & Sons, 2004. [Cited on page 12.]

[80] M. L. Calvo and V. Lakshminarayanan. *Optical waveguides: from theory to applied technologies*. CRC Press, 2007. [Cited on page 12.]

[81] G. Lifante. *Integrated photonics: fundamentals*. John Wiley & Sons, 2003. [Cited on page 12.]

[82] K. Iizuka. "Elements of Photonics, For Fiber and Integrated Optics, Vol. 2." 2002. [Cited on page 12.]

[83] E. Hecht. *Optics*. Addison Wesley, 4th edition, 2002. [Cited on pages 12 and 43.]

[84] G. Anetsberger, O. Arcizet, Q. P. Unterreithmeier, R. Rivière, A. Schliesser, E. M. Weig, J. P. Kotthaus, and T. J. Kippenberg. "Near-field cavity optomechanics with nanomechanical oscillators." Nat. Phys., **5**, 909–914, 2009. [Cited on page 13.]

[85] M. Fox. "Optical properties of solids.", 2002. [Cited on page 13.]

[86] D. J. Griffiths. *Introduction to electrodynamics*. Prentice Hall, 3rd edition, 1999. [Cited on page 14.]

[87] L. Chrostowski, N. Rouger, D. Deptuck, and N. A. F. Jaeger. "Silicon Nanophotonics Fabrication: An innovative graduate course." In "2010 17th Int. Conf. Telecommun.", 544–551. 2010. [Cited on page 14.]

[88] L. Chrostowski and M. Hochberg. *Silicon photonics design: from devices to systems*. Cambridge University Press, 2015. [Cited on page 14.]

[89] R. M. Knox and P. P. Toulios. "Integrated circuits for the millimeter through optical frequency range." In "Proc. Symp. Submillim. Waves," volume 20, 497–515. Brooklyn, NY, 1970. [Cited on page 14.]

[90] G. B. Hocker and W. K. Burns. “Mode dispersion in diffused channel waveguides by the effective index method.” Appl. Opt., **16** (1), 113–118, 1977. [Cited on page 14.]

[91] K. S. Chiang. “Dual effective-index method for the analysis of rectangular dielectric waveguides.” Appl. Opt., **25** (13), 2169–2174, 1986. [Cited on page 14.]

[92] R. G. Hunsperger. *Integrated optics*, volume 4. Springer, 1995. [Cited on page 15.]

[93] K. S. Chiang. “Analysis of the effective-index method for the vector modes of rectangular-core dielectric waveguides.” IEEE Trans. Microw. Theory Tech., **44** (5), 692–700, 1996. [Cited on page 16.]

[94] V. Van. *Optical Microring Resonators: Theory, Techniques, and Applications*. Taylor & Francis, 2017. [Cited on pages 16, 24, 29, 46, 126, and 158.]

[95] P. Dumon. *Ultra-Compact Integrated Optical Filters in Silicon-on-insulator by Means of Wafer-Scale Technology*. Ph.D. thesis, Universiteit Gent, 2007. [Cited on pages 17 and 46.]

[96] K. Yamada. “Silicon Photonic Wire Waveguides: Fundamentals and Applications.” In D. J. Lockwood and L. Pavesi, editors, “Silicon Photonics II Components Integr.”, volume 119, chapter 1, 1–29. Springer, 2011. [Cited on page 17.]

[97] C.-Y. Chao, W. Fung, and L. J. Guo. “Polymer Microring Resonators for Biochemical Sensing Applications.” IEEE J. Sel. Top. Quantum Electron., **12** (1), 134–142, 2006. [Cited on page 17.]

[98] B. Jalali and S. Fathpour. “Silicon photonics.” J. Light. Technol., **24** (12), 4600–4615, 2006. [Cited on page 17.]

[99] R. Soref. “The past, present, and future of silicon photonics.” IEEE J. Sel. Top. quantum Electron., **12** (6), 1678–1687, 2006. [Cited on page 17.]

[100] D.-X. Xu, J. H. Schmid, G. T. Reed, G. Z. Mashanovich, D. J. Thomson, M. Nedeljkovic, X. Chen, D. Van Thourhout, S. Keyvaninia, and S. K. Selvaraja. “Silicon photonic integration platform – Have we found the sweet spot?” IEEE J. Sel. Top. Quantum Electron., **20** (4), 189–205, 2014. [Cited on page 17.]

[101] D. Bachman. *Femtosecond laser modification of silicon photonic integrated devices*. Ph.D. thesis, University of Alberta, 2016. [Cited on page 18.]

[102] P. N. Prasad. “Polymers for photonics.” Int. J. Nonlinear Opt. Phys., **3** (4), 531–541, 1994. [Cited on page 18.]

[103] P. Rabiei, W. H. Steier, C. Zhang, and L. R. Dalton. “Polymer micro-ring filters and modulators.” J. Light. Technol., **20** (11), 1968–1975, 2002. [Cited on page 18.]

[104] J. K. S. Poon, L. Zhu, G. A. DeRose, and A. Yariv. “Polymer Microring Coupled-Resonator Optical Waveguides.” J. Light. Technol., **24** (4), 1843–1849, 2006. [Cited on page 18.]

[105] Y.-G. Zhao, W.-K. Lu, Y. Ma, S.-S. Kim, S. T. Ho, and T. J. Marks. “Polymer waveguides useful over a very wide wavelength range from the ultraviolet to infrared.” Appl. Phys. Lett., **77** (19), 2961, 2000. [Cited on page 18.]

[106] A. Gorin, A. Jaouad, E. Grondin, V. Aimez, and P. Charette. "Fabrication of silicon nitride waveguides for visible-light using PECVD: a study of the effect of plasma frequency on optical properties." Opt. Express, **16** (18), 13509–13516, 2008. [Cited on page 18.]

[107] M.-S. Kwon and W. H. Steier. "Microring-resonator-based sensor measuring both the concentration and temperature of a solution." Opt. Express, **16** (13), 9372–9377, 2008. [Cited on page 18.]

[108] P. Barclay, K. Srinivasan, and O. Painter. "Nonlinear response of silicon photonic crystal microresonators excited via an integrated waveguide and fiber taper." Opt. Express, **13** (3), 801–820, 2005. [Cited on pages 18, 40, and 137.]

[109] A. C. Hryciw, M. Wu, B. Khanaliloo, and P. E. Barclay. "Tuning of nanocavity optomechanical coupling using a near-field fiber probe." Optica, **2** (5), 491, 2015. [Cited on page 18.]

[110] T. J. Kippenberg, H. Rokhsari, T. Carmon, A. Scherer, and K. J. Vahala. "Analysis of Radiation-Pressure Induced Mechanical Oscillation of an Optical Microcavity." Phys. Rev. Lett., **95** (3), 033901, 2005. [Cited on pages 18 and 33.]

[111] L. Yang, B. Yang, Z. Sheng, J. Wang, D. Dai, and S. He. "Compact 2x2 tapered multimode interference couplers based on SU-8 polymer rectangular waveguides." Appl. Phys. Lett., **93** (20), 1–4, 2008. [Cited on page 18.]

[112] M. C. Estevez, M. Alvarez, and L. M. Lechuga. "Integrated optical devices for lab-on-a-chip biosensing applications." Laser Photon. Rev., **6** (4), 463–487, 2012. [Cited on page 19.]

[113] Q. Quan, D. L. Floyd, I. B. Burgess, P. B. Deotare, I. W. Frank, S. K. Y. Tang, R. Ilic, and M. Loncar. "Single particle detection in CMOS compatible photonic crystal nanobeam cavities." Opt. Express, **21** (26), 5976–5979, 2013. [Cited on page 19.]

[114] Z. Cheng, X. Chen, C. Y. Wong, K. Xu, and H. K. Tsang. "Apodized focusing subwavelength grating couplers for suspended membrane waveguides." Appl. Phys. Lett., **101** (10), 101104, 2012. [Cited on page 19.]

[115] W. Shi, X. Wang, W. Zhang, H. Yun, C. Lin, L. Chrostowski, and N. A. F. Jaeger. "Grating-coupled silicon microring resonators." Appl. Phys. Lett., **100** (12), 121118, 2012. [Cited on page 19.]

[116] C. Errando-Herranz, F. Saharil, A. M. Romero, N. Sandstrom, R. Z. Shafagh, W. V. D. Wijngaart, T. Haraldsson, and K. B. Gylfason. "Integration of microfluidics with grating coupled silicon photonic sensors by one-step combined photopatterning and molding of OSTE." Opt. Express, **21** (18), 21293–21298, 2013. [Cited on page 19.]

[117] Y. Wang, X. Wang, J. Flueckiger, H. Yun, W. Shi, R. Bojko, N. A. F. Jaeger, and L. Chrostowski. "Focusing sub-wavelength grating couplers with low back reflections for rapid prototyping of silicon photonic circuits." Opt. Express, **22** (17), 20652–62, 2014. [Cited on pages 19 and 55.]

[118] Z. Diao, J. E. Losby, V. T. K. Sauer, J. N. Westwood, M. R. Freeman, and W. K. Hiebert. "Confocal Scanner for Highly Sensitive Photonic Transduction of Nanomechanical Resonators." Appl. Phys. Express, **6** (6), 065202, 2013. [Cited on pages 19, 41, 43, and 80.]

[119] G. Roelkens and D. Van Thourhout. "Interfacing Silicon Nanophotonic Integrated Circuits and Single-Mode Optical Fibers with Diffraction Gratings." In L. Pavesi and D. J. Lockwood, editors, "Silicon Photonics II Components Integr.", 71–94. Springer, 2011. [Cited on page 20.]

[120] F. Van Laere, T. Claes, J. Schrauwen, S. Scheerlinck, W. Bogaerts, D. Taillaert, L. O'Faolain, D. Van Thourhout, and R. Baets. "Compact focusing grating couplers for silicon-on-insulator integrated circuits." IEEE Photonics Technol. Lett., **19** (23), 1919–1921, 2007. [Cited on page 21.]

[121] J. D. Witmer, J. A. Valery, P. Arrangoiz-Arriola, C. J. Sarabalis, J. T. Hill, and A. H. Safavi-Naeini. "High-Q photonic resonators and electro-optic coupling using silicon-on-lithium-niobate." Sci. Rep., **7**, 46313, 2017. [Cited on page 21.]

[122] W. Bogaerts, P. De Heyn, T. Van Vaerenbergh, K. De Vos, S. Kumar Selvaraja, T. Claes, P. Dumon, P. Bienstman, D. Van Thourhout, and R. Baets. "Silicon microring resonators." Laser Photon. Rev., **6** (1), 47–73, 2012. [Cited on pages 22 and 30.]

[123] E. Dulkeith, F. Xia, L. Schares, W. M. J. Green, and Y. A. Vlasov. "Group index and group velocity dispersion in silicon-on-insulator photonic wires." Opt. Express, **14** (9), 3853–3863, 2006. [Cited on page 22.]

[124] K. J. Ebeling. *Integrated optoelectronics: waveguide optics, photonics, semiconductors*. Springer Berlin Heidelberg, 1993. [Cited on page 23.]

[125] M. Pu, N. Yao, C. Hu, X. Xin, Z. Zhao, C. Wang, and X. Luo. "Directional coupler and nonlinear Mach-Zehnder interferometer based on metal-insulator-metal plasmonic waveguide." Opt. Express, **18** (20), 21030, 2010. [Cited on page 23.]

[126] Q. Wang and S. He. "Optimal design of planar wavelength circuits based on Mach-Zehnder interferometers and their cascaded forms." J. Light. Technol., **23** (3), 1284–1290, 2005. [Cited on page 23.]

[127] A. Yariv. "Critical Coupling and Its Control in Optical Waveguide-Ring Resonator Systems." IEEE Photonics Technol. Lett., **14** (4), 2001–2003, 2002. [Cited on page 24.]

[128] A. Yariv and P. Yeh. *Photonics : optical electronics in modern communications*. The Oxford series in electrical and computer engineering. New York : Oxford University Press, 2007., 2007. [Cited on page 24.]

[129] C. Baker, C. Belacel, A. Andronico, P. Senellart, A. Lemaitre, E. Galopin, S. Ducci, G. Leo, and I. Favero. "Critical optical coupling between a GaAs disk and a nanowaveguide suspended on the chip." Appl. Phys. Lett., **99** (15), 151117, 2011. [Cited on page 24.]

[130] M. Cai, O. Painter, and K. J. Vahala. "Observation of critical coupling in a fiber taper to a silica-microsphere whispering-gallery mode system." Phys. Rev. Lett., **85** (1), 74–7, 2000. [Cited on page 24.]

[131] A. Yariv. "Universal relations for coupling of optical power between microresonators and dielectric waveguides." Electron. Lett., **36** (4), 321–322, 2000. [Cited on page 26.]

[132] M. Kuznetsov and H. A. Haus. "Radiation Loss in Dielectric Waveguide Structures by the Volume Current Method." IEEE J. Quantum Electron., **19** (10), 1505–1514, 1983. [Cited on page 26.]

[133] J. Cardenas, C. B. Poitras, J. T. Robinson, K. Preston, L. Chen, and M. Lipson. "Low loss etchless silicon photonic waveguides." Opt. Express, **17** (6), 4752, 2009. [Cited on page 26.]

[134] A. Nitkowski, L. Chen, and M. Lipson. "Cavity-enhanced on-chip absorption spectroscopy using microring resonators." Opt. Express, **16** (16), 11930–6, 2008. [Cited on page 26.]

[135] D. Marcuse. “Mode Conversation Caused by Surface Imperfections of a Dielectric Slab Waveguide.” Bell Syst. Tech. J., **48**, 3187–3215, 1969. [Cited on page 26.]

[136] K. K. Lee, D. R. Lim, H.-C. Luan, A. Agarwal, J. Foresi, and L. C. Kimerling. “Effect of size and roughness on light transmission in a Si/SiO2 waveguide: Experiments and model.” Appl. Phys. Lett., **77** (11), 1617–1619, 2000. [Cited on page 26.]

[137] C. G. Poulton, C. Koos, M. Fujii, A. Pfrang, T. Schimmel, J. Leuthold, and W. Freude. “Radiation modes and roughness loss in high index-contrast waveguides.” IEEE J. Sel. Top. Quantum Electron., **12** (6), 1306–1320, 2006. [Cited on page 26.]

[138] T. Tsuchizawa, K. Yamada, H. Fukuda, T. Watanabe, J. I. Takahashi, M. Takahashi, T. Shoji, E. Tamechika, S. I. Itabashi, and H. Morita. “Microphotonics devices based on silicon microfabrication technology.” IEEE J. Sel. Top. Quantum Electron., **11** (1), 232–239, 2005. [Cited on page 26.]

[139] M. Gnan, S. Thoms, D. S. Macintyre, R. M. De La Rue, and M. Sorel. “Fabrication of low-loss photonic wires in silicon-on-insulator using hydrogen silsesquioxane electron-beam resist.” Electron. Lett., **44** (2), 2008. [Cited on page 26.]

[140] K. K. Lee, D. R. Lim, and L. C. Kimerling. “Fabrication of ultralow-loss Si/SiO2 waveguides by roughness reduction.” Opt. Lett., **26** (23), 1888–1890, 2001. [Cited on page 26.]

[141] P. Dumon, W. Bogaerts, V. Wiaux, J. Wouters, S. Beckx, J. Van Campenhout, D. Taillaert, B. Luyssaert, P. Bienstman, D. Van Thourhout, and R. Baets. “Low-loss SOI photonic wires and ring resonators fabricated with deep UV lithography.” IEEE Photonics Technol. Lett., **16** (5), 1328–1330, 2004. [Cited on page 26.]

[142] Y. A. Vlasov and S. J. McNab. “Losses in single-mode silicon-on-insulator strip waveguides and bends.” Opt. Express, **12** (8), 1622, 2004. [Cited on pages 26 and 63.]

[143] M. Aspelmeyer, T. J. Kippenberg, and F. Marquardt. “Cavity optomechanics.” Rev. Mod. Phys., **86**, 1391–1452, 2014. [Cited on pages 29, 34, 36, and 141.]

[144] B. E. Little, S. T. Chu, H. A. Haus, J. Foresi, and J. P. Laine. “Microring resonator channel dropping filters.” J. Light. Technol., **15** (6), 998–1005, 1997. [Cited on page 29.]

[145] F. Morichetti, A. Canciamilla, C. Ferrari, M. Torregiani, A. Melloni, and M. Martinelli. “Roughness induced backscattering in optical silicon waveguides.” Phys. Rev. Lett., **104** (3), 1–4, 2010. [Cited on page 30.]

[146] F. Morichetti, A. Canciamilla, M. Martinelli, A. Samarelli, R. M. De La Rue, M. Sorel, and A. Melloni. “Coherent backscattering in optical microring resonators.” Appl. Phys. Lett., **96** (8), 081112, 2010. [Cited on pages 30 and 101.]

[147] B. E. Little, J. P. Laine, and S. T. Chu. “Surface-roughness-induced contradirectional coupling in ring and disk resonators.” Opt. Lett., **22** (1), 4–6, 1997. [Cited on pages 30, 31, and 32.]

[148] T. J. Kippenberg and K. J. Vahala. “Cavity optomechanics: back-action at the mesoscale.” Science, **321**, 1172–6, 2008. [Cited on page 32.]

[149] B. P. Abbott and et al. “GW170104: Observation of a 50-Solar-Mass Binary Black Hole Coalescence at Redshift 0.2.” Phys. Rev. Lett., **118**, 221101, 2017. [Cited on page 32.]

[150] M. Eichenfield, J. Chan, R. M. Camacho, K. J. Vahala, and O. Painter. "Optomechanical crystals." Nature, **462** (7269), 78–82, 2009. [Cited on page 33.]

[151] C. Metzger, I. Favero, A. Ortlieb, and K. Karrai. "Optical self cooling of a deformable Fabry-Perot cavity in the classical limit." Phys. Rev. B, **78**, 035309, 2008. [Cited on page 33.]

[152] P. Meystre, E. M. Wright, J. D. McCullen, and E. Vignes. "Theory of radiation-pressure-driven interferometers." J. Opt. Soc. Am. B, **2** (11), 1830–1840, 1985. [Cited on page 33.]

[153] O. Arcizet, P.-F. Cohadon, T. Briant, M. Pinard, and A. Heidmann. "Radiation-pressure cooling and optomechanical instability of a micromirror." Nature, **444** (7115), 71–74, 2006. [Cited on page 33.]

[154] F. Marquardt, J. G. E. Harris, and S. M. Girvin. "Dynamical multistability induced by radiation pressure in high-finesse micromechanical optical cavities." Phys. Rev. Lett., **96** (10), 1–4, 2006. [Cited on pages 33 and 118.]

[155] A. Schliesser, R. Rivière, G. Anetsberger, O. Arcizet, and T. J. Kippenberg. "Resolved-sideband laser cooling of a micro-mechanical oscillator." 2008 Conf. Quantum Electron. Laser Sci. Conf. Lasers Electro-Optics, CLEO/QELS, 415–419, 2008. [Cited on page 33.]

[156] K. C. Neuman and A. Nagy. "Single-molecule force spectroscopy: Optical tweezers, magnetic tweezers and atomic force microscopy." Nat. Methods, **5** (6), 491–505, 2008. [Cited on page 33.]

[157] M. Li, W. H. P. Pernice, and H. X. Tang. "Reactive Cavity Optical Force on Microdisk-Coupled Nanomechanical Beam Waveguides." Phys. Rev. Lett., **103** (22), 223901, 2009. [Cited on pages 33, 37, and 101.]

[158] M. Wu, A. C. Hryciw, C. Healey, D. P. Lake, H. Jayakumar, M. R. Freeman, J. P. Davis, and P. E. Barclay. "Dissipative and dispersive optomechanics in a nanocavity torque sensor." Phys. Rev. X, **4** (2), 1–11, 2014. [Cited on pages 33 and 101.]

[159] M. L. Gorodetksy, A. Schliesser, G. Anetsberger, S. Deleglise, and T. J. Kippenberg. "Determination of the vacuum optomechanical coupling rate using frequency noise calibration." Opt. Express, **18** (22), 23236–23246, 2010. [Cited on page 34.]

[160] M. Hossein-Zadeh and K. J. Vahala. "Observation of optical spring effect in a microtoroidal optomechanical resonator." Opt. Lett., **32** (12), 1611–1613, 2007. [Cited on page 34.]

[161] M. Bagheri, M. Poot, M. Li, W. P. H. Pernice, and H. X. Tang. "Dynamic manipulation of nanomechanical resonators in the high-amplitude regime and non-volatile mechanical memory operation." Nat. Nanotechnol., **6** (11), 726–732, 2011. [Cited on pages x, 34, 35, and 84.]

[162] B. S. Sheard, M. B. Gray, C. M. Mow-Lowry, D. E. McClelland, and S. E. Whitcomb. "Observation and characterization of an optical spring." Phys. Rev. A, **69** (5), 051801, 2004. [Cited on pages 36 and 106.]

[163] H. Rokhsari, T. J. Kippenberg, T. Carmon, and K. J. Vahala. "Radiation-pressure-driven micro-mechanical oscillator." Opt. Express, **13** (14), 5293, 2005. [Cited on pages 37, 110, and 132.]

[164] M. Gao, F. C. Lei, C. G. Du, and G. L. Long. "Self-sustained oscillation and dynamical multistability of optomechanical systems in the extremely-large-amplitude regime." Phys. Rev. A, **91** (1), 1–7, 2015. [Cited on page 37.]

[165] M. Poot, K. Y. Fong, M. Bagheri, W. H. P. Pernice, and H. X. Tang. "Backaction limits on self-sustained optomechanical oscillations." Phys. Rev. A, **86** (5), 1–8, 2012. [Cited on pages 37, 110, and 135.]

[166] F. Liu, S. Alaie, Z. C. Leseman, and M. Hossein-Zadeh. "Sub-pg mass sensing and measurement with an optomechanical oscillator." Opt. Express, **21** (17), 19555–67, 2013. [Cited on pages 38 and 118.]

[167] J. K. S. Poon, L. Zhu, G. A. Derose, and A. Yariv. "Transmission and group delay of microring coupled-resonator optical waveguides." Opt. Lett., **31** (4), 456–458, 2006. [Cited on page 40.]

[168] J. N. Westwood, V. T. K. Sauer, J. K. Kwan, W. K. Hiebert, and J. C. Sit. "Fabrication of nanoelectromechanical systems via the integration of high surface area glancing angle deposition thin films." J. Micromechanics Microengineering, **24** (6), 065021, 2014. [Cited on page 42.]

[169] J. A. Curcio and C. C. Petty. "The Near Infrared Absorption Spectrum of Liquid Water." J. Opt. Soc. Am., **41** (5), 302, 1951. [Cited on page 45.]

[170] Lumerical Solutions Inc. "Lumerical Solutions FDTD."
URL `http://www.lumerical.com/tcad-products/fdtd/` [Cited on page 45.]

[171] Lumerical Solutions Inc. "Lumerical Solutions MODE."
URL `http://www.lumerical.com/tcad-products/mode/` [Cited on pages 45, 59, 63, 105, 126, 138, 167, and 175.]

[172] Y. Wang. *Grating Coupler Design Based on silicon-on-insulator*. Ph.D. thesis, University of British Columbia, 2013. [Cited on page 46.]

[173] S. S. Verbridge, L. M. Bellan, J. M. Parpia, and H. G. Craighead. "Optically driven resonance of nanoscale flexural oscillators in liquid." Nano Lett., **6** (9), 2109–2114, 2006. [Cited on pages 46 and 47.]

[174] S. Olcum, N. Cermak, S. C. Wasserman, K. S. Christine, H. Atsumi, K. R. Payer, W. Shen, J. Lee, A. M. Belcher, S. N. Bhatia, and S. R. Manalis. "Weighing nanoparticles in solution at the attogram scale." Proc. Natl. Acad. Sci. U. S. A., **111** (4), 1310–5, 2014. [Cited on page 48.]

[175] R. A. Barton, B. Ilic, S. S. Verbridge, B. R. Cipriany, J. M. Parpia, and H. G. Craighead. "Fabrication of a nanomechanical mass sensor containing a nanofluidic channel." Nano Lett., **10** (6), 2058–63, 2010. [Cited on page 48.]

[176] K. L. Ekinci, V. Yakhot, S. Rajauria, C. Colosqui, and D. M. Karabacak. "High-frequency nanofluidics: a universal formulation of the fluid dynamics of MEMS and NEMS." Lab Chip, **10** (22), 3013–25, 2010. [Cited on page 48.]

[177] H. Zhang, Z. Zhao, Y. Wang, Q. Huang, and J. Xia. "Femtogram scale high frequency nano- optomechanical resonators in water." Opt. Express, **25** (2), 1066–1069, 2017. [Cited on page 48.]

[178] C. H. Mastrangelo and C. H. Hsu. "Mechanical stability and adhesion of microstructures under capillary forces - Part II: Experiments." J. Microelectromechanical Syst., **2** (1), 44–55, 1993. [Cited on page 49.]

[179] P. S. Nunes, P. D. Ohlsson, O. Ordeig, and J. P. Kutter. "Cyclic olefin polymers: Emerging materials for lab-on-a-chip applications." Microfluid. Nanofluidics, **9**, 145–161, 2010. [Cited on page 49.]

[180] Applied Nanotools Inc. "NanoSOI fabrication service."
URL `https://www.appliednt.com/` [Cited on page 55.]

[181] C. J. Sarabalis, Y. D. Dahmani, R. N. Patel, J. T. Hill, and A. H. Safavi-Naeini. "Release-free silicon-on-insulator cavity optomechanics." Optica, **4** (9), 1147–1150, 2017. [Cited on page 56.]

[182] H. A. Stone, A. D. Stroock, and A. Ajdari. "Engineering flows in small devices." Annu. Rev. Fluid Mech., **36**, 381, 2004. [Cited on page 57.]

[183] L. Convert, V. Chabot, P. J. Zermatten, R. Hamel, J. P. Cloarec, R. Lecomte, V. Aimez, and P. G. Charette. "Passivation of KMPR microfluidic channels with bovine serum albumin (BSA) for improved hemocompatibility characterized with metal-clad waveguides." Sensors Actuators, B Chem., **173**, 447–454, 2012. [Cited on page 58.]

[184] TOPAS. "TOPAS Cyclic Olefin Copolymer.", 2011. [Cited on page 58.]

[185] F. Xu, P. Datta, H. Wang, S. Gurung, M. Hashimoto, S. Wei, J. Goettert, R. L. McCarley, and S. A. Soper. "Polymer microfluidic chips with integrated waveguides for reading microarrays." Anal. Chem., **79** (23), 9007–9013, 2007. [Cited on page 58.]

[186] P. I. Okagbare, J. M. Emory, P. Datta, J. Goettert, and S. A. Soper. "Fabrication of a cyclic olefin copolymer planar waveguide embedded in a multi-channel poly(methyl methacrylate) fluidic chip for evanescence excitation." Lab Chip, **10**, 66–73, 2010. [Cited on page 58.]

[187] H. Xu, M. Hafezi, J. Fan, J. M. Taylor, G. F. Strouse, and Z. Ahmed. "Ultrasensitive chip-based photonic temperature sensor using ring resonator structures." Opt. Express, **22** (3), 3098–104, 2014. [Cited on page 58.]

[188] E. A. J. Marcatili and S. E. Miller. "Improved Relations Describing Directional Control in Electromagnetic Wave Guidance." Bell Syst. Tech. J., **48** (7), 2161–2188, 1969. [Cited on page 63.]

[189] L. Zhuang, D. Marpaung, M. Burla, W. Beeker, A. Leinse, and C. Roeloffzen. "Low-loss, high-index-contrast Si3N4/SiO2 optical waveguides for optical delay lines in microwave photonics signal processing." Opt. Express, **19** (23), 23162–23170, 2011. [Cited on page 63.]

[190] S. Keller, G. Blagoi, M. Lillemose, D. Haefliger, and A. Boisen. "Processing of thin SU-8 films." J. Micromechanics Microengineering, **18** (12), 125020, 2008. [Cited on page 66.]

[191] S. Dohn, W. Svendsen, A. Boisen, and O. Hansen. "Mass and position determination of attached particles on cantilever based mass sensors." Rev. Sci. Instrum., **78** (10), 103303, 2007. [Cited on page 75.]

[192] S. R. Compton. *Nanofabrication Methods Towards a Photonically-Based Torque Magnetometer for Measurement of Individual Single-Crystalline Yttrium-Iron-Garnet Microstructures*. Ph.D. thesis, 2012. [Cited on page 75.]

[193] S. Dohn, R. Sandberg, W. Svendsen, and A. Boisen. "Enhanced functionality of cantilever based mass sensors using higher modes." Appl. Phys. Lett., **86** (23), 233501, 2005. [Cited on page 77.]

[194] J. E. Sader, M. S. Hanay, A. P. Neumann, and M. L. Roukes. "Mass Spectrometry Using Nanomechanical Systems: Beyond the Point-Mass Approximation." Nano Lett., **18** (3), 1608–1614, 2018. [Cited on pages xiii, 77, and 79.]

[195] A. K. Naik, M. S. Hanay, W. K. Hiebert, X. L. Feng, and M. L. Roukes. "Towards single-molecule nanomechanical mass spectrometry." Nat. Nanotechnol., **4** (7), 445–450, 2009. [Cited on page 78.]

[196] M. L. Povinelli, M. Loncar, M. Ibanescu, E. J. Smythe, S. G. Johnson, F. Capasso, and J. D. Joannopoulos. "Evanescent-wave bonding between optical waveguides." Opt. Lett., **30** (22), 3042–3044, 2005. [Cited on page 81.]

[197] N. Kacem, S. Hentz, D. Pinto, B. Reig, and V. Nguyen. "Nonlinear dynamics of nanomechanical beam resonators: improving the performance of NEMS-based sensors." Nanotechnology, **20** (27), 275501, 2009. [Cited on pages 82, 83, 119, and 121.]

[198] A. H. Nayfeh, W. Kreider, and T. J. Anderson. "Investigation of natural frequencies and mode shapes of buckled beams." AIAA J., **33** (6), 1121–1126, 1995. [Cited on page 84.]

[199] E. Iwase, P.-C. Hui, D. Woolf, A. W. Rodriguez, S. G. Johnson, F. Capasso, and M. Loncar. "Control of buckling in large micromembranes using engineered support structures." J. Micromechanics Microengineering, **22** (6), 065028, 2012. [Cited on page 85.]

[200] V. T. K. Sauer, Z. Diao, J. N. Westwood-Bachman, M. R. Freeman, and W. K. Hiebert. "Single laser modulated drive and detection of a nano-optomechanical cantilever." AIP Adv., **7** (1), 015115, 2017. [Cited on pages xiii, 86, 89, 91, and 93.]

[201] T. Faust, P. Krenn, S. Manus, J. P. Kotthaus, and E. M. Weig. "Microwave cavity-enhanced transduction for plug and play nanomechanics at room temperature." Nat. Commun., **3**, 728, 2012. [Cited on page 86.]

[202] O. E. DeLange. "Optical heterodyne detection." IEEE Spectr., **5** (10), 77–85, 1968. [Cited on page 86.]

[203] S. Gröblacher, K. Hammerer, M. R. Vanner, and M. Aspelmeyer. "Observation of strong coupling between a micromechanical resonator and an optical cavity field." Nature, **460** (7256), 724–727, 2009. [Cited on pages 86 and 160.]

[204] S. Weis, R. Riviere, S. Deleglise, E. Gavartin, O. Arcizet, A. Schliesser, and T. J. Kippenberg. "Optomechanically Induced Transparency." Science (80-.)., **330** (6010), 1520–1523, 2010. [Cited on pages 86, 160, and 161.]

[205] M. R. Kan, D. C. Fortin, E. Finley, K. M. Cheng, M. R. Freeman, and W. K. Hiebert. "Super-rolloff electron tunneling transduction of nanomechanical motion using frequency downmixing." Appl. Phys. Lett., **97** (25), 2010. [Cited on page 87.]

[206] C. Reinhardt, T. Müller, and J. C. Sankey. "Simple delay-limited sideband locking with heterodyne readout." Opt. Express, **25** (2), 1582, 2017. [Cited on page 101.]

[207] A. Yilmaz, S. Schuster, P. Wolf, D. Schmidt, M. Eisele, C. Zimmermann, and S. Slama. "Optomechanical damping of a nanomembrane inside an optical ring cavity." New J. Phys., **19** (1), 013038, 2017. [Cited on page 109.]

[208] G. Anetsberger. *Novel cavity optomechanical systems at the micro-and nanoscale and quantum measurements of nanomechanical oscillators*. Ph.D. thesis, 2010. [Cited on page 109.]

[209] N. Kacem, J. Arcamone, F. Perez-Murano, and S. Hentz. "Dynamic range enhancement of nonlinear nanomechanical resonant cantilevers for highly sensitive NEMS gas/mass sensor applications." J. Micromechanics Microengineering, **20** (4), 045023, 2010. [Cited on pages 118, 119, and 120.]

[210] L. G. Villanueva, E. Kenig, R. B. Karabalin, M. H. Matheny, R. Lifshitz, M. C. Cross, and M. L. Roukes. "Surpassing Fundamental Limits of Oscillators Using Nonlinear Resonators." Phys. Rev. Lett., **110** (17), 177208, 2013. [Cited on page 118.]

[211] X. Y. Lü, J. Q. Liao, L. Tian, and F. Nori. "Steady-state mechanical squeezing in an optomechanical system via Duffing nonlinearity." Phys. Rev. A, **91** (1), 1–7, 2015. [Cited on page 118.]

[212] C. Chen, D. H. Zanette, J. R. Guest, D. A. Czaplewski, and D. Lòpez. "Self-Sustained Micromechanical Oscillator with Linear Feedback." Phys. Rev. Lett., **117** (1), 1–5, 2016. [Cited on page 118.]

[213] S. Krylov, B. R. Ilic, D. Schreiber, S. Seretensky, and H. G. Craighead. "The pull-in behavior of electrostatically actuated bistable microstructures." J. Micromechanics Microengineering, **18** (5), 055026, 2008. [Cited on pages 118 and 120.]

[214] I. Kozinsky, H. W. C. Postma, I. Bargatin, and M. L. Roukes. "Tuning nonlinearity, dynamic range, and frequency of nanomechanical resonators." Appl. Phys. Lett., **88** (25), 1–4, 2006. [Cited on pages 118 and 121.]

[215] C. Doolin, B. D. Hauer, P. H. Kim, A. J. R. MacDonald, H. Ramp, and J. P. Davis. "Nonlinear optomechanics in the stationary regime." Phys. Rev. A, **89** (5), 1–6, 2014. [Cited on pages 118 and 132.]

[216] A. G. Krause, J. T. Hill, M. Ludwig, A. H. Safavi-Naeini, J. Chan, F. Marquardt, and O. Painter. "Nonlinear Radiation Pressure Dynamics in an Optomechanical Crystal." Phys. Rev. Lett., **115** (23), 1–5, 2015. [Cited on pages 118 and 153.]

[217] J. C. Sankey, C. Yang, B. M. Zwickl, A. M. Jayich, and J. G. E. Harris. "Strong and Tunable Nonlinear Optomechanical Coupling in a Low-Loss System." Nat. Phys., **6**, 707–712, 2010. [Cited on page 118.]

[218] G. A. Brawley, M. R. Vanner, P. E. Larsen, S. Schmid, A. Boisen, and W. P. Bowen. "Nonlinear optomechanical measurement of mechanical motion." Nat. Commun., **7**, 10988, 2016. [Cited on pages 118, 160, and 161.]

[219] H. Li, Y. Chen, J. Noh, S. Tadesse, and M. Li. "Multichannel cavity optomechanics for all-optical amplification of radio frequency signals." Nat. Commun., **3**, 1091, 2012. [Cited on pages 118, 119, 120, 121, 132, 136, 137, 146, and 153.]

[220] A. H. Nayfeh, M. I. Younis, and E. M. Abdel-Rahman. "Dynamic pull-in phenomenon in MEMS resonators." Nonlinear Dyn., **48** (1-2), 153–163, 2007. [Cited on page 120.]

[221] R. Lifshitz and M. C. Cross. "Nonlinear Dynamics of Nanomechanical and Micromechanical Resonators." In "Rev. Nonlinear Dyn. Complex.", 1–52. 2009. [Cited on page 120.]

[222] S. Schmid, L. G. Villanueva, and M. L. Roukes. *Fundamentals of Nanomechanical Resonators*. Springer, 2016. [Cited on pages 120 and 121.]

[223] A. H. Nayfeh and D. T. Mook. *Nonlinear Oscillations*. Wiley Classics Library. Wiley, 2008. [Cited on page 121.]

[224] C. Horvath, D. Bachman, R. Indoe, and V. Van. "Photothermal nonlinearity and optical bistability in a graphene-silicon waveguide resonator." Opt. Lett., **38** (23), 5036–9, 2013. [Cited on pages 123 and 126.]

[225] L. Yin and G. P. Agrawal. "Impact of two-photon absorption on self-phase modulation in silicon waveguides." Opt. Lett., **32** (14), 2031, 2007. [Cited on page 123.]

[226] P. B. Deotare, I. Bulu, I. W. Frank, Q. Quan, Y. Zhang, R. Ilic, and M. Loncar. "All optical reconfiguration of optomechanical filters." Nat. Commun., **3** (May), 846, 2012. [Cited on page 123.]

[227] H. K. Tsang, C. S. Wong, T. K. Liang, I. E. Day, S. W. Roberts, A. Harpin, J. Drake, and M. Asghari. "Optical dispersion, two-photon absorption and self-phase modulation in silicon waveguides at 1.5μm wavelength." Appl. Phys. Lett., **80** (3), 416, 2002. [Cited on page 123.]

[228] W. H. P. Pernice, M. Li, and H. X. Tang. "Time-domain measurement of optical transport in silicon micro-ring resonators." Opt. Express, **18** (17), 18438–52, 2010. [Cited on page 123.]

[229] J. Leuthold, C. Koos, and W. Freude. "Nonlinear silicon photonics." Nat. Photonics, **4** (8), 535–544, 2010. [Cited on page 125.]

[230] Q. Lin, O. J. Painter, and G. P. Agrawal. "Nonlinear optical phenomena in silicon waveguides: modeling and applications." Opt. Express, **15** (25), 16604, 2007. [Cited on page 125.]

[231] J. Komma, C. Schwarz, G. Hofmann, D. Heinert, and R. Nawrodt. "Thermo-optic coefficient of silicon at 1550nm and cryogenic temperatures." Appl. Phys. Lett., **101** (4), 041905, 2012. [Cited on page 125.]

[232] V. R. Almeida and M. Lipson. "Optical bistability on a silicon chip." Opt. Lett., **29** (20), 2387–2389, 2004. [Cited on page 125.]

[233] F. Liu and M. Hossein-Zadeh. "Characterization of optomechanical rf frequency mixing/down-conversion and its application in photonic rf receivers." J. Light. Technol., **32** (2), 309–317, 2014. [Cited on page 132.]

[234] C. Huang, J. Fan, R. Zhang, and L. Zhu. "Internal frequency mixing in a single optomechanical resonator." Appl. Phys. Lett., **101** (23), 231112, 2012. [Cited on page 132.]

[235] S. K. Roy. *Characterization of nano-optomechanical system sensor and designing a novel gas chromatography NOMS system for ambient condition gas sensing*. Ph.D. thesis, 2018. [Cited on page 156.]

[236] A. H. Safavi-Naeini, S. Gröblacher, J. T. Hill, J. Chan, M. Aspelmeyer, and O. Painter. "Squeezed light from a silicon micromechanical resonator." Nature, **500** (7461), 185–189, 2013. [Cited on pages 160 and 161.]

[237] Y. Lu, J. Yao, X. Li, and P. Wang. "Tunable asymmetrical Fano resonance bistability in a microcavity-resonator-coupled Mach Zehnder interferometer." Opt. Lett., **30** (22), 3069–3071, 2005. [Cited on pages 160, 163, and 167.]

[238] V. Van and W. N. Herman. "Linearized microring-loaded Mach-Zehnder modulator with RF gain." J. Light. Technol., **24** (4), 1850–1854, 2006. [Cited on page 160.]

[239] S. Darmawan, Y. M. Landobasa, P. Dumon, R. Baets, and M. K. Chin. "Nested-Ring Mach Zehnder Interferometer in silicon-on-insulator." IEEE Photonics Technol. Lett., **20** (1), 9–11, 2008. [Cited on page 160.]

[240] C. Yu, Y. Zhang, X. Zhang, K. Wang, C. Yao, P. Yuan, and Y. Guan. "Nested fiber ring resonator enhanced Mach-Zehnder interferometer for temperature sensing." Appl. Opt., **51** (36), 8873–6, 2012. [Cited on page 160.]

[241] A. Schliesser, G. Anetsberger, R. Rivière, O. Arcizet, and T. J. Kippenberg. "High-sensitivity monitoring of micromechanical vibration using optical whispering gallery mode resonators." New J. Phys., **10**, 095015, 2008. [Cited on page 161.]

[242] J. A. Cox, A. L. Lentine, D. C. Trotter, and A. L. Starbuck. "Control of integrated micro-resonator wavelength via balanced homodyne locking." Opt. Express, **22** (9), 11279–11289, 2014. [Cited on page 161.]

[243] F. Raffaelli, G. Ferranti, D. H. Mahler, P. Sibson, J. E. Kennard, A. Santamato, G. Sinclair, D. Bonneau, M. G. Thompson, and J. C. Matthews. "A homodyne detector integrated onto a photonic chip for measuring quantum states and generating random numbers." Quantum Science and Technology, **3** (2), 025003, 2018. [Cited on page 161.]

[244] A. E. J. Lim, J. Song, Q. Fang, C. Li, X. Tu, N. Duan, K. K. Chen, R. P. C. Tern, and T. Y. Liow. "Review of Silicon Photonics Foundry Efforts." IEEE J. Sel. Top. Quantum Electron., **20** (4), 8300112, 2014. [Cited on page 164.]

[245] W. A. Zortman, D. C. Trotter, and M. R. Watts. "Silicon photonics manufacturing." Opt. Express, **18** (23), 23598–23607, 2010. [Cited on page 167.]

[246] A. V. Krishnamoorthy, X. Zheng, G. Li, J. Yao, T. Pinguet, A. Mekis, H. Thacker, I. Shubin, Y. Luo, K. Raj, and J. E. Cunningham. "Exploiting CMOS Manufacturing to Reduce Tuning Requirements for Resonant Optical Devices." IEEE Photonics J., **3** (3), 567–579, 2011. [Cited on pages 167 and 176.]

[247] A. Liu, L. Liao, D. Rubin, H. Nguyen, B. Ciftcioglu, Y. Chetrit, N. Izhaky, and M. Paniccia. "High-speed optical modulation based on carrier depletion in a silicon waveguide." Opt. Express, **15** (2), 660, 2007. [Cited on page 168.]

[248] D. Patel, V. Veerasubramanian, S. Ghosh, A. Samani, Q. Zhong, and D. V. Plant. "High-speed compact silicon photonic Michelson interferometric modulator." Opt. Express, **22** (22), 26788–802, 2014. [Cited on page 168.]

[249] G. T. Reed, G. Mashanovich, F. Y. Gardes, and D. J. Thomson. "Silicon optical modulators." Nat. Photonics, **4**, 518–526, 2010. [Cited on page 168.]

[250] X. Wang and H. Yun. "OpSIS-IME-001 UBC Measurement Results.", 2013. [Cited on page 168.]